Experiments and Simulations of Autonomous Microscale Robotics

by

JINGFAN YANG

M.S. Chemical Engineering Practice, Massachusetts Institute of Technology, 2019

B.Eng. Chemical and Biomolecular Engineering, Nanyang Technological University, 2017

Submitted to the Department of Chemical Engineering

in partial fulfillment of the requirements for the degree of

DOCTOR OF PHILOSOPHY IN CHEMICAL ENGINEERING

at the

MASSACHUSETTS INTITUTE OF TECHNOLOGY

February 2023

Signature of Author……

Department of Chemical Engineering

Certified by:……...……

Michael S. Strano

Carbon P. Dubbs Professor of Chemical Engineering

Thesis Supervisor

Accepted by:……..……

Patrick S. Doyle

Robert T. Haslam (1911) Professor of Chemical Engineering

Chair, Department Committee on Graduate Students

Experiments and Simulations of Autonomous Microscale Robotics

by

Jingfan Yang

Submitted to the Department of Chemical Engineering on September 21st, 2022 in partial fulfillment of the requirements for the degree of Doctor of Philosophy in Chemical Engineering.

ABSTRACT

Sub-millimeter microscale machines capable of navigating inaccessible spaces and remote locations are steadily approaching reality, with a rich literature emerging on externally actuated and supervised agents. In comparison, progress is slow towards autonomous, intelligent microscale agents. This thesis builds towards fundamental aspects of this pursuit, tackling unanswered questions in robotic functionalities, fabrication techniques, applications, and control. Specifically, (i) I expanded upon the cleanroom-free autoperforation technology to allow facile metal patterning on 2D material surfaces, with which I fabricated mobile electronic microparticles; (ii) Based on experimental observations of autoperforated micro-architectures, I designed and theoretically validated an electrical circuit which integrates real-time access to memory, sensing, and actuation with compatibility to additive technologies and materials as well as significantly reduced design complexity; (iii) I built an *in silico* modeling toolbox which predicts the performance of a user-defined glucose-responsive insulin (GRI) in animals and humans. I demonstrated the model's applicability to aiding the design of microrobotic delivery and monitoring systems circulating in the human body, as well as to the investigation of the unsuccessful clinical translation of a unimolecular GRI; (iv) Lastly, I explored the collective intelligence in the form of emergent self-oscillation, among a group of simple, unassuming microparticles. I studied the counter-intuitive order arising from intentional breakage of the collective's symmetry, and harnessed the stable periodic mechanical motion for the generation of oscillatory electrical currents as well as cyclically driving microrobotic loads. These advances pave the way towards microscale machine intelligence

– either through on-board integration of functionalities or through collective behavior – which enables sophisticated microrobotic tasks without external supervision or manipulation.

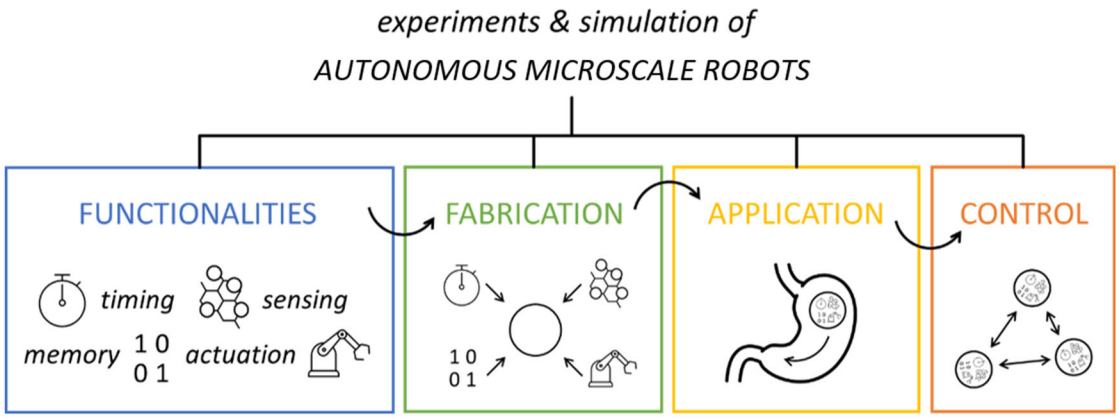

Thesis Supervisor: Michael S. Strano

Title: Carbon P. Dubbs Professor in Chemical Engineering

ACKNOWLEDGEMENTS

I have heard many state that obtaining a PhD degree has been the most difficult thing they have done, but I cannot say that was my personal experience here at MIT – not because my PhD journey has been without challenges (far from it, in fact), but because I am tremendously fortunate to have many wonderful mentors, friends, and family who made my five years in graduate school very enjoyable and rewarding.

First and foremost, I owe my deepest gratitude to my thesis advisor, Prof. Michael Strano, whose passion and vision for science are unparalleled. I am time and again amazed by his breadth and depth of knowledge, by his out-of-the-box way of ideation and problem-solving, and by his leadership which created a lovely environment in the group with intellectual freedom and a culture for teamwork and collaboration. I am confident to say that I have grown significantly professionally and personally working with him, and what I learned from him has transformed me and shaped who I am today. I would also like to thank my thesis committee members, Profs. Daniel Anderson, Jeehwan Kim, and Todd Murphey, for the guidance and wisdom along the way. The opportunity to discuss my work with such a panel of world experts has truly been wonderful. The insights and feedback from their diverse range of perspectives have been extraordinarily valuable to my thesis.

Throughout my PhD I have had the honor to work with many a great scientist in many a research domain. I am thankful for my MURI collaborators, Profs. Dana Randall, Andrea Richa, Daniel Goldman, and Jeremy England, as well as their gifted students Joshua Daymude and Shengkai Li, among many others. I am particularly thankful for my experience working together with Thomas Berrueta, with whom I formed a true $1 + 1 > 2$ collaboration in spite of our vastly different backgrounds and domains of expertise. My theoretical projects on GRI modeling would not have been possible without the expert advice from Profs. Michael Weiss, Faramarz Ismail-Beigi, and Alan Cherrington. Outside of work, I am also indebted to Prof. Charles Cooney, my co-TA Anirudh Nambiar, and my students for a fulfilling experience teaching 10.490. I have the utmost respect for Prof. Cooney's dedication to the education of the next generation of chemical engineers, as well as his antique cartograph collection. I have also found my Communication Fellow and

Teaching Development Fellow roles extremely rewarding thanks to Caitlin Stier, Diana Chien, and Benjamin Hansberry.

My talented colleagues in the Strano Research Group have always supported and inspired me. In particular, I would like to thank Ge Zhang, the brilliantly intelligent and humorous desk clump mate whose camaraderie I will always cherish; Albert Liu, a dear friend, collaborator, and mentor to whom I look up; Volodymyr Koman (Olya, Ezra, and Brielle) and Matthias Kuehne (Dominique), excellent scientists and role models to whom I am grateful for our deep, intellectual conversations; Pingwei Liu, Xun Gong, and Naveed Bakh, who selflessly showed me the ropes at the early stages of my PhD; Allan Brooks and Sungyun Yang, with whom I have the special bond working in the cleanroom together with the bunny suits on. My PhD would have been a lot duller if not for the remarkable friendship with Leslie Cui and Cindy Jin, the scary but fun outdoor adventures and food-coma-inducing dinner parties with whom I will never forget. It has been a great pleasure to get to know and work with amazing visiting scholars and postdocs such as Prof. Mahesh Kumar, Yuwen Zeng, Guangwei He, Yu-Ming Tu, Hyunah Kim, Ivy Dong, Sooyeon Cho, Dorsa Parviz, Daichi Kozawa, Pavlo Gordiichuk, Takeo Ichihara, Sylvia Li, Manki Son, and Cody Ritt; fellow graduate students Zhe Yuan, Kevin Silmore, Daniel Lundberg, Minkyung Park, Tedrick Lew, Thomas Porter, Michelle Quien, Nathan Stover, Gabriel Sanchez, Hohyung Kang, Mike Lee, Ananth Govind Rajan, Cache Hamilton, Anton Cottrill, Daniel Salem, Amandine Ucko, among others; administrators Brenda Pelletier and Aylin Temeloglu; as well as my UROP Allison Wang.

I am very grateful to my many friends made before and during my time at MIT. I owe special thanks to Zhenshu Wang and Nian Liu, for their most sincere friendship and most altruistic support; Liang-Hsun Chen, Srinivasa Pujari, Chun Man Chow, Xiaorui Dong, and Qihui Qian, whose dedication and diligence always inspired me; Yi Ren Sng, my travel companion; Chuliang Song and Jingtian Chen, my dependable buddies who are always there when I need someone to talk to; Qi He, Chin-Chia Hsu, Tzyy-Shyang Lin, Kuangye Lu, Haoran Cai, Siyu Chen, Yiwen Huang, and Wenjie Wang, for the trips we went on, games we played, and meals we shared; Sarah Young, George Fei, and Monica Agrawal, whose cheerfulness and optimism are ever contagious; Kashmira Jirafe, Min Lim, Rongjia Chang, and Erickson Tjoa, who, despite the great distance from me, remain my close friends. I owe my unforgettable Practice School experience to Bridget

Derksen, Michael Pan, Venkat Tirumala, Cameron Halliday, Yohanes Agustinus, Tanvi Kulkarni, as well as the station directors Brian Stutts and Doug Harrison. I am grateful to Profs. Le Yu, David Lou, and Mary Chan for sparking my interest in scientific research as an undergraduate, without whom I would not have come to MIT.

I cannot begin to express my amount of gratitude to my loving family. Being away from home for over a decade, I never have had enough in-person time with my parents, especially since the beginning of the pandemic. Despite the distance, my parents have always supported me unwaveringly. They may not understand everything I work on, but never for a minute stopped believing in me, for which I am grateful. Finally, it was at MIT where I got to know and grew close to the magnificent Joy Zeng. I am fortunate to have her in my life.

RESEARCH OUTPUTS *from* THIS THESIS

Parts of this thesis were published, or will be published, as follows:

Chapters 1 and 2:

Jing Fan Yang, Pingwei Liu, Volodymyr B. Koman, Albert Tianxiang Liu, and Michael S. Strano. 2019. "Synthetic Cells: Colloidal-Sized State Machines." Pp. 361–86 in *Robotic Systems and Autonomous Platforms*. Elsevier.

Albert T. Liu*, Jing Fan Yang*, Lexy N. LeMar, Ge Zhang, Ana Pervan, Todd D. Murphey, and Michael S. Strano. 2021. "Autoperforation of Two-Dimensional Materials to Generate Colloidal State Machines Capable of Locomotion." *Faraday Discussions* 227:213–32.

(* Equal contribution)

Chapter 3:

Jing Fan Yang, Albert Tianxiang Liu, Thomas A. Berrueta, Ge Zhang, Allan M. Brooks, Volodymyr B. Koman, Sungyun Yang, Xun Gong, Todd D. Murphey, and Michael S. Strano. 2022. "Memristor Circuits for Colloidal Robotics: Temporal Access to Memory, Sensing, and Actuation." *Advanced Intelligent Systems* 4(4):2100205.

Chapter 4:

Jing Fan Yang, Xun Gong, Naveed A. Bakh, Kelley Carr, Nelson F. B. Phillips, Faramarz Ismail-Beigi, Michael A. Weiss, and Michael S. Strano. 2020. "Connecting Rodent and Human Pharmacokinetic Models for the Design and Translation of Glucose-Responsive Insulin." *Diabetes* 69(8):1815–26.

Chapter 5:

Jing Fan Yang, Sungyun Yang, Xun Gong, Naveed A. Bakh, Ge Zhang, Allison B. Wang, Michael A. Weiss, and Michael S. Strano. 2022. "In silico investigation of the clinical translatability of competitive clearance glucose-responsive insulins." *In preparation*.

Chapters 6 and 7:

Jing Fan Yang*, Thomas A. Berrueta*, Allan M. Brooks, Albert Tianxiang Liu, Ge Zhang, David Gonzalez-Medrano, Sungyun Yang, Volodymyr B. Koman, Pavel Chvykov, Lexy N. LeMar, Marc Z. Miskin, Todd D. Murphey, and Michael S. Strano. 2022. "Emergent Microrobotic Oscillators via Asymmetry-Induced Order." arXiv: 2205.09814. *Nature Communications.*

(* Equal contribution)

TABLE *of* CONTENTS

Chapter 1:

Introduction

Chapter 2:

Autoperforation of 2D materials as a cleanroom-free integration platform for electronic microscale machines

Chapter 3:

On-board temporal access to memory, sensing, and actuation via a simple memristor array

Chapter 4:

Connecting rodent and human pharmacokinetic models for the design and translation of GRIs

Chapter 5:

In silico investigation of the clinical translatability of competitive clearance glucose-responsive insulins

Chapter 6:

Emergent low-frequency self-oscillation in the microscale and its application as an autonomous oscillatory microgenerator

Chapter 7:

Mechanistic modeling of the emergent microrobotic oscillators

LIST *of* FIGURES

LIST *of* TABLES

CHAPTER 1

Introduction

1.1. Introduction to Microscale Robotics

Microscale robotics started out as a vastly unrealistic artistic concept in science fiction novels and films. For example, in 1966's Fantastic Voyage, referenced in numerous microrobotics publications as a remote research motivation (1–6), a submarine was miraculously shrunken down to the size of a red blood cell, which allowed the crew to repair a wounded brain from inside the patient's body (Figure 1-1A). Far-fetched as it sounded, we have witnessed consistent scientific efforts to make macroscopic robots compact in size, which, on the sub-meter scale, have found real-life applications in rescue assistance and archeological exploration. As shown in Figure 1-1B, miniaturized centimeter- and millimeter-scale "insect-size" robots have been invented owing to massive strides made in materials, mechanical/electronic devices, integration technologies, and control algorithms (7–11).

There are, however, situations on an even smaller scale that are not accessible by these miniaturized but not yet microscopic robotic systems: geological surveys through tiny crevices, injury detection along remote oil and gas pipelines, sensing within enclosed chemical reactors and nanofluidic conduits, and probing, cargo delivery, and even surgery within the human body (12). Towards these application scenarios, devices on the micrometer-scale and under that can harvest energy, power embedded circuits for logic and computation, utilize sensor, and store information into memory present a vision of synthetic systems that function like cellular analogs (13).

As shown in Figure 1-1C, in recent years the field of micron-sized robotics have made strides in supervising and actuating micromachines externally using light (14,15), sound (16,17), and magnetic/electric fields (18–20). These robots have been shown to be particularly relevant to certain biomedical tasks which can be accomplished within a reasonably short time frame and in a controlled environment, such as during a magnetic resonance imaging (MRI) scan (19,21,22). They were also envisioned to act as immobile sensor nodes suitable for Internet-of-Things (IoT) applications (15,23,24), yet their potential to this end remains uncertain given the need for external machinery for wireless power supply and information readout. Additionally, many of these externally controlled "marionettes" were found to be ideal, well-controlled platforms for studying intriguing emergent physics (25–27) as well as testing out novel microrobotic components and methods of integration (14,20).

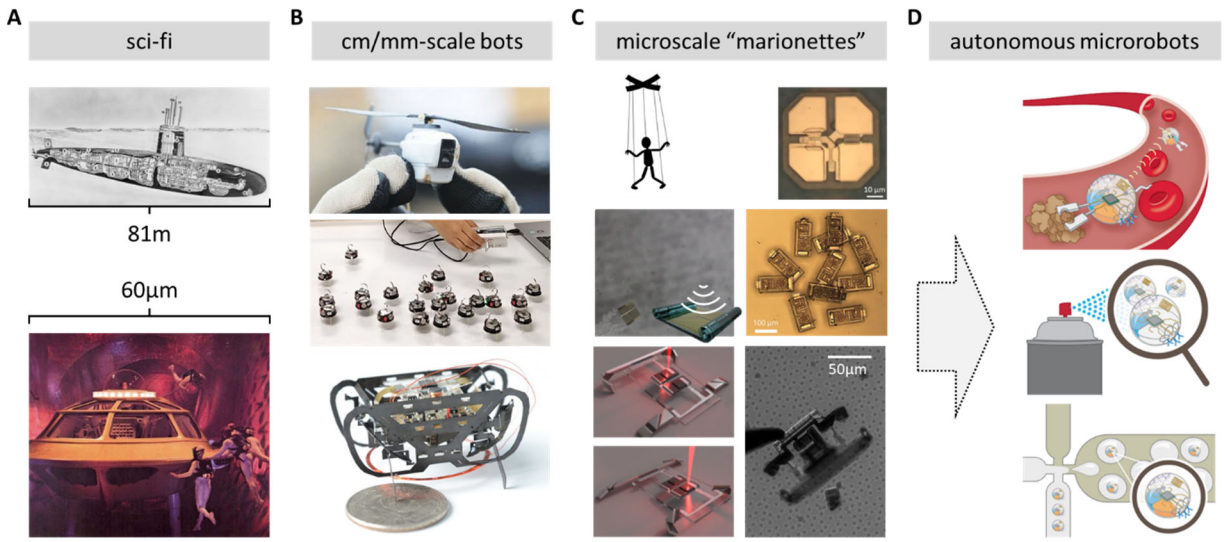

Figure 1-1. Roadmap of microscale robotics. Despite the concept started with (*A*) a vastly unrealistic artistic rendition, years of advancement in materials, devices, integration technologies, and control algorithms pushed the idea towards reality as we witnessed first (*B*) the miniaturization of macroscopic robots to the centimeter- and millimeter-scale, and then recently (*C*) the realization of truly micrometer-scale "marionettes". However, it remains a daunting and central challenge to impart autonomy onto microscale robotics (*D*), required for a multitude of applications where external human monitoring and intervention are impractical.

In contrast to the rich body of literature on microscale robots monitored and supervised by an external operator, complementary progress towards fully autonomous and tetherless agents has been far more gradual (28). While tethered or teleoperated systems offer utility in many a scenario such as microrobot-assisted surgeries as discussed earlier (29), autonomy is necessary in situations where large, remote, or enclosed spaces are to be accessed, or when the targeted missions span a long period of time (Figure 1-2). For instance, should a microrobot be tasked with continuously circulating in the bloodstream of a patient and delivering therapeutics in a targeted fashion, it is impractical to confine the patient over an extended period to an MRI or ultrasound machine for external manipulation and monitoring. Instead, autonomous microscale robots should be able to execute the "sense-think-act" paradigm independently like the envisioned construct sketched in Figure 1-2 (right), where the coordinated interactions among integrated sensing, memory, and actuation functions enable intelligent and simultaneous cargo delivery and long-term monitoring.

More specifically, if the on-board sensor measures local glucose concentrations in the body, and if the actuator triggers a controlled release of insulin, the design essentially composes a

microrobotic form of glucose-responsive insulin (GRI). While GRIs have had a long history of development tracing back to the late-1970s (30), the mechanism has always been dependent on biomolecular and/or polymer properties whose responsiveness is designed by tuning the (bio)chemistry (31,32). A microrobotic GRI (mrGRI), which combines on-board electronics with material properties, could allow for an enhanced freedom of design as well as better control. While existing molecular and polymeric GRIs respond to the real-time local blood glucose, analogous to a proportional controller, mrGRI's designed ability to read its own sensing history opens the possibility of the full proportional-integral-derivative (PID) scheme. Known to enhance the control robustness significantly compared to just a proportional controller, an onboard PID scheme would be particularly beneficial to a task as delicate as blood glucose regulation in a diabetic patient (33). This vision, once realized, could replace existing insulin pump therapies which rely on bulky mechanical devices and sophisticated algorithms to achieve an optimal blood glucose profile.

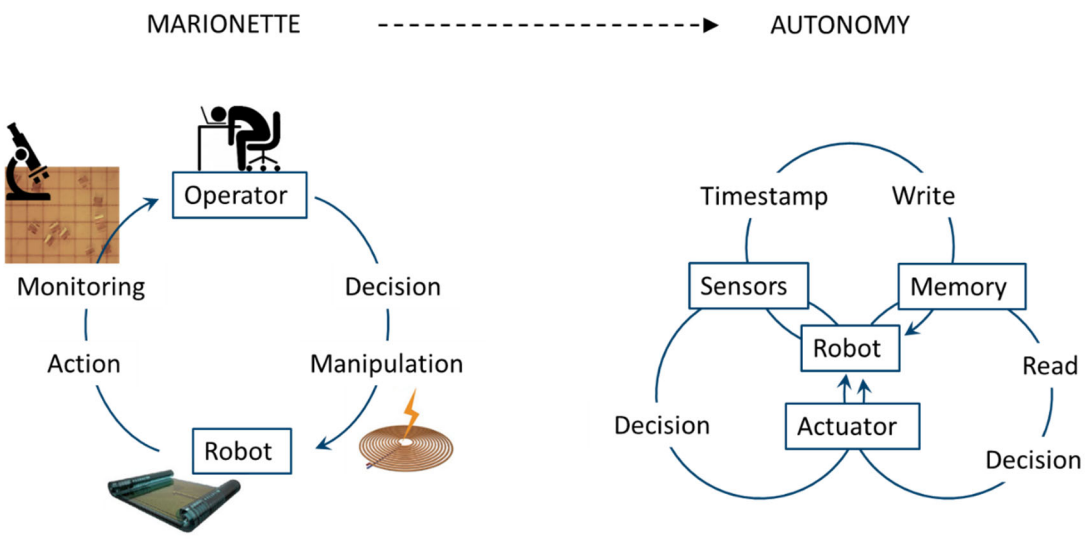

Figure 1-2. Comparison between a "marionette" and an autonomous microscale robot.

1.2. Thesis Organization and Overview

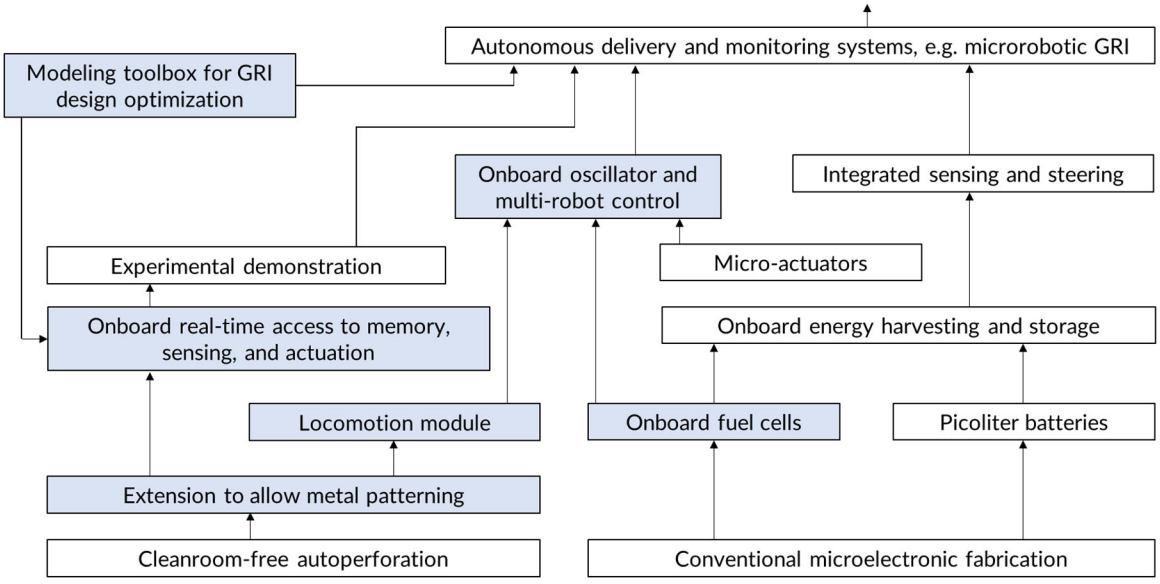

Figure 1-3. Unified vision of an autonomous microrobotic delivery and monitoring system and its relation to the building blocks constructed within our research group and by our collaborators in recent years. The blocks shaded blue are my scientific contributions which will be discussed in detail in this thesis.

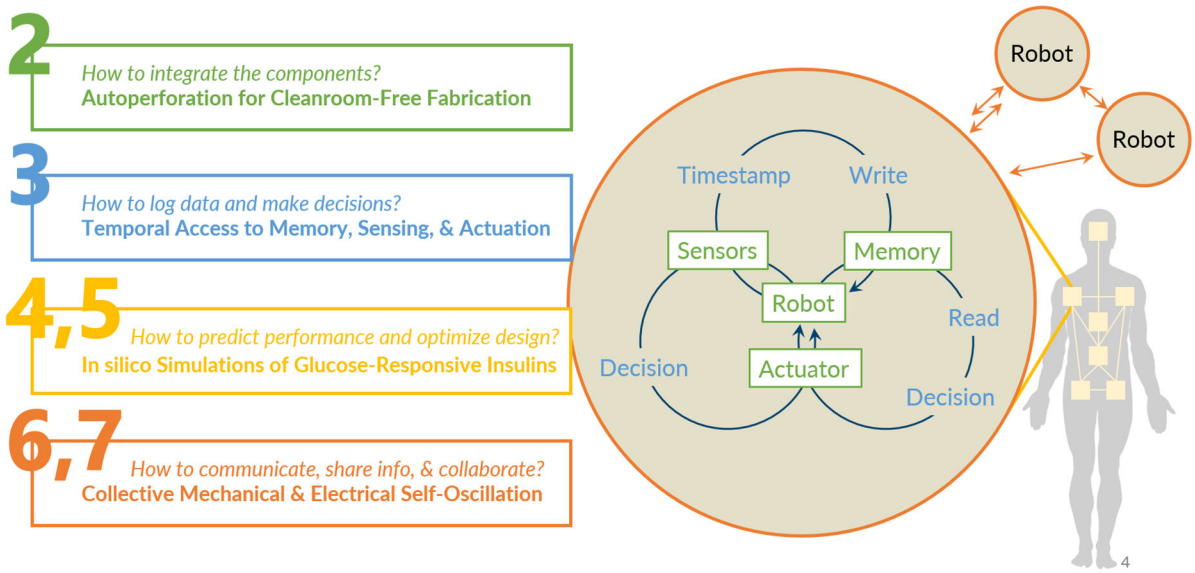

Figure 1-4. Graphic visualization of the thesis' organization and the topic of each chapter.

In this thesis, I detail my scientific contributions to addressing a number of key challenges in autonomous microscale machines via the development of microrobotic functionalities/components, fabrication techniques, architecture for integration, in silico modelling toolbox, as well as control strategies. My thesis fits into a broader vision of the Strano research group as seen in Figure 1-3, where projects are organized to support one another and oriented towards the demonstration of an autonomous delivery and monitoring system such as a mrGRI. Although my research efforts over the past 5 years were far from linear as illustrated in Figure 1-3, I have organized them in this thesis into 4 topics covered in a total of 7 chapters (Figure 1-4).

Specifically, Chapter 2 summarizes the cleanroom-free autoperforation platform for the fabrication of electronic microparticles (34) and introduces my collaborative work in extending the technology to allow surface patterning (35). I demonstrate a facile motility module added to otherwise stationary microparticles, enabled by the patterning of a catalytic metal surface.

On the basis of the architecture of autoperforated microparticles, Chapter 3 describes a lean and compact electrical circuit design that allows micron-scale robots to have real-time access to memory, sensing, and actuation (36), the integration of which had only been attempted with extremely complex integrated circuit. In contrast, our design based on memristor arrays permits the use of a wide range of micrometer-resolution but facile, additive fabrication technologies and correspondingly an expanded set of compatible materials. I computationally study designs that accomplish four autonomous microrobotic tasks of increasing complexity, eventually confirming the feasibility of microrobotic GRIs with coupled circuit and pharmacokinetic simulations.

The pharmacokinetic modeling toolbox, PAMERAH, is described in Chapters 4. The physiology-based model predicts the therapeutic efficacy of GRI candidates from their user-specified mechanism of action, kinetics, and dosage (37,38). While experimental trial-and-errors are costly and time-consuming, PAMERAH is able to scan a large design space for optimal ranges of design parameters. Our parameterized models of humans, rats, mice, and miniature swine further allow us to probe the clinical translatability of a GRI candidate based on its performance across species. At the end of Chapter 2, I use PAMERAH in conjunction with circuit simulations to find the optimal design of a memristor-based microrobotic GRI without having to build a physical prototype first.

In Chapter 5, on the other hand, I apply an upgraded version of PAMERAH called IM^{3}PACT to an existing GRI, MK-2640. As the only GRI to date to have entered the clinical trial stage, MK-2640 failed to replicate its glucose responsiveness promised in the preclinical studies (39–41). With the newly added capability of minipig simulation as well as a mechanistic model of GRIs in the competitive clearance GRI family, I query the potential causes of the unsuccessful translation and whether any variants within the same GRI class could have succeeded.

Contrary to the individual "smart" micromachines with integrated functionalities, Chapter 6 explores an alternative route (and possibly a shortcut) of leveraging the collective behavior in a collective of simple particles (42). Specifically, I show that a collective of Pt-decorated microdisks pinned at the air-H_2O_2 interface exhibit emergent, self-sustained chemo-mechanical oscillations. Interestingly, a stable emergent oscillation is only achieved in many-particle systems when the permutation symmetry is intentionally broken, via a mechanism termed asymmetry-induced order. I devise an on-board fuel cell which translates the periodic mechanical motion into oscillatory electrical signals, which cyclically drive the relaxation and contraction of a state-of-the-art micro-actuator. In Chapter 7, I construct a physics-based mechanistic model which describes the emergent oscillatory behavior with high fidelity, thereby elucidating the roles of the global and local interactions within the particle system.

1.3. References

1. Sitti M. Voyage of the microrobots. Nature. 2009;458(7242):1121–2.
2. Moran JL. Robotic colloids: Engineered self-propulsion at the microscale (and smaller). In: Robotic Systems and Autonomous Platforms [Internet]. Elsevier; 2019. p. 129–77. Available from: http://dx.doi.org/10.1016/B978-0-08-102260-3.00007-X
3. Dey KK, Wong F, Altemose A, Sen A. Catalytic motors - Quo vadimus? Curr Opin Colloid Interface Sci [Internet]. 2016;21:4–13. Available from: https://doi.org/10.1016/j.cocis.2015.12.001
4. Wang W, Duan W, Ahmed S, Mallouk TE, Sen A. Small power: Autonomous nano- and micromotors propelled by self-generated gradients. Nano Today [Internet]. 2013;8(5):531–54. Available from: http://dx.doi.org/10.1016/j.nantod.2013.08.009
5. Wang B, Kostarelos K, Nelson BJ, Zhang L. Trends in micro-/nanorobotics: Materials development, actuation, localization, and system integration for biomedical applications. Adv Mater [Internet]. 2020 Dec 4;2002047:2002047. Available from: https://onlinelibrary.wiley.com/doi/10.1002/adma.202002047
6. Bandari VK, Schmidt OG. System-engineered miniaturized robots: From structure to intelligence. Adv Intell Syst. 2021;3(10):2000284.
7. Slavkov I, Carrillo-Zapata D, Carranza N, Diego X, Jansson F, Kaandorp J, et al. Morphogenesis in robot swarms. Sci Robot. 2018;3(25):eaau9178.
8. Goldberg B, Zufferey R, Doshi N, Helbling EF, Whittredge G, Kovac M, et al. Power and control autonomy for high-speed locomotion with an insect-scale legged robot. IEEE Robot Autom Lett. 2018;3(2):987–93.
9. Jafferis NT, Helbling EF, Karpelson M, Wood RJ. Untethered flight of an insect-sized flapping-wing microscale aerial vehicle. Nature [Internet]. 2019;570(7762):491–5. Available from: http://www.nature.com/articles/s41586-019-1322-0
10. Chen Y, Zhao H, Mao J, Chirarattananon P, Helbling EF, Hyun N seung P, et al. Controlled flight of a microrobot powered by soft artificial muscles. Nature [Internet]. 2019;575(7782):324–9. Available from: http://dx.doi.org/10.1038/s41586-019-1737-7
11. Li S, Batra R, Brown D, Chang H-D, Ranganathan N, Hoberman C, et al. Particle robotics based on statistical mechanics of loosely coupled components. Nature [Internet]. 2019

Mar 20;567(7748):361–5. Available from: https://doi.org/10.1038/s41586-019-1022-9

12. Liu AT, Hempel M, Yang JF, Brooks AM, Koman VB, Zhang G, et al. Colloidal robotics. Under Rev. 2022;
13. Yang JF, Liu P, Koman VB, Liu AT, Strano MS. Synthetic Cells: Colloidal-sized state machines. In: Robotic Systems and Autonomous Platforms [Internet]. 1st Ed. Elsevier; 2019. p. 361–86. Available from: https://linkinghub.elsevier.com/retrieve/pii/B9780081022603000159
14. Miskin MZ, Cortese AJ, Dorsey K, Esposito EP, Reynolds MF, Liu Q, et al. Electronically integrated, mass-manufactured, microscopic robots. Nature [Internet]. 2020 Aug 27;584(7822):557–61. Available from: http://dx.doi.org/10.1038/s41586-020-2626-9
15. Cortese AJ, Smart CL, Wang T, Reynolds MF, Norris SL, Ji Y, et al. Microscopic sensors using optical wireless integrated circuits. Proc Natl Acad Sci [Internet]. 2020 Apr 28;117(17):9173–9. Available from: http://www.pnas.org/lookup/doi/10.1073/pnas.1919677117
16. Esteban-Fernández De Ávila B, Angell C, Soto F, Lopez-Ramirez MA, Báez DF, Xie S, et al. Acoustically propelled nanomotors for intracellular siRNA delivery. ACS Nano. 2016;10(5):4997–5005.
17. Garcia-Gradilla V, Orozco J, Sattayasamitsathit S, Soto F, Kuralay F, Pourazary A, et al. Functionalized ultrasound-propelled magnetically guided nanomotors: Toward practical biomedical applications. ACS Nano. 2013;7(10):9232–40.
18. Hu W, Lum GZ, Mastrangeli M, Sitti M. Small-scale soft-bodied robot with multimodal locomotion. Nature [Internet]. 2018 Feb 24;554(7690):81–5. Available from: http://www.nature.com/articles/nature25443
19. Yu J, Wang B, Du X, Wang Q, Zhang L. Ultra-extensible ribbon-like magnetic microswarm. Nat Commun [Internet]. 2018;9(1):1–9. Available from: http://dx.doi.org/10.1038/s41467-018-05749-6
20. Bandari VK, Nan Y, Karnaushenko D, Hong Y, Sun B, Striggow F, et al. A flexible microsystem capable of controlled motion and actuation by wireless power transfer. Nat Electron [Internet]. 2020;3(3):172–80. Available from: http://dx.doi.org/10.1038/s41928-020-0384-1
21. Wu Z, Li L, Yang Y, Hu P, Li Y, Yang SY, et al. A microrobotic system guided by

photoacoustic computed tomography for targeted navigation in intestines in vivo. Sci Robot. 2019;4(32).

22. Sitti M. Miniature soft robots — road to the clinic. Nat Rev Mater [Internet]. 2018;3(June):1–2. Available from: http://dx.doi.org/10.1038/s41578-018-0001-3
23. Hempel M, Schroeder V, Park C, Koman VB, Xue M, McVay E, et al. SynCells: A 60 × 60 μm2 electronic platform with remote actuation for sensing applications in constrained environments. ACS Nano [Internet]. 2021 May 25;15(5):8803–12. Available from: https://pubs.acs.org/doi/10.1021/acsnano.1c01259
24. Lee S, Cortese AJ, Gandhi AP, Agger ER, McEuen PL, Molnar AC. A 250 μm × 57 μm microscale opto-electronically transduced electrodes (MOTEs) for neural recording. IEEE Trans Biomed Circuits Syst [Internet]. 2018 Dec;12(6):1256–66. Available from: https://ieeexplore.ieee.org/document/8491379/
25. Guzmán-Lastra F, Kaiser A, Löwen H. Fission and fusion scenarios for magnetic microswimmer clusters. Nat Commun. 2016;7.
26. Aubret A, Youssef M, Sacanna S, Palacci J. Targeted assembly and synchronization of self-spinning microgears. Nat Phys [Internet]. 2018;14(11):1114–8. Available from: http://dx.doi.org/10.1038/s41567-018-0227-4
27. Palacci J, Sacanna S, Steinberg AP, Pine DJ, Chaikin PM. Living crystals of light-activated colloidal surfers. Science (80-) [Internet]. 2013 Feb 22;339(6122):936–40. Available from: http://www.sciencemag.org/content/339/6122/936.full.pdf
28. Brooks AM, Strano MS. A conceptual advance that gives microrobots legs. Nature. 2020 Aug 27;584(7822):530–1.
29. Wu Z, Troll J, Jeong HH, Wei Q, Stang M, Ziemssen F, et al. A swarm of slippery micropropellers penetrates the vitreous body of the eye. Sci Adv. 2018;4(11):1–11.
30. Brownlee M, Cerami A. A glucose-controlled insulin-delivery system: Semisynthetic insulin bound to lectin. Science (80-). 1979 Dec 7;206(4423):1190–1.
31. Shen D, Yu H, Wang L, Khan A, Haq F, Chen X, et al. Recent progress in design and preparation of glucose-responsive insulin delivery systems. J Control Release [Internet]. 2020;321(February):236–58. Available from: https://doi.org/10.1016/j.jconrel.2020.02.014
32. Hoeg-Jensen T. Review: Glucose-sensitive insulin. Mol Metab [Internet]. 2021

Apr;46(xxxx):101107. Available from: https://doi.org/10.1016/j.molmet.2020.101107

33. Benesch C, Kuhlenkötter M, Nosek L, Heise T. New clamp-PID algorithm for automated glucose clamps improves clamp quality. J Diabetes Sci Technol. 2022;16(2):408–14.
34. Liu P, Liu AT, Kozawa D, Dong J, Yang JF, Koman VB, et al. Autoperforation of 2D materials for generating two-terminal memristive Janus particles. Nat Mater. 2018 Nov 23;17(11):1005–12.
35. Liu AT, Yang JF, LeMar LN, Zhang G, Pervan A, Murphey TD, et al. Autoperforation of two-dimensional materials to generate colloidal state machines capable of locomotion. Faraday Discuss [Internet]. 2021;227:213–32. Available from: http://pubs.rsc.org/en/Content/ArticleLanding/2020/FD/D0FD00030B
36. Yang JF, Liu AT, Berrueta TA, Zhang G, Brooks AM, Koman VB, et al. Memristor circuits for colloidal robotics: Temporal access to memory, sensing, and actuation. Adv Intell Syst [Internet]. 2022 Apr 23;4(4):2100205. Available from: https://onlinelibrary.wiley.com/doi/10.1002/aisy.202100205
37. Yang JF, Gong X, Bakh NA, Carr K, Phillips NFB, Ismail-Beigi F, et al. Connecting rodent and human pharmacokinetic models for the design and translation of glucose-responsive insulin. Diabetes [Internet]. 2020 Aug 9;69(8):1815–26. Available from: http://diabetes.diabetesjournals.org/lookup/doi/10.2337/db19-0879
38. Taylor SI, DiMarchi RD. Smarter modeling to enable a smarter insulin. Diabetes. 2020;69(August):1608–10.
39. Krug AW, Visser SAG, Tsai K, Kandala B, Fancourt C, Thornton B, et al. Clinical evaluation of MK-2640: An insulin analog with glucose-responsive properties. Clin Pharmacol Ther. 2019 Feb;105(2):417–25.
40. Kaarsholm NC, Lin S, Yan L, Kelly T, Van Heek M, Mu J, et al. Engineering glucose responsiveness into insulin. Diabetes. 2018;67(2):299–308.
41. Moore MC, Kelley DE, Camacho RC, Zafian P, Ye T, Lin S, et al. Superior glycemic control with a glucose-responsive insulin analog: Hepatic and nonhepatic impacts. Diabetes. 2018;67(6):1173–81.
42. Yang JF, Berrueta TA, Brooks AM, Liu AT, Zhang G, Gonzalez-Medrano D, et al. Emergent microrobotic oscillators via asymmetry-induced order. 2022 May 19 [cited 2022 May 24]; Available from: http://arxiv.org/abs/2205.09814

CHAPTER 2

Autoperforation of 2D materials as a cleanroom-free integration platform for electronic microscale machines

This chapter has been adapted from:

Jing Fan Yang, Pingwei Liu, Volodymyr B. Koman, Albert Tianxiang Liu, and Michael S. Strano. 2019. "Synthetic Cells: Colloidal-Sized State Machines." Pp. 361–86 in *Robotic Systems and Autonomous Platforms*. Elsevier.

Albert T. Liu*, Jing Fan Yang*, Lexy N. LeMar, Ge Zhang, Ana Pervan, Todd D. Murphey, and Michael S. Strano. 2021. "Autoperforation of Two-Dimensional Materials to Generate Colloidal State Machines Capable of Locomotion." *Faraday Discussions* 227:213–32.

(* Equal contribution)

2.1. Abstract

In this chapter, I introduce a facile nanofabrication technique called autoperforation for top-down, cleanroom-free fabrication of highly customizable micrometer-sized microstructures. Developed in the Strano group, autoperforation uses controlled brittle fracture to spontaneously cut out these structures sandwiched between 2D materials like graphene, hexagonal boron nitride (hBN), and MoS_2. In addition to the choice of the 2D sheets, the technique also allows flexibility regarding surface functionalization, particle size, and composition of the sandwiched ink. In a follow-up work, I reported an extension to the autoperforation technique which patterns metal onto the particle surfaces via an inversion molding process. We demonstrated the capability of autoperforation with proof-of-concept metal/ion sensing applications in waterbody and soil matrix. Importantly, when memristive inks were used, we showed how each autoperforated cell was equivalent to an array of cross-plane memristive devices connected in parallel, which directly inspired the memristor array architecture for time awareness in §3. Autoperforation has the potential to be a user-friendly and versatile platform technology for facile integration of electronic and materials-based microrobotic modules.

2.2. Introduction to Autoperforation

Top-down photolithography has been the go-to option for microscale robotics with any electronic parts aboard, including sensors (1,2), actuators (3), and energy harvesting modules (4,5). Although conventional top-down lithography is well-suited for extreme fine control over nanoelectronics, it is also known to be time-consuming and requires considerable research infrastructure. With the anticipated increase in circuit complexity as the field matures, the design and fabrication of these lithography-fabricated electronic microrobots will inevitably require involvement of integrated circuit professionals and semiconductor foundries, rendering the research accessible to very few in the academic world. I was part of a team in the Strano group that developed an alternative technique to lithography in the fabrication and integration of electronic microparticles (6). This top-down, cleanroom-free technique, which we call autoperforation, is founded on controlled fracture of two-dimensional materials (2DM).

Although there are indeed precedents for utilizing mechanical failure for fabrication, such as the creation of nanowire tunnel junctions by electromigrative breakage (7,8), reproducibility remains a limitation (9) due to the inherent stochasticity of mechanical breakdown. We found that this may be overcome, however, by specifically imposing a strain field as predicted by Griffith theory, hence obtaining a decent control (10). In his 1921 paper, A. A. Griffith developed the pioneering theory of fraction mechanics, proposing that a crack propagates once the intensity of stress concentration surpasses a critical value specific to the brittle material (11). The criticality emerges because the energy required for overcoming chemical bonding of a certain material scales quadratically with strain, while the relation is linear for the surface energy released upon cracking (6). Length of the crack at which the criticality occurs is referred to as the Griffith length, beyond which cracks extend. As CVD-grown large-area graphene (12), and other 2DMs as well, naturally carries randomly distributed and oriented nanometer-sized defects, crack formation may take place – destined to be stochastic and of no value without a designed strain field, as the Griffith length is uniform across the surface. Engineered Gaussian curvatures (G) in the two-dimensional sheet, nevertheless, induce non-uniform curvature potential (Φ) following Poisson's equation

$$\nabla^2\Phi(\mathbf{x}) = -G(\mathbf{x}), \tag{2-1}$$

which translates to heterogeneous distribution of stress (linked by Young's modulus) and hence

Griffith lengths, as shown in Figure 2-4b. Crack propagation, as a result, has a directional preference and is no longer stochastic, creating an opportunity of guided fracture upon stretching controlled by the strain field. Experimentally confirmed on a macroscopic decimeter-scale polydimethylsiloxane (PDMS) membrane by Mitchell *et al.*, the phenomenon is expected to apply across scales as Equation 2-1 is independent of material properties (10). Indeed, the Monte Carlo simulation presented in Figure 2-4a predicted a guided crack trajectory along the maximal hoop strain path at a scale thousand-fold smaller.

We experimentally confirmed the theoretical analyses following the methodology in Figure 2-4e, with the central idea of creating a strain field by inkjet-printed, isolated islands. Guided by a pair of "invisible scissors", brittle fracture "cuts" the 2DM sheets around an island (Figure 2-4d), forming a dumpling-like structure with the ink sandwiched between a pair of 2DM layers (Figure 2-4f). This is to our best knowledge the first work utilizing 2DM fracture as a tool, since the field of 2DM mechanics had only focused on the fracture mechanism and arresting propagating cracks previously (13,14). Of note, the 2D sheets, ink composition, and microparticle size are all customizable (Figure 2-4c), offering considerable flexibility for particle design and integration of functionalities (6).

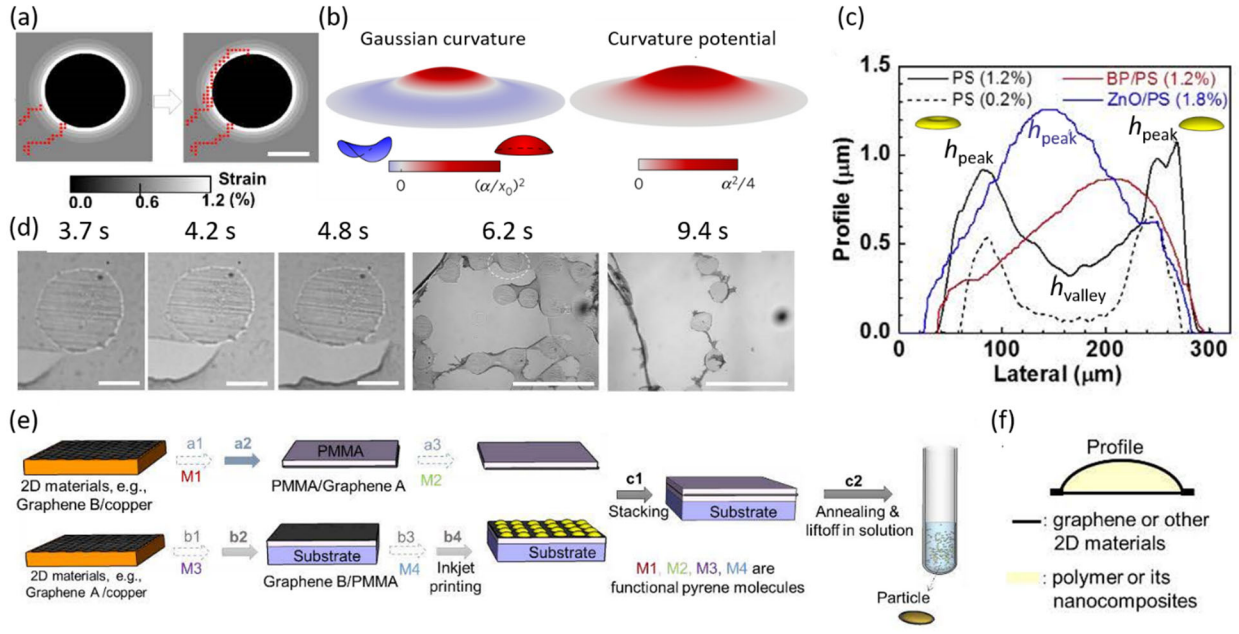

Figure 2-1. Autoperforation of 2DMs. (a) Numerical simulation of the propagating cracks in graphene conforming to a micropillar of h = 1 μm, following the model outlined in Ref. (10). Scale bar: 100 μm. (b) An example showing

how curvatures engineer a strain potential field which can guide fracture growth. (c) Lateral profiles of four autoperforated particles fabricated with 1 nL ink each of different compositions or concentrations. PS filler alone leads to a toroid cell geometry while BP/PS and ZnO/PS fillers lead to convex ellipsoids. (d) Time-resolved fracture propagation in graphene during the liftoff process as observed under an optical microscope. Scale bars: 100 μm for t = 3.7 to 4.8 s, 1 mm for the remainder. (e) Autoperforation protocol with graphene as an example, although other 2DMs may be used as well. (f) Schematic showing the autoperforated structure. Subfigure (b) is adapted from Ref. (10) while the remainder is from Ref. (6).

2.3. Autoperforation-Compatible Metal Patterning

My follow-up work to the original autoperforation report described, among other contributions, an inversion molding technique allowing metals to be patterned on autoperforated cell surfaces (15). As detailed in Figure 2-2, instead of directly printing the ink of choice, we first patterned a graphene sheet with sodium carboxymethyl cellulose (CMC) via inkjet printing. Subsequently, a thin layer of polymethyl methacrylate (PMMA) was spin-coated onto the CMC pattern, filling in the gaps between the CMC features. Given the ionic nature of CMC, immersion of the stack in water overnight leaves behind only PMMA on graphene. Parts of the graphene not covered by polymer, which had been underneath the CMC pattern initially, were then exposed to an electrolyte solution from which a metal can be electroplated onto the 2D material. In Figure 2-2 for instance, we showed the patterning of platinum onto graphene using a platinum (IV) chloride ($PtCl_4$) solution. The rest of the experimental protocol is identical to that used in the original autoperforation technique: We covered the metal-patterned graphene with an additional layer of PMMA and flipped it over. We printed onto the flipped graphene an array of ink dots before covering it with a second sheet of 2DM. The end result following lift-off is an autoperforated microparticle patterned with metal on its surface. A demonstration that became immediately possible is shown in Figure 2-3, where two Pt-decorated autoperforated microparticles were made mobile thanks to the catalyzed H_2O_2 decomposition reaction. As we will see in §7, this demonstration became the basis of my later work on emergent microrobotic oscillators.

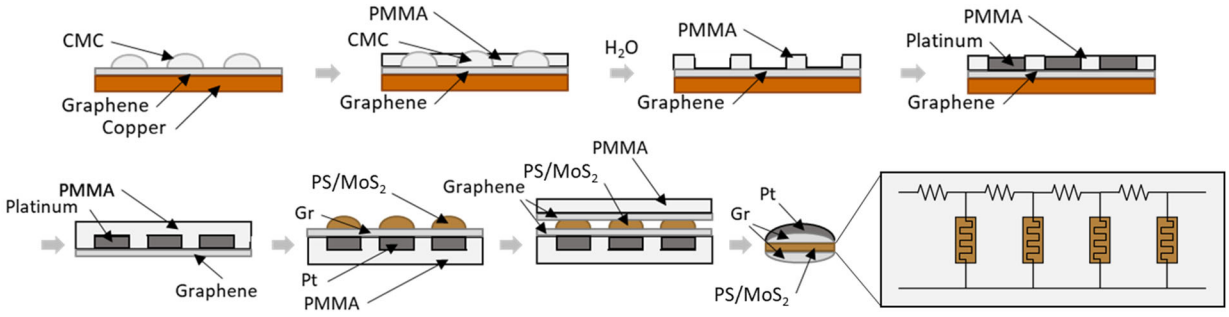

Figure 2-2. Inversion molding technique for metal-patterned autoperforated cells.

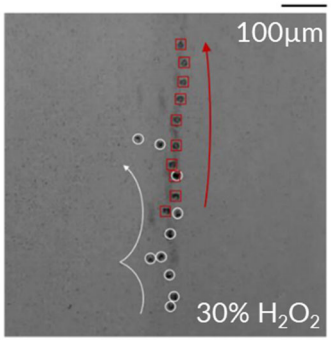

Figure 2-3. Superimposed images of sequential frames show the locomotion of two mobile Pt/graphene microparticles (white circles and red squares). Arrows indicate the migration direction. Scale bar, 100 µm.

2.4. Autoperforation for Integration of Electronic Memory

The utility as micron-scale electronics that handles the storage and processing of sensed information is a key component of our vision (Figure 1-2). Graphene has a well-documented high electrical conductivity (16) as confirmed by experiments (6), which showed that the in-plane electrical conductance values differ greatly between graphene-polystyrene-graphene cells ($\approx 10^{-5}$ S) and the polystyrene filler alone ($\approx 10^{-15}$ S). Given that the two graphene terminals are isolated from each other as confirmed by electrical characterization, the drastic discrepancy in in-plane conductivity enables autoperforated graphene particles to function as two-terminal through-plane electronics when in prolate orientation. By compositing the polystyrene ink with 0.9 wt% of memristive phosphorene nanoflakes, we could fabricate memristive switches across the particle interior (6).

It would be worthwhile to spend a paragraph here introducing memristors, or memory resistors, which are particularly promising non-volatile information storage modules for microscale robots

such as autoperforated electronic particles. Conceptualized by Chua in 1971 and materialized in 2008, a memristor is a device whose resistance is a function of its voltage history (17–19). As the physical state variable is no longer voltage nor electrical charge but the resistance, information storage without the need of a constant power supply becomes feasible, thus the so-called "non-volatility" (19). In digital applications, memristors are switched "ON" beyond V_{th} and are kept "OFF" otherwise. V_{th} of typical memristors spans 1 to 3 V (20), though recent years have witnessed the emergence of many devices of low programming voltages, such as the MoO_x/MoS_2 sandwiched heterostructure reported by Bessonov and co-workers (21). The readers are directed to a number of recent review articles where a rich library of memristive materials is documented (22,23).

The two-terminal resistive switching characteristic to memristors was observed in graphene-phosphorene/polystyrene-graphene particles (Figure 2-4a), consistent with the earliest reports of memristive behaviors by the Williams team at Hewlett-Packard (18,24). During a 0 to 4 to 0 V voltage scan, a memristive particle switched from its high-resistance state (HRS) to low-resistance state (LRS) at a threshold voltage (≈ 1.5 V as in the right half of Figure 2-4a). The switching was reversed when a negative bias was applied during a 0 to -4 to 0 V scan, shown in the plot's left half. Despite the low weight fraction of phosphorene, the memristor ON/OFF ratio reached as high as 10^4 when read at 0.2 V, while in the meantime the undoped graphene-polystyrene-graphene controls were merely memristive (Figure 2-4a). Akin to a number of memristors previously reported (18,25,26), electromigration of mobile oxygen vacancies and ions governed the reversible resistive switching behavior. The observed memristivity at such a low phosphorene content was ascribed to the percolated network formed by loading phosphorene into intra-particle spaces among polystyrene nanoparticles (6).

It is important to note how the sandwiched memristive ink functions as a group of submicron-scale vertical memristor devices connected in parallel, each linked to two graphene terminals (Figure 2-4c). The memristor elements in the same autoperforated cell may be individually turned on and off by local application of a voltage across the cell at any two contact points – one on each graphene sheet. The domain size, or how fine the resolution can be, is defined by the current spreading radius in the ink and practically by the probe (for reading/writing/erasing) dimensions, whichever is larger. The claim was supported by the demonstration in Figure 2-4b. Using a 5 μm tip, an

autoperforated cell ($d \approx 250$ µm) was divided into a 15-bit memory on which each bit could be separately written (by a positive scan to 4 V), erased (by a negative scan to –4 V), or read (at 0.2 V). The letters "M", "I", and "T" were selectively written onto the cell sequentially with an average ON/OFF ratio on the order of 10^4. While the memory had 15 bits in the demonstration, a higher resolution can be realized with smaller probes, only bounded by current spreading. With the inversion molding technique for metal patterning (15), incorporation of metal contacts under the top 2DM layer could provide reference points for the individual bits, aiding manual reading and writing operations.

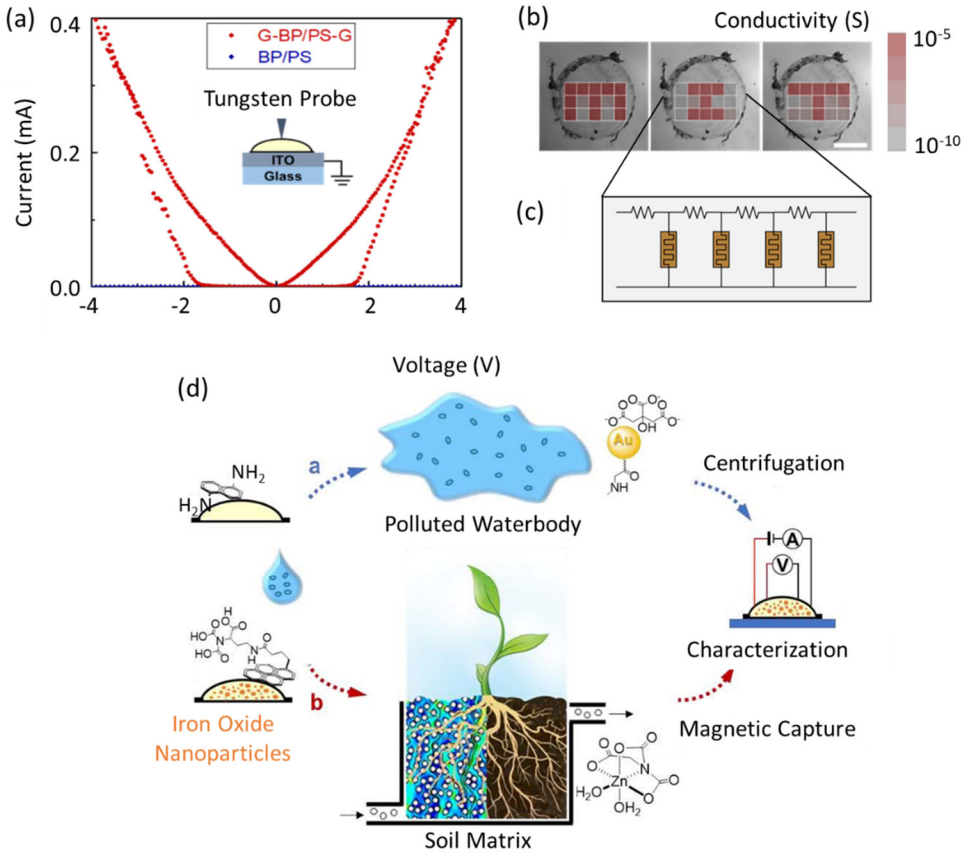

Figure 2-4. Memristive properties and demonstrated applications of autoperforated electronic particles. (a) Cross-plane *I-V* curves for memristive graphene-phosphorene/polystyrene-graphene (0.9 wt% of phosphorene in the ink) and just polystyrene. Switching from OFF to ON for the previous takes place at approximately 1.5 V, while no memristive behavior is seen in the insulating polystyrene ink. (b) Mapping of "M", "I", and "T" onto a 3 × 5 grid on a graphene-phosphorene/polystyrene-graphene cell by selective writing (with 0 to 4 V scans) and erasing (with 0 to -4 V scans). Scale bar: 100 µm. (c) Schematic illustrating how each memristive particle is equivalent to a cross-plane array of memristor elements connected in parallel. (d) Schematic illustrating the demonstrated applications of surface-

functionalized autoperforated particles as waterbody (the upper route) and soil matrix (the bottom route) sensors for metals or ions. The particles may be dispersed into the respective environments and recaptured by centrifugation or magnet (if a ferromagnetic ink is used), before the stored information is read out. Adapted from Ref. (6).

2.5. Applications Demonstrated

Figure 2-4d displays the schematic of two environmental monitoring applications in water and soil. Surface functionalizability of autoperforation encouraged incorporation of sensor modules that capture metals or ions in the environment. For waterbody sensing, we functionalized graphene-polystyrene-graphene particles with surface amine groups capable of capturing citrate-coated gold nanoparticles present at a concentration of 6×10^{12} particles per mL. Dispersed into a polluted waterbody, the cells were recollected via centrifugation and characterized by conductance measurement or Raman spectroscopy (Figure 2-4d, top). Similarly, magnetic cells modified with nitrilotriacetic acid (NTA) detected zinc cations through ligand binding while infiltrating the soil matrix. An essential nutrient for plant proteins, zinc in excess could however lead to intoxication (28). With iron oxide in the ink, the particles could be magnetically propelled and captured, before being read out optically or electrically (Figure 2-4d, bottom). Presence of gold nanoparticles raised the cell surface conductance by an order in contrast to the control, in addition to a redshift of the graphene 2D Raman peak for optical characterization. Zinc cations lowered the surface conductance by two orders of magnitude while causing a blueshift in graphene 2D peak. Note that, nevertheless, the sensing applications demonstrated in this publication did not utilize the memristive property. Information was instead stored in the entire surface of the cell, while a parallel array of memristors could greatly enhance the memory density.

2.6. References

1. Koman VB, Liu P, Kozawa D, Liu AT, Cottrill AL, Son Y, et al. Colloidal nanoelectronic state machines based on 2D materials for aerosolizable electronics. Nat Nanotechnol [Internet]. 2018 Sep 23;13(9):819–27. Available from: http://www.nature.com/articles/s41565-018-0194-z
2. Hempel M, Schroeder V, Park C, Koman VB, Xue M, McVay E, et al. SynCells: A 60 × 60 μm2 electronic platform with remote actuation for sensing applications in constrained environments. ACS Nano [Internet]. 2021 May 25;15(5):8803–12. Available from: https://pubs.acs.org/doi/10.1021/acsnano.1c01259
3. Miskin MZ, Cortese AJ, Dorsey K, Esposito EP, Reynolds MF, Liu Q, et al. Electronically integrated, mass-manufactured, microscopic robots. Nature [Internet]. 2020 Aug 27;584(7822):557–61. Available from: http://dx.doi.org/10.1038/s41586-020-2626-9
4. Cortese AJ, Smart CL, Wang T, Reynolds MF, Norris SL, Ji Y, et al. Microscopic sensors using optical wireless integrated circuits. Proc Natl Acad Sci [Internet]. 2020 Apr 28;117(17):9173–9. Available from: http://www.pnas.org/lookup/doi/10.1073/pnas.1919677117
5. Bandari VK, Nan Y, Karnaushenko D, Hong Y, Sun B, Striggow F, et al. A flexible microsystem capable of controlled motion and actuation by wireless power transfer. Nat Electron [Internet]. 2020;3(3):172–80. Available from: http://dx.doi.org/10.1038/s41928-020-0384-1
6. Liu P, Liu AT, Kozawa D, Dong J, Yang JF, Koman VB, et al. Autoperforation of 2D materials for generating two-terminal memristive Janus particles. Nat Mater. 2018 Nov 23;17(11):1005–12.
7. Park H, Lim AKL, Alivisatos AP, Park J, McEuen PL. Fabrication of metallic electrodes with nanometer separation by electromigration. Appl Phys Lett. 1999;75(2):301–3.
8. Bellisario DO, Liu AT, Kozawa D, Han R, Harris JK, Zabala RB, et al. Experimental observation of real time molecular dynamics using electromigrated tunnel junctions. J Phys Chem C [Internet]. 2017 Oct 12;121(40):22550–8. Available from: https://doi.org/10.1021/acs.jpcc.7b08228
9. Bellisario DO, Ulissi Z, Strano MS. A quantitative and predictive model of

electromigration-induced breakdown of metal nanowires. J Phys Chem C. 2013;117(23):12373–8.

10. Mitchell NP, Koning V, Vitelli V, Irvine WTM. Fracture in sheets draped on curved surfaces. Nat Mater. 2017;16(1):89–93.
11. Griffith AA. The phenomena of rupture and flow in solids. Philos Trans R Soc A Math Phys Eng Sci [Internet]. 1921;221(582–593):163–98. Available from: http://rsta.royalsocietypublishing.org/cgi/doi/10.1098/rsta.1921.0006
12. Li X, Cai W, An J, Kim S, Nah J, Yang D, et al. Large-area synthesis of high-quality and uniform graphene films on copper foils. Science (80-) [Internet]. 2009 Jun 5;324(5932):1312–4. Available from: http://www.sciencemag.org/cgi/doi/10.1126/science.1171245
13. Wang S, Qin Z, Jung GS, Martin-Martinez FJ, Zhang K, Buehler MJ, et al. Atomically sharp crack tips in monolayer MoS2 and their enhanced toughness by vacancy defects. ACS Nano [Internet]. 2016 Nov 22;10(11):9831–9. Available from: http://pubs.acs.org/doi/10.1021/acsnano.6b05435
14. Cao C, Mukherjee S, Howe JY, Perovic DD, Sun Y, Singh CV, et al. Nonlinear fracture toughness measurement and crack propagation resistance of functionalized graphene multilayers. Sci Adv [Internet]. 2018 Apr 6;4(4):eaao7202. Available from: http://advances.sciencemag.org/lookup/doi/10.1126/sciadv.aao7202
15. Liu AT, Yang JF, LeMar LN, Zhang G, Pervan A, Murphey TD, et al. Autoperforation of two-dimensional materials to generate colloidal state machines capable of locomotion. Faraday Discuss [Internet]. 2021;227:213–32. Available from: http://pubs.rsc.org/en/Content/ArticleLanding/2020/FD/D0FD00030B
16. Liu P, Cottrill AL, Kozawa D, Koman VB, Parviz D, Liu AT, et al. Emerging trends in 2D nanotechnology that are redefining our understanding of “Nanocomposites.” Nano Today [Internet]. 2018 Aug;21:18–40. Available from: https://doi.org/10.1016/j.nantod.2018.04.012
17. Chua L. Memristor-The missing circuit element. IEEE Trans Circuit Theory [Internet]. 1971;18(5):507–19. Available from: http://ieeexplore.ieee.org/document/1083337/
18. Strukov DB, Snider GS, Stewart DR, Williams RS. The missing memristor found. Nature. 2008;453(7191):80–3.

19. Borghetti J, Snider GS, Kuekes PJ, Yang JJ, Stewart DR, Williams RS. Memristive switches enable stateful logic operations via material implication. Nature [Internet]. 2010;464(7290):873–6. Available from: http://dx.doi.org/10.1038/nature08940
20. Sangwan VK, Jariwala D, Kim IS, Chen KS, Marks TJ, Lauhon LJ, et al. Gate-tunable memristive phenomena mediated by grain boundaries in single-layer MoS2. Nat Nanotechnol [Internet]. 2015;10(5):403–6. Available from: http://dx.doi.org/10.1038/nnano.2015.56
21. Bessonov AA, Kirikova MN, Petukhov DI, Allen M, Ryhänen T, Bailey MJA. Layered memristive and memcapacitive switches for printable electronics. Nat Mater. 2015;14(2):199–204.
22. Wang Z, Wu H, Burr GW, Hwang CS, Wang KL, Xia Q, et al. Resistive switching materials for information processing. Nat Rev Mater [Internet]. 2020;5(3):173–95. Available from: http://dx.doi.org/10.1038/s41578-019-0159-3
23. Yang JJ, Strukov DB, Stewart DR. Memristive devices for computing. Nat Nanotechnol [Internet]. 2013;8(1):13–24. Available from: http://dx.doi.org/10.1038/nnano.2012.240
24. Yang JJ, Pickett MD, Li X, Ohlberg DAA, Stewart DR, Williams RS. Memristive switching mechanism for metal/oxide/metal nanodevices. Nat Nanotechnol [Internet]. 2008 Jul 15;3(7):429–33. Available from: http://www.nature.com/articles/nnano.2008.160
25. Shibuya K, Dittmann R, Mi S, Waser R. Impact of defect distribution on resistive switching characteristics of Sr2TiO4 thin films. Adv Mater. 2010;22(3):411–4.
26. Lee M-J, Lee CB, Lee D, Lee SR, Chang M, Hur JH, et al. A fast, high-endurance and scalable non-volatile memory device made from asymmetric Ta2O5-x/TaO2-x bilayer structures. Nat Mater [Internet]. 2011;10(8):625–30. Available from: http://dx.doi.org/10.1038/nmat3070
27. Hanlon D, Backes C, Doherty E, Cucinotta CS, Berner NC, Boland C, et al. Liquid exfoliation of solvent-stabilized few-layer black phosphorus for applications beyond electronics. Nat Commun [Internet]. 2015 Dec 15;6(1):8563. Available from: http://www.nature.com/articles/ncomms9563
28. Broadley MR, White PJ, Hammond JP, Zelko I, Lux A. Zinc in plants. New Phytol [Internet]. 2007 Mar;173(4):677–702. Available from: http://doi.wiley.com/10.1111/j.1469-8137.2007.01996.x

CHAPTER 3

On-board temporal access to memory, sensing, and actuation via a simple memristor array

This chapter has been adapted from:

Jing Fan Yang, Albert Tianxiang Liu, Thomas A. Berrueta, Ge Zhang, Allan M. Brooks, Volodymyr B. Koman, Sungyun Yang, Xun Gong, Todd D. Murphey, and Michael S. Strano. 2022. "Memristor Circuits for Colloidal Robotics: Temporal Access to Memory, Sensing, and Actuation." Advanced Intelligent Systems 4(4):2100205.

3.1. Abstract

Micrometer-scale robots capable of navigating enclosed spaces and remote locations are approaching reality. However, true autonomy remains an open challenge despite substantial progress made with externally supervised and manipulated systems. To accelerate the development of autonomous microrobots, we seek alternatives to conventional top-down lithography. Such additive technologies like printing, coating, and colloidal self-assembly allows for rapid prototyping and access to novel materials, such as polymers, bio- and nanomaterials. On the basis of recent experimental findings that memristive networks can be rapidly printed and lifted off as electronic microparticles, we introduce an alternative design paradigm based on arrays of two-terminal memristive elements that enables real-time use of memory, sensing, and actuation in microrobots. We validate several memristor-based designs representing key building blocks towards robotic autonomy: tracking elapsed time, timestamping a rare event, continuously cataloguing time-indexed data, and accessing the collected information for a feedback-controlled response as in a robotic glucose-responsive insulin, as a test problem. Our computational results establish an actionable framework for microrobotic design – Tasks normally requiring complex circuits can now be achieved with self-assembled and printed memristor arrays within microparticles.

3.2. Introduction

The potential impact of robots capable of realizing *sense-think-act* cycles at the micrometer scale has been widely appreciated across fields for decades (1–3). While recent work has made strides in supervising and actuating micromachines externally using light (4,5), sound (6,7), and magnetic/electric fields (8–10), complementary progress towards fully autonomous and tetherless agents has been more gradual (11). To date, the critical challenge of integrating various on-board microscale components (12) has been targeted using integrated circuit (IC) microfabrication. As an alternative, recent experimental findings have shown that parallel arrays of memristors can be rapidly printed *en masse* and lifted-off as a microparticle swarm with the use of facile additive technologies. Based on these results, we present and validate the design of an alternative memristor-based circuit architecture compatible with additive fabrication methods and emerging materials. Our materials-based design of on-board electronics enables untethered autonomous microrobots to sense, think, and act via temporal access to on-board sensing, memory, and actuation. These capabilities embody surprisingly powerful computation within a simple circuit comprising only two-terminal resistive elements.

Over the course of miniaturizing macroscopic robotics to centi- and millimeter scales, innovations in individual robotic components such as actuators (13–15), controllers (16), and power electronics (17,18) have proven critical, exemplified by the recent autonomous flight of an insect-sized robot (19). These improved components are still tied together by on-board IC chips in miniature robots, unchanged from their larger-scale counterparts (20,21).

On the other hand, IC chips are less common in microrobots, or colloidal robots, which we define as micrometer-scale robots that can be dispersed in a fluid (22). To this end, a few research groups have fabricated sophisticated immobile sensor nodes (23–26) that exceed 250 μm in size and are externally supervised or monitored, with key tasks outsourced off-board such as recording of the sensed information. The infrequent breakthroughs in this area are contrasted with a rich body of literature on actuation (4,27–30), locomotion (31–35), energy harvesting/storage (36,37), and sensing modules (38–41) for autonomous colloidal robotics. These components, which often tolerate a lower fabrication resolution but require IC-incompatible novel materials, present an opportunity for emerging fabrication platforms like inkjet printing (38,42–44), screen printing

(45,46), stamping (47), and colloidal self-assembly (48,49). Naturally, an accompanying micrometer-resolution construct is needed to integrate and coordinate the individual robotic functionalities on a micron-sized entity.

To this end, there have been efforts towards robotic components that are inherently dual-functional. For example, sensing is integrated with actuation (29) or locomotion (50) using responsive materials, which have found wide applicability in autonomous targeted delivery (51–53). Nonetheless, tasks such as autonomous data gathering remain challenging with intrinsic material properties alone. On the other front, self-propelled micromotors can develop additional capabilities as a collective, such as swarming and self-assembly (54). Advanced collective tasks such as separation and peer recruitment, however, are not yet demonstrated in micrometer-scale systems, as they require coordinated execution of sensing, data processing, memory updating, and actuation steps on-board (55–57).

Moreover, certain robotic components lack a design at the micrometer scale realizable with additive fabrication unlike on-board sensors and actuators. The most prominent example is a timekeeping mechanism, which is essential for feedback control and computation (58–60). While timekeeping may seem ancillary to autonomy, all Turing-equivalent models of computation rely on sequential logging of states as they evolve (61), which tracking time allows one to do. In the absence of chronometry, basic control-theoretic notions of stability, robustness, and task-performance become impossible to guarantee in any but the most trivial of control problems (62,63). While there have been relevant efforts based on time-dependent diffusion (64), materials erosion (41), and biological cell activity (65), their temporal information is only communicated to the operator in the end and isolated from other robotic elements, if any. By contrast, temporal access to the memory, sensors, and actuators on-board is desired for microrobots that sense, think, and act autonomously.

Herein, we develop a design framework that allows micron-scale robots to have real-time access to memory, sensing, and actuation. The lean and compact electrical circuit only comprises simple, two-terminal resistive elements: memristors in parallel bridged by fixed or chemiresistors. This dramatic reduction in complexity from conventional microchips thus permits the use of a wide range of micrometer-resolution but facile fabrication technologies. In turn, they expand the arsenal

of compatible materials to include polymers, biomaterials, nanoparticles, and their composites (42,66,67). We computationally study designs that accomplish four autonomous microrobotic tasks of increasing complexity: (i) logging a robot's excursion time; (ii) detecting and timestamping a rare chemical event; (iii) collecting and cataloging a series of time-indexed data; and (iv) accessing the measurement data stored on-board and implementing feedback control, as in a closed-loop insulin delivery system. These results validate our framework based exclusively on two-terminal resistive elements whereby tasks that normally require complex circuit design can be achieved with relatively simple components and connectivity.

3.3. Colloidal Robotics Based on Memristors

A memristor is a *memory-resistor* whose resistance is modulated by its current history (68,69), switching between a high- and a low-resistance state (R_{OFF} and R_{ON}, Figure 3-1A). Each memristor doubles as both a simple two-terminal switch as well as a non-volatile memory bit. Unlike a typical random-access memory, a memristor sustains the stored information without a power source. The switch/memory dual functionality, together with memristors' small footprint and stackability (70), makes possible a compact and energy-efficient electrical circuit compatible with colloidal robotics.

The classical model of a memristor's switching dynamics (68,71–73) is illustrated in Figure 3-1B: A moving phase boundary partitions a memristor into two interconvertible regions of resistivity R_{OFF} and R_{ON}. A memristor n's instantaneous resistance – or *memristance* – is:

$$M_n(t) = R_{ON} w_n(t) + R_{OFF}\left[1 - w_n(t)\right] \tag{3-1}$$

where $w_n(t) \in [0, 1]$ is the nondimensionalized location of the partition. When an electrical current $I_n(t)$ passes through the memristor, its dynamics is governed by:

$$\frac{d}{dt} w_n(t) = \frac{\mu R_{ON}}{L^2} I_n(t) \tag{3-2}$$

for a device of effective length L and an average mobility μ which characterizes the electromigrative drift of the charged dopants. $M_n(t)$ is in turn a function of the entire current history $I_n(0 \rightarrow t)$. The current-voltage relation over a single memristor n (I_n-V_n) takes a nonlinear form:

$$V_n(t) = M_n(t) I_n(t) = \left\{ R_{\mathrm{ON}} w_n(t) + R_{\mathrm{OFF}} \left[1 - w_n(t) \right] \right\} I_n(t), \tag{3-3}$$

which explains the pinched hysteresis loop in the experimental *I-V* curve in Figure 3-1A, a key fingerprint of a memristor (74). If the initial condition is given for w_n and the driving voltage $V_n(t)$ is known, the memristance can be tracked over time by solving the differential equation.

Although a number of more involved memristor models have emerged over the years that include detailed descriptions of the complex microscopic physics (75,76), we base our simulations in this work on the widely-employed classical compact model above, which is proven to be optimal for circuit- and system-level simulations and validation (77,78). That said, all our results forward hinge only on the most general memristive behaviors, and the conclusions remain true should a different mathematical model be applied.

3.4. On-Board Time Awareness

Shown in Figure 3-1C, the simple memristor array architecture comprises a voltage source V_0., an array of memristors in parallel (M_n, n = 1, 2, 3…), and the interspersing resistors – all two-terminal elements. The simplest task is to record on-board the single variable of *excursion time*, defined as the global time that has passed since the robot's deployment, independent of the events encountered. This passive task can be accomplished without any sensing and actuation functions. In this work, we set V_0 = 1V unless otherwise noted. The voltage may be supplied by either harvested (e.g. a solar cell or a photodiode) or stored energy (e.g. a zinc-air battery), both of which have been miniaturized for sub-100μm-scale applications (5,39,79,80). While the basic fixed resistors are commonly found in memristor circuits as secondary parasitic electrical elements, for instance to account for the wiring resistance (81), they are essential in our architecture to create the *one-at-a-time switching sequence* that encodes time (Figure 3-1D): Assuming an initial condition where all memristors are ON ($M_n = R_{\mathrm{ON}}$, $\forall n$), any current would preferentially pass through M_1 closest to the energy source. Consequently, M_1 is selectively switched OFF, or at least largely, before the current bypasses the now highly resistive M_1 and starts switching OFF M_2. Likewise, M_3, M_4, and so forth are sequentially shut OFF, thereby encoding the passage of time in the respective memristive states.

We replicate the one-at-a-time switching sequence with circuit simulations of a 7-memristor discrete array (M_n, n = 1 to 7, §3.8.1). Shown in Figure 3-1G, the final set of memory states is a function of the excursion time. For example, if we release the autonomous robots are retrieved at t = 144s, the final memristor states read [OFF OFF OFF ON ON ON ON]. In comparison, robots remaining in the environment for a longer 180s report [OFF OFF OFF OFF ON ON ON], since more memristors are switched OFF as time progresses. This mechanism of reading time off the collective memristor states is an exact analogy to the renowned Galileo thermometer (Figure 3-12), for which temperature is encoded as the rise/fall states of a set of floats of varying densities (82).

An array of memristors in parallel can also be fabricated by laying down a continuous layer of memristive ink between two resistive 2D sheets (Figure 3-1E) via, for instance, inkjet printing (38,83). Memristive inks have been reported to be made from an array of polymers, composites, and nanoparticles/flakes (39,84). Our prior experimental works (38,83) show that arrays of electronic particles 20 to 1000μm in size can be stamped out from the sandwich stack *en masse* (Figure 3-1F, §3.9.4). The technique allows a memristor array to be fabricated altogether via high-throughput coating or printing (85,86), saving the trouble of defining discrete memristors and interconnects. This continuous implementation is represented by a mathematical model built upon the single memristor dynamics and cable theory (§3.8.2). We numerically simulate the resultant coupled partial differential equations with the method of lines. Figure 3-1H shows the same sequential switching behavior observed in the discrete simulations. In this case, location of the spatial boundary between ON-state memristors and those switched OFF marks the excursion time. As time passes, an increasing portion of the memristive layer adopts the highly resistive state. The ON/OFF boundary thus propagates further away from V_0 with time. Experimentally, the boundary's location would be marked by an abrupt drop in the local cross-plane resistance, which can be pinpointed by sampling with a basic probe (38).

The readout variability introduced by measuring the memristor states is an important practical consideration. Similarly, cost-effective additive fabrication platforms such as printing and coating may introduce a higher degree of device variability as compared to lithography, where uniformity is an ultimate pursuit. To test our design's robustness to variations, we simulate large populations of discrete memristor arrays with a series of variabilities in their intrinsic ON-state memristance

R_{ON}, fixed resistor resistivity R_R, voltage supply V_0, or extrinsic measurement accuracy. Assuming normal distribution, we draw 400 samples for each level of relative standard deviation (0 to 20%) and for each of the four parameters. The data presented in Figure 3-1I state that even with a large variability of 20% in any of the parameters, accurate excursion time is read from at least 56.0% of the arrays. Since autonomous cell-sized robots are by default deployed in sizable batches, an accurate collective readout is affirmed so long as the majority (> 50%) report the same reading. In other words, this memristor array is robust to more than 20% of intrinsic and extrinsic variabilities. To put this wide error tolerance in perspective, the relative variation in R_{ON} can be consistently controlled below 8% in the latest spin-coated memristor devices of a wide range of materials (87–90).

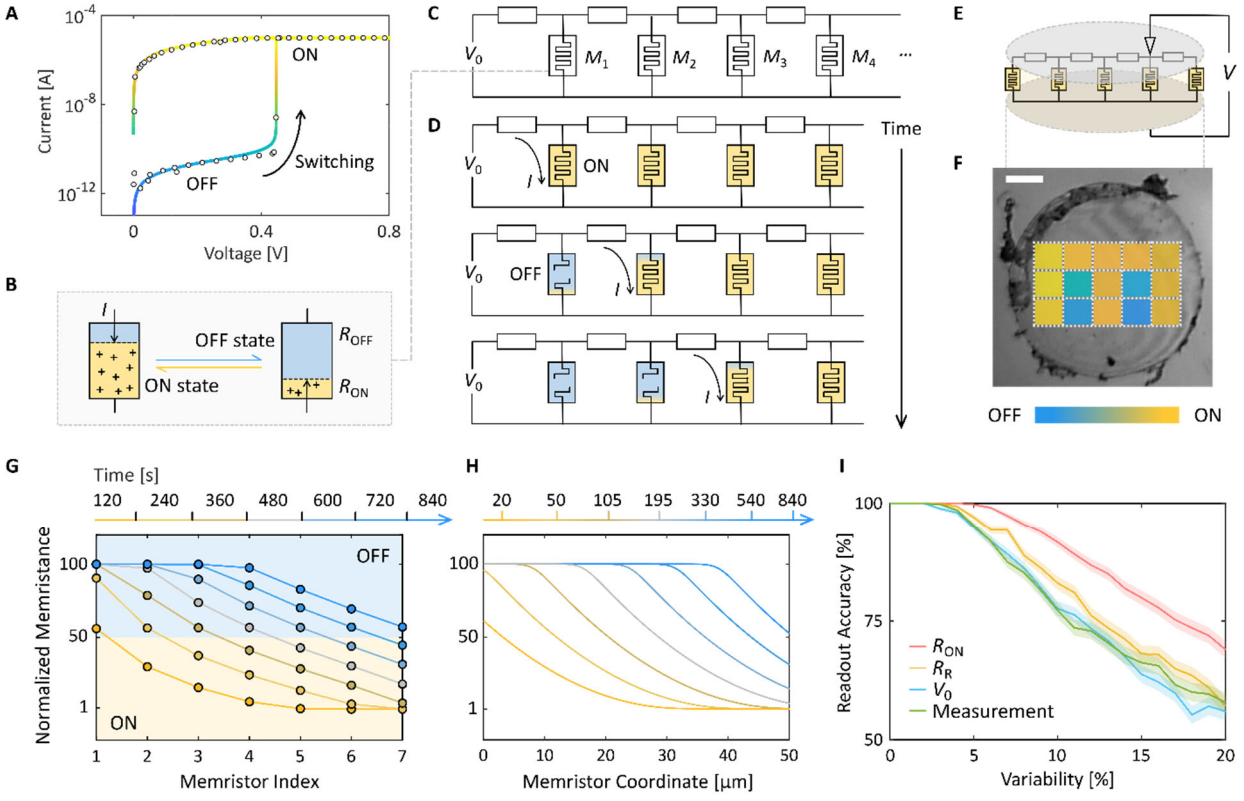

Figure 3-1. *A*: The experimental (circles) and simulated (colored curve) I-V relations of a representative memristor which is switched from OFF to ON. Experimental data digitized from Ref. (91). The memristance ranges from 37.5kΩ (ON, yellow) to 10GΩ (OFF, blue). *B*: The classical model of a single memristor's switching dynamics, in which the memristor is turned OFF or ON as a current *I* shifts the phase boundary. *C*: The memristor array architecture which comprises an energy input V_0, memristors M_n in parallel bridged by either fixed resistors for logging excursion time or chemiresistors as sensors. *D*: The sequential switching phenomenon along a memristor array illustrated. As time elapses, the initially ON memristors are switched OFF sequentially. The final memristor states therefore encode time.

E: Literature has shown that a continuous matrix of memristive ink material printed or coated between resistive 2D sheets is equivalent to an array of memristors in parallel. *F*: On a particle stamped out from the sandwich stack, different regions of the continuous memristive layer can be selectively switched ON/OFF by an applied voltage with the currents diffusing slowly. Scale bar, 50μm. Data adapted from Ref. (38). *G*: Simulated normalized memristance of 7 discrete memristors in parallel. Memristors are sequentially switched OFF as time elapses. $V_0 = 1\text{V}$, $\mu/L^2 = 1\text{s}^{-1}\text{V}^{-1}$, $\alpha = R_{OFF}/R_{ON} = 100$. *H*: Simulated normalized memristance of a continuous memristor array. The switched OFF region of the memristive layer expands over time. $V_0 = 1\text{V}$, $\mu/L^2 = 1\text{s}^{-1}\text{V}^{-1}$, $R_R = 1.75\text{k}\Omega/\mu\text{m}$, $\alpha = 100$. *I*: Even with a high variability in R_{ON}, R_R, V_0, or with a high measurement error of 20%, the majority of the 400 simulated memristor arrays report the correct excursion time. As microrobots are deployed and retrieved in batches, this allows the correct time to be interpreted.

3.5. Detecting and Timestamping a Rare Event

In addition to passively recording the excursion time, a microrobot with basic sensors should allow its history to be tracked. In the example scenario illustrated in Figure 3-2A, a robot travels down a pipeline where the oxygen concentration is low throughout except for a leaky region. The leak's location and length are of interest.

We integrate the sensing capability with timing and memory by simply substituting the fixed resistors in Figure 3-1C with chemiresistors, whose conductance is modulated by the concentration of an analyte. Chemiresistors have already been used in cell-sized robots as a sensing device. Examples include ammonia and triethylamine sensors fabricated from just a sheet of MoS_2 monolayer (39,92). The rich literature of chemiresistive materials offers solution to sense pH, metal ions, biomolecules, as well as small and large gas molecules with a relative resistivity change (the response ratio) of up to several thousands (93–95).

In a memristor array, if the circuit's chemiresistance increases as a response to a change in the local chemical environment, sequential switching of the parallel memristors slows down and vice versa. With a high chemiresistor sensitivity, the presence of an analyte beyond a threshold can in essence pause subsequent switching, and in turn pause the propagation of the ON/OFF boundary seen in Figure 3-1H above. The chemiresistors may be *reversible*, meaning they resume the pristine resistance once the analyte is no longer sensed. The discrepancy between the time recorded by this array and the excursion time therefore signals the duration of exposure to a high analyte concentration. On the other hand, the halt to memristor switching is permanent if the analyte binds

irreversibly to the chemiresistors as in the case of the aforementioned MoS_2 sensing surface (39). The very instant of entering the analyte-rich region is thus frozen in this case. As a result, the tri-array configuration in Figure 3-2B records the onset time of a sensing event, its duration, and the excursion time respectively with memristors bridged via irreversible chemiresistors, reversible chemiresistors, and fixed resistors. On the contrary, if a lower-than-usual chemical concentration is to be detected, there are chemiresistors of inverted responsiveness available that are only conductive under sufficient analyte exposure (94).

Figure 3-2C shows the circuit simulation results for the pipeline leak scenario, where the memristor arrays together detect and timestamp a sensing event. Before the robot enters the leaky region, memristor arrays with reversible and irreversible chemiresistors behave identically to an ordinary, non-responsive array (left panels, t = 100s). Upon entering the leaky region, however, arrays with chemiresistors paused as the excursion time advances (center panels, t = 320s). Of the two, only the array with reversible chemiresistors (green) is released from the interruption after the robot travels past the leak after t = 320s. The simulation in the right panels shows that, of the 450s excursion time, eventually, the irreversible array (red) clocks only the 100s preceding the leaky region, whereas the reversible array clocks 230s: 100s prior to as well as 130s after experiencing the leak. That is, from the final memristor array states, we can extract the robot's temporal history regarding the sensing event – in this case an onset at t = 100s and a duration Δt = 220s. With the average longitudinal velocity computed from the pipeline length and the excursion time, the temporal information can then be translated into the leak location and length. While we focus on probing the chemical micro-environment here, the local temperature, pressure, and presence of light may be detected as well by substituting the chemiresistors with thermistors, force-sensing resistors, or photoresistors, all of which printing-compatible or solution-processable (96–98).

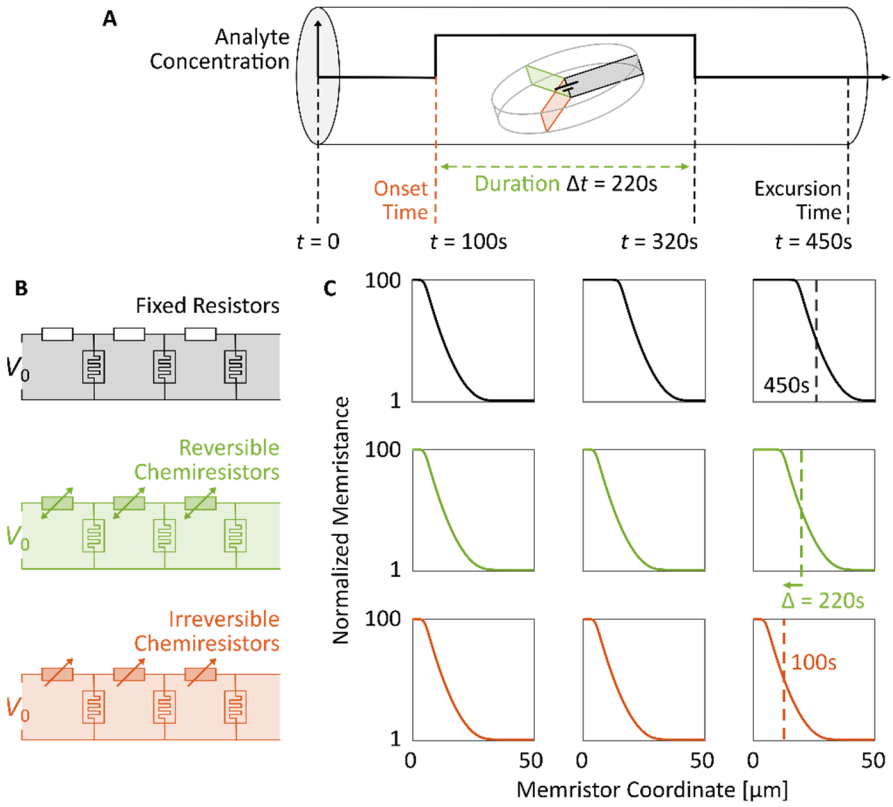

Figure 3-2. *A*: Illustration of a sensing robot traveling down a pipeline with an oxygen-rich leak region to be detected and reported. *B*: Memristor arrays with fixed resistors, reversible chemiresistors, and irreversible chemiresistors. *C*: Memristor states of the three respective arrays (top down: black, green, and red) at t = 100s, 320s, and 450s (left to right), which corresponds to the time right before the robot enters the leak region, exits the leak region, and ends the voyage. The panel for t = 450s shows that the final memristor states allow the excursion time, the duration, and the onset time to be extracted, and in turn location and length of the leak. V_0 = 1V, μ/L^2 = 1 $s^{-1}V^{-1}$, α = 100, oxygen concentration $[O_2]$ = 250ppm for $t \in$ [100s, 320s] and 0 otherwise. The chemiresistor response $R_R([O_2])$ follows that described in Ref. (99).

3.6. Extension to Multivariable Sensing

We expanded upon the 1D time-recording array design above for logging multi-variable information in the form of a 2D set of memristor states. A 2D memristor array further exploits the planarity of electronic microparticles stamped out of a continuous sandwich stack, previously seen in Figure 3-1F (§3.9.4). A multi-variable sensing robot allows, for instance, detection of the locations and sizes of an unknown number of separate leaks (Figure 3-16), or more generally

registration of time-indexed data of the immediate surroundings. As an example, Figure 3-3A presents a scenario where an enclosed space's spatial distribution of an analyte is to be probed in the form of time-concentration tuples.

The 2D architecture in Figure 3-3B consists of a series of 1D sensing arrays branching out along the *y* axis from another 1D memristor array with fixed resistors (the *trunk*) along the *x* axis. As demonstrated by the schematics and simulation results in Figure 3-3B-E (§3.8.3), the trunk memristors are sequentially shut OFF as time progresses, successively delivering electric voltage to the branches further away. Meanwhile, a *circuit breaker* memristor joins each branch to the trunk. A short while after a branch is delivered power, this circuit breaker is switched OFF, thereby blocking further current flow. The non-volatile memristors on the branch are thus frozen thereafter. The overall effect is a sequential activation of the branch arrays along *y*, each activated for only a short time window.

From the perspective of a single memristor branch, it is powered only after some time *t* as the trunk memristors switch progressively along *x*. The memristors on this branch then start to sequentially switch OFF for Δt, the timescale of switching a circuit breaker. Importantly, because the speed of sequential memristor switching along a branch is modulated by the chemiresistance, the extent each branch is turned OFF during Δt is a monotonic function of the instantaneous analyte concentration in the local environment. The concentrations experienced by the colloidal robot at t_1, t_2, t_3, *etc.* can be quantitatively read out from the respective branches. The two dimensions of the memristor state map (the branches along *y* and trunk along *x*) therefore encode the two variables of data we collect (analyte concentration and time, respectively), as seen in Figure 3-3F. The full 2D circuit simulation shown corroborates the design concept: The hypothesized sinusoidal profile (the solid curve) is very well matched by the memristor states of the array (the 2D map overlaid underneath). In the case of a realistic time trajectory recorded in a jacketed continuously stirred tank reactor (100,101), the memristor array readout again conforms to the actual concentration profile (Figure 3-3G), suggesting that colloidal robots equipped with a 2D memristor array could function as ubiquitous, mobile sensor nodes within otherwise inaccessible chemical and bioreactors.

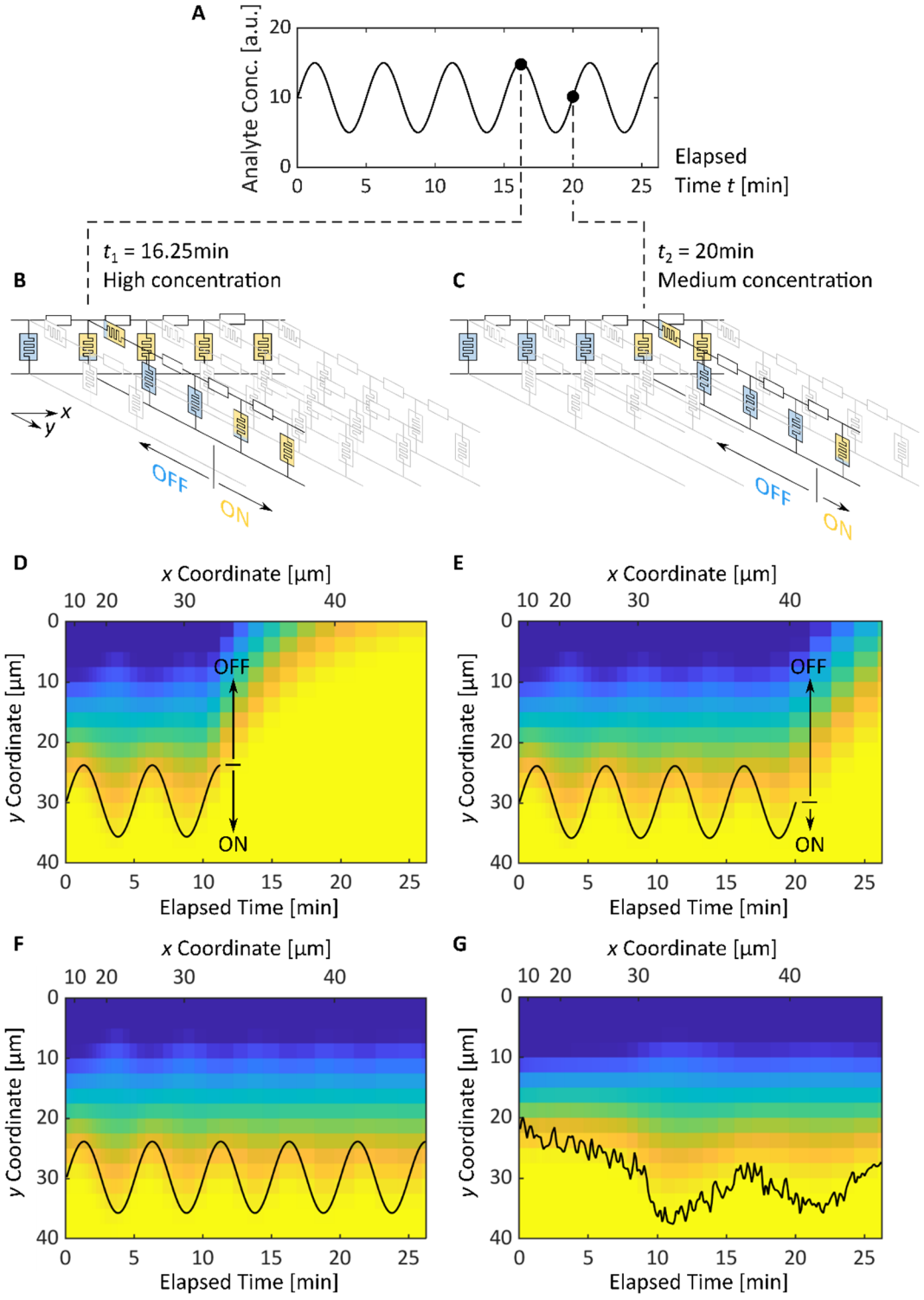

Figure 3-3. *A*: An example of a colloidal robot's history to be recovered from the 2D memristor states. *B* and *C*: Schematics of the 2D memristor array architecture at t = 16.25min and 20min, when the robot detected a high and medium concentration of analyte, respectively. The different concentrations are reflected in the corresponding branches as the different extent of switching. Blue, OFF; yellow, ON. α = 200. *D* and *E*: The 2D memristor states at t

= 16.25min and 20min. The branches are sequentially activated over time, and each encoding the analyte concentration of a certain *t*. *F* and *G*: The final 2D memristor states of a robot experiencing a sinusoidal and realistic analyte profile, respectively. The profiles overlaid on top as solid curves conform well to memristor array readouts. Parameter values used in the simulations are listed in §3.8.3.

3.7. Feedback-Controlled Autonomous Drug Delivery

As an example of more complex colloidal robotic tasks of biomedical relevance, we consider intelligent cargo delivery. Many works have shown that it can be accomplished at high precision via external supervision and control (9,27,32,102), well suited for short-term biomedical applications (11). Complementarily, for scenarios where external communication or localization is difficult, or where the robots carry out long-term missions, autonomy is valuable.

Some passive drug delivery systems are occasionally referred to as autonomous microrobots. They are typically polymeric particles responsive to local cues such as abnormal pH or certain biomolecules (103,104). For example, a *glucose-responsive insulin* (GRI) analogue circulates through a diabetic patient's body unsupervised, releasing doses of insulin whenever the local blood glucose (BG) level – a chemical cue – spikes. The GRI's autonomy liberates the patients from the burden of constant monitoring and painful injections (105–107). Compared to the autonomy, however, the adaptability and modularity of these particles are limited. Using the GRI as a model engineering application, we instead dock the memristor array circuit with an *electric* actuation mechanism found in immobile *implantable chips*. Such an actuation scheme allows for scheduled dosing of multiple medications (108–110), and the clean-cut electric switching enables controlled and pulsatile delivery (108,111). Our architecture is illustrated in Figure 3-4A, where a drug-loaded electric actuation module accesses a memristor array's time-indexed data and delivers cargo accordingly.

In an inhomogeneous environment, the analyte's instantaneous local concentration modulates the memristive states on the corresponding branch. Beyond (below) a threshold concentration (e.g., of glucose, $[G]_{th}$), memristors on the entire said branch would be switched OFF if equipped with chemiresistors that are conductive at a higher (lower) concentration. If so, the voltage at the terminus reaches a threshold V_{th} and actuates the release of a cargo electrically from either an electroactive polymer pocket (112) or a microreservoir (113,114). Loading drugs into reversible

electroactive polymers is a standard procedure in the literature (115). Therefore, a glucose-sensing memristor array coupled with an insulin-loaded reservoir compose a microrobotic GRI, which we simulate as a proof-of-concept.

We confirm the feasibility of the microrobotic GRI concept via *in silico* pharmacokinetic modeling with PAMERAH (116), a published full-body diabetes model trained with rodent data (§3.8.4, Figure 3-7). Given any user-specified reservoir kinetics, PAMERAH translates the electrical response of a memristor circuit into a diabetic subject's BG trajectory. Figure 3-4B(i) shows one such trajectory corresponding to a particular memristor array with an insulin load of 0.018IU, a reservoir release half-life $t_{1/2}$ of 6h, and $[G]_{th}$ = 225mg/dL. The simulated colloidal robot performs adequately as a GRI: Initially with a BG beyond the 240-mg/dL hyperglycemic limit (117), the electrified reservoir releases insulin into the surrounding bloodstream. Owing to the quick release kinetics, the GRI is able to bring the BG down to the non-threatening range within 2 hours – an important criterion for good GRIs (118). By reversibly pausing the release whenever BG drops below $[G]_{th}$, the microrobotic GRI also prevents overdoses of insulin at all times (signified by BG < 75mg/dL), which may lead to dangerous and sometimes fatal hypoglycemia (119,120). The memristor array maintained the BG at a healthy level throughout the 24-hour period, during which it effectively suppressed three postprandial (*after meal*) glucose excursions within 2 hours.

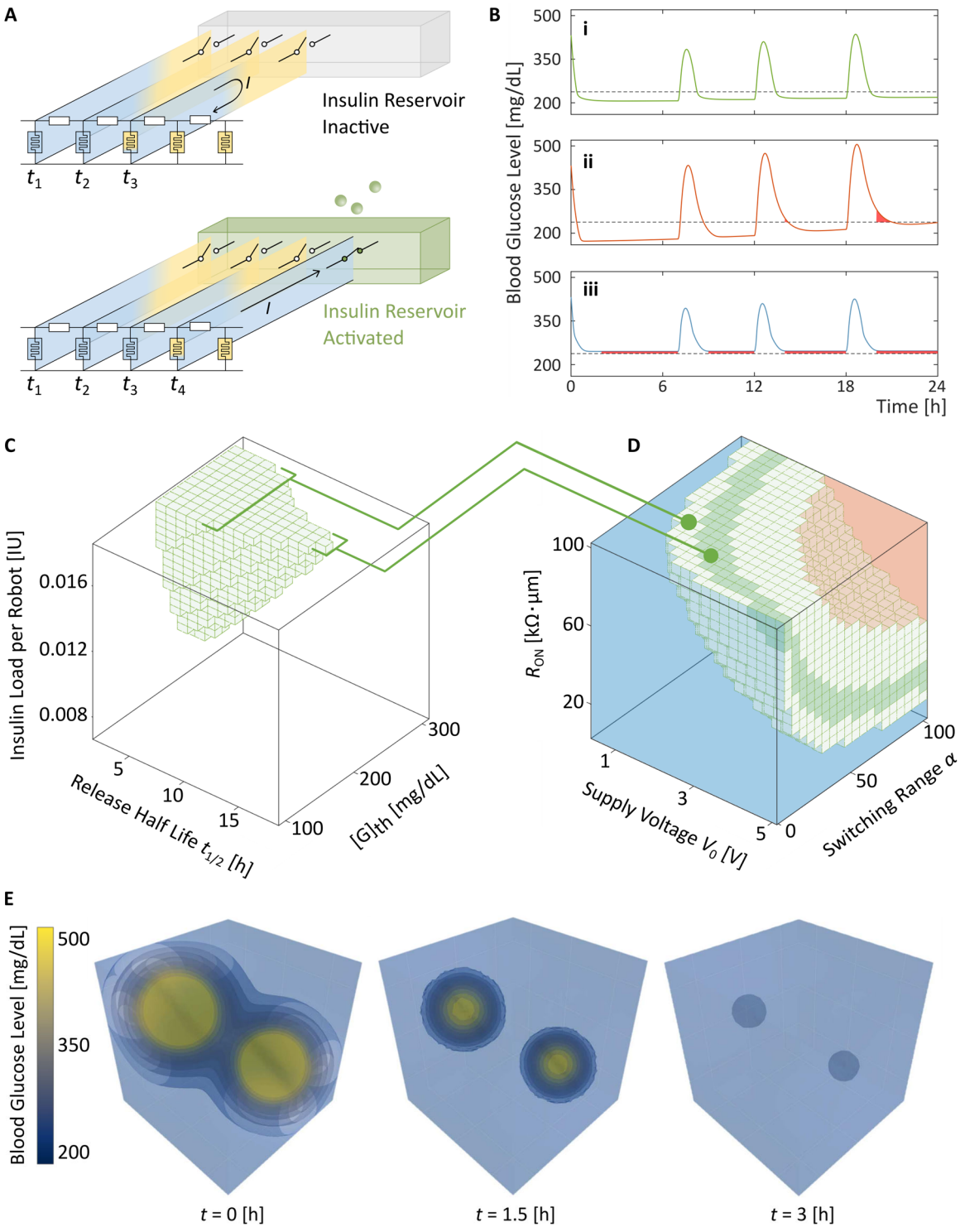

Figure 3-4. *A*: A microrobotic glucose-responsive insulin module can be built by appending a reversible voltage-actuated insulin reservoir to the end of the memristor branches. When the chemiresistors detect a glucose concentration higher than the threshold $[G]_{th}$, the reservoir is activated and vice versa. *B*: Representative trajectories of a diabetic subject's blood glucose level in response to a microrobotic GRI of (i) adequate, (ii) low, and (iii) high $[G]_{th}$ of 225, 175, and 300mg/dL respectively. The deviations from an adequate GRI are highlighted in red. The three spikes in each

trajectory correspond to BG hikes after meals. *C*: Pharmacokinetic modeling facilitates design of the microrobotic GRIs by finding constraints for a qualified GRI on $[G]_{th}$, insulin load, and the release half-life $t_{1/2}$. *D*: The GRI constraints are translated to optimal ranges of the memristor array's circuit parameters (V_0, R_{ON}, and α) via circuit simulations. *E*: Spatiotemporal simulation of a swarm of 100 microrobotic GRIs responding to spatially localized BG spikes with $[G]_{th}$ of 225 mg/dL. The combination of closed-loop insulin release and ergodic diffusion allows the microrobot swarm to regulate complex spatial distributions of glucose without the need for large amounts of computation.

Moreover, we can optimize the memristor array for a maximized GRI efficacy via scanning the parameter space with parallel runs of PAMERAH (Figure 3-4C). The scan returns the constraints on $[G]_{th}$ for an adequate GRI performance: Given a load of 0.018IU and a $t_{1/2}$ of 6h, the memristor array should be designed such that $[G]_{th}$ falls between 180 and 290mg/dL. For a longer $t_{1/2}$ of 12h, the sluggishness in insulin release must be compensated by a tighter requirement on $[G]_{th}$ (210 to 240mg/dL) as shown. Figure 3-4B(ii) and (iii) exemplify poor GRIs corresponding to glucose thresholds below and over the optimal range, leading to premature depletion of insulin and weak BG regulation, respectively.

The GRI parameter requirements extracted from PAMERAH are translated by circuit simulations into targets for array parameters like V_0, R_{ON}, and the switching range $\alpha = R_{OFF}/R_{ON}$. They are the upstream knobs one turns when designing the robot. Regions shaded dark green in Figure 3-4D encompass the permissible combinations of V_0, R_{ON}, and α that yield a desired $[G]_{th}$ for a $t_{1/2}$ of 12h. Relaxed constraints on $[G]_{th}$ imposed by $t_{1/2}$ of 6h in comparison translate to wider ranges of circuit parameters, shown in light green. The geometry, which resembles a fragment of a melon rind, is expected: Combinations of high V_0, R_{ON}, and α (shaded red) result in fast switching along a memristor array branch. The insulin release is triggered prematurely at a lower-than-desired BG, corresponding to the oversensitive and non-lasting GRI in Figure 3-4B(ii). The opposite extreme, shaded blue, conversely yields a threshold too high and a GRI not adequately responsive (Figure 3-4B(iii)). The simulation workflow, as demonstrated here and sketched as Figure 3-7, forms a complete sandbox for testing and optimizing memristor array designs before any physical prototype is built.

PAMERAH addresses the GRI's system-level performance by modeling the full-body physiology as a network of spatially uniform compartments. On the other hand, the spatiotemporal simulations of a swarm of 100 GRI microrobots show that their ergodic diffusion alone creates the coverage

required to regulate complex distributions of glucose without the need for large amounts of on-board computation (Figure 3-4E, Figure 3-17, and §3.8.5). In the absence of glucose or insulin diffusion, the inhomogenously hyperglycemic environment at $t = 0$ evolves over time until the BG level universally drops to the healthy range.

The GRI simulations are a proof-of-concept demonstration of how a memristor array enables autonomous cargo delivery via a feedback-controlled response to its surroundings. Thinking further, we anticipate the memristor array platform to enable even more diverse cargo delivery programs and beyond. For example, irreversibly activated reservoirs, such as an electrodeposited polypyrrole film (112), could enable the administration of an emergency pulse of epinephrine when a large amount of allergen is picked up by the chemiresistor sensors. Substituting a GRI's positive chemiresistors with negative ones, and hence establishing a lower threshold for glucose, offers a viable path towards glucose-responsive glucagon delivery for hypoglycemia prevention (120). The memristor array also offers a means to responsively administer multiple drugs either simultaneously or sequentially, all the while recording the analyte concentration as memristor states. The sequential, scheduled delivery is a particularly relevant application in the field of chronotherapeutics (121,122), which adapts the treatment according to the patient's circadian rhythms via, for instance, separate day and night regimens.

3.8. Discussion

In this computational study, we design and demonstrate the capabilities of memristor-based arrays that integrate timing, memory, sensing, and actuation on-board micrometer-scale robots. Instead of miniaturizing the existing electronics used in macroscale robotics, we show that the distinct functionalities can be combined into one lean circuit comprising only two-terminal resistive elements; Among them, the memristors register to the memory, chemiresistors sense analytes, and they collaboratively translate time into measurable resistance states. Throughout the study, we make sure the design is accessible to a diverse assortment of technology platforms and material systems, opening up avenues for high-throughput fabrication of complex autonomous robots from inexpensive printing, stamping, and coating techniques. The simplest array may be constructed by just laying down a continuous layer of memristive film between sheet electrodes. Our simulations

further show that the potential variabilities in array fabrication and measurement are not a major concern thanks to an error tolerance exceeding 20%.

It is worth noting that while the memristive switching process is increasingly well understood in terms of the microscopic physics and chemistry, the time-dependent switching dynamics is rarely considered for engineering applications. Its pivotal role in our array's on-board awareness of time elevates memristors beyond the role of individual datum-storage units in microrobotics. Interestingly, as time is encoded spatially and sequentially thanks to the delay introduced by each memristor, our design is well compatible with slow-acting, non-state-of-the-art memristors which are otherwise considered unsuitable for computing tasks (123).

Beyond the basic task of registering the excursion time, we devise three extensions to the minimal array to enable advanced capabilities not yet available to autonomous microrobotics. Based upon prior reports of using reversible and irreversible chemiresistors as on-board sensor elements, we design an array that senses and timestamps a major event, for instance encountering an oxygen-rich leak of unknown location and size in a remote pipeline. Leveraging the planar nature of patterning platforms, we expand the minimal array to two dimensions for collection and cataloging time-indexed data, such as the time trajectory of a pollutant's concentration. Finally, since the sensing, memory, and timing functions all communicate via electrical signals, the sensor data stored on-board is readily accessible to additional robotic components. As we quantitatively confirm with circuit simulation and pharmacokinetic modeling, this allows an electroactive polymer module to deliver insulin in a glucose-responsive and/or scheduled manner within a diabetic patient.

Looking further, as we consider tasks that extend beyond those illustrated, circuits of more involved topologies and connectivity within the planar memristor matrix can be designed. For tasks that can be expressed as optimization problems, techniques from the fields of combinatorial optimization (124), simulated annealing (125), optimal control (126), and pareto optimization (127) can be used. For complex tasks that cannot be obviously framed as an optimization, recent advances in the reinforcement learning literature can be applied (128). As memristors are simple two-terminal elements, most automated design approaches will benefit from a substantial complexity reduction relative to circuits based on three-terminal transistors.

We note that this study is illustrative rather than exhaustive. While we examine memristors with the most general switching behavior, certain memristive devices may exhibit experimental non-idealities deviating from the simplest electromigrative drift depiction. For example, conductive-bridging memristors typically require a one-time forming step before the memristors can be repeatably switched ON and OFF (129). In the context of memristor array operation, skipping this pre-treatment may give rise to faster sequential switching and thus a shorter timing window. Another example is the recently reported "discrete state" memristor whose resistance switches stepwise (130,131); Our simulations, in contrast, describe a continuously changing "analog" resistance. Interestingly, these discrete state memristors may work even better in a memristor array with a more pronounced and abrupt ON/OFF boundary. If desired, one may mathematically model the details of these non-idealities by, for instance, introducing additional equivalent circuit elements like capacitors and rectifiers (69,132). As mentioned earlier, however, this report adopts the classical minimal model throughout for its simplicity and suitability for system-level simulation. The model's generality further echoes that our design relies only on the most fundamental feature of memristors – the resistive switching, unaffected by nuances in the mechanisms or material systems. In this study, we also consider each memristor array to experience a uniform chemical concentration across its volume. The approximation is made on the basis that the devices are significantly smaller than the scales of interest in typical microrobotic applications, such as sensing in pipelines and reactors. This treatment is consistent with prior studies on micrometer-sized sensor nodes, both mobile (39,41) and immobile (5,23). In the presence of a large chemical concentration gradient, however, the approximation may become less valid. One example is the gradient created by an H_2O_2 efflux immediately adjacent to a biological cell (133). In such cases, micrometer-sized sensors can provide only a fudged average and a qualitative temporal trajectory.

As we seek a general design that applies to diverse materials, we are unable to assert a single quantitative performance metric attainable, such as an ultimate temporal resolution. That said, the connection between material properties (e.g., μ, R_{ON}, and α) can be analyzed with the nondimensionalized model in §3.9.1. Once a particular material system is selected, the temporal resolution of a memristor array is capped by different factors in discrete and continuous arrays. In a discrete array where the individual memristors are separate, the limiting factor is the number of memristors one can package into a sub-100-µm robot. This is in turn limited by the affordable

spatial resolution of the patterning platform, which is on the order of a micrometer for printing, stamping, and colloidal assembly. The limiting role is played by the *measurement* platform's spatial resolution, on the other hand, in the case of a continuous array where the memristors are altogether embedded in a continuous memristive layer. For example, the *x*-*y* stage of a probe station – the traditional platform for memristor measurement – typically offers a resolution of a micrometer. If we use this probe to read the example memristor array in Figure 3-1H, the temporal resolution can be as small as ±1.8s for a time window of 15s and shorter. It gradually deteriorates, however, to ±26.3s after the cell-sized robot is stationed in the environment for 400s (Figure 3-10), a consequence of the decelerating sequential switching which is visible in Figure 3-1H and further analyzed in §3.9.1. The deceleration thus limits the array's worst-case temporal resolution and is mathematically a direct result of the uniform fixed resistors and constant voltage. As an alternative to the probe station, conductive atomic force microscope has become a common tool for memristor characterization (131,134,135), offering reduced measurement errors and more importantly, a nanometer-range resolution (136,137). This, then, translates to a temporal resolution of merely ±0.03s at t = 400s in the same benchmarking array simulated. As further analyzed in §3.9.3 and Table 3-3, memristor array circuits may be designed and proper measurement platforms selected to suit the temporal resolution demands of specific applications, such as sensing within a microfluidic channel, an industrial-scale flow reactor, and the digestive system.

Lastly, while circuit simulations have been proven to be trustworthy and indispensable to modern circuit design (138), experimental verifications are important in the case of microrobotics – a field at the intersection of engineering, physics, chemistry, and sometimes biology. For instance, experiments are needed to evaluate the stability of the memristors and chemiresistors over prolonged exposure to the environment, which has been studied in air but not yet in solution. The uncertain effects of unwanted absorbates, particle edges, and analyte diffusion on the sequential switching phenomenon should also be elucidated. Looking further, we see this work paving the way towards tools for multi-robot control, robot-to-robot communication, as well as self-organization and swarming – some of the key open questions identified in microrobotics (139).

3.9. Appendix A: Methods

The simulations in this work, including both the circuit simulations and pharmacokinetic modeling, are performed in MATLAB R2020a (The MathWorks, Inc. of Natick, MA).

3.9.1. Simulation of a Discrete 1D Memristor Array

In a discrete 1D memristor array, such as the one simulated in Figure 3-1G, the N cross-plane memristors are individually defined and bridged in between by resistors. The simulation of this scenario is simple. We define the instantaneous memristance of the n^{th} memristor $M_n(t) \in [R_{\text{ON}}, R_{\text{OFF}}]$ and the resistance of the n^{th} fixed resistor $R_{\text{R}n}$. The lumped resistance of the array to the right of the n^{th} memristor (itself included), $\text{R}_{\text{L}n}(t)$, can be expressed recursively as:

$$R_{\text{L}n}(t) = \left(M_n^{-1} + R_{\text{L}n+1}^{-1} \right)^{-1} + R_{\text{R}n} \tag{3-4}$$

At the terminus with the n^{th} memristor, $R_{\text{L}N} = M_N + R_N$. With a supply voltage V_0, the combined current passing through the power source $I_0(t)$ is thus:

$$I_0(t) = V_0 / R_{\text{L}1} \tag{3-5}$$

By Kirchhoff's first law, the current passing through the n^{th} memristor, $I_n(t)$, is:

$$I_n(t) = \left(I_0 - \sum_{j=1}^{n-1} I_j \right) \cdot \frac{R_{\text{L}n+1}}{M_n + R_{\text{L}n+1}} \tag{3-6}$$

Returning to the dynamics of a single memristor outlined in Equations 1-3, we arrive at the memristor array dynamics here:

$$\frac{d}{dt} w_n(t) = \frac{\mu R_{\text{ON}}}{L^2} I_n(t) f_{\text{W}}(w_n) \tag{3-7}$$

μ, R_{ON}, and L are respectively the dopant mobility, the ON-state memristance, and the effective device length L. The additional term, f_{W}, is a window function dependent on the state variable which enforces numerical stability and adds nonlinearity near the device bounds. A number of window functions have been proposed in the literature, such as $f_{\text{W}}(w) = w - w^2$,

$f_{\mathrm{W}}(w,I)=1-\left[w-\left(I<0\right)\right]^{2p}$, $f_{\mathrm{W}}(w)=1-\left[\left(w-0.5\right)^{2}+0.75\right]^{p}$, and $f_{\mathrm{W}}(w)=1-\left(2w-1\right)^{2p}$ (68,72,140).

The last window function is used throughout this work, where p = 10. The instantaneous memristance is defined by the state variable by:

$$M_n(t)=w_n(t)\cdot R_{\mathrm{ON}}+\left[1-w_n(t)\right]\cdot R_{\mathrm{OFF}} \tag{3-8}$$

Setting the initial state variables of all N memristors to be 0.999, we can then trace the sequential switching behavior of the memristor array by solving the ordinary differential equations in 3-7.

Like a continuous memristor array, the sequential switching slows down as time elapses if the resistors bridging the memristors are identical. This phenomenon, described in §3.8 and §3.9.1 below, can be resolved in a discrete array via resistive tuning. That is, as the memristors and resistors are spatially defined and separate, the individual resistances may be tuned by, for instance, surface functionalization (38). Figure 3-1G shows the switching dynamics of a tuned 7-memristor array where the intervals are uniform between each memristor's switching and the subsequent one. For the specific simulation, the tuned resistances of the 7 resistors are respectively 50.0, 7.5, 4.0, 3.2, 3.2, 3.6, and 6.0kΩ.

3.9.2. Simulation of a Continuous 1D Memristor Array

As Figure 3-1H shows, an 1D memristor array can be made from a continuous phase of a memristive material. In this case, the memristance M_n of a standalone memristor is replaced by the local memristance measured at a location x, or M (x, t). Similarly, the local voltage V and longitudinal current along x I_{L} are now continuous functions of x and t as well. As shown in Figure 3-5, we can treat each memristor node as an infinitesimal unit within an otherwise homogenous layer of memristive material. In this limit, the spatial gradient of the local electrical potential down the longitudinal direction is:

$$\frac{\partial}{\partial x}V\left(x,t\right)=-R_{\mathrm{R}}(t)\cdot I_{\mathrm{L}}(x,t) \tag{3-9}$$

in accordance with the classical cable theory originally used to calculate the current and voltage along neurons. Incidentally, the Nobel-prize-winning Hodgkin-Huxley circuit used to model a neuron's axon has a mathematically equivalent form consisting of memristors, bearing striking

resemblance to the memristor array reported in our work (74,141). Note that since R_R (t) in the continuous model measures the instantaneous longitudinal resistance per unit length, it assumes the unit of Ω/μm. Anticipating experimental difficulty in doping the conductive surfaces with high spatial resolution, we assume R_R is not made a function of x. It may, however, be a function of time should chemiresistors be used such as in Figure 3-2, as the chemiresistance is modulated by the time-dependent chemical analyte profile.

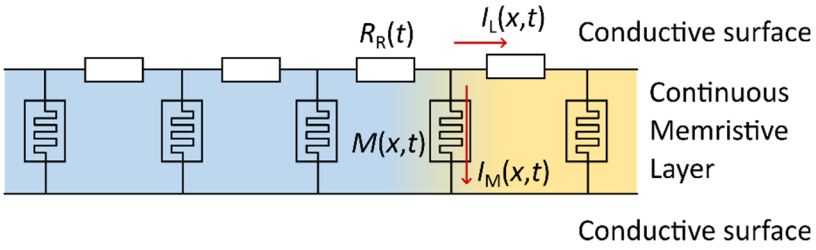

Figure 3-5. Schematic of the simulation of a continuous 1D memristor array fabricated by laying a continuous phase of memristive ink between two conductive surfaces.

Accounting for the transverse current I_M (x, t) per length that goes through the memristive layer, we establish the following relation:

$$\frac{\partial}{\partial x} I_L(x,t) = -I_M(x,t) = -\frac{V(x,t)}{M(x,t)} = -\frac{V(x,t)}{w(x,t)\cdot R_{ON} + \left[1 - w(x,t)\right]\cdot R_{OFF}} \tag{3-10}$$

where w (x, t) is naturally the instantaneous state variable for the particular locality on the memristive layer. Its dynamics is again described by Equation 3-1:

$$\frac{\partial}{\partial t} w(x,t) = \frac{\mu R_{ON}}{L^2} I_M(x,t) f_W \tag{3-11}$$

Note that the units for I_M (x, t) and M (x, t) are respectively A/μm and Ω·μm. Reorganizing Equations 3-9 to 3-11 yields the following system of highly coupled, non-linear partial differential equations (PDEs):

$$\begin{cases} \dfrac{\partial^2}{\partial x^2} V(x,t) = \dfrac{R_R(t)}{R_{ON}} \cdot \dfrac{V(x,t)}{w(x,t) + \left[1 - w(x,t)\right]\cdot \alpha} \\ \dfrac{\partial}{\partial t} w(x,t) = \dfrac{\mu}{L^2} \cdot \dfrac{V(x,t)}{w(x,t) + \left[1 - w(x,t)\right]\cdot \alpha} f_W \end{cases} \tag{3-12}$$

where $\alpha = R_{OFF}/R_{ON}$ is the switching range of a memristor. We used the method of lines (MOL) to simulate the PDE system by discretizing the spatial domain with a stencil of accuracy 2. We can also nondimensionalize the PDE system to better understand its mathematical characteristics, which is documented in detail in §3.9.1.

3.9.3. 2D Memristor Array Simulation

2D memristor arrays presented in Figure 3-3 feature 1D branch arrays along x grafted on a single 1D trunk array along y. The branch and trunk memristors, in addition to the circuit breaker memristors which switch off a branch's voltage access after a short window of time, are treated as distinct circuit elements in this simulation for generality. They may, however, be identical in practice if desired. For clarity, we define in Table 3-1 all quantities involved when simulating a 2D array.

Table 3-1. Physical quantities involved in simulating a 2D memristor array.

Symbol	Definition	Unit	Value
$V_x(x, t)$	Local voltage on the trunk at location x and time t	[V]	-
$V(x, y, t)$	Local voltage on the branches at location (x, y) and time t	[V]	-
$I_x(x, t)$	Local longitudinal current on the trunk at location x and time t	[A]	-
R_x	Resistance of fixed resistors on the trunk	[Ω / μm]	3×10^3
$R_y(t)$	Instantaneous resistance of chemiresistors on the branches at time t	[Ω]	-
$R_{ON,x}$	ON state resistance of memristors on the trunk	[Ω · μm]	1×10^2
$R_{ON,y}$	ON state resistance of memristors on the branches	[Ω · μm^2]	1×10^2
$R_{ON,s}$	ON state resistance of the circuit breaker memristors	[Ω · μm]	1×10^2
$w_x(x, t)$	State variable of the differential memristor on the trunk at location x and time t	[-]	[0, 1]
$w_y(x, y, t)$	State variable of the differential memristor on a branch at location (x, y) and time t	[-]	[0, 1]
$w_s(x, t)$	State variable of the circuit breaker memristor for the branch at location x and time t	[-]	[0, 1]
α_x	Switching range of memristors on the trunk, i.e., the ON/OFF ratio	[-]	2×10^2
α_y	Switching range of memristors on the branches	[-]	2×10^2
α_s	Switching range of the circuit breaker memristors	[-]	5×10^5

μ_x	Mobility of memristors on the trunk normalized by L^2	[min^{-1}V^{-1}]	4
μ_y	Mobility of memristors on the branches normalized L^2	[min^{-1}V^{-1}]	3.5×10^3
μ_s	Mobility of the circuit breaker memristors normalized L^2	[min^{-1}V^{-1}]	1×10^3

We again start by applying the classical cable theory to the trunk:

$$\frac{\partial V_x(x,t)}{\partial x} = -R_x I_x(x,t) \tag{3-13}$$

The reduction of the longitudinal current along the x-axis is due to two factors: current flowing through trunk memristors and that entering the local branch array:

$$\frac{\partial I_x(x,t)}{\partial x} = \underbrace{-\frac{1}{R_{\mathrm{ON},x}} \frac{V_x(x,t)}{w_x(x,t) + \left[1 - w_x(x,t)\right]\alpha_x}}_{\text{Current via trunk memristors}} + \underbrace{\left(\frac{1}{R_y(t)} \frac{\partial}{\partial y} V(x,y,t) \right)_{s+}}_{\text{Current via branch array}} \tag{3-14}$$

where $s+$ denotes the location right after the circuit breaker memristor along a branch array. Combining the two equations above yields:

$$\frac{\partial^2 V_x(x,t)}{\partial x^2} = R_x \left\{ \frac{1}{R_{\mathrm{ON},x}} \frac{V_x(x,t)}{w_x(x,t) + \left[1 - w_x(x,t)\right]\alpha_x} - \left(\frac{1}{R_y(t)} \frac{\partial}{\partial y} V(x,y,t) \right)_{s+} \right\} \tag{3-15}$$

Along the y-axis, on the other hand, Equation 3-12 still applies for each branch array:

$$\frac{\partial^2}{\partial y^2} V(x,y,t) = \frac{R_y(t)}{R_{ON,y}} \frac{V(x,y,t)}{w_y(x,y,t) + \left[1 - w_y(x,y,t)\right]\alpha_y} \tag{3-16}$$

As with before, the state variables w_x, w_y, and w_s are regulated by the currents going through the respective memristors:

$$\begin{cases} \dfrac{\partial}{\partial t} w_y(x,y,t) = -\mu_y \dfrac{V(x,y,t)}{w_y(x,y,t) + \left[1 - w_y(x,y,t)\right]\alpha_y} f_{\mathrm{W}}(w_y) \\ \dfrac{\partial}{\partial t} w_x(x,t) = -\mu_x \dfrac{V_x(x,t)}{w_x(x,t) + \left[1 - w_x(x,t)\right]\alpha_x} f_{\mathrm{W}}(w_x) \\ \dfrac{\partial}{\partial t} w_s(x,t) = -\mu_s \dfrac{V_x(x,t) - V(x,y_{s+},t)}{w_s(x,t) + \left[1 - w_s(x,t)\right]\alpha_s} f_{\mathrm{W}}(w_s) = \mu_s f_{\mathrm{W}}(w_s) R_{\mathrm{ON},s} \left(\dfrac{1}{R_y(t)} \dfrac{\partial}{\partial y} V(x,y,t) \right)_{s+} \end{cases} \tag{3-17}$$

The PDE system consisting of Equations 3-15 to 3-17 is again solved using the method of lines. We discretize the x and y dimension respectively into N_i and N_j points with step sizes Δx and Δy. As a result, $V_x(x, t)$, $V(x, y, t)$, $w_x(x, t)$, $w_y(x, y, t)$, and $w_s(x, t)$ become $V_i^x(t)$, $V_{i,j}(t)$, $w_i^x(t)$, $w_{i,j}(t)$, and $w_i^s(t)$.

The current entering a branch can be discretized with a finite difference stencil of accuracy 2:

$$\left(\frac{1}{R_y(t)}\frac{\partial}{\partial y}V(x,y,t)\right)_{s+} = \frac{1}{2\Delta y R_y(t)}\left(-3V_{i,1}(t)+4V_{i,2}(t)-V_{i,3}(t)\right) \tag{3-18}$$

The PDE system is then transformed into the following form:

$$\begin{cases} \left.\begin{aligned} &\frac{dw_{i,j}(t)}{dt} = -\mu_y\gamma_{i,j}(t)R_{\mathrm{ON},y}V_{i,j}(t)f_{\mathrm{W}}(w_{i,j}) \\ &\frac{dw_i^x(t)}{dt} = -\mu_x\gamma_i^x(t)R_{\mathrm{ON},x}V_i^x(t)f_{\mathrm{W}}(w_i^x) \\ &\frac{dw_i^s(t)}{dt} = \frac{\mu_s R_{\mathrm{ON},s}}{2\Delta y R_y(t)}\left[-3V_{i,1}(t)+4V_{i,2}(t)-V_{i,3}(t)\right]f_{\mathrm{W}}(w_i^s) \end{aligned}\right\}\text{ODEs} \\ \left.\begin{aligned} &\gamma_i^s(t)\left[V_i^x(t)-V_{i,1}(t)\right]+\frac{1}{2\Delta y R_y(t)}\left[-3V_{i,1}(t)+4V_{i,2}(t)-V_{i,3}(t)\right]=0 \\ &V_{i-1}^x(t)-\left\{2+R_x(\Delta x)^2\left[\gamma_i^x(t)+\gamma_i^s(t)\right]\right\}V_i^x(t)+V_{i+1}^x(t)+R_x(\Delta x)^2\gamma_i^s(t)V_{i,1}(t)=0 \\ &V_{i,j-1}(t)-\left\{2+R_y(t)(\Delta y)^2\gamma_{i,j}(t)\right\}V_{i,j}(t)+V_{i,j+1}(t)=0 \end{aligned}\right\}\text{Linear Equations} \end{cases} \tag{3-19}$$

where $\gamma_{i,j}=\left\{R_{ON,y}\left[w_{i,j}+(1-w_{i,j})\alpha_y\right]\right\}^{-1}$, $\gamma_i^s=\left\{R_{\mathrm{ON},s}\left[w_i^s+(1-w_i^s)\alpha_s\right]\right\}^{-1}$, $\gamma_i^x=\left\{R_{\mathrm{ON},x}\left[w_i^x+(1-w_i^x)\alpha_x\right]\right\}^{-1}$ are all functions of time. At each time point, therefore, we update voltages at all locations over the 2D space by solving the linear equations. We then use these updated parameters, as well as the chemiresistance $R_y(t)$ determined by the instantaneous analyte concentration, to progress the ODE solution. To make use of MATLAB's extremely efficient backslash operator, it is best to put the linear equations in their matrix form:

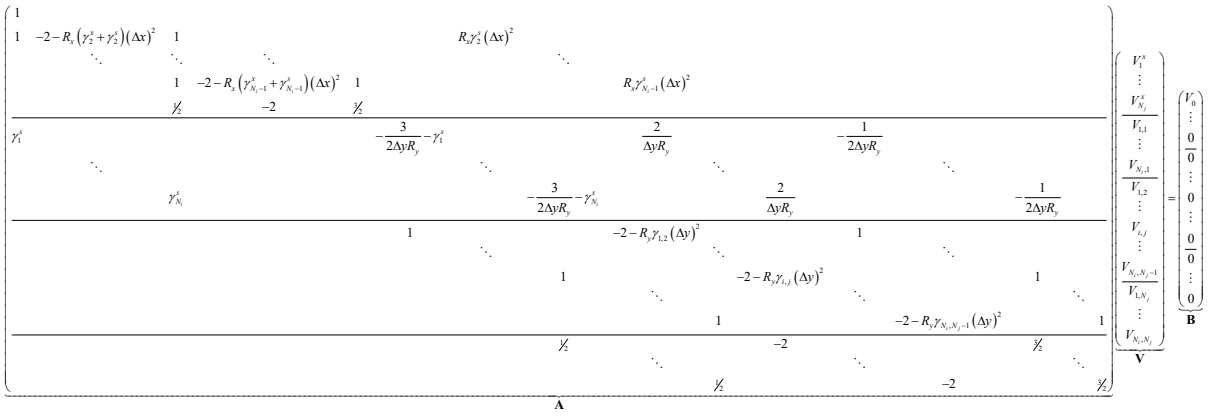

(3-20)

where **A** is a N_i (N_j+1)-by-N_i (N_j+1) square matrix and **V** is a N_i (N_j+1)-by-1 vector. At each time point, the linear equations are then solved simply by computing **V** = **A\B**. For the simulations shown in Figure 3-3, all w, w^x, and w^s are set to 0.999 initially.

We finally address the calibration of 2D memristor arrays illustrated in Figure 3-6. As discussed and mathematically analyzed in §3.9.1, the ON/OFF boundary propagates slower with time. In the context of a 2D memristor array, the voltage is initially passed down the trunk (x-axis) swiftly but slows down gradually: Figure 3-6A shows that although a 2D memristor array can log a temporal sinusoidal profile, the corresponding map of raw memristor states is skewed, with the original periodic oscillation compressed at later times (i.e., larger x). We consequently calibrate the x-axis so that the memristor states faithfully represent the form of the sensed chemical profile. The calibration relation between elapsed time and coordinates along x, such as the one shown in Figure 3-6B, is established with a quick 1D simulation of just the standalone trunk array. Specifically, we track the frontier location of the ON/OFF boundary, defined as the x coordinate where w = 0.99, as a function of time. Rescaling the x coordinates of the raw data with the calibration relation yields the periodic readout shown in Figure 3-6C, where the peaks and valleys map very well onto those of the sinusoidal profile sensed by the array, despite the deteriorating resolution at later times. The result validates using a 1D memristor array as a proxy for the trunk, suggesting that the branches impact only to a minimal degree the sequential switching along x. We note that the calibration relation is an intrinsic property of the circuit and independent of the analyte profile: the same calibration relation is applied to Figure 3-13Figure 3-16.

Somewhat surprisingly, the analyte-responsive sequential switching along the branches (y) is unaffected by the distortion along x. For example, while the four peaks in Figure 3-6A are not evenly spaced along the x dimension, they correspond to the same y location on the branches. A more telling example is given in Figure 3-15A, where the constant profile is not distorted along y and the final ON/OFF boundary locations on all branches are identical. This observation is caused by the deceleration along x and that along y cancelling each other. As §3.9.1 shows mathematically, the slowing switching further down the trunk is a direct result of the lower voltage across the memristor. Incidentally, this is the same voltage sustaining the switching of the corresponding branch. The sluggish switching along y, caused by the lower input voltage at the trunk, is therefore sustained for a proportionately longer time window as the propagation along x slows down as well. The two factors thus cancel each other and ensure the same analyte concentration always corresponds to the same set of memristor states on all branches.

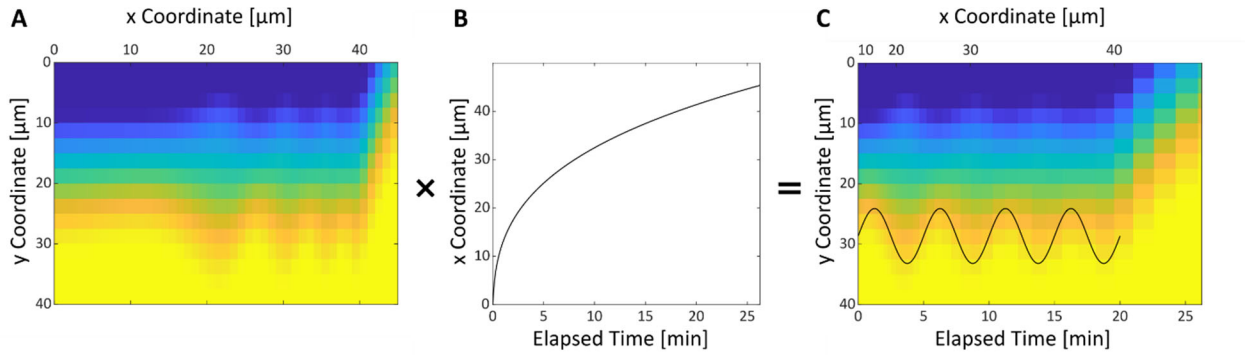

Figure 3-6. Calibration of a 2D memristor array. *A*: Memristor states as measured show that the ON/OFF front resembles the sinusoidal analyte profile but is distorted. *B*: A calibration relation between location of the activated branch on x and time can be established by simulating the trunk as a 1D memristor array. *C*: Scaling the x-axis with the calibration location yields a memristor state map that agrees well with the sensed analyte profile.

3.9.4. Pharmacokinetic and Circuit Simulations of Glucose-Responsive Insulins

In §3.7, we optimized the design of a microrobotic glucose-responsive insulin (GRI) through circuit and pharmacokinetic simulations. While the latter determined constraints on the intermediate GRI parameters such as the threshold glucose level $[G]_{th}$, they are translated by circuit simulation into optimal ranges of memristor array parameters such as V_0, R_{ON}, and α (Figure 3-7).

We used a pharmacokinetic model named PAMERAH that has been published and validated in the literature (116). The model is composed of two parts: a physiological model of the full-body glucoregulatory system and a user-defined GRI kinetics. As seen in Figure 3-8, the physiological model approximates the organs participating in glucose metabolism as an interconnected network of well-mixed compartments, in which glucose, glucagon, native insulin, and GRI are circulated, produced, consumed, or cleared. For example, the concentration of active insulin [I] in the adipose compartments is governed by:

$$\frac{d[\mathrm{I}]_\mathrm{v}}{dt} = \underbrace{\frac{Q}{V_\mathrm{v}}([\mathrm{I}]_\mathrm{heart}\text{-}[\mathrm{I}]_\mathrm{v})}_{\text{Inflow and outflow}} - \underbrace{\frac{V_\mathrm{i}}{V_\mathrm{v}\tau_\mathrm{T}}([\mathrm{I}]_\mathrm{v} - [\mathrm{I}]_\mathrm{i})}_{\text{Transcapillary diffusion}} + \underbrace{r_\mathrm{GRI,v}}_{\text{Changes due to GRI action}} \tag{3-21}$$

The subscripts v and i denote vascular and interstitial volumes respectively. τ_T is the transcapillary diffusion time constant, V the adipose compartmental volumes, and Q the local blood flow rate. In PAMERAH, a GRI affects glucoregulation via the final r_GRI term, which depends on the mode of action of the particular GRI. Readers are referred to the original publication for the detailed mathematical formulations. In the current work, we did not modify the physiological model and only specified the glucose-responsive release kinetics of our microrobotic GRI. If at a certain time the insulin reservoir contains N_I units of insulin to be released and the local glucose concentration sensed is [G], the instantaneous release rate is:

$$r_\mathrm{GRI} = -\frac{dN_\mathrm{I}}{Vdt} = \underbrace{\frac{\ln 2 N_\mathrm{I}}{t_{1/2}V}}_{\text{Nonlinear depletion}} \cdot \underbrace{\left\{1+\exp\left[-0.25\left([\mathrm{G}]-[\mathrm{G}]_\mathrm{th}\right)\right]\right\}^{-1}}_{\text{Glucose responsiveness}} \tag{3-22}$$

where V is the compartmental volume. The first term on the right-hand side signifies that the release becomes slower as the reservoir depletes, characterized by the half-life $t_{1/2}$. The second term takes care of the glucose responsiveness: minimal insulin release for [G] < $[\mathrm{G}]_\mathrm{th}$ and vice versa. Note that in a microrobotic GRI, this comparator is realized with the voltage passed down to the branch terminus. If the terminus voltage exceeds a threshold voltage V_th, the reservoir is activated. As a result, $[\mathrm{G}]_\mathrm{th}$ is an intermediate parameter dependent upon circuit parameters like V_0, R_ON, and α. For the simulation in Figure 3-4C, we started with 100 robots each with an initial reservoir load ($N_{\mathrm{I}0}$) of 0.007 to 0.018 IU. Assuming a 2500 μm^3 reservoir filled with 20%wt of insulin (142), each robot has an insulin capacity of 14.4 IU, some three orders-of-magnitude more

than the conservative range we chose. The ranges we explored for $t_{1/2}$ and $[G]_{th}$ are respectively 0.5 to 18 hours and 100 to 300 mg/dL. We simulated the GRI's action in a model parameterized previously with data from male Lewis rats (116). By definition, a satisfactory GRI should:

(i) maintain the blood glucose concentration with in the normoglycemic range – 75 to 240 mg/dL for rats (117) – for 24 hours unless the GRI is just administered or a meal is consumed;
(ii) bring the initial hyperglycemic glucose level down to the normal range within two hours following the GRI's administration;
(iii) curb the postprandial glucose hikes by returning the glucose level to the normal range within two hours following 1 g/kg oral glucose meals.

Mathematically, any deviation from the said criteria is counted towards either a hyper- or hypoglycemia risk score. Only GRIs free from both risks are considered adequate, which are represented by the shaded region in Figure 3-4C.

The subsequent circuit simulation is straightforward and not so different from the earlier sections. Considering the computational efficiency, we approximated the dynamics of each memristor branch as a standalone 1D array described in §3.8.2. The approximation is valid as the distance travelled by a branch's ON/OFF boundary along y is independent of the branch location x on the trunk, evidenced by the final memristor states in a sinusoidal profile (Figure 3-3D) as well as Figure 3-15A. In a 2D memristor array, each branch is supplied power for only a short window of time. This temporary voltage input to the branch, $V_0(t)$, is approximated as a Gaussian pulse with a peak voltage ranging from 0.5 to 5V and a standard deviation of 20min. The peak location is inconsequential so long as the entire pulse is supplied. Note that the Gaussian approximation is exact if the transmission line model is adopted (§3.9.2). The variable resistance of the branch chemiresistors R_R is ultimately a function of the analyte concentration, in the GRI case [G]:

$$R_R([G]) = \left[1+100\tanh\left(\left[G\right]-150\middle/200\right)\right]^{-1} \text{ MΩ/μm} \tag{3-23}$$

which follows the theoretical fit used in Koman *et al.* (39). This chemiresistor offers a 20-fold reduction in its resistance as the analyte concentration increases from 150 to 250mg/dL, which is within the typical range of chemiresistor responsiveness. Furthermore, the sensor sensitivity is reduced towards larger [G], typical of chemiresistors as well.

The voltage passed down the 1D memristor array as a function of time is tracked by an ODE solver. For a specific combination of the peak voltage, R_{ON}, and α, we can find a corresponding threshold glucose concentration $[G]_{th}$ (V_0, R_{ON}, α) that causes the maximal voltage at the branch terminus to reach V_{th} = 0.15V. The insulin reservoir is set to be 75μm away from V_0. We may then compare the corresponding $[G]_{th}$ with its desired range from the pharmacokinetic model to determine if the V_0-R_{ON}-α combination is acceptable (Figure 3-7B).

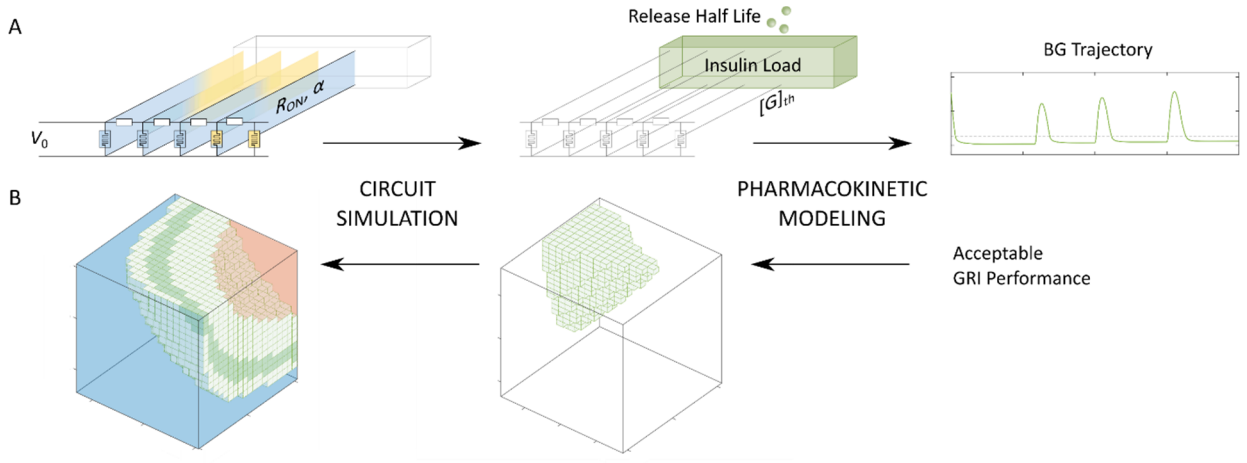

Figure 3-7. *A*: Starting with a set of circuit parameters such as V_0, R_{ON}, and α, we run circuit simulations to obtain the corresponding threshold glucose level beyond which the insulin reservoir is activated by the terminal voltage. $[G]_{th}$ and the reservoir parameters are then used to predict the GRI's performance in the body of a diabetic subject. *B*: The parameter optimization process goes the opposite way. Based on criteria for adequate GRIs, requirements on the GRI parameters can be established via pharmacokinetic modeling. With circuit simulations, optimal ranges of the circuit parameters are then found which would yield acceptable GRI parameters.

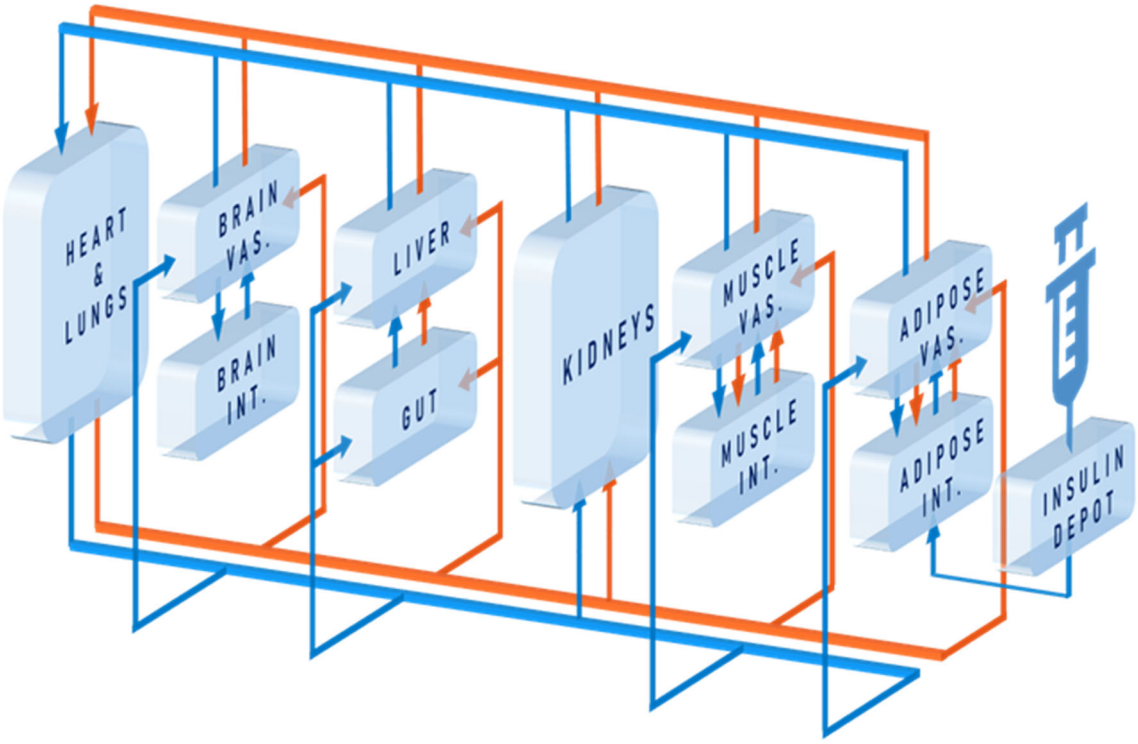

Figure 3-8. Schematic of PAMERAH's physiological model. The blue and red arrows represent respectively the circulation of glucose and insulin/GRI. Adapted from Ref. (116).

3.9.5. Spatiotemporal Simulations of a Microrobotic GRI Swarm

This simulation is designed to be illustrative of the use of microrobotic GRIs to regulate nontrivial spatial distributions of glucose over an environment (e.g., glucose agglomeration in specific tissues). We begin by framing the assumptions and design choices of our microrobotic GRI swarm simulation. First, we do not endow the glucose and insulin concentrations with diffusive dynamics. This choice is made so as to illustrate the role movement and spatial effects play on the performance of the microrobotic GRIs in an environment with persistent structural features. Otherwise, the initial glucose and insulin distributions diffuse evenly through the simulated volume, making the glucose regulation problem spatially homogenous and visually opaque. Here, by insisting on spatially heterogenous glucose concentrations, we highlight the dynamic nature of the closed-loop insulin release of each microrobotic agent. Second, we assume that due to well-mixed flow conditions the agent dynamics are captured by Langevin diffusion with drift (i.e., a spatially isotropic diffusion tensor with a linear drift term capturing a net flow). An important note is that in this class of diffusion processes (or flow conditions) the movement of particles through

space is ergodic. That is, for any finite volume of space particles are guaranteed to visit every location in space in a finite amount of time (also referred to as achieving coverage over the space). Third, we make use of periodic boundary conditions to maintain a constant microrobot density without the need for deploying additional agents over time.

The simulation procedure itself requires tracking and evolving the state of three different objects over time: The environmental glucose concentration [G] (x, y, z, t), the environmental insulin concentration [I] (x, y, z, t), and the state of each agent. The state of glucose and insulin concentrations are given by the local levels of each chemical throughout the environment domain, and their joint evolution is described by a simplified set of coupled ordinary differential equations adapted from the PAMERAH model (116):

$$\begin{cases} \underbrace{\frac{d[\mathrm{GRI}]}{dt}}_{\text{Depletion of reservoir}} = -r_{\mathrm{GRI}} = -\underbrace{\frac{\ln 2[\mathrm{GRI}]}{t_{1/2}}}_{\text{Nonlinear depletion}} \cdot \underbrace{\left\{1+\exp\left[-0.25\left([\mathrm{G}]-[\mathrm{G}]_{\mathrm{th}}\right)\right]\right\}^{-1}}_{\text{Glucose responsiveness}} \\ \underbrace{d[\mathrm{G}]/dt}_{\text{Glucose uptake rate}} = -r^{\mathrm{B}}_{\text{glucose uptake}} \underbrace{\left[6.28+6.52\tanh\left(0.78[\mathrm{I}]-1.98\right)\right]}_{\text{Impact of insulin on glucose uptake rate}} \\ d[\mathrm{I}]/dt = r_{\mathrm{GRI}} - \underbrace{[\mathrm{I}]/9.39}_{\text{Insulin clearance rate}} \end{cases} \tag{3-24}$$

At each moment in time, the insulin released by each agent is added locally to the environmental insulin distribution, which then jointly evolves with the glucose distribution according to their coupled dynamics. The variables and their values are listed in Table 3-2. With only these basic interactions, agents are able to regulate glucose levels via closed-loop insulin release. To simulate the environmental glucose-insulin dynamics we make use of a fourth-order deterministic Runge-Kutta scheme. The state of each agent is given by their location in space, as well as the amount of insulin in their internal reservoir [GRI] (i, t). Since the insulin reservoir levels deplete according to a simple nonlinear function of the local glucose levels, we make use of a computationally efficient Euler scheme to describe the slow-moving insulin reservoir dynamics of each agent. To integrate the stochastic differential equations describing the diffusive trajectories of each microrobotic GRI over time we make use of a stochastic second-order Runge-Kutta scheme. At each time step, all agents move one step, measure their local glucose levels, release insulin to the environment in response, update their insulin reservoir levels, then the glucose and insulin

distributions interact and evolve. This main simulation loop is repeated with a time resolution of 0.1s for 100 microrobotic GRIs for the duration of the simulations in the manuscript.

Table 3-2. Variables and their values used in the spatiotemporal simulations of a GRI swarm.

Symbol	Definition	Unit	Value
[GRI] (i, t)	Concentration of remaining insulin in the reservoir of the i^{th} agent	mU/L	$[\mathrm{GRI}]\ (i,\ t=0)=7.12\times10^{3}$
[I] (x, y, z, t)	Local concentration of insulin at (x, y, z)	mU/L	$[\mathrm{I}]\ (x,y,z,t=0)=0$
[G] (x, y, z, t)	Local concentration of glucose at (x, y, z)	mg/dL	$[\mathrm{G}]\ (x,y,z,t=0)\in[230,425]$
r_{GRI}	Rate of insulin release	mU/L/min	-
$r^{B}_{\text{glucose uptake}}$	Base rate of glucose uptake	mU/L/min	1.67
$[\mathrm{G}]_{\mathrm{th}}$	Threshold glucose concentration beyond which insulin is released from the reservoir	mg/dL	225
$t_{1/2}$	Reservoir half life	min	360

3.10. Appendix B: Supplementary Simulations and Analyses

3.10.1. Nondimensionalized Model of the 1D Memristor Array

Equation 3-12 governing the 1D memristor array dynamics can be nondimensionalized as follows:

$$\begin{cases}\dfrac{\partial^2 U}{\partial X^2}=\dfrac{U}{w+[1-w]\cdot\alpha}\\[2ex]\dfrac{\partial w}{\partial \tau}=\dfrac{U}{w+[1-w]\cdot\alpha}f_{\mathrm{W}}\end{cases}\tag{3-25}$$

where $U(X,\tau)=V(x,t)/V_0$, $X=x\sqrt{R_{\mathrm{R}}(t)/R_{\mathrm{ON}}}$, and $\tau=\left(\mu V_0/L^2\right)t$ are the dimensionless voltage, location, and time, respectively. U and w are both functions of X and τ, and f_{W} denotes the window function of choice. While we used the dimensional simulations earlier to put the actual electrical element parameters in quantitative perspective, the nondimensionalized model in Equation S22 is easier to analyze and particularly helpful in elucidating the deceleration of an array's ON/OFF boundary at a later time. This phenomenon is visible in Figure 3-1H and discussed in the

Discussions section. If we adopt the quasi-steady state approximation and view w as just a function of X for a given time, Equation S22 becomes an ODE of U:

$$\frac{d^2U}{dX^2} = \frac{1}{w + [1 - w] \cdot \alpha} U \tag{3-26}$$

Qualitatively, as the voltage polarity stays the same along the memristor array for a fixed source and $|U\ (X > 0)| < |U\ (0)|$, magnitude of the voltage unavoidably diminishes further away. Qualitatively, if we make the easy but numerically inaccurate assumption that w is uniform, the voltage profile can be analytically solved and U exponentially decays along X. In reality, the memristors further away remain ON while the ones closer to the voltage source start to be switched OFF not too long after $t = 0$. In the region already affected by the voltage source, then, the distribution of w is approximately linear. Solution of this ODE suggests that the voltage distribution along the array takes the form of a modified Bessel function, which also decays with X. Substituting the decaying U into the second PDE in Equation S22 reveals how memristors further away switch slower. As described in §3.8, the decelerating sequential switching further away from the voltage source limits the usable length of a continuous memristor array: Beyond a certain x, the sluggish propagation of the ON/OFF boundary can no longer be detected due to the measuring probe's spatial resolution. The limitation is fortunately countered by the increasing availability of high-resolution characterization platforms like conductive atomic force microscopy (cAFM), which presents a thousand-fold enhancement compared to traditional micromanipulator probes. In a discrete memristor array, on the other hand, resistive tuning may be used (§3.8.1).

3.10.2. 2D Memristor Array with a Transmission Line

In addition to grafting memristor array branches onto a memristor array trunk, we studied the feasibility of voltage propagation by a transmission line due to its mathematical simplicity and uniform speed. The transmission line, or telegraph line, which supplies voltage to the branches in this design, is governed by the elegant telegrapher's equations by Heaviside:

$$\begin{cases} \dfrac{\partial V(x,t)}{\partial x} = -L_{\mathrm{T}} \dfrac{\partial I(x,t)}{\partial t} - R_{\mathrm{T}} I(x,t) \\ \dfrac{\partial I(x,t)}{\partial x} = -C_{\mathrm{T}} \dfrac{\partial V(x,t)}{\partial t} - G_{\mathrm{T}} V(x,t) \end{cases} \tag{3-27}$$

Coupling Equation 3-27 with Equation 3-12 which describes the 1D memristor array dynamics, we arrive at the governing system of PDEs:

$$\begin{cases} \dfrac{\partial V(x,0,t)}{\partial x} = -L_{\mathrm{T}} \dfrac{\partial I(x,0,t)}{\partial t} - R_{\mathrm{T}} I(x,0,t) \\ \dfrac{\partial I(x,0,t)}{\partial x} = -C_{\mathrm{T}} \dfrac{\partial V(x,0,t)}{\partial t} - G_{\mathrm{T}} V(x,0,t) + \left(\dfrac{\partial V(x,y,t)}{R_y(t) \partial y} \right)_{y=0+} \\ \dfrac{\partial^2}{\partial y^2} V(x,y,t) = \dfrac{R_y(t)}{R_{\mathrm{ON}}} \dfrac{V(x,y,t)}{w(x,y,t) + \left[1 - w(x,y,t)\right]\alpha} \\ \dfrac{\partial}{\partial t} w(x,y,t) = \mu_y \dfrac{V(x,y,t)}{w(x,y,t) + \left[1 - w(x,y,t)\right]\alpha} f_{\mathrm{W}} \end{cases} \tag{3-28}$$

V (x, 0, t) and I (x, 0, t) are respectively the voltage and current on the transmission line. L_{T}, C_{T}, G_{T}, and R_{T} are parameters describing the telegraph line characteristics, among which the latter two determine the energy loss. As with previous simulations, $w \in [0, 1]$ represents the instantaneous state variable that determines the local memristance at (x, y): $M(x,y,t) = \left\{ w(x,y,t) + \left[1 - w(x,y,t)\right]\alpha \right\} R_{\mathrm{ON}}$ where α is the switching range and R_{ON} is the ON-state memristance with the unit of $\Omega \cdot \mu m^2$ (*cf.* $R_{\mathrm{ON},\,y}$ in Table 3-1).

Again, we simulated the set of PDEs in Equation 3-28 with the method of lines. We approximated the spatial derivatives via finite differencing of accuracy 2, transforming the PDEs into a system of ODEs:

$$\begin{cases} \left.\begin{aligned} \dfrac{\partial I_{i,1}(t)}{\partial t} &= -\dfrac{1}{2L_{\mathrm{T}}\Delta x}\left[V_{i+1,1}(t) - V_{i-1,1}(t)\right] - \dfrac{R_{\mathrm{T}}}{L_{\mathrm{T}}} I_{i,1}(t) \\ \dfrac{\partial V_{i,1}(t)}{\partial t} &= -\dfrac{1}{2C_{\mathrm{T}}\Delta x}\left[I_{i+1,1}(t) - I_{i-1,1}(t)\right] - \dfrac{G_{\mathrm{T}}}{C_{\mathrm{T}}} V_{i,1}(t) + \dfrac{-3V_{i,1}(t) + 4V_{i,2}(t) - V_{i,3}(t)}{2C_{\mathrm{T}} R_y(t) \Delta y} \\ \dfrac{\partial w_{i,j>1}(t)}{\partial t} &= \mu \gamma_{i,j} R_{\mathrm{ON}} V_{i,j}(t) f_{\mathrm{W}} \end{aligned} \right\} \text{ODEs} \\ V_{i,j-1}(t) - \left[2 + \gamma_{i,j} R_y(t) (\Delta y)^2\right] V_{i,j}(t) + V_{i,j+1}(t) = 0 \end{cases} \tag{3-29}$$

where $\gamma_{i,j}(t) = \left\{ R_{\mathrm{ON}} \left[w_{i,j} + \left(1 - w_{i,j}\right)\alpha \right] \right\}^{-1}$. The (i, j) tuple refers to the location at the i^{th} node along the x axis and j^{th} node along y on the mesh with a resolution of Δx by Δy. The voltage pulse V_0 (t) is

initiated at (1, 1). As with §3.8.3, the linear algebraic equation in Equation 3-29 can be solved efficiently with the backslash operator:

$$\mathbf{V} = \begin{pmatrix} V_{1,1} \\ \vdots \\ V_{N_i,1} \\ \hline V_{1,2} \\ \vdots \\ V_{i,j} \\ \vdots \\ V_{N_i,N_j-1} \\ \hline V_{1,N_j} \\ \vdots \\ V_{N_i,N_j} \end{pmatrix} = \begin{pmatrix} 1 & & & & & & & & & & \\ & \ddots & & & & & & & & & \\ & & 1 & & & & & & & & \\ \hline 1 & & \beta_{1,2} & & 1 & & & & & & \\ & \ddots & & \ddots & & \ddots & & & & & \\ & & 1 & & \beta_{i,j} & & & 1 & & & \\ & & & \ddots & & \ddots & & & \ddots & & \\ & & & & 1 & & \beta_{N_i,N_j-1} & & & 1 & \\ \hline & & & & & -\tfrac{1}{2} & -2 & \tfrac{3}{2} & & & \\ & & & & & & \ddots & \ddots & \ddots & & \\ & & & & & & & -\tfrac{1}{2} & -2 & \tfrac{3}{2} \end{pmatrix}^{-1} \begin{pmatrix} V_{1,1} \\ \vdots \\ V_{N_i,1} \\ \hline 0 \\ \vdots \\ 0 \\ \vdots \\ 0 \\ \hline 0 \\ \vdots \\ 0 \end{pmatrix} \quad (3\text{-}30)$$

where $\beta_{i,j}(t) = -2 - \gamma_{i,j} R_y(t) (\Delta y)^2$ and any $V_{i,1}(t)$ is updated from the differential equations. The ODEs are solved as a standard initial value problem with the initial condition of $w = 0.999$ at all locations. For each branch to receive only temporary power restricted to a short time window, a voltage pulse is applied at (0, 0) and passed down the trunk along x. For the simulations in Figure 3-9, we used no-flux boundary conditions at large x and y, as well as a transient voltage input at (0, 0) in the form of a Gaussian pulse with a peak voltage of 5V and a standard deviation of 10min. This 2D memristor array powered by a transmission line works well for both a sinusoidal and a realistic analyte profile, evident from the agreement between the profiles and the ON/OFF fronts. Furthermore, the memristor states are not distorted as in §3.8.3 thanks to the constant propagation speed along the transmission line, and hence no calibration is required. Nonetheless, we note that the transmission line 2D array is more of an analytical tool than an engineering design, considering the challenges involved in patterning micron-scale inductors as well as the large $L_T C_T$ product required to slow down the trunk transmission. In comparison, a trunk in the form of a memristor array – the design we eventually chose – can be designed with experimentally relevant parameters and fabricated by facile patterning of materials.

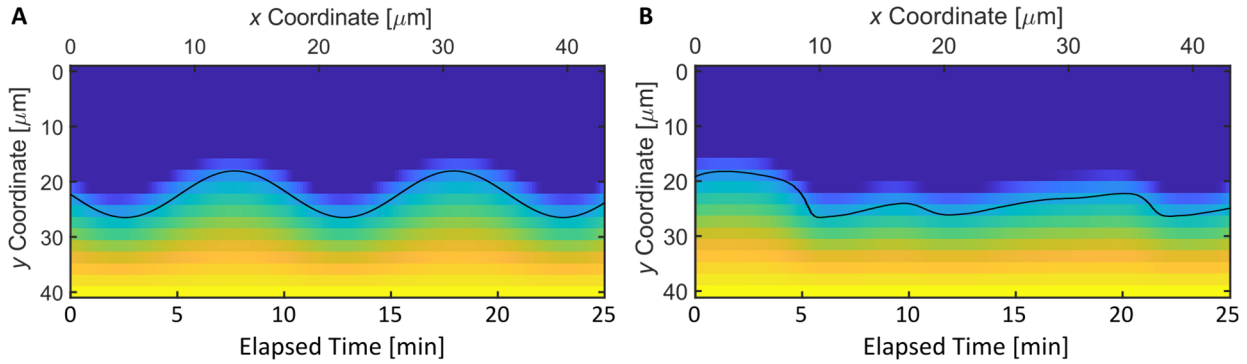

Figure 3-9. *A* and *B*: Simulated final memristor states of a 2D memristor array powered by a transmission line. The ON/OFF fronts conform well to both the *(A)* sinusoidal and (*B*) realistic temporal analyte profile shown as black curves. The transmission line (trunk) parameters used are: $C_T = 0.18$F/μm, $L_T = 0.6$MH/μm, $R_T = 0$, and $G_T = 0$, i.e., a "lossless" line. The branch parameters are: $\mu_y = 0.05 s^{-1}V^{-1}$, $\alpha = 10$, and $R_{ON} = 50k\Omega$. The realistic profile is extracted from Ref. (101).

3.10.3. Further Analyses of Application-Specific Temporal Resolution Constraints

We described in §3.8 how the sequential switching in a memristor array slows down over time. This feature leads to a high temporal resolution attainable earlier on, which gradually worsens as time elapses. For example, Figure 3-1H shows that the same spacing among the ON/OFF boundaries corresponds to a larger time window at a larger *t*. In this section, we further analyze how memristor arrays can be designed and measured such that even the worst temporal resolution towards the end of the robot's journey can suit the intended application. Note that the minimum resolution an application requires typically scales with the residence time; A task over the course of several hours typically do not require each second to be accounted for.

The 1st row of Table 3-3 shows that the memristor array studied in Figure 3-1H offers sufficient temporal resolution to pinpoint, within a 6-stage microfluidic chip reactor, which stage corresponds to a recorded event. However, the same memristor array fails to provide enough temporal resolution in an industrial flow reactor with a tenfold residence time (2nd row) if it is still read with a micrometer-resolution probe station.

We present two solutions to enhance the resolution. First, as thoroughly discussed in *Discussion*, an array's temporal resolution at each timepoint is ultimately limited by the spatial measurement

resolution of the readout platform. As a result, enhancing the spatial accuracy of circuit readout effectively helps tell apart ON/OFF boundaries corresponding to different times, even when t is large (3rd vs. 2nd row, also Figure 3-10). This can be achieved by, for instance, replacing the probe station with cAFM, which is an alternative tool for memristor characterization (134,135). Alternatively, the memristor array parameters may be designed differently to suit the temporal resolution this specific application targets (4th vs. 2nd row). Similarly, we designed a memristor array to satisfy the requirements of a canine GI tract sensor as well (5th row). While the final (worst-case) temporal resolution is ±28.5min at the end of 8 hours, the resolution is at least ±7.2min within the first 2 hours and ±3.6min within the first hour, as expected.

Table 3-3. Analyses of memristor arrays designed to satisfy the temporal resolution requirements of several specific application scenarios.

Example Application	Ref.	Typical Residence Time	Memristor Array Parameters			Spatial Measurement Resolution	Worst-Case Temporal Resolution[a]	
			μ/L^2 [$s^{-1}V^{-1}$]	R_R [kΩ/μm]	α		Target	Simulated
6-stage microfluidic synthesis	(143)	7min	1[b]	1.75[bc]	100[b]	±1μm (probe station)	±35s[d]	±27.6s
Industrial flow reactor	(144)	70min	1	1.75	100	±1μm (probe station)	±210s	±251.5s
Industrial flow reactor	(144)	70min	1	1.75	100	±1nm (cAFM)	±210s	±0.25s
Industrial flow reactor	(144)	70min	1	1[c]	100	±1μm (probe station)	±210s	±190.1s
Canine gastric emptying	(145)	8hr	1	1.75	100	±1μm (probe station)	±30min	±28.5min

[a] Because the temporal resolution is varying over time, we consider here the minimum (worst-case) temporal resolution towards the end of the residence time and compare it to the minimum requirement (the target resolution) specific to each intended application. The temporal resolution is much higher earlier on in all cases.

[b] This set of memristor array parameters is identical to that simulated in Figure 3-1H as well as Figure 3-10 below.

[c] Both simulated parameter values of R_R = 1kΩ/μm and 1.75kΩ/μm are consistent with material properties reported in the literature. For example, the sheet resistance of a graphene film ranges from 2×10^2 to 6×10^5Ω/□ depending on the method of synthesis and chemical modification (146,147). This corresponds to an R_R between 0.4 and 1200kΩ/μm assuming a 2μm-wide 1D memristor array.

[d] The target temporal resolution of ±35s is chosen such that even in the worst-case scenario, one stage out of the 6-stage microfluidic platform can be identified which corresponds to the sensing event picked up by the memristor array.

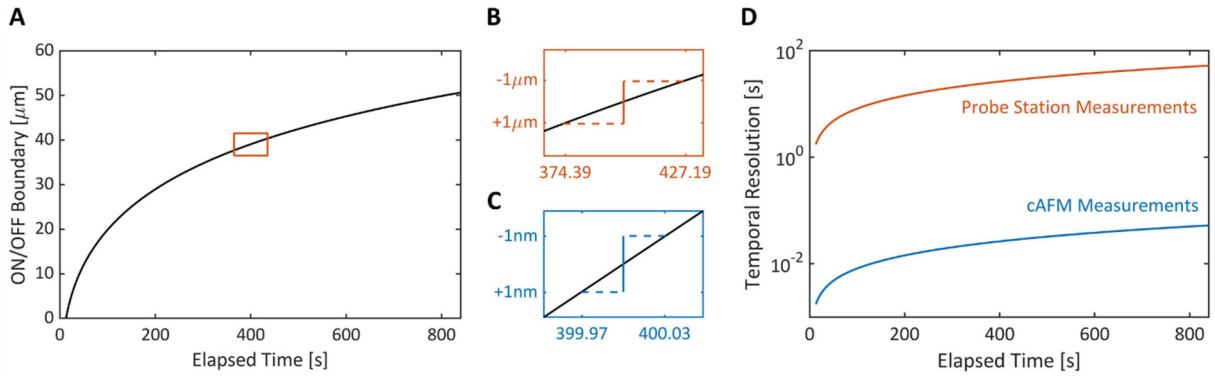

Figure 3-10. *A*: The simulated relation between the ON/OFF boundary location along a continuous 1D memristor array and time elapsed shows that the sequential switching slows down gradually. This relation is calculated the same way as the calibration curve used for correcting a 2D memristor array as discussed in §3.8.3. The red box corresponds to the magnified region shown in (*B*). *B*: The spatial resolution of a traditional probe station measurement platform, which is approximately 1μm as marked by the vertical interval, translates to a temporal resolution of ±26.3s at t = 400s shown as the horizontal dashed lines. *C*: In comparison, the nanometer-range spatial resolution of a cAFM drastically refines the temporal resolution to ±0.03s. *D*: The temporal resolution as a function of time and the spatial resolution of the measurement platform.

3.10.4. Overview of Additive Fabrication of Memristor Arrays

The design of an array of memristors connected in parallel is inspired by previous findings that matrices of memristors can be facilely stamped out *en masse* from materials additively stacked together, a technology termed *autoperforation* (38). Specifically, as seen in Figure 3-11A, user-defined inks are printed onto a 2D sheet of graphene, MoS_2, or hexagonal boron nitride in the form of a dot array. The ink can be made memristive by, for instance, compositing polystyrene beads with black phosphorus or MoS_2 nanoflakes. Subsequently, a second 2D sheet is transferred on top, thereby forming a sandwich stack. Finally, the said stack is lifted off in solution, during which individual microparticles are "stamped out" and collected, the size of each dictated by the size of the printed ink disc (20 to 1000μm in diameter). The height of each microparticle is typically less than a micrometer, thus making the particles effectively planar.

Mechanistically, the particles are cut out from a continuous materials stack by strain-guided fracture. Seen in Figure 3-11B, the strain field imposed by the printed ink disc ensures any crack in the materials propagate along the disc's periphery, acting like a pair of invisible microscopic scissors. The autoperforation technique does not require the ink spots to be printed. Alternative micrometer-scale additive platforms like stamping, coating, and colloidal self-assembly are applicable as well.

Figure 3-11C presents the full set of data from which Figure 3-1F is adapted. Parts of the 3-by-5 grid on a single memristive microparticle, defined by the measurement probe, can be selectively switched ON by applying a writing voltage to each spot. The letters "M", "I", and "T" spelt out on the same autoperforated particle demonstrate that each particle is equivalent to an array of cross-plane memristors wired in parallel. Of note, the technology has been shown to be highly customizable, as the microparticle's size, geometry, and ink compositions are all tunable. More importantly, the fabrication process allows for facile surface chemical modifications and patterning as well (83). For the current work, this enables spatial tuning of surface resistivity (R_R) as well as definition of memristor array branches.

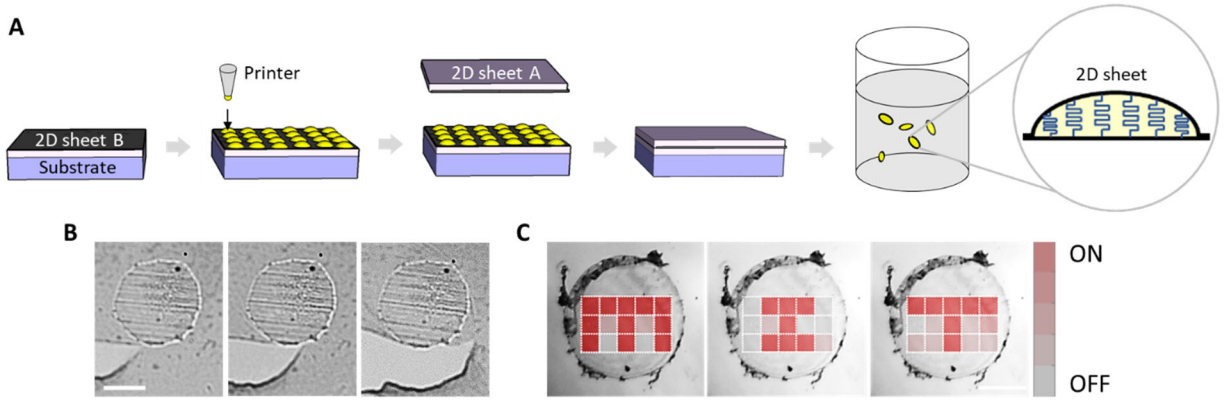

Figure 3-11. *A* and *B*: (*A*) Overview of the autoperforation process for fabricating micrometer-scale ink particles encapsulated between 2D sheets. (*B*) Microscopic process of the fracture-assisted lift-off step during which microparticles are stamped out of the continuous stack of materials. Scale bar, 100μm. (*C*) Selective switching experiments demonstrated that each memristive microparticle is effectively an 2D array of memristors connected in parallel. Scale bar, 100μm. All panels are adapted from Ref. (38).

3.11. Appendix C: Supplementary Figures

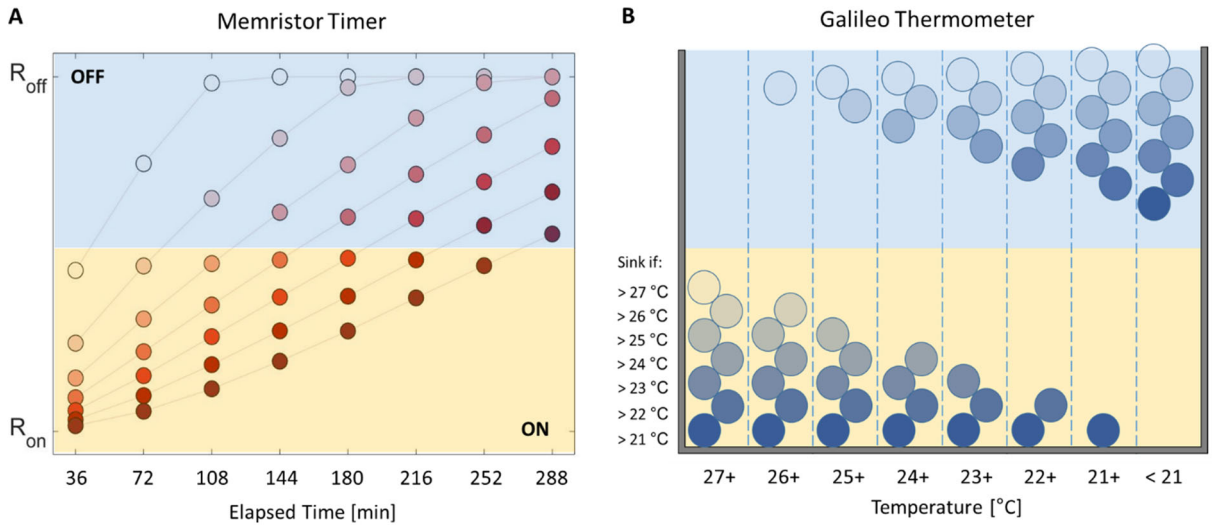

Figure 3-12. *A* and *B*: The 1D memristor array (*A*) records time exactly how a Galileo thermometer (*B*) records temperature. The simulated data in panel (*A*) are identical to those in Figure 3-1G but are visualized differently to show the parallelism.

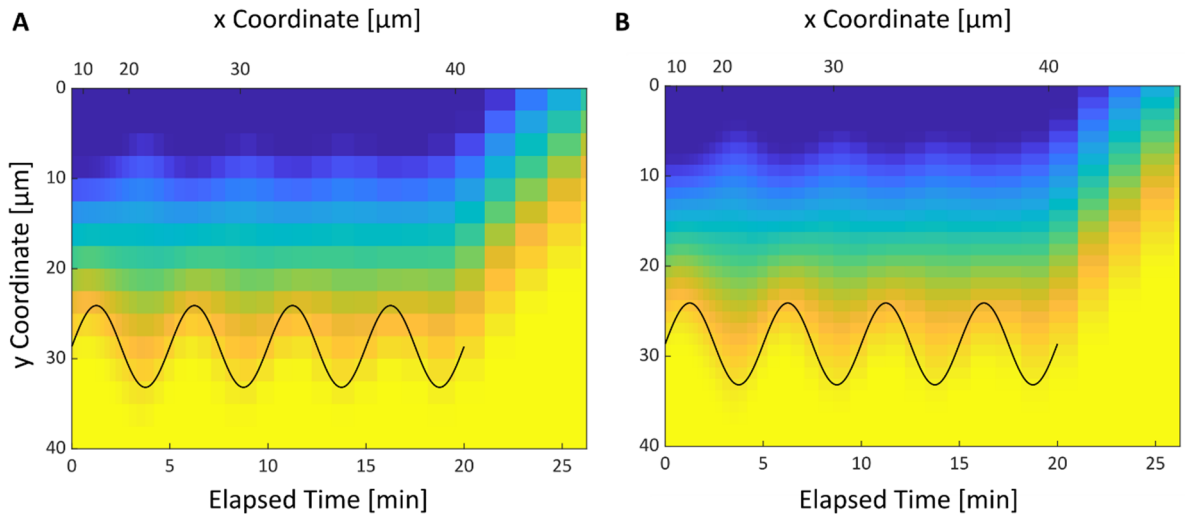

Figure 3-13. *A* and *B*: States of a 2D memristor array at t = 20min simulated with a (*A*) coarse and (*B*) fine degree of branch discretization with a resolution (Δy) of 0.25 and 0.125µm, respectively. The simulations are comparable.

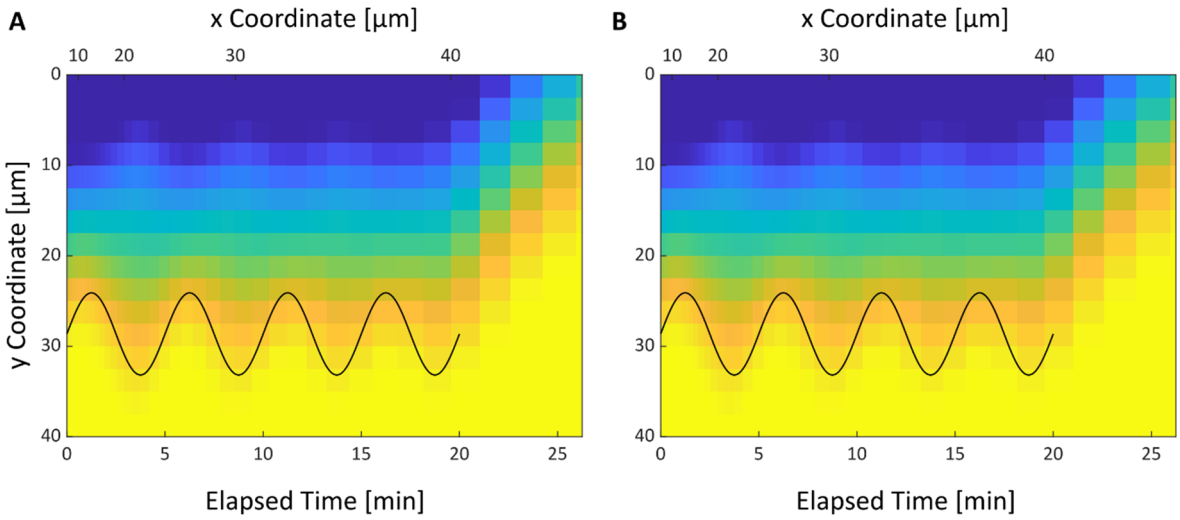

Figure 3-14. *A* and *B*: States of a 2D memristor array at t = 20min simulated with a simulation boundary at (*A*) x = 100µm and (*B*) x = 80µm. The comparable results suggest that a dimension of 80µm along x is sufficient for the time span.

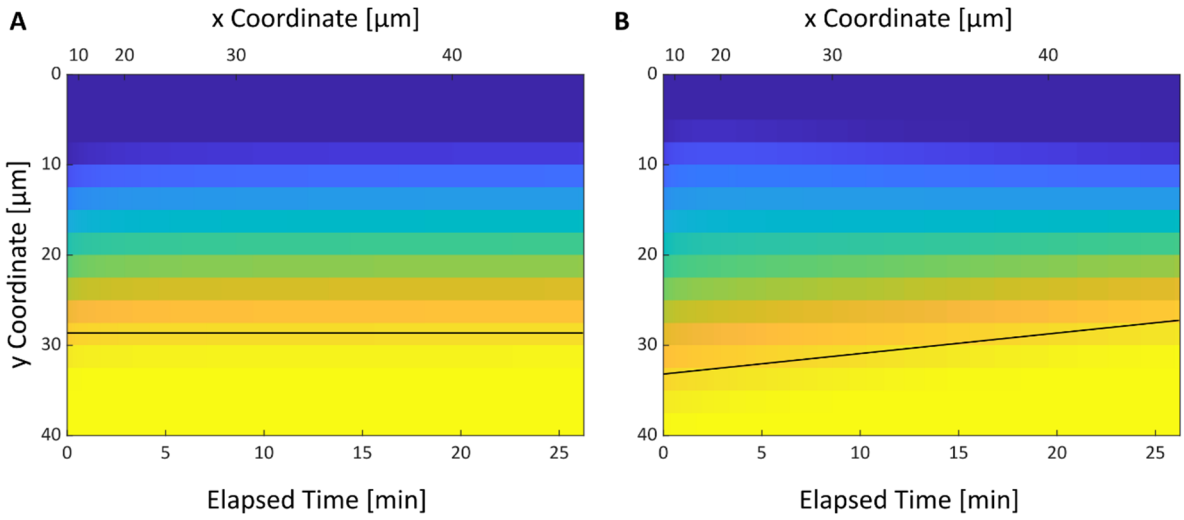

Figure 3-15. *A* and *B*: States of a 2D memristor array at t = 40min responding to (*A*) a constant and (*B*) a linearly ramping profile. Note the absence of distortion across all branches in (*A*). The agreement between the linear profile in (*B*) and the linear ON/OFF front demonstrates the use of the calibration process.

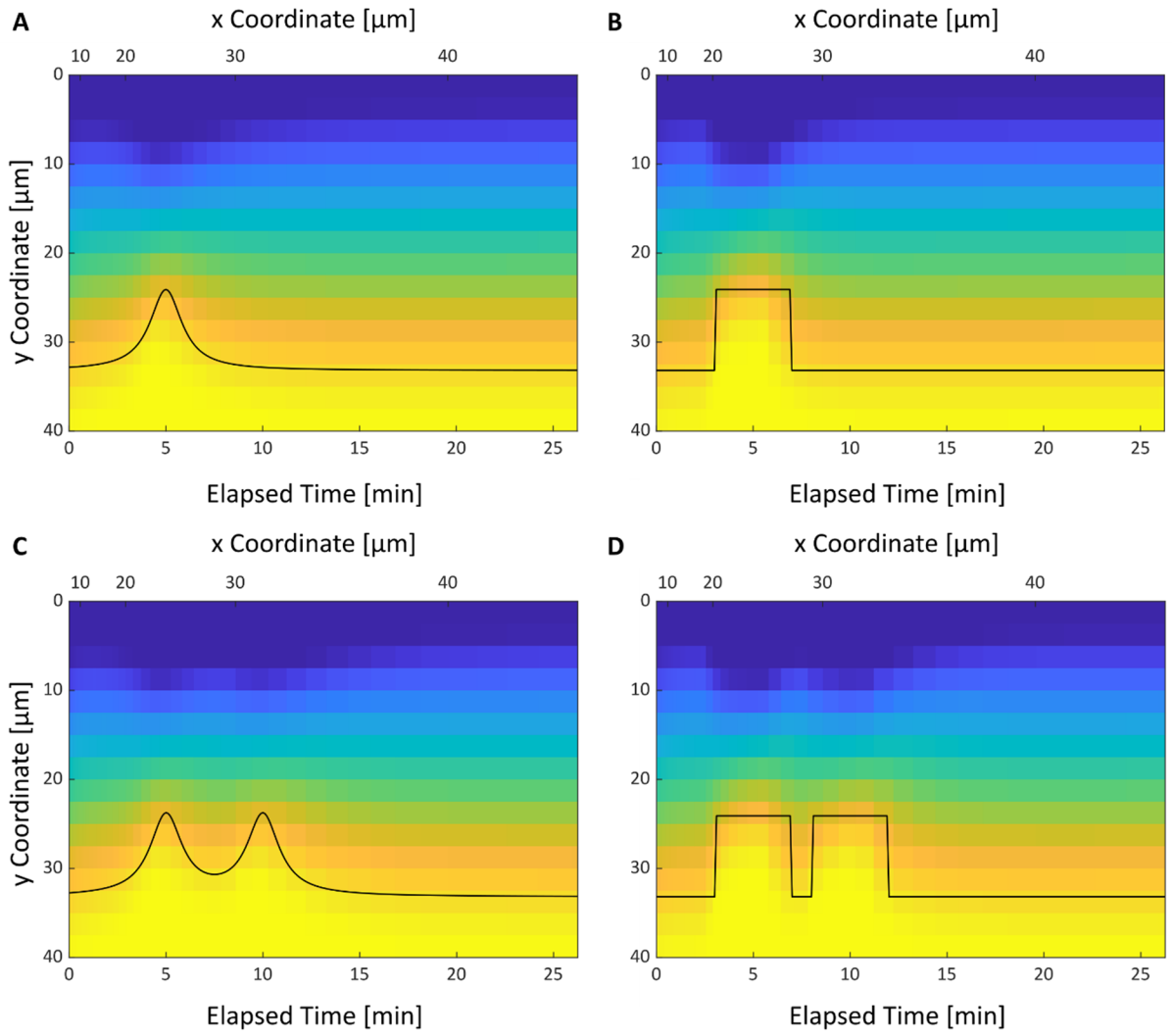

Figure 3-16. *A-D*: States of a 2D memristor array at t = 40min responding to analyte concentration profiles with (*A*) a smooth pulse, (*B*) an abrupt pulse, (*C*) two closely spaced smooth pulses, and (*D*) two closely spaced abrupt pulses. The smooth profiles (*A*, *C*) are modeled following Ref. (99) as $R_y(t) = 5 + 10 / [1 + (t - 5)^2]$ and $R_y(t) = 5 + 10 / [1 + (t - 5)^2] + 10 / [1 + (t - 10)^2]$, respectively. The square profiles (*B*, *D*) respectively follow $R_y(t) = \{15, t \in [3, 7]; 5, \text{otherwise}\}$ and $R_y(t) = \{15, t \in [3, 7] \cup [8, 12]; 5, \text{otherwise}\}$.

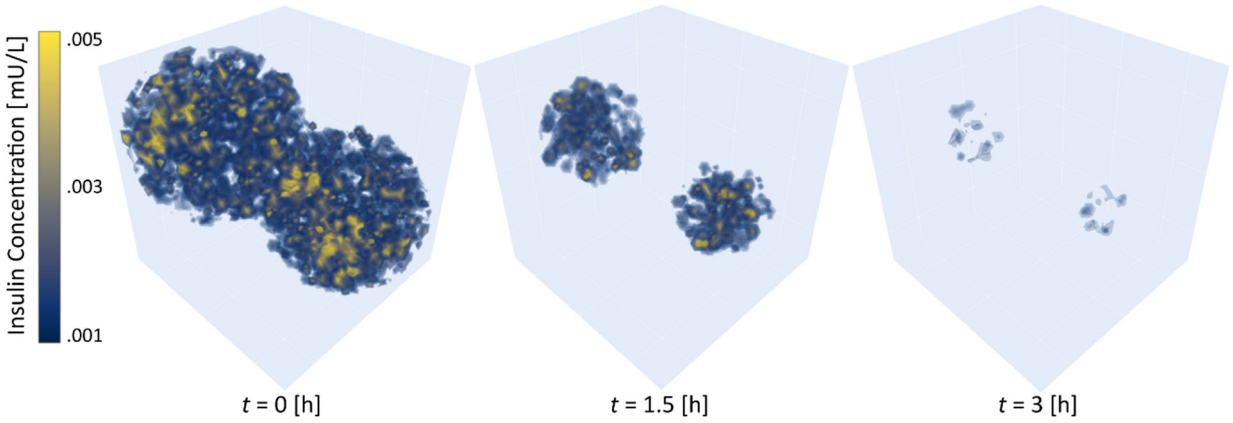

Figure 3-17. Progression of the spatial distribution of insulin released over time by a swarm of 100 microrobotic GRIs with a $[G]_{th}$ of 225 mg/dL in response to the glucose distribution shown in Figure 3-4E. When the microrobotic agents sense a local glucose level above the threshold they release insulin in accordance with the measured magnitude. This closed-loop insulin release in concert with their diffusive motion allows the robots to regulate glucose levels over the spatial domain. As the agents successfully reduce glucose levels, they release less insulin over time.

3.12. References

1. Hey A. There's plenty of room at the bottom. In: Feynman and Computation. CRC Press; 2018. p. 63–76.
2. Fischer P, Nelson BJ. Tiny robots make big advances. Sci Robot [Internet]. 2021 Mar 31;6(52):eabh3168. Available from: https://robotics.sciencemag.org/lookup/doi/10.1126/scirobotics.abh3168
3. Sitti M. Voyage of the microrobots. Nature. 2009;458(7242):1121–2.
4. Miskin MZ, Cortese AJ, Dorsey K, Esposito EP, Reynolds MF, Liu Q, et al. Electronically integrated, mass-manufactured, microscopic robots. Nature [Internet]. 2020 Aug 27;584(7822):557–61. Available from: http://dx.doi.org/10.1038/s41586-020-2626-9
5. Cortese AJ, Smart CL, Wang T, Reynolds MF, Norris SL, Ji Y, et al. Microscopic sensors using optical wireless integrated circuits. Proc Natl Acad Sci [Internet]. 2020 Apr 28;117(17):9173–9. Available from: http://www.pnas.org/lookup/doi/10.1073/pnas.1919677117
6. Esteban-Fernández De Ávila B, Angell C, Soto F, Lopez-Ramirez MA, Báez DF, Xie S, et al. Acoustically propelled nanomotors for intracellular siRNA delivery. ACS Nano. 2016;10(5):4997–5005.
7. Garcia-Gradilla V, Orozco J, Sattayasamitsathit S, Soto F, Kuralay F, Pourazary A, et al. Functionalized ultrasound-propelled magnetically guided nanomotors: Toward practical biomedical applications. ACS Nano. 2013;7(10):9232–40.
8. Hu W, Lum GZ, Mastrangeli M, Sitti M. Small-scale soft-bodied robot with multimodal locomotion. Nature [Internet]. 2018 Feb 24;554(7690):81–5. Available from: http://www.nature.com/articles/nature25443
9. Yu J, Wang B, Du X, Wang Q, Zhang L. Ultra-extensible ribbon-like magnetic microswarm. Nat Commun [Internet]. 2018;9(1):1–9. Available from: http://dx.doi.org/10.1038/s41467-018-05749-6
10. Bandari VK, Nan Y, Karnaushenko D, Hong Y, Sun B, Striggow F, et al. A flexible microsystem capable of controlled motion and actuation by wireless power transfer. Nat Electron [Internet]. 2020;3(3):172–80. Available from: http://dx.doi.org/10.1038/s41928-020-0384-1

11. Brooks AM, Strano MS. A conceptual advance that gives microrobots legs. Nature [Internet]. 2020 Aug 27;584(7822):530–1. Available from: http://www.nature.com/articles/d41586-020-02421-2
12. Jin D, Zhang L. Embodied intelligence weaves a better future. Nat Mach Intell [Internet]. 2020;2(11):663–4. Available from: http://dx.doi.org/10.1038/s42256-020-00250-6
13. Tang Y, Chen C, Khaligh A, Penskiy I, Bergbreiter S. An ultracompact dual-stage converter for driving electrostatic actuators in mobile microrobots. IEEE Trans Power Electron. 2014;29(6):2991–3000.
14. Chen Y, Zhao H, Mao J, Chirarattananon P, Helbling EF, Hyun N seung P, et al. Controlled flight of a microrobot powered by soft artificial muscles. Nature [Internet]. 2019;575(7782):324–9. Available from: http://dx.doi.org/10.1038/s41586-019-1737-7
15. Suzuki H, Wood RJ. Origami-inspired miniature manipulator for teleoperated microsurgery. Nat Mach Intell [Internet]. 2020;2(8):437–46. Available from: http://dx.doi.org/10.1038/s42256-020-0203-4
16. Saito K, Takato M, Sekine Y, Uchikoba F. Biomimetics micro robot with active hardware neural networks locomotion control and insect-like switching behaviour. Int J Adv Robot Syst. 2012;9.
17. Goldberg B, Zufferey R, Doshi N, Helbling EF, Whittredge G, Kovac M, et al. Power and control autonomy for high-speed locomotion with an insect-scale legged robot. IEEE Robot Autom Lett. 2018;3(2):987–93.
18. Lok M, Helbling EF, Zhang X, Wood R, Brooks D, Wei G-Y. A low mass power electronics unit to drive piezoelectric actuators for flying microrobots. IEEE Trans Power Electron [Internet]. 2018 Apr;33(4):3180–91. Available from: http://ieeexplore.ieee.org/document/7927723/
19. Jafferis NT, Helbling EF, Karpelson M, Wood RJ. Untethered flight of an insect-sized flapping-wing microscale aerial vehicle. Nature [Internet]. 2019;570(7762):491–5. Available from: http://www.nature.com/articles/s41586-019-1322-0
20. Savoie W, Berrueta TA, Jackson Z, Pervan A, Warkentin R, Li S, et al. A robot made of robots: Emergent transport and control of a smarticle ensemble. Sci Robot [Internet]. 2019 Sep 18;4(34):eaax4316. Available from: https://robotics.sciencemag.org/lookup/doi/10.1126/scirobotics.aax4316

21. Chen B, Yang H, Song B, Meng D, Yan X, Li Y, et al. A memristor-based hybrid analog-digital computing platform for mobile robotics. Sci Robot [Internet]. 2020 Oct 21;5(47):eabb6938. Available from: https://robotics.sciencemag.org/lookup/doi/10.1126/scirobotics.abb6938
22. Dario P, Valleggi R, Carrozza MC, Montesi MC, Cocco M. Microactuators for microrobots: A critical survey. J Micromechanics Microengineering. 1992;2(3):141–57.
23. Lee S, Cortese AJ, Mok A, Wu C, Wang T, Park JU, et al. Fabrication of injectable Micro-scale Opto-electronically Transduced Electrodes (MOTEs) for physiological monitoring. J Microelectromechanical Syst [Internet]. 2020;1–7. Available from: https://ieeexplore.ieee.org/document/9115624/
24. Lee S, Cortese AJ, Gandhi AP, Agger ER, McEuen PL, Molnar AC. A 250 μm × 57 μm microscale opto-electronically transduced electrodes (MOTEs) for neural recording. IEEE Trans Biomed Circuits Syst [Internet]. 2018 Dec;12(6):1256–66. Available from: https://ieeexplore.ieee.org/document/8491379/
25. Shi C, Costa T, Elloian J, Zhang Y, Shepard KL. A 0.065-mm3 monolithically-integrated ultrasonic wireless sensing mote for real-time physiological temperature monitoring. IEEE Trans Biomed Circuits Syst. 2020;14(3):412–24.
26. Shi C, Andino-Pavlovsky V, Lee SA, Costa T, Elloian J, Konofagou EE, et al. Application of a sub-0.1-mm3 implantable mote for in vivo real-time wireless temperature sensing. Sci Adv. 2021;7(19):1–10.
27. Malachowski K, Jamal M, Jin Q, Polat B, Morris CJ, Gracias DH. Self-folding single cell grippers. Nano Lett. 2014;14(7):4164–70.
28. Xu W, Qin Z, Chen C-T, Kwag HR, Ma Q, Sarkar A, et al. Ultrathin thermoresponsive self-folding 3D graphene. Sci Adv [Internet]. 2017 Oct 20;3(10):1036–40. Available from: https://www.science.org/doi/10.1126/sciadv.1701084
29. Li J, Angsantikul P, Liu W, Esteban-Fernández de Ávila B, Thamphiwatana S, Xu M, et al. Micromotors spontaneously neutralize gastric acid for pH-responsive payload release. Angew Chemie Int Ed [Internet]. 2017 Feb 13;56(8):2156–61. Available from: http://doi.wiley.com/10.1002/anie.201611774
30. Liu Q, Wang W, Reynolds MF, Cao MC, Miskin MZ, Arias TA, et al. Micrometer-sized electrically programmable shape-memory actuators for low-power microrobotics. Sci

Robot [Internet]. 2021 Mar 17;6(52):eabe6663. Available from: https://robotics.sciencemag.org/lookup/doi/10.1126/scirobotics.abe6663

31. Somasundar A, Ghosh S, Mohajerani F, Massenburg LN, Yang T, Cremer PS, et al. Positive and negative chemotaxis of enzyme-coated liposome motors. Nat Nanotechnol [Internet]. 2019;14(12):1129–34. Available from: http://dx.doi.org/10.1038/s41565-019-0578-8
32. Alapan Y, Yasa O, Schauer O, Giltinan J, Tabak AF, Sourjik V, et al. Soft erythrocyte-based bacterial microswimmers for cargo delivery. Sci Robot [Internet]. 2018;3(17):eaar4423. Available from: http://robotics.sciencemag.org/lookup/doi/10.1126/scirobotics.aar4423
33. Palacci J, Sacanna S, Abramian A, Barral J, Hanson K, Grosberg AY, et al. Artificial rheotaxis. Sci Adv [Internet]. 2015 May;1(4):e1400214. Available from: http://arxiv.org/abs/1505.05111%0Ahttp://dx.doi.org/10.1126/sciadv.1400214
34. Dekanovsky L, Khezri B, Rottnerova Z, Novotny F, Plutnar J, Pumera M. Chemically programmable microrobots weaving a web from hormones. Nat Mach Intell [Internet]. 2020 Nov 10;2(11):711–8. Available from: http://dx.doi.org/10.1038/s42256-020-00248-0
35. Khezri B, Villa K, Novotný F, Sofer Z, Pumera M. Smartdust 3D-printed graphene-based Al/Ga robots for photocatalytic degradation of explosives. Small [Internet]. 2020 Aug 7;16(33):2002111. Available from: https://onlinelibrary.wiley.com/doi/10.1002/smll.202002111
36. Ding J, Challa VR, Prasad MG, Fisher FT. Vibration energy harvesting and its application for nano- and microrobotics. In: Selected Topics in Micro/Nano-robotics for Biomedical Applications [Internet]. New York, NY: Springer New York; 2013. p. 59–83. Available from: http://link.springer.com/10.1007/978-1-4419-8411-1_5
37. Zhang H, Qu Z, Tang H, Wang X, Koehler R, Yu M, et al. On-chip integration of a covalent organic framework-based catalyst into a miniaturized Zn-air battery with high energy density. ACS Energy Lett [Internet]. 2021 Jun 15;2491–8. Available from: https://pubs.acs.org/doi/10.1021/acsenergylett.1c00768
38. Liu P, Liu AT, Kozawa D, Dong J, Yang JF, Koman VB, et al. Autoperforation of 2D materials for generating two-terminal memristive Janus particles. Nat Mater. 2018 Nov 23;17(11):1005–12.

39. Koman VB, Liu P, Kozawa D, Liu AT, Cottrill AL, Son Y, et al. Colloidal nanoelectronic state machines based on 2D materials for aerosolizable electronics. Nat Nanotechnol [Internet]. 2018 Sep 23;13(9):819–27. Available from: http://www.nature.com/articles/s41565-018-0194-z
40. Vervacke C, Bof Bufon CC, Thurmer DJ, Schmidt OG. Three-dimensional chemical sensors based on rolled-up hybrid nanomembranes. RSC Adv. 2014;4(19):9723–9.
41. Hempel M, Schroeder V, Park C, Koman VB, Xue M, McVay E, et al. SynCells: A 60 × 60 μm2 electronic platform with remote actuation for sensing applications in constrained environments. ACS Nano [Internet]. 2021 May 25;15(5):8803–12. Available from: https://pubs.acs.org/doi/10.1021/acsnano.1c01259
42. Molina-Lopez F, Gao TZ, Kraft U, Zhu C, Öhlund T, Pfattner R, et al. Inkjet-printed stretchable and low voltage synaptic transistor array. Nat Commun [Internet]. 2019 Dec 18;10(1):2676. Available from: http://dx.doi.org/10.1038/s41467-019-10569-3
43. Samardzic N, Mionic M, Dakic B, Hofmann H, Dautovic S, Stojanovic G. Analysis of quantized electrical characteristics of microscale TiO2 ink-jet printed memristor. IEEE Trans Electron Devices [Internet]. 2015 Jun;62(6):1898–904. Available from: http://ieeexplore.ieee.org/document/7094244/
44. Yoon KJ, Han JW, Moon D Il, Seol ML, Meyyappan M, Kim HJ, et al. Electrically-generated memristor based on inkjet printed silver nanoparticles. Nanoscale Adv. 2019;1(8):2990–8.
45. Carey BJ, Ou JZ, Clark RM, Berean KJ, Zavabeti A, Chesman ASR, et al. Wafer-scale two-dimensional semiconductors from printed oxide skin of liquid metals. Nat Commun [Internet]. 2017 Apr 28;8(1):14482. Available from: http://www.nature.com/articles/ncomms14482
46. Kim YD, Hone J. Screen printing of 2D semiconductors. Nature [Internet]. 2017 Apr 5;544(7649):167–8. Available from: http://www.nature.com/articles/nature21908
47. Yalcintas EP, Ozutemiz KB, Cetinkaya T, Dalloro L, Majidi C, Ozdoganlar OB. Soft electronics manufacturing using microcontact printing. Adv Funct Mater. 2019;29(51):1–13.
48. Demirörs AF, Pillai PP, Kowalczyk B, Grzybowski BA. Colloidal assembly directed by virtual magnetic moulds. Nature [Internet]. 2013 Nov 20;503(7474):99–103. Available

from: http://www.nature.com/articles/nature12591

49. Tan ATL, Beroz J, Kolle M, Hart AJ. Direct-write freeform colloidal assembly. Adv Mater [Internet]. 2018 Nov;30(44):1803620. Available from: http://doi.wiley.com/10.1002/adma.201803620
50. Magdanz V, Stoychev G, Ionov L, Sanchez S, Schmidt OG. Stimuli-responsive microjets with reconfigurable shape. Angew Chemie - Int Ed. 2014;53(10):2673–7.
51. Li J, de Ávila BE-F, Gao W, Zhang L, Wang J. Micro/nanorobots for biomedicine: Delivery, surgery, sensing, and detoxification. Sci Robot. 2017;2(4).
52. Li J, Mooney DJ. Designing hydrogels for controlled drug delivery. Nat Rev Mater. 2016;1(12).
53. Mostaghaci B, Yasa O, Zhuang J, Sitti M. Bioadhesive Bacterial Microswimmers for Targeted Drug Delivery in the Urinary and Gastrointestinal Tracts. Adv Sci [Internet]. 2017 Jun;4(6):1700058. Available from: https://onlinelibrary.wiley.com/doi/10.1002/advs.201700058
54. Solovev AA, Sanchez S, Schmidt OG. Collective behaviour of self-propelled catalytic micromotors. Nanoscale. 2013;5(4):1284–93.
55. Cannon S, Daymude JJ, Randall D, Richa AW. A Markov chain algorithm for compression in self-organizing particle systems. In: Proceedings of the 2016 ACM Symposium on Principles of Distributed Computing [Internet]. New York, New York, USA: ACM Press; 2016. p. 279–88. Available from: http://dl.acm.org/citation.cfm?doid=2933057.2933107
56. Cannon S, Daymude JJ, Gokmen C, Randall D, Richa AW. A local stochastic algorithm for separation in heterogeneous self-organizing particle systems. In: Proceedings of the 2018 ACM Symposium on Principles of Distributed Computing [Internet]. New York, NY, USA: ACM; 2018. p. 483–5. Available from: http://arxiv.org/abs/1805.04599
57. Li S, Batra R, Brown D, Chang H-D, Ranganathan N, Hoberman C, et al. Particle robotics based on statistical mechanics of loosely coupled components. Nature [Internet]. 2019 Mar 20;567(7748):361–5. Available from: https://doi.org/10.1038/s41586-019-1022-9
58. Lamperski A, Cowan N. Optimal control with noisy time. IEEE Trans Automat Contr [Internet]. 2015;61(2):1–1. Available from: http://ieeexplore.ieee.org/document/7122256/
59. Lorand C, Bauer PH. Stability analysis of closed-loop discrete-time systems with clock

frequency drifts. In: Proceedings of the 2003 American Control Conference [Internet]. IEEE; 2003. p. 3323–8. Available from: http://ieeexplore.ieee.org/document/1244044/

60. Nilles AQ, Pervan A, Berrueta TA, Murphey TD, LaValle SM. Information requirements of collision-based micromanipulation. In: Proceedings of the 14th Workshop on the Algorithmic Foundations of Robotics [Internet]. Cham, Germany: Springer; 2021. p. 210–26. Available from: http://link.springer.com/10.1007/978-3-030-66723-8_13
61. Turing AM. On computable numbers, with an application to the Entscheidungsproblem. Proc London Math Soc [Internet]. 1937;s2-42(1):230–65. Available from: https://onlinelibrary.wiley.com/doi/10.1112/plms/s2-42.1.230
62. LaValle SM, Egerstedt M. An information space view of "time": From clocks to open-loop control. In: Emergent Problems in Nonlinear Systems and Control [Internet]. 2009. p. 93–106. Available from: http://link.springer.com/10.1007/978-3-642-03627-9_6
63. LaValle SM, Egerstedt MB. On time: Clocks, chronometers, and open-loop control. In: 2007 46th IEEE Conference on Decision and Control [Internet]. IEEE; 2007. p. 1916–22. Available from: http://ieeexplore.ieee.org/document/4434862/
64. Gerber LC, Rosenfeld L, Chen Y, Tang SKY. Time capsule: An autonomous sensor and recorder based on diffusion-reaction. Lab Chip. 2014;14(22):4324–8.
65. Park J, Lim JM, Jung I, Heo S-J, Park J, Chang Y, et al. Recording of elapsed time and temporal information about biological events using Cas9. Cell [Internet]. 2021 Feb;184(4):1047-1063.e23. Available from: https://linkinghub.elsevier.com/retrieve/pii/S0092867421000143
66. Rogers JA, Bao Z, Meier M, Dodabalapur A, Schueller OJA, Whitesides GM. Printing, molding, and near-field photolithographic methods for patterning organic lasers, smart pixels and simple circuits. Synth Met. 2000;115(1):5–11.
67. Kelly AG, Hallam T, Backes C, Harvey A, Esmaeily AS, Godwin I, et al. All-printed thin-film transistors from networks of liquid-exfoliated nanosheets. Science (80-). 2017;356(6333):69–73.
68. Strukov DB, Snider GS, Stewart DR, Williams RS. The missing memristor found. Nature. 2008;453(7191):80–3.
69. Yang JJ, Pickett MD, Li X, Ohlberg DAA, Stewart DR, Williams RS. Memristive switching mechanism for metal/oxide/metal nanodevices. Nat Nanotechnol [Internet].

2008 Jul 15;3(7):429–33. Available from: http://www.nature.com/articles/nnano.2008.160

70. Wang Z, Wu H, Burr GW, Hwang CS, Wang KL, Xia Q, et al. Resistive switching materials for information processing. Nat Rev Mater [Internet]. 2020 Mar 13;5(3):173–95. Available from: http://dx.doi.org/10.1038/s41578-019-0159-3
71. Joglekar YN, Wolf SJ. The elusive memristor: Properties of basic electrical circuits. Eur J Phys. 2009;30(4):661–75.
72. Biolek Z, Biolek D, Biolková V. SPICE model of memristor with nonlinear dopant drift. Radioengineering. 2009;18(2):210–4.
73. Radwan AG, Zidan MA, Salama KN. On the mathematical modeling of memristors. In: Proceedings of the International Conference on Microelectronics, ICM. IEEE; 2010. p. 284–7.
74. Chua L. Memristor, hodgkin-huxley, and edge of chaos. Nanotechnology. 2013;24(38).
75. Kim S, Choi S, Lu W. Comprehensive physical model of dynamic resistive switching in an oxide memristor. ACS Nano. 2014;8(3):2369–76.
76. Padovani A, Larcher L, Pirrotta O, Vandelli L, Bersuker G. Microscopic modeling of HfOx RRAM operations: From forming to switching. IEEE Trans Electron Devices [Internet]. 2015 Jun;62(6):1998–2006. Available from: http://ieeexplore.ieee.org/document/7086008/
77. Sun W, Gao B, Chi M, Xia Q, Yang JJ, Qian H, et al. Understanding memristive switching via in situ characterization and device modeling. Nat Commun [Internet]. 2019 Dec 1;10(1):3453. Available from: http://dx.doi.org/10.1038/s41467-019-11411-6
78. Williams RS. Summary of the Faraday Discussion on New memory paradigms: Memristive phenomena and neuromorphic applications. Faraday Discuss [Internet]. 2019;213:579–87. Available from: http://xlink.rsc.org/?DOI=C8FD90061B
79. Cao L, Fang G, Cao H, Duan X. Photopatterning and electrochemical energy storage properties of an on-chip organic radical microbattery. Langmuir [Internet]. 2019 Dec 10;35(49):16079–86. Available from: https://pubs.acs.org/doi/10.1021/acs.langmuir.9b02079
80. Liu AT, Kunai Y, Cottrill AL, Kaplan A, Zhang G, Kim H, et al. Solvent-induced electrochemistry at an electrically asymmetric carbon Janus particle. Nat Commun [Internet]. 2021 Dec 7;12(1):3415. Available from:

http://www.nature.com/articles/s41467-021-23038-7

81. Li H, Huang P, Gao B, Chen B, Liu X, Kang J. A SPICE model of resistive random access memory for large-scale memory array simulation. IEEE Electron Device Lett. 2014;35(2):211–3.

82. Puglisi A, Sarracino A, Vulpiani A. Temperature in and out of equilibrium: A review of concepts, tools and attempts. Phys Rep [Internet]. 2017 Nov;709–710:1–60. Available from: https://linkinghub.elsevier.com/retrieve/pii/S0370157317303265

83. Liu AT, Yang JF, LeMar LN, Zhang G, Pervan A, Murphey TD, et al. Autoperforation of two-dimensional materials to generate colloidal state machines capable of locomotion. Faraday Discuss [Internet]. 2021;227:213–32. Available from: http://pubs.rsc.org/en/Content/ArticleLanding/2020/FD/D0FD00030B

84. Zhuang XD, Chen Y, Liu G, Zhang B, Neoh KG, Kang ET, et al. Preparation and memory performance of a nanoaggregated dispersed red 1-functionalized poly (N-vinylcarbazole) film via solution-phase self-assembly. Adv Funct Mater. 2010;20(17):2916–22.

85. Edwards AH, Barnaby HJ, Campbell KA, Kozicki MN, Liu W, Marinella MJ. Reconfigurable memristive device technologies. Proc IEEE. 2015;103(7):1004–33.

86. Chen Y, Liu G, Wang C, Zhang W, Li RW, Wang L. Polymer memristor for information storage and neuromorphic applications. Mater Horizons. 2014;1(5):489–506.

87. Fu T, Liu X, Gao H, Ward JE, Liu X, Yin B, et al. Bioinspired bio-voltage memristors. Nat Commun [Internet]. 2020 Dec 20;11(1):1861. Available from: http://dx.doi.org/10.1038/s41467-020-15759-y

88. McFarlane T, Bandera Y, Grant B, Zdyrko B, Foulger SH, Vilčáková J, et al. Carbazole derivatized n-alkyl methacrylate polymeric memristors as flexible synaptic substitutes. Adv Electron Mater [Internet]. 2020 Jun 11;6(6):2000042. Available from: https://onlinelibrary.wiley.com/doi/abs/10.1002/aelm.202000042

89. Qian W, Cheng X, Zhou J, He J, Li H, Xu Q, et al. Lead-free perovskite MASnBr3-based memristor for quaternary information storage. InfoMat [Internet]. 2020 Jul 25;2(4):743–51. Available from: https://onlinelibrary.wiley.com/doi/abs/10.1002/inf2.12066

90. Qi M, Cao S, Yang L, You Q, Shi L, Wu Z. Uniform multilevel switching of graphene oxide-based RRAM achieved by embedding with gold nanoparticles for image pattern recognition. Appl Phys Lett. 2020;116(16).

91. Feng X, Li Y, Wang L, Chen S, Yu ZG, Tan WC, et al. A fully printed flexible MoS2 memristive artificial synapse with femtojoule switching energy. Adv Electron Mater [Internet]. 2019 Dec 19;5(12):1900740. Available from: https://onlinelibrary.wiley.com/doi/abs/10.1002/aelm.201900740
92. Hempel M, Schröder V, Park C, Xue M, Park J, Swager T, et al. SynCells - Electronic microparticles for sensing applications. Cambridge, MA; 2019.
93. Lee CW, Suh JM, Jang HW. Chemical sensors based on two-dimensional (2D) materials for selective detection of ions and molecules in liquid. Front Chem [Internet]. 2019 Nov 15;7(November):1–21. Available from: https://www.frontiersin.org/article/10.3389/fchem.2019.00708/full
94. Ammu S, Dua V, Agnihotra SR, Surwade SP, Phulgirkar A, Patel S, et al. Flexible, all-organic chemiresistor for detecting chemically aggressive vapors. J Am Chem Soc [Internet]. 2012 Mar 14;134(10):4553–6. Available from: https://pubs.acs.org/doi/10.1021/ja300420t
95. Yamazoe N, Sakai G, Shimanoe K. Oxide semiconductor gas sensors. Catal Surv from Asia. 2003;7(1):63–75.
96. Turkani VS, Maddipatla D, Narakathu BB, Bazuin BJ, Atashbar MZ. A carbon nanotube based NTC thermistor using additive print manufacturing processes. Sensors Actuators A Phys [Internet]. 2018 Aug;279:1–9. Available from: https://doi.org/10.1016/j.sna.2018.05.042
97. Cao X, Wei X, Li G, Hu C, Dai K, Guo J, et al. Strain sensing behaviors of epoxy nanocomposites with carbon nanotubes under cyclic deformation. Polymer (Guildf) [Internet]. 2017;112:1–9. Available from: http://dx.doi.org/10.1016/j.polymer.2017.01.068
98. Nishikubo R, Saeki A. Solution-processed Bi2S3 photoresistor film to mitigate a trade-off between morphology and electronic properties. J Phys Chem Lett. 2018;9(18):5392–9.
99. Ghods N, Krstic M. Source seeking with very slow or drifting sensors. J Dyn Syst Meas Control [Internet]. 2011 Jul 1;133(4). Available from: https://asmedigitalcollection.asme.org/dynamicsystems/article/doi/10.1115/1.4003639/443917/Source-Seeking-With-Very-Slow-or-Drifting-Sensors
100. Bequette BW. Process Dynamics: Modeling, Analysis, and Simulation. Prentice Hall

International Series in the Physical and Chemical Engineering Sciences. Upper Saddle River, NJ: Prentice Hall PTR; 1998.

101. The MathWorks Inc. Non-adiabatic continuous stirred tank reactor: MATLAB file modeling with simulations in Simulink® [Internet]. Available from: https://www.mathworks.com/help/ident/ug/non-adiabatic-continuous-stirred-tank-reactor-matlab-file-modeling-with-simulations-in-simulink.html#d122e43522
102. Jin Q, Yang Y, Jackson JA, Yoon C, Gracias DH. Untethered single cell grippers for active biopsy. Nano Lett. 2020;20(7):5383–90.
103. Kamaly N, Yameen B, Wu J, Farokhzad OC. Degradable controlled-release polymers and polymeric nanoparticles: Mechanisms of controlling drug release. Chem Rev [Internet]. 2016 Feb 24;116(4):2602–63. Available from: http://pubs.acs.org/doi/10.1021/acs.chemrev.5b00346
104. Torchilin VP. Multifunctional, stimuli-sensitive nanoparticulate systems for drug delivery. Nat Rev Drug Discov. 2014;13(11):813–27.
105. Veiseh O, Tang BC, Whitehead KA, Anderson DG, Langer R. Managing diabetes with nanomedicine: Challenges and opportunities. Nat Rev Drug Discov. 2014;14(1):45–57.
106. Hoeg-Jensen T. Review: Glucose-sensitive insulin. Mol Metab [Internet]. 2021 Apr;46(xxxx):101107. Available from: https://doi.org/10.1016/j.molmet.2020.101107
107. Webber MJ, Anderson DG. Smart approaches to glucose-responsive drug delivery. J Drug Target. 2015;23(7–8):651–5.
108. Santini JT, Cima MJ, Langer R. A controlled-release microchip. Nature [Internet]. 1999 Jan;397(6717):335–8. Available from: http://www.nature.com/articles/16898
109. Villarruel Mendoza LA, Scilletta NA, Bellino MG, Desimone MF, Catalano PN. Recent advances in micro-electro-mechanical devices for controlled drug release applications. Front Bioeng Biotechnol. 2020;8(July):1–28.
110. Sutradhar KB, Sumi CD. Implantable microchip: The futuristic controlled drug delivery system. Drug Deliv. 2016;23(1):1–11.
111. Farra R, Sheppard NF, McCabe L, Neer RM, Anderson JM, Santini JT, et al. First-in-human testing of a wirelessly controlled drug delivery microchip. Sci Transl Med. 2012;4(122).
112. Zinger B, Miller LL. Timed release of chemicals from polypyrrole films. J Am Chem Soc

[Internet]. 1984 Oct;106(22):6861–3. Available from: https://pubs.acs.org/doi/abs/10.1021/ja00334a076

113. Maloney JM, Uhland SA, Polito BF, Sheppard NF, Pelta CM, Santini JT. Electrothermally activated microchips for implantable drug delivery and biosensing. J Control Release. 2005;109(1–3):244–55.
114. Li Y, Duc HLH, Tyler B, Williams T, Tupper M, Langer R, et al. In vivo delivery of BCNU from a MEMS device to a tumor model. J Control Release. 2005;106(1–2):138–45.
115. Pillay V, Tsai TS, Choonara YE, Du Toit LC, Kumar P, Modi G, et al. A review of integrating electroactive polymers as responsive systems for specialized drug delivery applications. J Biomed Mater Res - Part A. 2014;102(6):2039–54.
116. Yang JF, Gong X, Bakh NA, Carr K, Phillips NFB, Ismail-Beigi F, et al. Connecting rodent and human pharmacokinetic models for the design and translation of glucose-responsive insulin. Diabetes [Internet]. 2020 Aug 9;69(8):1815–26. Available from: http://diabetes.diabetesjournals.org/lookup/doi/10.2337/db19-0879
117. Maheandiran M, Mylvaganam S, Wu C, El-Hayek Y, Sugumar S, Hazrati L, et al. Severe hypoglycemia in a juvenile diabetic rat model: Presence and severity of seizures are associated with mortality. Bader M, editor. PLoS One [Internet]. 2013 Dec 30;8(12):e83168. Available from: https://dx.plos.org/10.1371/journal.pone.0083168
118. Bakh NA, Bisker G, Lee MA, Gong X, Strano MS. Rational design of glucose-responsive insulin using pharmacokinetic modeling. Adv Healthc Mater. 2017;6(22):1–10.
119. Cryer PE, Davis SN, Shamoon H. Hypoglycemia in diabetes. Diabetes Care. 2003 Jun 1;26(6):1902–12.
120. GhavamiNejad A, Li J, Lu B, Zhou L, Lam L, Giacca A, et al. Glucose-responsive composite microneedle patch for hypoglycemia-triggered delivery of native glucagon. Adv Mater [Internet]. 2019 Jun 5;31(30):1901051. Available from: https://onlinelibrary.wiley.com/doi/abs/10.1002/adma.201901051
121. Smolensky MH, Peppas NA. Chronobiology, drug delivery, and chronotherapeutics. Adv Drug Deliv Rev [Internet]. 2007 Aug;59(9–10):828–51. Available from: https://linkinghub.elsevier.com/retrieve/pii/S0169409X0700124X
122. Ruben MD, Smith DF, Fitzgerald GA, Hogenesch JB. Dosing time matters. Science.

2019;365(6453):547–50.

123. Wang Z, Wu H, Burr GW, Hwang CS, Wang KL, Xia Q, et al. Resistive switching materials for information processing. Nat Rev Mater [Internet]. 2020;5(3):173–95. Available from: http://dx.doi.org/10.1038/s41578-019-0159-3

124. Barahona F, Grötschel M, Jünger M, Reinelt G. An application of combinatorial optimization to statistical physics and circuit layout design. Oper Res [Internet]. 1988 Jun;36(3):493–513. Available from: http://pubsonline.informs.org/doi/abs/10.1287/opre.36.3.493

125. Gielen GGE, Walscharts HCC, Sansen WMC. Analog circuit design optimization based on symbolic simulation and simulated annealing. IEEE J Solid-State Circuits [Internet]. 1990 Jun;25(3):707–13. Available from: http://ieeexplore.ieee.org/document/102664/

126. Pervan A, Murphey TD. Low complexity control policy synthesis for embodied computation in synthetic cells. In: Proceedings of the 13th Workshop on the Algorithmic Foundations of Robotics. 2018.

127. Censi A. A mathematical theory of co-design. arXiv [Internet]. 2015 Dec 25;1512.08055. Available from: http://arxiv.org/abs/1512.08055

128. Mirhoseini A, Goldie A, Yazgan M, Jiang JW, Songhori E, Wang S, et al. A graph placement methodology for fast chip design. Nature [Internet]. 2021;594(7862):207–12. Available from: http://dx.doi.org/10.1038/s41586-021-03544-w

129. Choi S, Tan SH, Li Z, Kim Y, Choi C, Chen P-Y, et al. SiGe epitaxial memory for neuromorphic computing with reproducible high performance based on engineered dislocations. Nat Mater [Internet]. 2018; Available from: http://www.nature.com/articles/s41563-017-0001-5

130. Goswami S, Rath SP, Thompson D, Hedström S, Annamalai M, Pramanick R, et al. Charge disproportionate molecular redox for discrete memristive and memcapacitive switching. Nat Nanotechnol [Internet]. 2020 May 23;15(5):380–9. Available from: http://dx.doi.org/10.1038/s41565-020-0653-1

131. Goswami S, Deb D, Tempez A, Chaigneau M, Rath SP, Lal M, et al. Nanometer-scale uniform conductance switching in molecular memristors. Adv Mater. 2020;32(42):1–11.

132. Bessonov AA, Kirikova MN, Petukhov DI, Allen M, Ryhänen T, Bailey MJA. Layered memristive and memcapacitive switches for printable electronics. Nat Mater.

2015;14(2):199–204.

133. Cho S-Y, Gong X, Koman VB, Kuehne M, Moon SJ, Son M, et al. Cellular lensing and near infrared fluorescent nanosensor arrays to enable chemical efflux cytometry. Nat Commun [Internet]. 2021 Dec 25;12(1):3079. Available from: http://dx.doi.org/10.1038/s41467-021-23416-1
134. Fan F, Zhang B, Cao Y, Yang X, Gu J, Chen Y. Conjugated polymer covalently modified graphene oxide quantum dots for ternary electronic memory devices. Nanoscale. 2017;9(30):10610–8.
135. Brivio S, Tallarida G, Perego D, Franz S, Deleruyelle D, Muller C, et al. Low-power resistive switching in Au/NiO/Au nanowire arrays. Appl Phys Lett [Internet]. 2012 Nov 26;101(22):223510. Available from: http://aip.scitation.org/doi/10.1063/1.4769044
136. Hui F, Lanza M. Scanning probe microscopy for advanced nanoelectronics. Nat Electron [Internet]. 2019;2(6):221–9. Available from: http://dx.doi.org/10.1038/s41928-019-0264-8
137. Zuo Y, Lin H, Guo J, Yuan Y, He H, Li Y, et al. Effect of the pressure exerted by probe station tips in the electrical characteristics of memristors. Adv Electron Mater. 2020;6(3):1–8.
138. Najm FN. Circuit Simulation [Internet]. Hoboken, NJ, USA: John Wiley & Sons, Inc.; 2010. Available from: http://link.springer.com/10.1007/978-1-4613-1687-9_1
139. Sitti M. Mobile Microrobotics. Arkin RC, editor. Cambridge, MA: MIT Press; 2017.
140. Prodromakis T, Peh BP, Papavassiliou C, Toumazou C. A versatile memristor model with nonlinear dopant kinetics. IEEE Trans Electron Devices. 2011;58(9):3099–105.
141. Chua L, Sbitnev V, Kim H. Hodgkin-Huxley axon is made of memristors. Int J Bifurc Chaos [Internet]. 2012 Mar;22(03):1230011. Available from: http://www.worldscientific.com/doi/abs/10.1142/S021812741230011X
142. Yu J, Wang J, Zhang Y, Chen G, Mao W, Ye Y, et al. Glucose-responsive insulin patch for the regulation of blood glucose in mice and minipigs. Nat Biomed Eng [Internet]. 2020;1–8. Available from: http://www.nature.com/articles/s41551-019-0508-y
143. Baek J, Shen Y, Lignos I, Bawendi MG, Jensen KF. Multistage microfluidic platform for the continuous synthesis of III–V core/shell quantum dots. Angew Chemie Int Ed [Internet]. 2018 Aug 20;57(34):10915–8. Available from: https://onlinelibrary.wiley.com/doi/10.1002/anie.201805264

144. Cole KP, Groh JM, Johnson MD, Burcham CL, Campbell BM, Diseroad WD, et al. Kilogram-scale prexasertib monolactate monohydrate synthesis under continuous-flow CGMP conditions. Science (80-) [Internet]. 2017 Jun 16;356(6343):1144–50. Available from: https://www.science.org/doi/10.1126/science.aan0745
145. Boillat CS, Gaschen FP, Hosgood GL. Assessment of the relationship between body weight and gastrointestinal transit times measured by use of a wireless motility capsule system in dogs. Am J Vet Res [Internet]. 2010 Aug;71(8):898–902. Available from: https://avmajournals.avma.org/doi/10.2460/ajvr.71.8.898
146. Jo G, Choe M, Lee S, Park W, Kahng YH, Lee T. The application of graphene as electrodes in electrical and optical devices. Nanotechnology. 2012;23(11).
147. Liu P, Cottrill AL, Kozawa D, Koman VB, Parviz D, Liu AT, et al. Emerging trends in 2D nanotechnology that are redefining our understanding of "Nanocomposites." Nano Today [Internet]. 2018 Aug;21:18–40. Available from: https://doi.org/10.1016/j.nantod.2018.04.012

CHAPTER 4

Connecting rodent and human pharmacokinetic models for the design and translation of GRIs

This chapter has been adapted from:

Jing Fan Yang, Xun Gong, Naveed A. Bakh, Kelley Carr, Nelson F. B. Phillips, Faramarz Ismail-Beigi, Michael A. Weiss, and Michael S. Strano. 2020. "Connecting Rodent and Human Pharmacokinetic Models for the Design and Translation of Glucose-Responsive Insulin." Diabetes 69(8):1815–26.

4.1. Abstract

Despite considerable progress, development of glucose-responsive insulins (GRI) still largely depends on empirical knowledge and tedious experimentation – especially on rodents. To assist the rational design and clinical translation of the therapeutic, we present a Pharmacokinetic Algorithm Mapping GRI Efficacies in Rodents and Humans (PAMERAH), built upon our previous human model. PAMERAH constitutes a framework for predicting the therapeutic efficacy of a GRI candidate from its user-specified mechanism of action, kinetics, and dosage, which we show is accurate when checked against data from experiments and literature. Results from simulated glucose clamps also agree quantitatively with recent GRI publications. We demonstrate that the model can be used to explore the vast number of permutations constituting the GRI parameter space, and thereby identify the optimal design ranges that yield desired performance. A design guide aside, PAMERAH more importantly can facilitate GRI's clinical translation by connecting each candidate's efficacies in rats, mice, and humans. The resultant mapping helps find GRIs which appear promising in rodents but underperform in humans (*i.e. false-positives*). Conversely, it also allows for the discovery of optimal human GRI dynamics not captured by experiments on a rodent population (*false-negatives*). We condense such information onto a *translatability grid* as a straightforward, visual guide for GRI development.

4.2. Introduction

Diabetes mellitus (DM) is a growing condition affecting upwards of 425 million people worldwide with a healthcare burden of 727 billion USD in 2017 (1). In the US alone, the total estimated cost of diagnosed DM exceeds $320 billion yearly, which saw a 26% increase from 2012 to 2017 (2). The condition is marked by high blood glucose levels, or hyperglycemia, resulting from either impaired insulin production (DM type 1) or insulin resistance (DM type 2). If left unchecked, hyperglycemia can result in organ damage, disabilities, and other life-threatening complications (1). Insulin, the 51 amino acid hormone secreted from pancreatic β-cells, remains a mainstay therapeutic for all diabetics.

Conventionally, glycemic control is accomplished by scheduled insulin injections and regular blood glucose monitoring. The open-loop nature of such a dosing scheme renders substantial patient compliance a requirement. Alarmingly, three quarters of physicians reported non-adherence to the prescribed regimen in their patients, which can be attributed to both the uncomfortable and time-consuming nature of the traditional therapy (3). The intrinsic drawbacks of an open-loop therapy are further highlighted by factors such as: inter-individual variations, the lag between blood glucose measurement and insulin administration, delayed absorption, as well as the conservatism in dosing due to hypoglycemia concerns (4,5). Resnick *et al.* estimated that the desired glycemic control is not achieved by half of the diabetic patients surveyed (6). Efforts have thus been aimed towards a closed-loop, automated system in which insulin dosing is modulated in accordance with the real-time glucose concentration in the patient's bloodstream, akin to a functional pancreas (7). Recently, integration of continuous glucose sensing and insulin pumps has shown promise in hypoglycemia reduction and sustained blood glucose suppression, although it is currently still expensive and associated with increased risks of complications such as infection, inflammation and scarring (8).

An alternative is the concept of a glucose-responsive insulin (GRI). In the absence of external devices, these therapeutics achieve controlled insulin activity in response to the local environment through their glucose-binding chemistries and subsequent triggered insulin release or potency enhancement (9). A multitude of GRI constructs have been reported over the years, often relying on glucose-mediated degradation, swelling, gelling, or disassembly of insulin-encapsulating carriers, which can be reversible or irreversible (10). Recently, freely circulating GRIs, not

polymer-encapsulated formations, have been designed by Chou *et al.* with simplified chemical kinetics (11), echoing the first GRI concept conceived by Brownlee and Cerami in 1979 (12).

GRIs are shown to enforce tighter glycemic control, reduce the incidence of hypoglycemic episodes, and lessen the burden of multiple daily injections in a multitude of experimental studies (4,10), yet efforts towards a mathematical framework for their rational design have been limited to date (9). While the localized release kinetics from certain GRIs have been modeled before, they have not been translated into therapeutic efficacy for design purposes. Specifically, GRI models were not pieced together with the underlying insulin-glucose-glucagon metabolism (13,14). Our previous work (5) established the first framework that linked GRI designs to their therapeutic effectiveness through pharmacokinetic modeling of type 1 diabetic patients.

However, the majority of GRI research relies on substantial testing in animal models and specifically rodents (11,15). We identify the critical importance of extending this said mathematical framework to bridge the gap between widely used animal models and the prediction of human clinical observations so as to expedite the search for viable drug candidates. Given that pharmacokinetics cannot be simply scaled between organisms in general (16) and that almost all therapeutics are inevitably tested on animal models such as rodents as a start, the rational design of GRI may therefore greatly benefit from a mathematical approach specifically developed for predicted testing in mice and rats. In this work, we present a Pharmacokinetic Algorithm Mapping GRI Efficacies in Rodents and Humans (PAMERAH). This *in silico* modeling framework couples GRI kinetics to the first full-body physiology-based model describing murine glycemic control, and maps rodent physiology to that of humans for therapeutic design.

PAMERAH can serve as a standardized platform for GRI construction, candidate screening, design optimization, and preclinical trial planning. Prior to any experimentation, the model is able to predict average GRI performances and narrow down the vast parameter space to a set of optimal combinations of design variables, for the user-defined population and GRI mode of action. Such model-aided preclinical research would alleviate the burden of many trials and errors required in the traditional drug development workflow – an implication for not just GRIs.

Moreover, our mathematical formulation allows for a cross-comparison among mice, rats, and humans, highlighting their commonalities and differences. PAMERAH shows that the optimal GRI parameter spaces overlap, but not to a large extent, between the species, echoing the frequent

difficulty of replicating animal studies in humans (17,18): the long-standing practice of informing clinical trials with animal data is now coming under scrutiny, wittily described by Mak *et al.* as "lost in translation" (19). PAMERAH further allows a zoned grid to be drawn, on which GRI candidates are sectioned by their predicted viabilities along the train of medicinal translation. We expect the so-called *translatability grid* to serve as a straightforward visual guide for planning animal testing and clinical trials.

4.3. Research Design and Methods

4.3.1. Modeling the Full-Body Glucoregulatory System

A physiological model simulating a rodent's full-body pharmacokinetics of glucose, insulin, and glucagon is first constructed, followed by its integration with GRI kinetics. The overall workflow is summarized in Figure 4-7.

Mathematical modeling of the human glucoregulatory system has attracted sustained attention from the diabetes community over the years. While semi-mechanistic parsimonious models have seen some success recently (20,21), their compartmentalization is not based on physiology, which renders GRI integration difficult. This is contrasted by the whole-body model by Sorensen (22) and its variants. The Sorensen-like models (23–25) explicitly consider the physiology, taking into account the blood flowrates, volumes, and connectivity of organs. This allows dynamic concentrations to be probed and the glucose-hormone metabolism to be altered at the organ, rather than organism, level (26). As with our prior physiological model of humans (5,26), PAMERAH is divided into well-mixed compartments symbolizing participating body parts, each equivalent numerically to an ideal continuous stirred-tank reactor (CSTR), as illustrated by Figure 4-1. Blood circulates through vascular compartments of gut, liver, kidneys, brain, muscle and adipose tissues, carrying glucose, insulin, and glucagon; the composition in the outlet of a vascular volume is approximated to be identical to that within the compartment – just like a CSTR. The solutes diffuse freely between the vascular and interstitial compartments as well where applicable, dictated by the concentration gradients. Naturally then, each solute s in each organ k is described as:

$$V^s_{k,\mathrm{v}} \frac{d[s]_{k,\mathrm{v}}}{dt} = Q^s_k([s]_{\mathrm{heart}} - [s]_{k,\mathrm{v}}) - \frac{V^s_{k,\mathrm{i}}}{T^s_k}([s]_{k,\mathrm{v}} - [s]_{k,\mathrm{i}}) + R^s_{k,\mathrm{v,prod}} - R^s_{k,\mathrm{v,uptake}} \quad (4\text{-}1)$$

$$V^s_{k,\mathrm{i}} \frac{d[s]_{k,\mathrm{i}}}{dt} = \frac{V^s_{k,\mathrm{i}}}{T^s_k}([s]_{k,\mathrm{v}} - [s]_{k,\mathrm{i}}) + R^s_{k,\mathrm{i,prod}} - R^s_{k,\mathrm{i,uptake}} \quad (4\text{-}2)$$

where subscripts v and i denote the vascular and interstitial volumes, respectively. V represents the compartmental volume, $[s]$ the solute concentration, Q the arterial flowrate through the organ, and T the characteristic transcapillary time of mass transfer. The production and uptake rates, R_{prod} and R_{uptake}, when applicable, are modulated by the compartment's glucose, insulin, and glucagon concentrations through logistic transfer functions. As with our prior work (5), the subcutaneous injection depot is described by a hexamer-dimer-monomer equilibrium of which only the dimeric/monomeric insulins (or GRIs), lumped as a single state, are absorbed (Table 4-2).

As the existing Sorensen-like mathematical models are parameterized based on the physiology of a healthy 70-kg man, the parameters have to be re-examined meticulously during the model's extension to rats and mice. While exponential scaling laws are followed for interspecies adaptation of parsimonious compartmental models (27), the allometric exponents are empirical and bear little physical meaning. On the other hand, for a physiology-backed model like PAMERAH, *a priori* animal anatomical measurements are used to adjust the physiological parameters accordingly, such as the organ sizes, cardiac outputs, arterial flows, and blood volumes (Table 4-1). As the transfer functions, which characterize the organs' responsiveness to glucoregulation, are not directly adaptable to rodents, these metabolic parameters are estimated numerically from blood glucose time trajectories measured in rats and mice. The same method is applied to the base generation/clearance rates which lack consistent measured values in the published literature. The insulin response data for rats and mice are collected experimentally and from literature (11) (male Lewis rats and C57BL/6J mice, healthy or with streptozotocin-induced diabetes; also see §4.6). To avoid overfitting, sensitivity analyses (28,29) are performed for dimension reduction. The model reduction is shown to yield consistent results for mice and rats (Figure 4-6). The most impactful 15 unknown parameters identified, out of more than 120, are subsequently fitted to data while keeping the remainder fixed (Table 4-2). The dimension of estimated parameters is minimal as compared to published physiology-based models (24,30,31). Parameter estimation is performed in MATLAB R2017a (the MathWorks, Inc.) with a pattern search algorithm.

The Sorensen model and its many extensions treat a type 1 diabetic subject simply as a healthy individual with the pancreatic parameters negated and starting concentrations modified (5,22). In addition to introducing these distinctions between type 1 diabetic and healthy rodents, we also acknowledge the more subtle differences reported between the two populations, such as the changes in glucose/hormonal sensitivities and organ-specific base metabolic rates upon diabetes development (32–34). These inter-population distinctions are addressed by estimating the 8 relevant parameters separately for the type 1 and healthy rodents (Table 4-2), consistent with current published works (21,24,35). In fact, attempts to simulate both groups with a single, unified set of values do not render satisfactory predictions that globally match experiments, thus highlighting the need of the distinguishing parameterization. Such was concurred and discussed in detail by Schaller *et al.* (24), who differentiated the healthy and diabetic populations by 26 separately fitted variables.

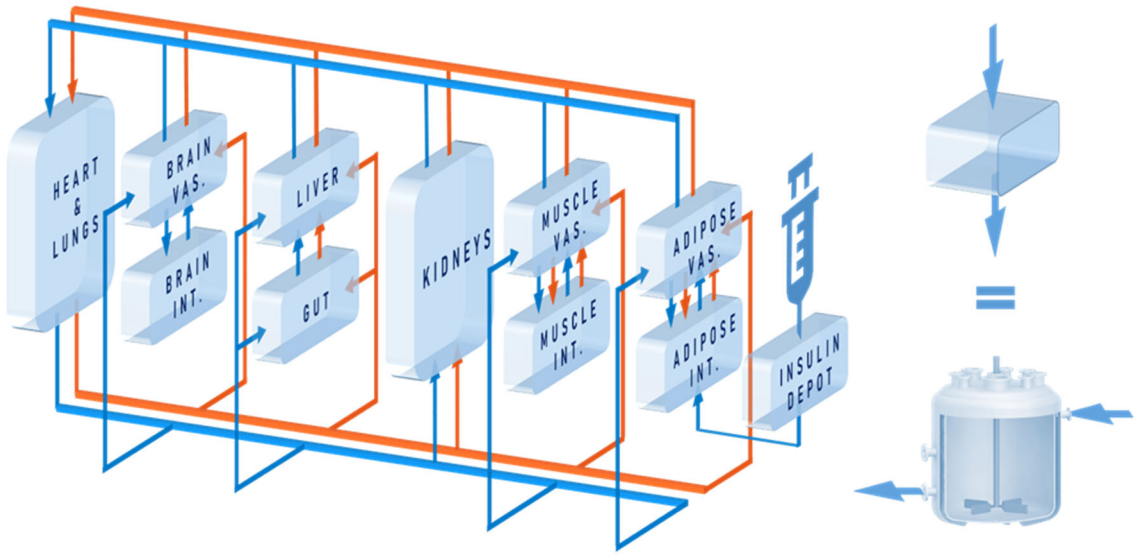

Figure 4-1. Schematic of the model structure. Glucose (blue) circulates around the body along with blood, which is pumped by the heart and flows through vascular compartments of gut, liver, kidneys, brain, muscle and adipose tissues. For the latter three, transcapillary diffusion of glucose into interstitial spaces are captured by the interstitial compartments. Insulin or GRI (red), introduced into the circulation via the subcutaneous injection depot, flows through all but the brain interstitial compartment, into which insulin is unable to penetrate. Each compartment is equivalent to a continuous stirred-tank reactor (CSTR, as shown on the right), where perfect mixing is assumed.

4.3.2. Modeling the GRI

GRIs of different working mechanisms, once expressed in mathematical terms, can be integrated with the as-constructed full-body physiological model, assembling into PAMERAH. Of all GRIs, the freely circulating class presents the simplest chemical kinetics. An example was recently reported by Chou and associates (11), who introduced responsiveness into their insulin analog by chemical modification with phenylboronic acid (PBA) as a glucose-sensing element. Note that although Chou *et al.* also demonstrated a long-lasting activity with the GRI by incorporation of an aliphatic domain, our model focuses on the glucose-responsiveness for now.

Action of the said class of GRIs can be condensed into the following two-state kinetics, where a dormant GRI (D) is reversibly activated by glucose (G), turning into the active form (I):

$$\mathrm{G} + \mathrm{D} \underset{k_\mathrm{r}}{\overset{k_\mathrm{f}}{\rightleftharpoons}} \mathrm{I} \qquad K_\mathrm{eq} = k_\mathrm{f} / k_\mathrm{r} \tag{4-3}$$

k_f is the forward rate constant, k_r is the reverse rate constant, and K_eq is the equilibrium constant. Consequently for any solute s – where s can now be glucose, insulin, glucagon, or dormant GRI each with a stoichiometric coefficient (v) of -1, 1, 0, and -1 respectively – the defining Equations 1 and 2 in compartment k become:

$$V_{k,\mathrm{v}}^{s}\frac{d[s]_{k,\mathrm{v}}}{dt} = Q_k^s([s]_{\mathrm{heart}} - [s]_{k,\mathrm{v}}) - \frac{V_{k,\mathrm{i}}^{s}}{T_k^s}([s]_{k,\mathrm{v}} - [s]_{k,\mathrm{i}}) + R_{k,\mathrm{v,prod}}^{s} - R_{k,\mathrm{v,uptake}}^{s} + V_{k,\mathrm{v}}^{\mathrm{I}}\nu_s r_{\mathrm{GRI}} \tag{4-4}$$

$$V_{k,\mathrm{i}}^{s}\frac{d[s]_{k,\mathrm{i}}}{dt} = \frac{V_{k,\mathrm{i}}^{s}}{T_k^s}([s]_{k,\mathrm{v}} - [s]_{k,\mathrm{i}}) + R_{k,\mathrm{i,prod}}^{s} - R_{k,\mathrm{i,uptake}}^{s} + V_{k,\mathrm{i}}^{\mathrm{I}}\nu_s r_{\mathrm{GRI}} \tag{4-5}$$

where $r_{\mathrm{GRI}} = k_f[\mathrm{G}]_k[\mathrm{D}]_k - k_r[\mathrm{I}]_k$ for freely circulating GRIs described by Equation 3. We adopt the kinetics of these GRIs for all PAMERAH simulations presented hereafter in this report for the mathematical simplicity and recent attention attracted. Of note, it is assumed throughout this report that the dormant GRI does not perturb the metabolic or hormone kinetics while the activated GRI behaves identically as native insulin. For scenarios where the activated analog differs in potency from insulin, the assumption may be relaxed by treating them as separate solutes, each with a distinct set of ODEs.

The complete system of ODEs for all compartments and all solutes concerned can be constructed from the simple general Equations 4-4 and 4-5. A comprehensive tutorial is provided in the §4.7 to walk the reader through the process. Note that the equations are given in a generalizable form, not just specific to the current model architecture, so that a reader attempting to modify or to supplement the model may follow exactly the same procedures outlined in the tutorial.

4.3.3. Simulating GRI in a Clamp

In addition to tracking the response of the blood glucose concentration to a single GRI injection, clamp studies (36) are an alternative standard technique to assess glucose responsiveness. We program PAMERAH to also simulate glucose clamps, the results of which are compared to recent GRI experiments as a further validation of the model. We follow the two-period pancreatic clamp protocol outlined in Moore *et al.*, illustrated in Figure 4-9 (37). The glucose concentration is clamped for 150 min at 110 mg/dL (Period 1) and for another 150 min at 240 mg/dL (Period 2) by continuous infusion via the peripheral vascular compartment. The variable glucose infusion rate is adjusted by a simple feedback control. Meanwhile, either insulin lispro (1.2 mU/min) or GRI (24 mU/min) is infused continuously throughout the 300-min clamp, together with glucagon at its basal rate. The rates are consistent with prior reports (37,38). In Moore *et al.*, pancreatic endocrine release was completely suppressed by somatostatin (37), simulated as the corresponding differential equations bypassed in PAMERAH. Therefore, all circulating insulin and glucagon is accounted for by external infusion, except during the short initial equilibration. The hepatic glucose load (HGL) is calculated as $[G]_{\text{heart}} Q^{\text{G}}_{\text{hepatic artery}} + [G]_{\text{gut}} Q^{\text{G}}_{\text{gut}}$ and the net hepatic glucose balance (NHGB) is defined as $[G]_{\text{liver}} Q^{\text{G}}_{\text{liver}} - \text{HGL}$.

4.3.4. Elucidating the GRI Design Space

PAMERAH provides valuable assistance to the GRI development process by assessing the GRI's therapeutic efficacy in mice and rats based on its material and molecular design. Intuitively, an adequate GRI should reduce hyperglycemia in a diabetic subject for a prolonged period (with a single bolus), while not incurring any additional risk of hypoglycemia (9). Sometimes fatal, the latter is referred to as the "limiting factor" in glycemic management (39). The mathematical expression for said criteria is below:

$$\begin{cases} \text{Hyperglycemic Risk} \equiv \int_{t=2\text{h}}^{t=24\text{h}} \max([\text{G}]_{\text{blood}} - [\text{G}]_{\text{ub}}, 0)dt = 0 \\ \text{Hypoglycemic Risk} \equiv \int_{t=0}^{t=24\text{h}} \max([\text{G}]_{\text{lb}} - [\text{G}]_{\text{blood}}, 0)dt = 0 \end{cases} \quad (6)$$

in which $t = 0$ marks the time of GRI administration. $[\text{G}]_{\text{ub}}$ and $[\text{G}]_{\text{lb}}$ are the upper and lower bounds of the normoglycemic range, set to 240 and 75 mg/dl respectively for rats (40) and 250 and 40 mg/dl for mice (41). As described by Equations 6, normoglycemia should be maintained for a GRI design to be qualified: the blood glucose level should not deviate from the normal range within 24 hours of the single GRI bolus, except for the first 120 minutes allowed for the hyperglycemia to be put under control.

The properties of freely circulating GRIs are modulated by three design variables: k_{f}, K_{eq}, and the dosage. We term each distinct permutation of the three a potential GRI *design* or a *candidate*, with its own hyper- and hypoglycemic risks. By probing the k_{f}-K_{eq}-dosage parameter space, the *in silico* preclinical simulations identify regions free from the said risks. Finally, this simulation study is repeated for humans as well using the model of Bakh *et al.* (5). An interspecies cross-comparison reveals the similarities and dissimilarities among humans, rats, and mice, and provides insights on drug translatability.

4.4. Results

Blood glucose responses to an initial insulin injection, as predicted by the parameterized full-body physiological models, are presented in Figure 4-2A-D alongside murine *in vivo* data collected experimentally and from the published literature (11). We show that the temporal profiles match between model and animal data for various doses of subcutaneous insulin administration to healthy and type 1 rodents alike. Trajectories in Figure 4-2A-D also reveal how the effect of unmodified insulin decreases quickly despite large injection doses. In Figure 4-2E, F we present as an example the simulated action profiles of a freely circulating GRI in average diabetic rats and mice. PAMERAH predicts that, in addition to suppressing the blood glucose levels, this particular GRI candidate is also able to arrest three postprandial glycemic excursions within 120 minutes, each resultant from a 1 g/kg oral glucose meal (42), over the course of 24 hours. The corresponding insulin release patterns (Figure 4-8) resemble published results (15).

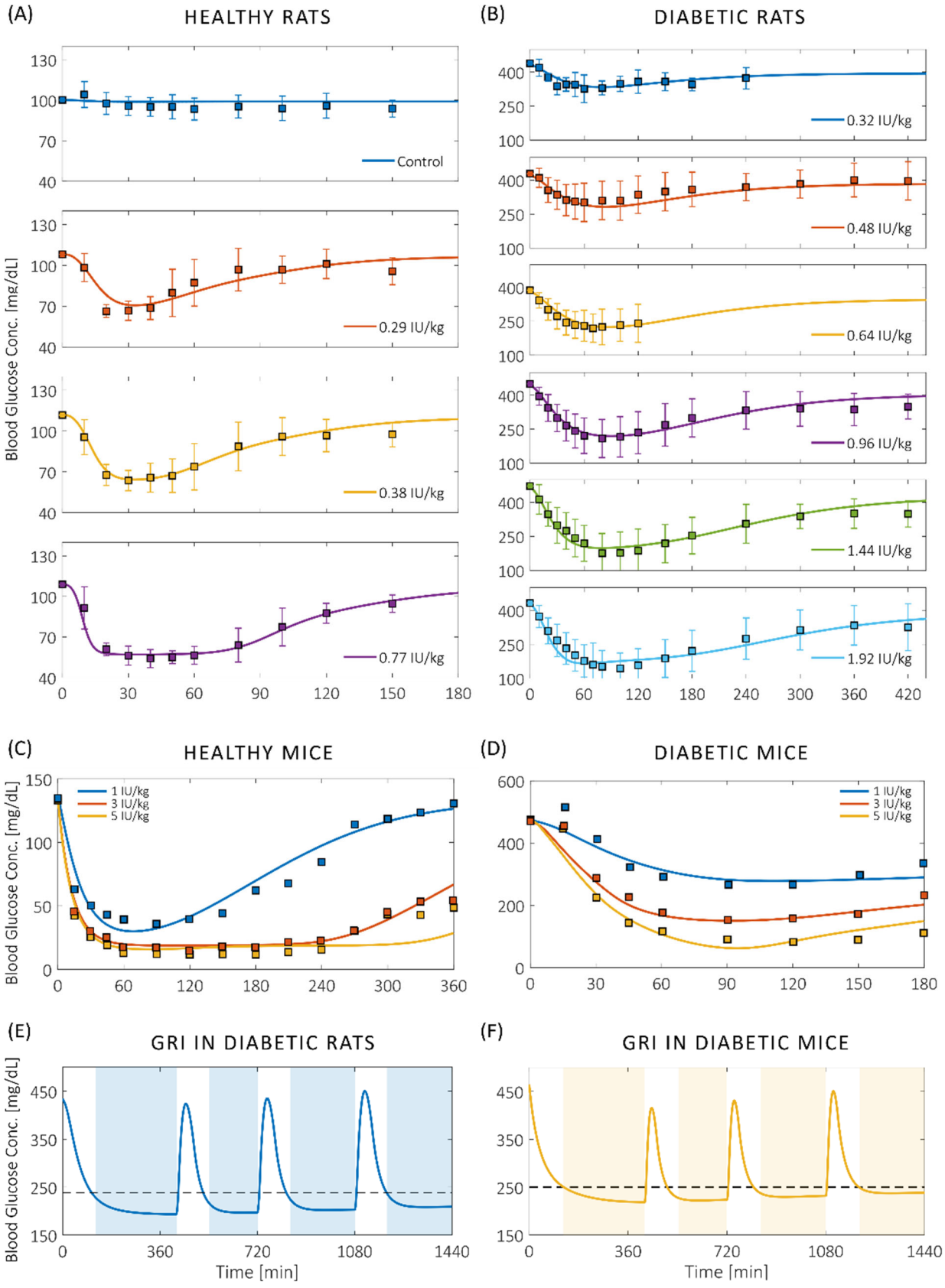
(A)
HEALTHY RATS
Control
0.29 IU/kg
0.38 IU/kg
0.77 IU/kg
Blood Glucose Conc. [mg/dL]
(B)
DIABETIC RATS
0.32 IU/kg
0.48 IU/kg
0.64 IU/kg
0.96 IU/kg
1.44 IU/kg
1.92 IU/kg
(C)
HEALTHY MICE
1 IU/kg
3 IU/kg
5 IU/kg
Blood Glucose Conc. [mg/dL]
(D)
DIABETIC MICE
1 IU/kg
3 IU/kg
5 IU/kg
(E)
GRI IN DIABETIC RATS
Blood Glucose Conc. [mg/dL]
Time [min]
(F)
GRI IN DIABETIC MICE
Time [min]

Figure 4-2. Blood glucose responses in rodents to a single insulin injection. Panels (A-D) show the agreement between murine *in vivo* data (squares) and the predicted glycemic responses (curves) to various doses of non-responsive insulin administered at $t = 0$. PAMERAH predictions match well with experimental measurements from healthy (A) and type 1 diabetic rats (B) as well as healthy (C) and type 1 diabetic mice (D). Curves for rats are presented individually to avoid overlapping of data points and confidence limits, which indicate ± 1 standard deviation. Data presented are collected from male Lewis rats, the diabetes of which is induced by STZ (§4.6). Measurements on mice (male C57BL/6J, STZ) are extracted from Chou and associates (11). The corresponding error bars are absent as they were undefined in Chou *et al.*, and the clustered error bars cannot be precisely digitized from the original figures. Panels (E, F) show the 24-hour action profiles of a GRI example (k_f = 0.1 $M^{-1}min^{-1}$, K_{eq} = 0.02 M^{-1}, dosage = 300 μg/kg) in average diabetic rats (E) and mice (F). The blood glucose concentration drops to the normoglycemic range within 120 min after the initial injection at $t = 0$ and each of the three meal ingestions (1 g/kg glucose, at t = 420, 720, and 1080 min), periods represented by the unshaded areas. The peak post-prandial concentrations are respectively 423.8, 434.9, 450.2 mg/dL for diabetic rats and 415.2, 430.5, 450.4 mg/dL for diabetic mice. The dashed lines indicate the upper bounds of normoglycemic ranges.

The validity of PAMERAH is further supported by the agreement between simulated clamp results and experimental data. In their two-period pancreatic clamp study, Moore *et al.* found that while the hepatic glucose loads were comparable between the GRI and insulin groups (Figure 4-3B), both the net and unidirectional hepatic glucose uptakes (HGU, Figure 4-3C, D respectively) for the GRI study were significantly higher than the non-responsive insulin control at the hyperglycemic clamp level (Period 2). All these findings are matched by PAMERAH simulation in rats (Figure 4-3A-D), in addition to correctly predicting the relative changes in each quantity after the clamp level shift. Curiously, the simulated and actual time courses of HGL, NHGB, and HGU agree quantitatively once normalized, despite that Moore *et al.*'s GRI was of a different working principle and tested on dogs. This seems to suggest a universal signature of glucose responsiveness: under hyperglycemic conditions, a GRI would enhance the liver glucose uptake more effectively than a dose of non-responsive insulin (37).

PAMERAH simulation is shown to also match a separate set of data provided by Kaarsholm *et al.* (43), who investigated the active GRI/insulin concentrations at various clamp levels following a similar protocol outlined above. Both our simulation and the data clearly show that a larger amount of active GRI is made available at a higher glucose level (Figure 4-3E), while such a dependence is absent in the control study (Figure 4-3F). The quantitative discrepancies are attributed to the different GRI mechanisms, to be addressed further in Discussion.

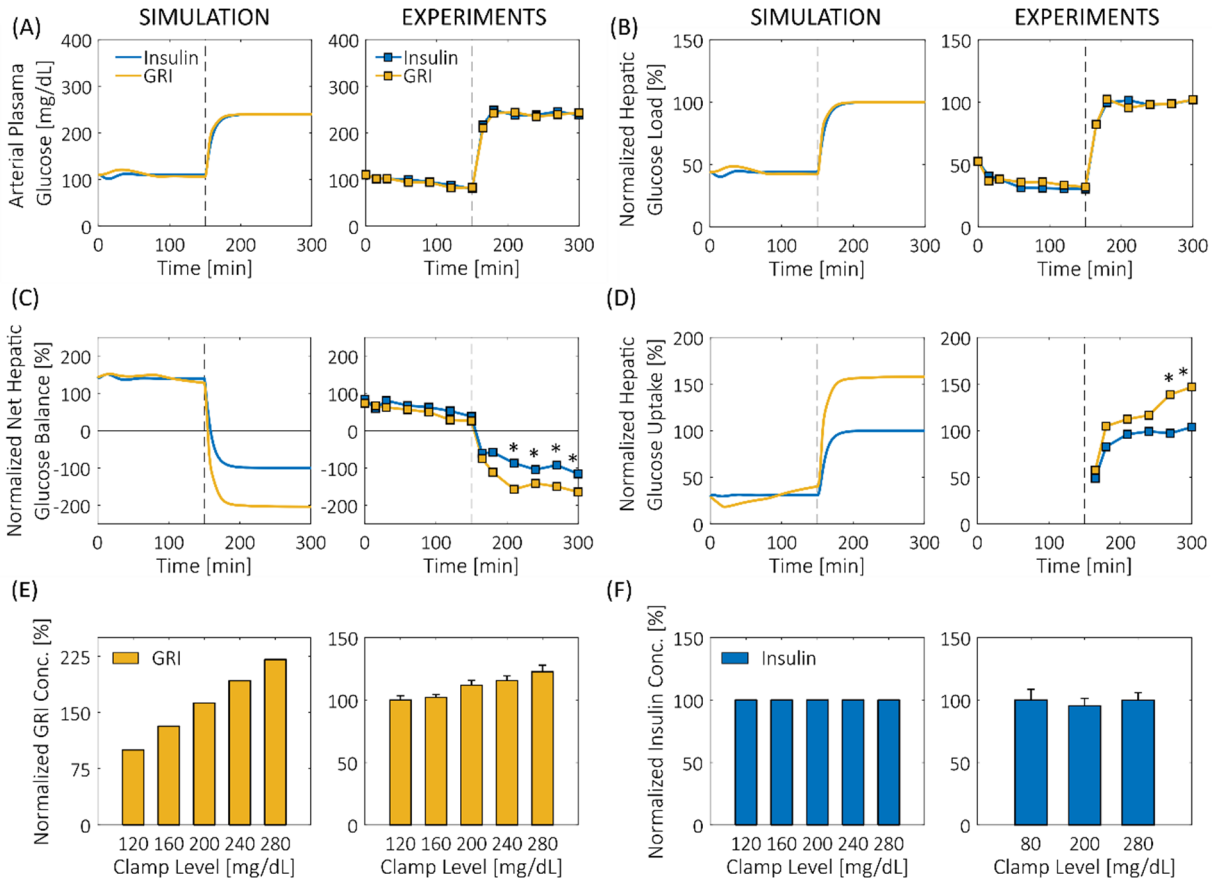

Figure 4-3. Glucose clamp results simulated by PAMERAH as compared to experiments. Shown in Panel (A), glucose is clamped at 110 (Period 1) and 240 mg/Dl (Period 2) for 150 min each with constant infusion of either non-responsive insulin or GRI. Consistent the experimental data published (37), the hepatic glucose loads (B) for insulin and GRI do not differ at either clamp level. While the net hepatic glucose balances (C) are positive in Period 1, they switch sign at the higher clamp level, indicating a change from net glucose production to consumption in the liver. As with experiments (right), GRI induces a larger change than the non-responsive control in Period 2. Similarly, while both the GRI and insulin groups trigger a surge in unidirectional hepatic glucose uptake (D) at t = 150 min, GRI is more effective, a feature captured by the simulation. Data in Panels (B-D) are normalized by the respective Period 2 steady state values for the insulin group due to the differences in GRI mechanisms and test animals. Asterisks indicate $P < 0.05$ for GRI *vs.* control. Responsiveness of GRI and insulin to different glucose levels is shown in Panels (E) and (F) alongside data from clamps (43). While the amount of active GRI released is increasing with the clamp level (E), the concentration of non-responsive insulin (F) shows no dependence. Note that in the clamps described, GRI is solely responsible for the observed responsiveness as the pancreatic insulin production is inhibited by somatostatin. The concentrations in Panels (E, F) are normalized by the corresponding values at 120 mg/dL. The pre-normalization GRI concentrations ranged from 165.8 (at 120 mg/dL) to 290.4 mU/L (at 280 mg/dL) for simulations in rats and 761.5 to 933.3 mU/L for MK-2640 in dogs. All experimental data are digitized from published figures.

Following its validation with experimental results, PAMERAH is subsequently applied to systematically screen the freely circulating GRI candidates by simulating the murine glycemic responses to each. The varied design parameters therefore form a three-dimensional GRI Design Space (GRIDS), shown as the boxes in Figure 4-4 and probed by PAMERAH. Each point in GRIDS represents a unique combination of k_f, K_{eq}, and dosage – which we term as one design. Our mathematical model gauges the hypo- and hyperglycemic risks associated with each such design and thereby identifies the qualified GRI candidates free of the risks – *i.e.* those predicted to maintain normoglycemia over at least 24 hours as governed by Equations 6. The qualified designs within GRIDS constitute what we call optimal design regions (ODRs), represented as the shaded geometries in Figure 4-4A–C, which are respectively ODRs of healthy rats, diabetic rats, and the intersection. Those for mice and humans are found in Figure 4-10. We observe that the diabetic ODR is bounded from beneath by a global minimum effective dose of 115 ± 5 μg/kg (marked by the grey planes in Figure 4-4B), below which no design is able to contain hyperglycemia for a day (Figure 4-4D). The global minimum doses for mice and humans are 105 ± 5 and 12.25 ± 0.25 μg/kg, respectively. The latter is of a reduced uncertainty as the low-dosage portion of the human GRIDS is explored with a refined resolution (Figure 4-10C).

A cross-comparison among the ODRs of rats, mice, and humans (Figure 4-5A, B) reveals the interspecies commonalities and distinctions. While the ODRs for rats and mice overlap to a moderate extent, a fairly limited subset of optimal GRI designs in rodents is predicted to be also acceptable to humans. Acknowledging the GRI dosage as an easily adjustable design parameter neglecting solubility, we relax the corresponding dimension (Figure 4-5C). The three-dimensional GRIDS is thereby collapsed into a two-dimensional plane, on which combinations of k_f and K_{eq} are zoned by their performances in different species: we are able to identify designs effective in rodents only, humans only, neither, or both, each respectively constituting 12.0%, 14.1%, 60.3%, and 13.6% of all designs within the particular variable bounds. This zoning scheme can serve as a simple guideline for GRI translation as discussed in more details below.

4.5. Discussion

In this work, we develop the modeling framework PAMERAH as a platform relating a GRI's design to its therapeutic efficacy in rats and mice. Based on the full-body physiology, the

pharmacokinetic model simulates the absorption, circulation, uptake, generation, and clearance of glucose, glucagon, as well as glucose-responsive or non-responsive insulin by treating each organ as a well-mixed CSTR. With key parameters calibrated by *in vivo* data, we demonstrate that PAMERAH predicts the dynamic blood glucose responses and clamp results in rodents, for insulin as well as GRIs of user-specified kinetics (Figure 4-2, Figure **4-3**). In the following discussions, we highlight how PAMERAH aids the rational design process of GRI and its translation to the clinic.

4.5.1. Model-Aided GRI Design

PAMERAH is able to explore the parameter space and predict the average performance of each combination of design variables, thus narrowing down the vast pool of GRI candidates *in silico*, thereby providing directions to GRI preclinical research as evidenced by GRIDS and ODRs in Figure 4-4. The ODR geometries also strengthen validity of the model predictions. We observe that the diabetic rat ODR assumes a signature *L* shape (Figure 4-4B, bottom), and consequently so does the ODR for normal and diabetic populations combined (Figure 4-4C). Concurring with prior reports (5), the *L* geometry results from the balance between rapid action and sustained control. On one hand, GRI candidates of slow kinetics, marked by a small k_f or K_{eq}, are unable to reduce blood glucose concentration in time to the normoglycemic range (Figure 4-4B, middle). On the other hand, GRIs of large k_f and K_{eq} rapidly convert to active insulin; consequently, they either deplete prematurely, unable to sustain the potency over 24 hours (Figure 4-4B, middle), or overcorrect the hyperglycemia, thus triggering hypoglycemic episodes (Figure 4-4B, top). The latter also explains the missing corner in Figure 4-4A which characterizes the ODR of the healthy population, for which the hyperglycemic risk is absent. Consistent with mouse and human GRIDS probed as well (Figure 4-10), the observations above suggest a good agreement between PAMERAH predictions and qualitative expectations.

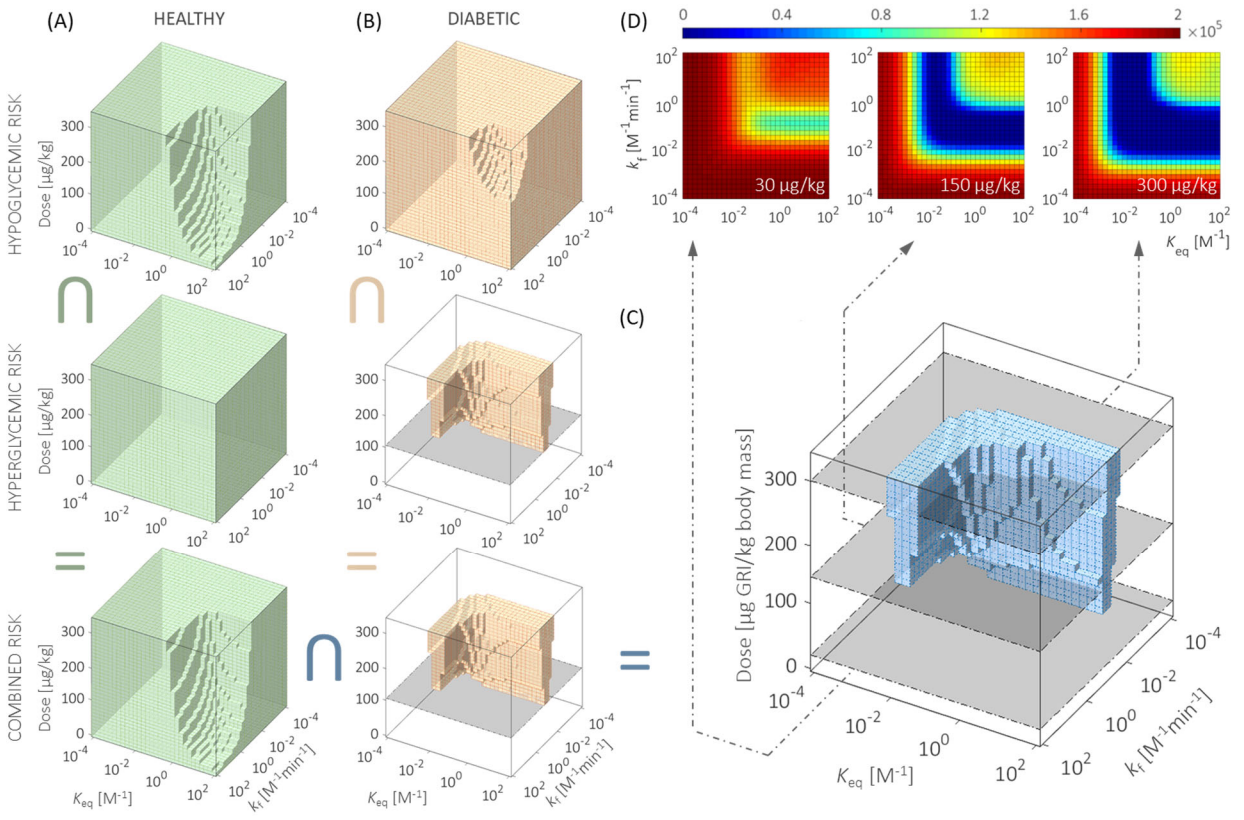

Figure 4-4. Exploring the optimal combinations of GRI design parameters for efficacy in rodents. PAMERAH explores the GRI Design Space (GRIDS) and evaluates the hypo- and hyperglycemic risks associated with each GRI candidate for both healthy (A) and diabetic (B) rats. The shaded areas in GRIDS are the optimal design regions (ODRs), which represent those combinations of k_f, K_{eq}, and dosage free of hypoglycemic (top), hyperglycemic (middle), or both risks (bottom, intersection of the other two single-risk ODRs). The grey planes in Panel (B) mark the global minimum effective dosage in diabetic rats. The GRI designs which incur neither risk in normal and diabetic rats alike are shaded blue in panel (C). The characteristic *L* shape is consistent with prior reports (5), better visualized by contour plots (D) sliced at fixed GRI dosages (30, 150, and 300 µg/kg, marked grey in the GRIDS). The colors in panel (D) correspond to the sum of all hypo-/hyperglycemic risks combined, with dark blue representing desirable GRI constructs which maintain normoglycemia over 24 hours. ODRs and GRIDS for mice and humans are found in Figure 4-10. The inverted *U* symbol means intersection.

We envisage the PAMERAH-aided rational design of GRI boosting the productivity of drug developers by (partially) substituting the conventional workflow, where each empirically designed and often laboriously synthesized candidate is experimented *in vitro* and *in vivo* for its efficacy evaluation (11,44). The same evaluation may now be performed *in silico* at effectively no cost, even before the physical existence of any GRI prototype – a benefit enjoyed only by mechanistic, physiological models like PAMERAH and not data-driven empirical models (45). The medicinal

chemists may then proceed focusing on just the optimized, most promising lot – the ODRs (46). This would be especially helpful to GRI researchers without access to automated combinatorial chemistry or screening. The facilitated designing process aside, PAMERAH also provides information on the minimum effective doses and may potentially lighten the dependency on animal testing, to which the model supplies a rational starting point. Furthermore, such a physiological model for preclinical species, supported by *in vivo* measurements, promotes the confidence in the corresponding human models, argued Jones and associates (47,48): simulations in rodents are an essential intermediate step towards accurate predictions of human pharmacokinetics at the clinical stage, as concluded from a PhRMA initiative (45).

4.5.2. Model-Aided GRI Translation

Cross-comparing the optimal designs for different species is shown to reveal the commonalities and distinctions among rats, mice, and humans (Figure 4-5), and therefore the potential interspecies translatability of drug candidates. While the ODRs for the diabetic all assume the characteristic *L* geometry, the minimal overlaps between rodent and human ODRs (Figure 4-5A, B) hint that a large portion of GRI designs, again each defined by a combination of k_f, K_{eq}, and dosage in this report, would render adequate, sustained glycemic control in rodents yet fail clinically, which we call *false-positive* (FP) preclinical results. In other words, PAMERAH predicts a high attrition rate if GRI constructs are translated to the clinical trial stage with the same parameters as in rodents, hence echoing the published poor rates of successful translation (18,49): the well-known estimate of Hackam and Redelmeier was that only 37% of animal studies were successfully replicated in human trials. A recent Tufts investigation further communicated that the clinical translation of anti-diabetic drugs was even riskier as compared to other pharmaceuticals (50). For instance, Merck's MK-2640, the only GRI we know of that entered the clinical trial stage, did not achieve the same level of glucose responsiveness in humans as in preclinical models (43,51).

In addition to the false-positives, the overlaid GRIDS in Figure 4-5 by the same token identify the GRI candidates deemed unsuitable in rodents but potentially effective in humans, *i.e.* the *false-negatives (*FN). While many agree that the opportunity cost of the FN is greater than the FP (52), little is known about the extent to which we wrongly discontinue a viable drug design based on negative preclinical outcomes, as such a candidate is usually eliminated from further confirmation.

The available analyses on this topic target FN at a single clinical stage, which is more of a decision variable controllable by the trial sample size (52) – conceptually distinct from the false-negatives pertaining to rodent model translatability. PAMERAH predictions on "what should have passed", in addition to "what should not have", therefore adds helpful new knowledge. We further note that the same methodology is applicable to therapeutics beyond GRIs. For example, Jones *et al.* simulated pharmacokinetic actions of several small-molecule candidates in both preclinical animals and humans (48); while the compounds had been finalized before the said study, the physiology-based models could have assisted the design and translation processes, akin to PAMERAH, were they available at the earlier stages of drug development.

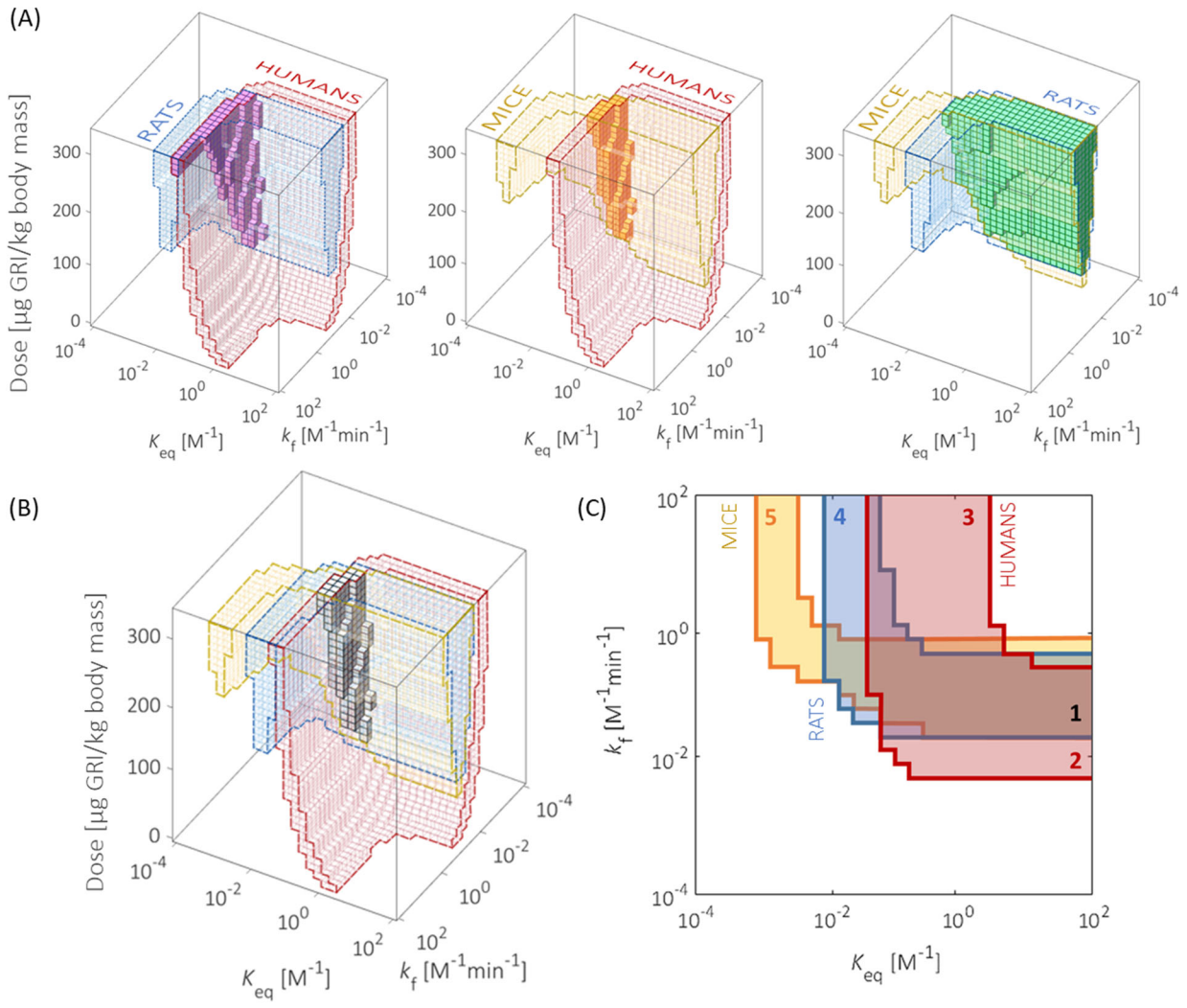

Figure 4-5. Evaluating the GRI translatability from rodents to humans. Panel (A) highlights the commonalities (solid) between ODRs (colored and outlined) of humans and rats (left), humans and mice (middle), as well as rats and

mice (right). Panel (B) marks the ODR intersection (solid) among all three species. The limited overlap between human and rodent ODRs forecasts the difficulties in interspecies translation of the therapeutic. By relaxing the dosage variable (0–330 μg/kg) and allowing it to assume flexible values for different species, we project the three-dimensional GRIDS onto a two-dimensional kf-Keq plot (C). We call the plot a translatability grid, on which GRI designs are zoned according to their translatability. GRI constructs in Zone 1 are predicted to be effective in both rodents and humans. They therefore translate well among species with appropriate dosages. Zones 2 and 3 represent the false-negative designs eliminated in rodent studies yet potentially clinically viable. Zones 4 and 5 are examples of false-positives which appear effective in rat/mouse trials but do not translate well into humans. They will likely meet attrition at the clinical stage.

We acknowledge that in contrast to kinetic variables k_f and K_{eq}, the GRI dosage is a more flexible dimension. Figure 4-5C displays the outcome when the dosage dimension is relaxed and allowed to assume different values (per body mass) for different species. Projecting the three-dimensional GRIDS along the dosage axis onto the k_f-K_{eq} plane issues a graphic (Figure 4-5C) loosely analogous to a Clarke error grid (53), but with zones representing the design's translatability instead of a measurement's clinical accuracy. We see that each three-dimensional ODR is now compressed to a two-dimensional L, inside which a GRI design (of a certain k_f-K_{eq} combination) is effective within *some* dosage range. The overlap between ODRs of humans and either rodent (mice or rats) marks the *true-positive* designs predicted to translate well into the clinic: they are effective regardless of species (Figure 4-5C Zone 1). They, nevertheless, only make up 13.6% of the total plane, comparable to the identified false-positives (12.0%; Zones 2, 3): the numbers are roughly interpreted as an attrition rate of almost half for the candidates successful in rodents. On the other hand, it is surprising that 14.1% of possible GRI constructs are wrongly disqualified (FN; Zones 4, 5), equivalent to approximately half of the clinically adequate designs being excluded from potentially entering the human trials. This observation highlights the need for predictive tools such as PAMERAH, since animal models can possess parametric regions that do not map to human performance. We note that the exact area percentages depend on the GRIDS bounds (Figure 4-11) and a reasonable upper dosage bound should be set based on, say, solubility limitations (54). Although the attrition in developing a GRI may also result from non-efficacy-related factors such as toxicity and commercial unprofitability (46), and that certain combinations of k_f-K_{eq} may be more attainable than the others, the idea of this *translatability grid*, drawn from model predictions, is widely applicable and offers a straightforward visualization for early-stage decision-making just like the Clarke error grid. The translatability grid makes possible a modified paradigm in medicinal

translation: a higher priority to clinical evaluation may now be granted to the true-positives over false-positives, and the false-negatives identified proceed to further trials in preclinical models closer to humans (*e.g.* pigs and non-human primates).

4.6. Outlook and Summary

The approach that we describe is of considerable flexibility. To start with, the application space is not constrained to just freely circulating GRIs taken as a proof-of-concept here, since GRI kinetics in PAMERAH are independent from the organism physiology and are therefore adaptable to reflect alternative glucose-responsive mechanisms, established or hypothetical. For example, one of our ongoing projects is to model the aforementioned MK-2640, which responds to glucose via a competitive clearance mechanism (43). We have already demonstrated that the predicted hepatic impacts of a freely circulating GRI match that of MK-2640 well, and that their trends of active GRI concentrations *vs.* clamp levels agree qualitatively (Figure 4-3). It is therefore reasonable to argue that PAMERAH can be extended to describe the MK-2640 action with an updated set of chemical kinetics. Although MK-2640's glucose-responsive activity is considerably more involved, we have shown that the competitive receptor binding and subsequent clearance can be modeled equally well as the simpler kinetics explored earlier. Ultimately, mapping MK-2640's animal and human design spaces can possibly reveal why the translation was difficult (51).

Along the same lines, PAMERAH may be built upon non-Sorenson-like physiology as well, such as the acclaimed Dalla Man, or UVa-Padova, model (55), the adaptability of which is demonstrated in our prior work on human pharmacokinetics (5). Similar procedures may be taken to develop mathematical models of other animal species as well. From a model customization perspective, the GRIDS can be subject-tailored by updating the parameter estimation with any new data available (45), alongside *a priori* parameterization of the individual physiology (24) discussed in detail by Peters (16). Such will supplement the future studies on intra-population variabilities (56) in GRI responses and the associated implications on ODRs. We acknowledge that, while information on population averages suffices for early GRI design and screening as in the case of this report, the capability to predict the variabilities will form the basis of individualized healthcare and fine-tuning of the drug. Such capability is lacking in the current iteration of PAMERAH and will be addressed. As described in Cobelli *et al.*, joint probability distribution of free parameters

can be reconstructed from population data, following which a pool of virtual individuals can be generated (57).

Future iterations of the model will also take into account additional factors impacting the overall GRI performance, such as pH, temperature, and exercises. Physical activities, for instance, redistribute the blood flow and modify the glucose production/uptake (25). From the modeling perspective, the corresponding variables can be correlated to the exercise intensity, following methodologies outlined previously (25,58). Lastly, we envision PAMERAH being used for planning GRI regimens in the future: will a recipe involving multiple kinetics be even superior to a single GRI?

GRIs represent "a new horizon in therapeutic technology" which offers a closed-loop control strategy alternative to continuous insulin infusion (9). However, their design and screening, largely at the early preclinical research stage, have been reliant on empirical knowledge and repeated experimentation. We present a modeling platform, PAMERAH, which predicts a GRI's efficacy in rats and mice from its properties. It is therefore able to explore the targeted GRI Design Space and identify the pool of optimal candidates before any experiments, thereby providing some rational guidance to the preclinical GRI research. Built upon prior human physiological models, our platform is shown to gauge a design's translatability from animal to clinical subjects and thereby generate the translatability grid. We hope PAMERAH helps establish an improved drug development workflow and accelerate the development of GRIs for individuals with type 1 diabetes.

4.7. Appendix A: Animal Preparation, Care, and Data Collection

As said, blood glucose time trajectories were collected from normal and diabetic rats for parameter estimation. Male Lewis rats weighing 250 to 300 grams were obtained from Envigo. Rats to be rendered diabetic were injected intraperitoneally with 48 mg/kg streptozotocin (STZ; from MP Biomedicals). Diabetes was confirmed after a 72-hour quarantine by blood glucose measurement of > 250 mg/dL. A second injection of 48 mg/kg STZ was given if rats did not become diabetic after the first injection. Rats were repeatedly used in experiments after two or more weeks of rest

period, and were used in experiments no longer than one year post stable induction of diabetes. For insulin studies, food was removed prior to the start of the experiment. The rats were weighed and the tip of the tail was snipped with a razor blade and milked for a small blood sample in which blood glucose levels were measured with standard glucometers (EasyMax V). Insulin lispro was injected subcutaneously in diabetic or normal (non-diabetic) rats. A time course of the insulin's action profile was created.

4.8. Appendix B: Mathematical Model Setup

In each organ *k*, the concentration of a solute *s* is governed by:

$$V_{k,\mathrm{v}}^{s}\frac{d[s]_{k,\mathrm{v}}}{dt}=Q_{k}^{s}([s]_{\mathrm{heart}}-[s]_{k,\mathrm{v}})-\frac{V_{k,\mathrm{i}}^{s}}{T_{k}^{s}}([s]_{k,\mathrm{v}}-[s]_{k,\mathrm{i}})+R_{k,\mathrm{v,prod/uptake}}^{s}+V_{k,\mathrm{v}}^{\mathrm{I}}\nu_{s}r_{\mathrm{GRI}} \tag{4-7}$$

$$V_{k,\mathrm{i}}^{s}\frac{d[s]_{k,\mathrm{i}}}{dt}=\frac{V_{k,\mathrm{i}}^{s}}{T_{k}^{s}}([s]_{k,\mathrm{v}}-[s]_{k,\mathrm{i}})+R_{k,\mathrm{i,prod/uptake}}^{s}+V_{k,\mathrm{i}}^{\mathrm{I}}\nu_{s}r_{\mathrm{GRI}} \tag{4-8}$$

$$r_{\mathrm{GRI}}=k_{f}[\mathrm{G}]_{k}[\mathrm{D}]_{k}-k_{r}[\mathrm{I}]_{k} \tag{4-9}$$

Where subscripts c and i denote vascular and interstitial (if applicable) volumes respectively, the transcapillary diffusion between which captured by T_k^s. The compartmental volumes and blood flow rates, denoted V_k^s and Q_k^s respectively, are based on anatomical measurements of rodents listed in Table 4-1. We simulate the actions of freely circulating GRIs in this report, for which the stoichiometric coefficients (ν) are -1, +1, -1, and 0 for the four solutes – glucose, insulin, dormant GRI, and glucagon – respectively. PAMERAH inherits the pancreatic insulin release as well as the oral dosing models from Bisker *et al.* (26) and follows the initialization protocol outlined in Bakh *et al.* (5) Parameters pertaining to insulin release are adapted to rodents based on Sorensen (22).

We further clarify, with the following short tutorial, how the concise general governing equations above generate a large network of differential equations needed for simulation. We take the adipose peripheral compartments as an example. Within each compartment, the rate of change in glucose level $V_{\mathrm{adipose,v/i}}^{\mathrm{G}}\,d[\mathrm{G}]_{\mathrm{adipose,v/i}}/dt$ equals rate of exchange with other organs summed with the glucose production/consumption rate within the compartment itself. For the adipose vascular compartment, the former encompasses incoming glucose carried from heart by blood flow ($Q_{\mathrm{adipose}}^{\mathrm{G}}[\mathrm{G}]_{\mathrm{heart}}$), the outgoing glucose circulated back ($-Q_{\mathrm{adipose}}^{\mathrm{G}}[\mathrm{G}]_{\mathrm{adipose,v}}$, with the negative sign

denoting that glucose exits the system), and the exchange with the interstitial compartment ($-(V^{\mathrm{G}}_{\mathrm{adipose,i}}/T^{\mathrm{G}}_{\mathrm{adipose}})([\mathrm{G}]_{\mathrm{adipose,v}}-[\mathrm{G}]_{\mathrm{adipose,i}})$). Inside the compartment, glucose reacts with dormant GRI and is consumed. Its rate is governed by the overall reaction rate $r_{\mathrm{GRI}}=k_f[\mathrm{G}]_{\mathrm{adipose}}[\mathrm{D}]_{\mathrm{adipose}}-k_r[\mathrm{I}]_{\mathrm{adipose}}$. This rate has to be corrected by the stoichiometric coefficient $\nu_{\mathrm{G}}=-1$, which states that one unit of glucose is consumed for each unit of reaction $\mathrm{G}+\mathrm{D}\rightleftharpoons\mathrm{I}$. The governing ODE for the adipose vascular compartment is then (*cf.* Equation 4-7):

$$\underbrace{V^{\mathrm{G}}_{\mathrm{adipose,v}}\frac{d[\mathrm{G}]_{\mathrm{adipose,v}}}{dt}}_{\text{rate of change in the compartment}}=\underbrace{Q^{\mathrm{G}}_{\mathrm{adipose}}([\mathrm{G}]_{\mathrm{heart}}-[\mathrm{G}]_{\mathrm{adipose,v}})}_{\text{inflow/outflow term}}\underbrace{-\frac{V^{\mathrm{G}}_{\mathrm{adipose,i}}}{T^{\mathrm{G}}_{\mathrm{adipose}}}([\mathrm{G}]_{\mathrm{adipose,v}}-[\mathrm{G}]_{\mathrm{adipose,i}})}_{\text{transcapillary exchange term}}\underbrace{-V^{\mathrm{I}}_{\mathrm{adipose,v}}r_{\mathrm{GRI,v}}}_{\text{GRI kinetics term}} \quad (7\text{-}10)$$

On the other hand, the interstitial space is not connected to any external organ (Figure 4-1), which allows us to drop the inflow/outflow terms ($Q[\mathrm{G}]$). In addition, glucose is taken up by the adipose tissues at a rate $R_{\mathrm{adipose\ PGU}}$ modulated by the local glucose and hormone concentrations (Table 4-2), where PGU stands for peripheral glucose uptake. The governing ODE for the adipose interstitial space is therefore:

$$\underbrace{V^{\mathrm{G}}_{\mathrm{adipose,i}}\frac{d[\mathrm{G}]_{\mathrm{adipose,i}}}{dt}}_{\text{rate of change in the compartment}}=\underbrace{\frac{V^{\mathrm{G}}_{\mathrm{adipose,i}}}{T^{\mathrm{G}}_{\mathrm{adipose}}}([\mathrm{G}]_{\mathrm{adipose,v}}-[\mathrm{G}]_{\mathrm{adipose,i}})}_{\text{transcapillary exchange term}}\underbrace{-R_{\mathrm{adipose\ PGU}}}_{\text{local prod/uptake term}}\underbrace{-V^{\mathrm{I}}_{\mathrm{adipose,i}}r_{\mathrm{GRI,i}}}_{\text{GRI kinetics term}} \quad (4\text{-}11)$$

which is exactly Equation S2 specific to the adipose tissues. Note that the transcapillary exchange term changes sign.

By the same method, we write the ODEs for active insulin in adipose compartments:

$$V^{\mathrm{I}}_{\mathrm{adipose,v}}\frac{d[\mathrm{I}]_{\mathrm{adipose,v}}}{dt}=Q^{\mathrm{I}}_{\mathrm{adipose}}([\mathrm{I}]_{\mathrm{heart}}\text{-}[\mathrm{I}]_{\mathrm{adipose,v}})-\frac{V^{\mathrm{I}}_{\mathrm{adipose,i}}}{T^{\mathrm{I}}_{\mathrm{adipose}}}([\mathrm{I}]_{\mathrm{adipose,v}}-[\mathrm{I}]_{\mathrm{adipose,i}})+V^{\mathrm{I}}_{\mathrm{adipose,v}}r_{\mathrm{GRI,v}} \quad (4\text{-}12)$$

$$V^{\mathrm{I}}_{\mathrm{adipose,i}}\frac{d[\mathrm{I}]_{\mathrm{adipose,i}}}{dt}=\frac{V^{\mathrm{I}}_{\mathrm{adipose,i}}}{T^{\mathrm{I}}_{\mathrm{adipose}}}([\mathrm{I}]_{\mathrm{adipose,v}}-[\mathrm{I}]_{\mathrm{adipose,i}})-R_{\mathrm{AIC}}+V^{\mathrm{I}}_{\mathrm{adipose,i}}r_{\mathrm{GRI,i}} \quad (4\text{-}13)$$

where R_{AIC} is the rate of adipose insulin clearance (Table 4-2). Note that the GRI kinetics terms change sign as compared to Equations 4-10 and 4-11 since the stoichiometric coefficient $\nu_{\mathrm{I}}=+1$ for insulin: each unit of GRI reaction produces one unit of insulin. With the steps outlined in this

tutorial, ODEs for other compartments and for other solutes can be generated likewise from Equations 4-7 and 4-8.

The rates of production/consumption of s, $R^{s}_{k,\text{prod/uptake}}$, are detailed below in Table 4-2 together with insulin absorption and clearance rates. Since the steady-state metabolism in rodents is not systematically characterized or published, its associated variables are estimated from experimental data. A number of multipliers, which characterize organs' responsiveness to hormonal regulations, are selected by sensitivity analyses (SA) and estimated. The same applies to the unknown insulin clearance fractions and transcapillary diffusion times (Figure 4-6). The latter turn out to carry insignificant impacts and are hence simply scaled by body mass (Table 4-1). For the PAMERAH ordinary differential equation system we concern, the parametric sensitivity of the blood glucose concentration on parameter p_j is defined as:

$$Z_j = \int_0^{360\,\text{min}} \sum_{\text{health}} \sum_{\text{doses}} \frac{[\text{G}]_{\text{heart}}}{p_j} \frac{dp_j}{d[\text{G}]_{\text{heart}}} dt \tag{4-13}$$

consistent with prior applications of SA (28,29). As said, only the numerically sensitive variables, marked in Figure 4-6, are subject to parametric estimation to avoid overfitting. The sets of estimated parameters are almost identical for the two rodents except $M^{\Gamma 0}_{\text{HGP}}$, which is impactful only in mice. The SA results in Figure 4-6 are obtained with the finalized parameter values as the basis.

Table 4-1. Physiological parameters for rats and mice based on *a priori* animal anatomical measurements.

	Physiological Parameter	Rats	Mice	Unit	Physiological Parameter	Rats	Mice	Unit
Volumes of Compartments[a]	$V^{G}_{brain,v}$	2.44E-03	1.69E-04	[dL]	V^{I}_{brain}	1.86E-04	1.21E-05	[L]
	$V^{G}_{brain,i}$	3.41E-03	1.07E-03					
	V^{G}_{heart}	4.89E-02	5.79E-03		V^{I}_{heart}	3.74E-03	4.14E-04	
	V^{G}_{lungs}	8.03E-02	1.78E-02		V^{I}_{lungs}	3.20E-03	6.86E-04	
	V^{G}_{gut}	2.97E-02	8.26E-03		V^{I}_{gut}	2.62E-03	7.43E-04	
	$V^{G}_{kidneys}$	1.90E-02	2.93E-03		$V^{I}_{kidneys}$	1.55E-03	2.43E-04	
	$V^{G}_{periphery,v}$	6.54E-02	5.20E-03		$V^{I}_{periphery,v}$	5.00E-03	3.72E-04	
	$V^{G}_{periphery,i}$	2.96E-01	1.62E-02		$V^{I}_{periphery,i}$	2.96E-02	1.62E-03	
Blood Flow Rates[b]	Q^{G}_{brain}	2.44E-02	8.88E-04	[dL/min]	Q^{I}_{brain}	1.86E-03	6.35E-05	[L/min]
	Q^{G}_{heart}	2.21E-01	5.12E-02		Q^{I}_{heart}	6.75E-02	3.66E-03	
	Q^{G}_{lungs}	1.61E-01	1.73E-02		Q^{I}_{lungs}	1.23E-02	1.24E-03	
	Q^{G}_{gut}	1.46E-01	1.47E-02		Q^{I}_{gut}	1.11E-02	1.05E-03	
	Q^{G}_{kidney}	1.46E-01	9.21E-03		Q^{I}_{kidney}	1.12E-02	6.59E-04	
	$Q^{G}_{periphery}$	5.51E-01	2.38E-02		$Q^{I}_{periphery}$	4.21E-02	1.70E-03	
	$Q^{G}_{hepatic\ artery}$	1.56E-02	2.66E-03		$Q^{I}_{hepatic\ artery}$	1.19E-03	1.91E-04	
	$Q_{muscle} / Q_{adipose}$	2.18E+00	2.74E+00	[-]				
TDT[c]	$T^{G}_{periphery}$	1.32E-01	2.52E-2	[min]	$T^{I}_{periphery}$	5.28E-01	1.01E-1	[min]
	T^{G}_{brain}	5.54E-02	1.06E-2					

[a] Compartmental volumes are based on measurements in Brown *et al.*, Thurlby and Trayhurn, and Peters (16,59,60).
[b] Blood flow rates are based on measurements in Ishise *et al.*, Wang *et al.*, Brown *et al.*, and Thurlby and Trayhurn (59–62).
[c] TDT, transcapillary diffusion time between the vascular and interstitial volumes. They are scaled by body mass from the human models (5,26). They are not estimated from experimental data given their low sensitivities in both mice and rats (Figure 4-6).

Table 4-2. Pharmacokinetic parameters for rats and mice. Estimated (*Est.*) and distinguishingly parameterized (*Dis.*; *i.e.* separately estimated for the healthy and diabetic populations) variables are marked by circles.

RATS			Healthy	Diabetic	Unit	Est.	Dis.
Hepatic Glucose Uptake	R_{HGU}	=	$R^{basal}_{HGU} M^{G}_{HGU} M^{I}_{HGU}$		[mg/min]		
	R^{basal}_{HGU}	=	4.01E+00	3.02E+00	[mg/min]	○[a]	○
	M^{G}_{HGU}	=	$2.37 + 1.67\tanh\{2.44([G]_{L,n} - 1.48)\}$		[-]	○[b]	
	$\frac{dM^{I}_{HGU}}{dt}$	=	$(M^{I\infty}_{HGU} - M^{I}_{HGU}) / \tau_1$		[min^{-1}]		
	$M^{I\infty}_{HGU}$	=	$2.00\tanh(0.55[I]_{L,n})$		[-]		
	τ_1	=	7.10E-03		[min]	○	
Hepatic Glucose Production	R_{HGP}	=	$R^{basal}_{HGP} M^{G}_{HGP} M^{I}_{HGP} M^{\Gamma}_{HGP}$		[mg/min]		
	R^{basal}_{HGP}	=	$\sum_{k=H,P,B,RBC,G} R^{basal}_{kGU}$		[mg/min]		
	M^{G}_{HGP}	=	$1.42 - 1.41\tanh\{0.62([G]_{L,n} - 0.50)\}$	$2.15 - 1.41\tanh\{2.30([G]_{L,n} - 0.50)\}$	[-]	○[b]	○

	$\frac{dM^{\mathrm{I}}_{\mathrm{HGP}}}{dt}$	=	$(M^{\mathrm{I}\infty}_{\mathrm{HGP}} - M^{\mathrm{I}}_{\mathrm{HGP}}) / \tau_1$	[min^{-1}]		
	$M^{\mathrm{I}\infty}_{\mathrm{HGP}}$	=	$1.16 - 0.16\tanh\{79.79([\mathrm{I}]_{\mathrm{L,n}} - 0.0003)\}$	[-]	○	
	$M^{\Gamma}_{\mathrm{HGP}}$	=	$M^{\Gamma 0}_{\mathrm{HGP}} - f_2$	[-]		
	$M^{\Gamma 0}_{\mathrm{HGP}}$	=	$2.70\tanh\{0.39[\Gamma]_{\mathrm{n}}\}$	[-]		
	df_2 / dt	=	$\{(M^{\Gamma 0}_{\mathrm{HGP}} - 1) / 2 - f_2\} / \tau_2$	[min^{-1}]		
	τ_2	=	1.00E-02	[min]	○	
Periphery Glucose Uptake	R_{PGU}	=	$R^{\mathrm{basal}}_{\mathrm{PGU}} M^{\mathrm{G}}_{\mathrm{PGU}} M^{\mathrm{I}}_{\mathrm{PGU}}$	[mg/min]		
	$R^{\mathrm{basal}}_{\mathrm{PGU}}$	=	1.02E+00 1.67E+00	[mg/min]	○[a]	○
	$M^{\mathrm{G}}_{\mathrm{PGU}}$	=	$[\mathrm{G}]_{\mathrm{periphery,i,n}}$	[-]		
	$M^{\mathrm{I}}_{\mathrm{PGU}}$	=	$7.03 + 6.52\tanh\{0.34([\mathrm{I}]_{\mathrm{periphery,i,n}} - 5.82)\}$	[-]		
Kidney Glucose Excretion[c]	R_{KGE}	=	$\begin{cases} 0.50 + 0.50\tanh[0.0081([\mathrm{G}]_{\mathrm{kidney}} - 584.77)] \\ \quad \text{if } 0 \le [\mathrm{G}]_{\mathrm{kidney}} < 584.77\,\mathrm{mg\,dL^{-1}} \\ -330 + 0.564[\mathrm{G}]_{\mathrm{kidney}} \\ \quad \text{if } [\mathrm{G}]_{\mathrm{kidney}} > 584.77\,\mathrm{mg\,dL^{-1}} \end{cases}$	[mg/min]		
Kidney Insulin Clearance	R_{KIC}	=	$F_{KIC} Q^{I}_{K} I_K$	[mU/min]		
	F_{KIC}	=	3.00E-01	[-]		
Liver Insulin Clearance	R_{LIC}	=	$F_{LIC}(Q^{\mathrm{I}}_{\mathrm{adipose}}[\mathrm{I}]_{\mathrm{heart}} + Q^{\mathrm{I}}_{\mathrm{gut}}[\mathrm{I}]_{\mathrm{gut}})$	[mU/min]		
	F_{LIC}	=	4.00E-01	[-]		
Muscle Insulin Clearance	R_{MIC}	=	$\frac{[\mathrm{I}]_{\mathrm{muscle,i}}}{\frac{1-F_{PIC}}{F_{PIC}}\frac{1}{Q^{\mathrm{I}}_{\mathrm{muscle}}} - \frac{T^{\mathrm{I}}_{\mathrm{muscle}}}{V^{\mathrm{I}}_{\mathrm{muscle,i}}}}$	[mU/min]		
	F_{PIC}	=	1.13E-02 4.90E-01	[-]	○	○
Adipose Insulin Clearance	R_{AIC}	=	$\frac{[\mathrm{I}]_{\mathrm{adipose,i}}}{\frac{1-F_{PIC}}{F_{PIC}}\frac{1}{Q^{\mathrm{I}}_{\mathrm{adipose}}} - \frac{T^{\mathrm{I}}_{\mathrm{adipose}}}{V^{\mathrm{I}}_{\mathrm{adipose,i}}}}$	[mU/min]		
Brain Glucose Uptake	R_{BGU}	=	1.59E+00 3.36E+00	[mg/min]	○[a]	○
Red Blood Cell Glucose Uptake	R_{RBCU}	=	7.36E-01 1.59E+00	[mg/min]	○[a]	○
Gut Glucose Uptake	R_{GGU}	=	3.50E+00 3.15E+00	[mg/min]	○[a]	○
Subcutaneous Insulin Absorption[d]	$R_{\mathrm{SIA,adipose,i}}$	=	$k_{\mathrm{abs}}[\mathrm{I}_{\mathrm{dm}}]_{\mathrm{depot}}$	[mU/L/min]		
	$\frac{d[\mathrm{I}_{\mathrm{dm}}]}{dt}$	=	$k_{\mathrm{h/dm}}[\mathrm{I}_{\mathrm{hex}}] - (k_{\mathrm{abs}} + k_{\mathrm{loss}})[\mathrm{I}_{\mathrm{dm}}]$	[mU/L/min]		
	$\frac{d[\mathrm{I}_{\mathrm{hex}}]}{dt}$	=	$-(k_{\mathrm{h/dm}} + k_{\mathrm{loss}})[\mathrm{I}_{\mathrm{hex}}]$	[mU/L/min]		
	k_{abs}	=	1.30E-02 6.70E-03	[min^{-1}]	○	○
	$k_{\mathrm{h/dm}}$	=	1.22E-02	[min^{-1}]	○	
	k_{loss}	=	$3D_{\mathrm{inj}}(3V_{\mathrm{inj}} / 4\pi)^{-2/3}$	[min^{-1}]		
	D_{inj}	=	9.00E-5	[cm^2/min]		

MICE			Healthy	Diabetic	Unit		
Hepatic Glucose Uptake	R_{HGU}	=	$R^{basal}_{HGU} M^{G}_{HGU} M^{I}_{HGU}$		[mg/min]		
	R^{basal}_{HGU}	=	1.64E-02	1.37E-02	[mg/min]	○[e]	○
	M^{G}_{HGU}	=	$5.66 + 5.66\tanh\{2.44([G]_{L,n} - 1.48)\}$		[-]	○[b]	
	$\frac{dM^{I}_{HGU}}{dt}$	=	$(M^{I\infty}_{HGU} - M^{I}_{HGU}) / \tau_1$		[min^{-1}]		
	$M^{I\infty}_{HGU}$	=	$2.00\tanh(0.55[I]_{L,n})$		[-]		
	τ_1	=	2.00E-03		[min]	○	
Hepatic Glucose Production	R_{HGP}	=	$R^{basal}_{HGP} M^{G}_{HGP} M^{I}_{HGP} M^{\Gamma}_{HGP}$		[mg/min]		
	R^{basal}_{HGP}	=	$\sum_{k=H, P, B, RBC, G} R^{basal}_{kGU}$		[mg/min]		
	M^{G}_{HGP}	=	$1.06 - 6.39\tanh\{0.02([G]_{L,n} - 0.50)\}$	$1.40 - 6.39\tanh\{0.13([G]_{L,n} - 0.50)\}$	[-]	○[b]	○
	$\frac{dM^{I}_{HGP}}{dt}$	=	$R^{basal}_{HGP} M^{G}_{HGP} M^{I}_{HGP} M^{\Gamma}_{HGP}$		[min^{-1}]		
	$M^{I\infty}_{HGP}$	=	$0.90 - 0.13\tanh\{1.67([I]_{L,n} - 1.56)\}$	$-5.25 - 8.49\tanh\{1.67([I]_{L,n} - 1.56)\}$	[-]	○[b]	○
	M^{Γ}_{HGP}	=	$M^{\Gamma 0}_{HGP} - f_2$		[-]		
	$M^{\Gamma 0}_{HGP}$	=	$1.00\tanh\{3.91[\Gamma]_n\}$		[-]	○[b]	
	df_2 / dt	=	$\{(M^{\Gamma 0}_{HGP} - 1) / 2 - f_2\} / \tau_2$		[min^{-1}]		
	τ_2	=	7.50E-03		[min]	○	
Periphery Glucose Uptake	R_{PGU}	=	$R^{basal}_{PGU} M^{G}_{PGU} M^{I}_{PGU}$		[mg/min]		
	R^{basal}_{PGU}	=	3.33E-02	2.48E-02	[mg/min]	○[e]	○
	M^{G}_{PGU}	=	$[G]_{periphery,i,n}$		[-]		
	M^{I}_{PGU}	=	$7.03 + 6.52\tanh\{0.34([I]_{periphery,i,n} - 5.82)\}$		[-]		
Kidney Glucose Excretion[c]	R_{KGE}	=	$\begin{cases} 0.50 + 0.50\tanh[0.0081([G]_{kidney} - 584.77)] \\ \quad \text{if } 0 \le [G]_{kidney} < 584.77\ \text{mg dL}^{-1} \\ -330 + 0.564[G]_{kidney} \\ \quad \text{if } [G]_{kidney} > 584.77\ \text{mg dL}^{-1} \end{cases}$		[mg/min]		
Kidney Insulin Clearance	R_{KIC}	=	$F_{KIC} Q^{I}_{K} I_K$		[mU/min]		
	F_{KIC}	=	3.00E-01		[-]		
Liver Insulin Clearance	R_{LIC}	=	$F_{LIC}(Q^{I}_{adipose}[I]_{heart} + Q^{I}_{gut}[I]_{gut})$		[mU/min]		
	F_{LIC}	=	4.00E-01		[-]		
Muscle Insulin Clearance	R_{MIC}	=	$\frac{[I]_{muscle,i}}{\frac{1 - F_{PIC}}{F_{PIC}} \frac{1}{Q^{I}_{muscle}} - \frac{T^{I}_{muscle}}{V^{I}_{muscle,i}}}$		[mU/min]		
	F_{PIC}	=	1.50E-01	9.00E-01	[-]	○	○
Adipose Insulin Clearance	R_{AIC}	=	$\frac{[I]_{adipose,i}}{\frac{1 - F_{PIC}}{F_{PIC}} \frac{1}{Q^{I}_{adipose}} - \frac{T^{I}_{adipose}}{V^{I}_{adipose,i}}}$		[mU/min]		
Brain Glucose Uptake	R_{BGU}	=	8.60E-03	1.71E-02	[mg/min]	○[e]	○
Red Blood Cell Glucose Uptake	R_{RBCU}	=	8.70E-03	9.00E-03	[mg/min]	○[e]	○
Gut Glucose Uptake	R_{GGU}	=	1.21E-02	1.21E-02	[mg/min]	○[e]	○

	$R_{SIA,adipose,i}$	=	$k_{abs}[I_{dm}]_{depot}$		[mU/L/min]		
	$\frac{d[I_{dm}]}{dt}$	=	$k_{h/dm}[I_{hex}]-(k_{abs}+k_{loss})[I_{dm}]$		[mU/L/min]		
Subcutaneous Insulin Absorption[d]	$\frac{d[I_{hex}]}{dt}$	=	$-(k_{h/dm}+k_{loss})[I_{hex}]$		[mU/L/min]		
	k_{abs}	=	2.28E-02	7.70E-03	[min^{-1}]	○	○
	$k_{h/dm}$	=	5.65E-02		[min^{-1}]		
	k_{loss}	=	$3D_{inj}(3V_{inj}/4\pi)^{-2/3}$		[min^{-1}]		
	D_{inj}	=	9.00E-5		[cm^2/min]		

[a] Base steady-state metabolic rates of rats are estimated from literature-based initial guesses (63–66).

[b] Note that the adaptation of transfer functions has only one degree of freedom for each. That is, only one parameter in each transfer function is estimated. $[G]_{k,n}$ and $[I]_{k,n}$ denotes glucose and insulin concentrations in compartment k normalized by the steady state levels. $[\Gamma]_n$ in turn represents the normalized glucagon concentration. All multipliers (Ms) should assume a value of 1 for a normalized concentration of 1.

[c] The kidney glucose excretion rate as a function of glucose concentration is based on data published by Robson *et al*. (67)

[d] Simulation of the subcutaneous injection depot follows the work by Bakh *et al.* (5), who adopted a model originally designed and validated by Wong *et al.* (68,69) for regular insulin. Among the states whose dynamic equilibrium dictates the subcutaneous absorption kinetics, dimeric and monomeric insulins are absorbed much faster than the hexameric state (I_{hex}). Wong and colleagues therefore lumped the former two together into the term I_{dm}, formed from the dissociation of hexamers with a rate constant $k_{h/dm}$. The dimers/monomers are then absorbed from the injection depot into the main circulation at a rate characterized by k_{abs}. Meanwhile, both states suffer from some diffusive loss described by the rate constant k_{loss}, computed from the injection volume V_{inj} and the insulin diffusivity D_{inj}. Numerical value for the latter is obtained from Vogel (70). Readers may substitute the injection depot for other subcutaneous absorption models as well, such as that by Tarín *et al.* which assumed only a hexamer-dimer equilibrium (71).

[e] Base steady-state metabolic rates of mice are estimated from literature-based initial guesses (72–75).

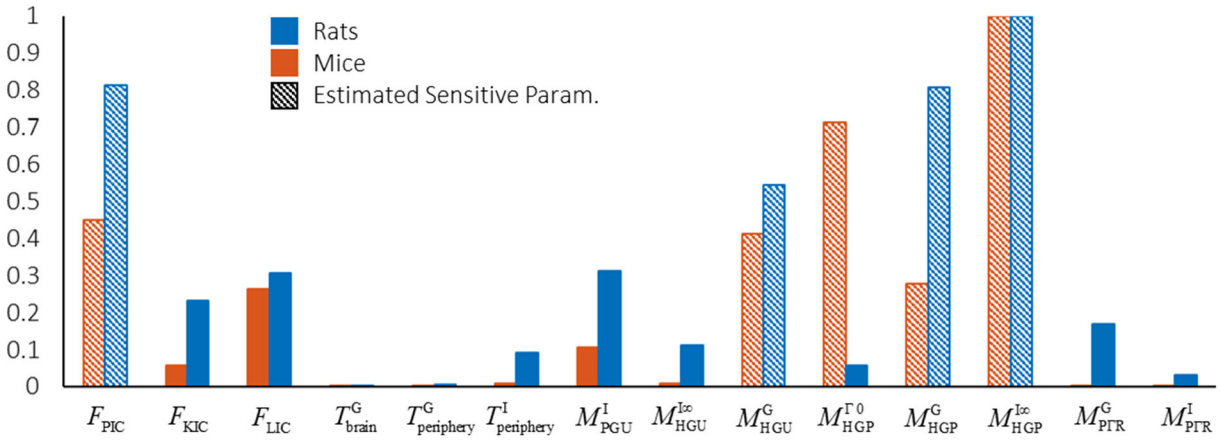

Figure 4-6. Sensitivities of insulin clearance fractions, transcapillary diffusion time constants, and multipliers for rats (blue) and mice (red). Only the highly sensitive, or impactful, variables are selected for parametric estimation (hatched bars). As the blood glucose level is relatively insensitive to murine transcapillary diffusion times, the latter are simply approximated via body mass scaling (Table 4-1). Note that the sensitivity analyses presented in this figure assume the finalized parameter values as the bases.

4.9. Appendix C: Supplementary Figures

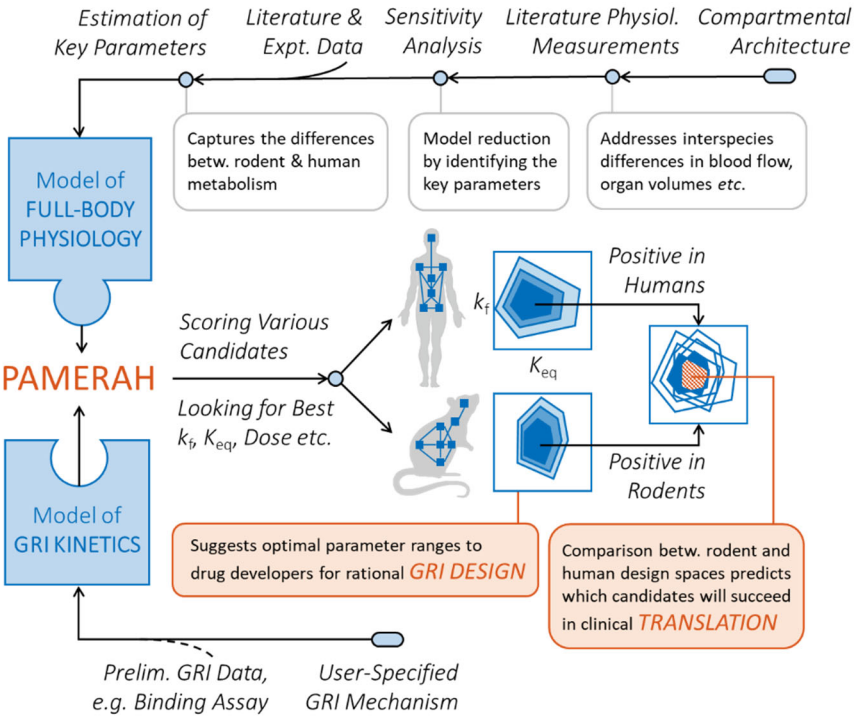

Figure 4-7. Schematic of the workflow of PAMERAH as well as its application to model-aided GRI design and translation. As described detailedly in §4.3, PAMERAH was assembled by piecing together a set of user-specified GRI kinetics to a model for the full-body physiology. PAMERAH is able to explore a large design space, predicting performances of GRI constructs of arbitrary parameter combinations, such as k_f, K_{eq}, dose *etc.*, thus aiding the rational design process. Furthermore, a cross-comparison between rodent and human design spaces identifies the optimal parameter ranges corresponding to adequate clinical translatability.

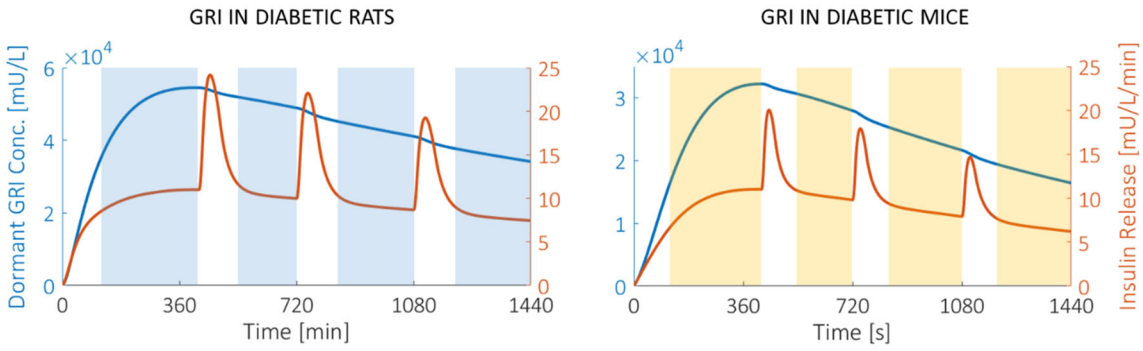

Figure 4-8. Time courses of the dormant GRI concentration (blue) and the insulin release rate (orange) simulated in average diabetic rats (left) and mice (right) respectively. They are the responses to a subcutaneous injection of a freely

circulating GRI (k_f = 0.1 $M^{-1}min^{-1}$, K_{eq} = 0.02 M^{-1}, dosage = 300 μg/kg) at t = 0. The curves correspond to the glucose concentration trajectories presented in Figure 4-2, and the shaded areas are identical to those in the said figure as well. Note that although the initial glucose concentrations are high in both diabetic rats and mice, we do not observe any initial spike in the insulin release rates. This is explained by the gradual absorption of GRI, as evidenced by the dormant GRI concentration curves.

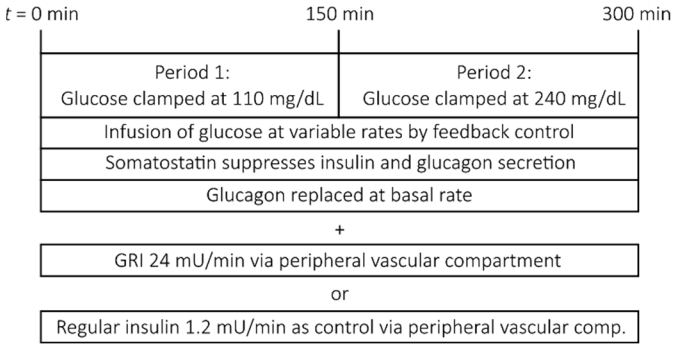

Figure 4-9. Protocol for the simulated pancreatic clamps corresponding to Figure 4-3. Prior to the simulated clamp, PAMERAH assumes the state of a healthy rat. While in Moore *et al.*, the dog plasma glucose was clamped at 80 mg/dL during Period 1 (37), the level is adjusted to 110 mg/DL for this simulation, within the typical range for rat clamps.

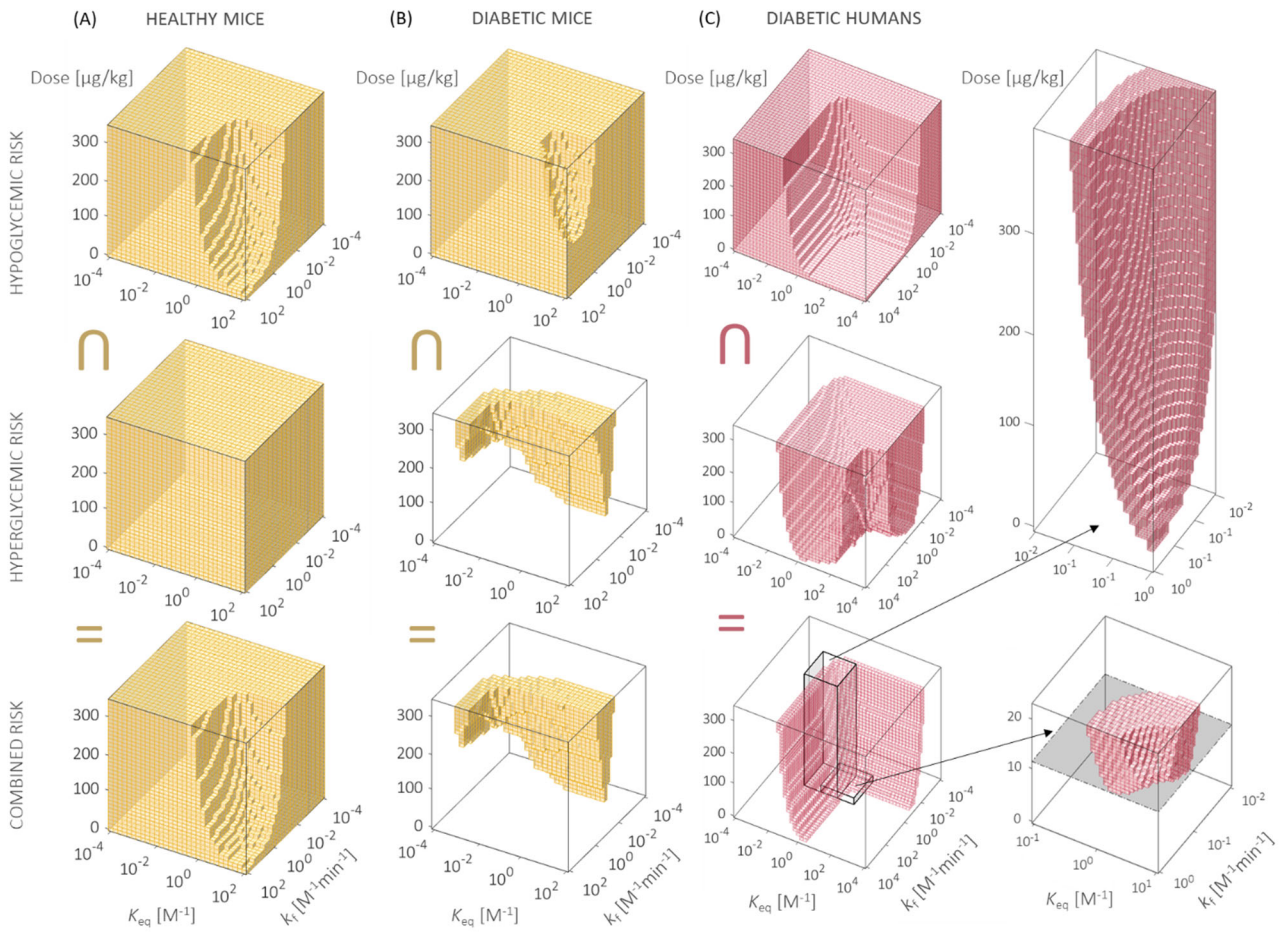

Figure 4-10. GRIDS and ODRs of (A) healthy mice, (B) diabetic mice, and (C) diabetic humans. The characteristic missing corner for healthy ODRs and *L* shape for the diabetic ODRs are observed in mice and humans as well. Parts of the human GRIDS are probed with refined resolutions, presented on the far right. The grey slice in panel (C) marks the predicted minimum effective dose for humans, 12.25 ± 0.25 µg/kg. Note that the bounds of human GRIDS are extended to accommodate a complete *L*-shaped cross-section. Only GRIDS for average diabetic humans is explored based on our previous work (5).

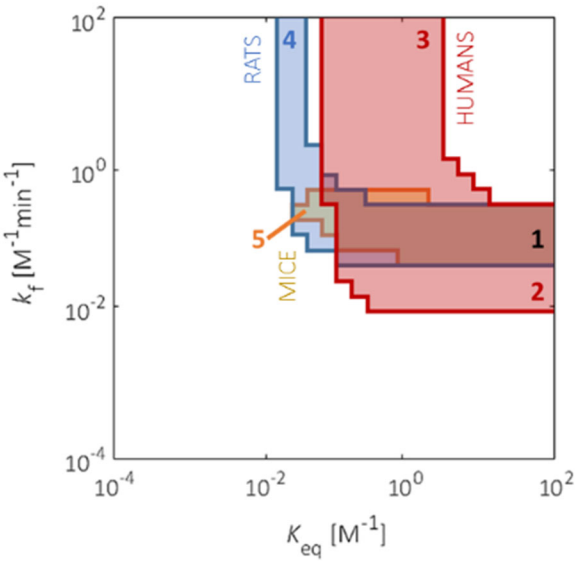

Figure 4-11. The translatability grid with a dosage range of 0 to 200 µg/kg, different from that in Figure 4-5. We see that the relative areas of true-positive (Zone 1), false-positive (Zones 4, 5), and false-negative (Zones 2, 3) regions are dependent on the bounds selected.

4.10. References

1. International Diabetes Federation. IDF Diabetes Atlas - 8th edition. 2017.
2. Yang W, Dall TM, Beronjia K, Lin J, Semilla AP, Chakrabarti R, et al. Economic costs of diabetes in the U.S. in 2017. Diabetes Care. 2018 May;41(5):917–28.
3. Peyrot M, Barnett AH, Meneghini LF, Schumm-Draeger P-M. Insulin adherence behaviours and barriers in the multinational Global Attitudes of Patients and Physicians in Insulin Therapy study. Diabet Med. 2012 May;29(5):682–9.
4. Veiseh O, Tang BC, Whitehead KA, Anderson DG, Langer R. Managing diabetes with nanomedicine: Challenges and opportunities. Nat Rev Drug Discov. 2014;14(1):45–57.
5. Bakh NA, Bisker G, Lee MA, Gong X, Strano MS. Rational design of glucose-responsive insulin using pharmacokinetic modeling. Adv Healthc Mater. 2017;6(22):1–10.
6. Resnick HE, Foster GL, Bardsley J, Ratner RE. Achievement of American Diabetes Association clinical practice recommendations among U.S. adults with diabetes, 1999-2002: the National Health and Nutrition Examination Survey. Diabetes Care. 2006 Mar;29(3):531–7.
7. Zaykov AN, Mayer JP, DiMarchi RD. Pursuit of a perfect insulin. Nat Rev Drug Discov. 2016 Jun 18;15(6):425–39.
8. Pickup JC. Management of diabetes mellitus: Is the pump mightier than the pen? Nat Rev Endocrinol. 2012;8(7):425–33.
9. Bakh NA, Cortinas AB, Weiss MA, Langer RS, Anderson DG, Gu Z, et al. Glucose-responsive insulin by molecular and physical design. Nat Chem. 2017;9(10):937–43.
10. VandenBerg MA, Webber MJ. Biologically inspired and chemically derived methods for glucose-responsive insulin therapy. Adv Healthc Mater. 2019 Jan 3;1801466:1801466.
11. Chou DH-C, Webber MJ, Tang BC, Lin AB, Thapa LS, Deng D, et al. Glucose-responsive insulin activity by covalent modification with aliphatic phenylboronic acid conjugates. Proc Natl Acad Sci. 2015;112(8):2401–6.
12. Brownlee M, Cerami A. A glucose-controlled insulin-delivery system: Semisynthetic insulin bound to lectin. Science (80-). 1979 Dec 7;206(4423):1190–1.
13. Drozdov AD, Christiansen J deC. Swelling of glucose-responsive gels functionalized with boronic acid. J Mech Behav Biomed Mater. 2017 Jan;65:533–41.

14. Abdekhodaie MJ, Wu XY. Modeling of a glucose sensitive composite membrane for closed-loop insulin delivery. J Memb Sci. 2009;335(1–2):21–31.
15. Matsumoto A, Tanaka M, Matsumoto H, Ochi K, Moro-Oka Y, Kuwata H, et al. Synthetic "smart gel" provides glucose-responsive insulin delivery in diabetic mice. Sci Adv. 2017;3(11):1–13.
16. Peters SA. Physiologically-Based Pharmacokinetic (PBPK) modeling and simulations: Principles, methods, and applications in the pharmaceutical industry. First Edit. Hoboken, New Jersey: John Wiley & Sons, Inc.; 2012.
17. Hackam DG, Redelmeier DA. Translation of research evidence from animals to humans. J Am Med Assoc. 2006;296(14).
18. Perel P, Roberts I, Sena E, Wheble P, Briscoe C, Sandercock P, et al. Comparison of treatment effects between animal experiments and clinical trials: Systematic review. Br Med J. 2007;334(7586):197–200.
19. Mak IWY, Evaniew N, Ghert M. Lost in translation : Animal models and clinical trials in cancer treatment. Am J Transl Res. 2014;6(2):114–8.
20. Hovorka R, Chassin LJ, Ellmerer M, Plank J, Wilinska ME. A simulation model of glucose regulation in the critically ill. Physiol Meas. 2008;29(8):959–78.
21. Silber HE, Jauslin PM, Frey N, Gieschke R, Simonsson USH, Karlsson MO. An integrated model for glucose and insulin regulation in healthy volunteers and type 2 diabetic patients following intravenous glucose provocations. J Clin Pharmacol. 2007;47(9):1159–71.
22. Sorensen JT. A physiologic model of glucose metabolism in man and its use to design and assess improved insulin therapies for diabetes. Massachusetts Institute of Technology; 1985.
23. Parker RS, Doyle FJ, Ward JH, Peppas NA. Robust H∞ glucose control in diabetes using a physiological model. AIChE J. 2000;46(12):2537–49.
24. Schaller S, Willmann S, Lippert J, Schaupp L, Pieber TR, Schuppert A, et al. A generic integrated physiologically based whole-body model of the glucose insulin-glucagon regulatory system. CPT Pharmacometrics Syst Pharmacol. 2013;2(8).
25. Hernández-Ordoñez M, Campos-Delgado DU. An extension to the compartmental model of type 1 diabetic patients to reproduce exercise periods with glycogen depletion and

replenishment. J Biomech. 2008 Jan;41(4):744–52.
26. Bisker G, Iverson NM, Ahn J, Strano MS. A pharmacokinetic model of a tissue implantable insulin sensor. Adv Healthc Mater. 2015;4(1):87–97.
27. Alskär O, Karlsson MO, Kjellsson MC. Model-based interspecies scaling of glucose homeostasis. CPT Pharmacometrics Syst Pharmacol. 2017;6(11):778–86.
28. Zhu JY, Dittmeyer R, Hofmann H. Application of sensitivity analysis to the reduction of a complex kinetic model for the homogeneous oxidative coupling of methane. Chem Eng Process. 1993;32(3):167–76.
29. Dickinson RP, Gelinas RJ. Sensitivity analysis of ordinary differential equation systems-A direct method. J Comput Phys. 1976;21(2):123–43.
30. Vahidi O, Kwok KE, Gopaluni RB, Knop FK. A comprehensive compartmental model of blood glucose regulation for healthy and type 2 diabetic subjects. Med Biol Eng Comput. 2016;54(9):1383–98.
31. Niederalt C, Kuepfer L, Solodenko J, Eissing T, Siegmund H-U, Block M, et al. A generic whole body physiologically based pharmacokinetic model for therapeutic proteins in PK-Sim. J Pharmacokinet Pharmacodyn. 2018 Apr 12;45(2):235–57.
32. Matzke GR, Frye RF, Early JJ, Straka RJ, Carson SW. Evaluation of the influence of diabetes mellitus on antipyrine metabolism and CYP1A2 and CYP2D6 activity. Pharmacotherapy. 2000;20(2):182–90.
33. Basu A, Basu R, Shah P, Vella A, Johnson CM, Jensen M, et al. Type 2 diabetes impairs splanchnic uptake of glucose but does not alter intestinal glucose absorption during enteral glucose feeding: Additional evidence for a defect in hepatic glucokinase activity. Diabetes. 2001;
34. Bergman RN, Phillips LS, Cobelli C. Physiologic evaluation of factors controlling glucose tolerance in man: Measurement of insulin sensitivity and beta-cell glucose sensitivity from the response to intravenous glucose. J Clin Invest. 1981 Dec 1;68(6):1456–67.
35. Schaller S, Lippert J, Schaupp L, Pieber TR, Schuppert A, Eissing T. Robust PBPK/PD-based model predictive control of blood glucose. IEEE Trans Biomed Eng. 2016 Jul;63(7):1492–504.
36. DeFronzo RA, Tobin JD, Andres R. Glucose clamp technique: A method for quantifying insulin secretion and resistance. Am J Physiol Metab. 1979 Sep 1;237(3):E214.

37. Moore MC, Kelley DE, Camacho RC, Zafian P, Ye T, Lin S, et al. Superior glycemic control with a glucose-responsive insulin analog: Hepatic and nonhepatic impacts. Diabetes. 2018;67(6):1173–81.
38. Rossetti L, Smith D, Shulman GI, Papachristou D, DeFronzo RA. Correction of hyperglycemia with phlorizin normalizes tissue sensitivity to insulin in diabetic rats. J Clin Invest. 1987 May 1;79(5):1510–5.
39. American Diabetes Association Workgroup on Hypoglycemia. Defining and reporting hypoglycemia in diabetes: A report from the American Diabetes Association Workgroup on Hypoglycemia. Diabetes Care. 2005 May 1;28(5):1245–9.
40. Maheandiran M, Mylvaganam S, Wu C, El-Hayek Y, Sugumar S, Hazrati L, et al. Severe hypoglycemia in a juvenile diabetic rat model: Presence and severity of seizures are associated with mortality. Bader M, editor. PLoS One [Internet]. 2013 Dec 30;8(12):e83168. Available from: https://dx.plos.org/10.1371/journal.pone.0083168
41. Grant CW, Duclos SK, Moran-Paul CM, Yahalom B, Tirabassi RS, Arreaza-Rubin G, et al. Development of standardized insulin treatment protocols for spontaneous rodent models of type 1 diabetes. Comp Med. 2012;62(5):381–90.
42. Pospisilik JA, Martin J, Doty T, Ehses JA, Pamir N, Lynn FC, et al. Dipeptidyl peptidase IV inhibitor treatment stimulates β-cell survival and islet neogenesis in streptozotocin-induced diabetic rats. Diabetes. 2003 Mar 1;52(3):741–50.
43. Kaarsholm NC, Lin S, Yan L, Kelly T, Van Heek M, Mu J, et al. Engineering glucose responsiveness into insulin. Diabetes. 2018;67(2):299–308.
44. Patek SD, Bequette BW, Breton M, Buckingham BA, Dassau E, Doyle FJ, et al. In silico preclinical trials: Methodology and engineering guide to closed-loop control in type 1 diabetes mellitus. J Diabetes Sci Technol. 2009 Mar;3(2):269–82.
45. Jones HM, Chen Y, Gibson C, Heimbach T, Parrott N, Peters SA, et al. Physiologically based pharmacokinetic modeling in drug discovery and development: A pharmaceutical industry perspective. Clin Pharmacol Ther. 2015 Mar;97(3):247–62.
46. van de Waterbeemd H, Gifford E. ADMET in silico modelling: Towards prediction paradise? Nat Rev Drug Discov. 2003;2(3):192–204.
47. Jones HM, Rowland-Yeo K. Basic concepts in physiologically based pharmacokinetic modeling in drug discovery and development. CPT Pharmacometrics Syst Pharmacol.

2013;2(8):1–12.

48. Jones HM, Parrott N, Jorga K, Lavé T. A novel strategy for physiologically based predictions of human pharmacokinetics. Clin Pharmacokinet. 2006;45(5):511–42.
49. van der Worp HB, Howells DW, Sena ES, Porritt MJ, Rewell S, O'Collins V, et al. Can animal models of disease reliably inform human studies? PLoS Med. 2010 Mar 30;7(3):e1000245.
50. The Tufts Center for the Study of Drug Development. Diabetes drug development is riskier compared to all drug development. Tufts CSDD Impact Reports. 2016;20(5).
51. Krug AW, Visser SAG, Tsai K, Kandala B, Fancourt C, Thornton B, et al. Clinical evaluation of MK-2640: An insulin analog with glucose-responsive properties. Clin Pharmacol Ther. 2019 Feb;105(2):417–25.
52. Lindborg SR, Persinger CC, Sashegyi A, Mallinckrodt C, Ruberg SJ. Statistical refocusing in the design of Phase II trials offers promise of increased R&D productivity. Nat Rev Drug Discov. 2014;13(8):638–40.
53. Clarke WL, Cox D, Gonder-Frederick LA, Carter W, Pohl SL. Evaluating clinical accuracy of systems for self-monitoring of blood glucose. Diabetes Care. 1987 Sep 1;10(5):622–8.
54. Williams HD, Trevaskis NL, Charman SA, Shanker RM, Charman WN, Pouton CW, et al. Strategies to address low drug solubility in discovery and development. Pharmacol Rev. 2013 Feb 3;65(1):315–499.
55. Dalla Man C, Rizza RA, Cobelli C. Meal simulation model of the glucose-insulin system. IEEE Trans Biomed Eng. 2007 Oct;54(10):1740–9.
56. Willmann S, Höhn K, Edginton A, Sevestre M, Solodenko J, Weiss W, et al. Development of a physiology-based whole-body population model for assessing the influence of individual variability on the pharmacokinetics of drugs. J Pharmacokinet Pharmacodyn. 2007;34(3):401–31.
57. Cobelli C, Dalla Man C, Sparacino G, Magni L, De Nicolao G, Kovatchev BP. Diabetes: Models, signals, and control. IEEE Rev Biomed Eng. 2009;2:54–96.
58. Roy A, Parker RS. Dynamic modeling of exercise effects on plasma glucose and insulin levels. J Diabetes Sci Technol. 2007 May 24;1(3):338–47.
59. Brown RP, Delp MD, Lindstedt SL, Rhomberg LR, Beliles RP. Physiological parameter

values for physiologically based pharmacokinetic models. Toxicol Ind Health. 1997 Jul 30;13(4):407–84.

60. Thurlby PL, Trayhurn P. Regional blood flow in genetically obese (ob/ob) mice. Pflügers Arch. 1980;385:193–201.
61. Ishise S, Pegram BL, Yamamoto J, Kitamura Y, Frohlich ED. Reference sample microsphere method: cardiac output and blood flows in conscious rat. Am J Physiol Circ Physiol. 1980 Oct;239(4):H443–H443.
62. Wang P, Ba ZF, Burkhardt J, Chaudry IH. Trauma-hemorrhage and resuscitation in the mouse: effects on cardiac output and organ blood flow. Am J Physiol. 1993;264(4 Pt 2):H1166-73.
63. Hutson NJ, Brumley FT, Assimacopoulos FD, Harper SC, Exton JH. Studies on the alpha-adrenergic activation of hepatic glucose output: I. Studies on the alpha-adrenergic activation of phosphorylase and gluconeogenesis and inactivation of glycogen synthase in isolated rat liver parenchymal cells. J Biol Chem. 1976 Sep 10;251(17):5200–8.
64. Duca FA, Côté CD, Rasmussen BA, Zadeh-Tahmasebi M, Rutter GA, Filippi BM, et al. Metformin activates a duodenal Ampk-dependent pathway to lower hepatic glucose production in rats. Nat Med. 2015 Apr 6;21(5):506–11.
65. Bachelard HS, Daniel PM, Love ER, Pratt OE. The transport of glucose into the brain of the rat in vivo. Proc R Soc B Biol Sci. 1973 Feb 27;183(1070):71–82.
66. Goodman MN, Dluz SM, McElaney MA, Belur E, Ruderman NB. Glucose uptake and insulin sensitivity in rat muscle: Changes during 3-96 weeks of age. Am J Physiol Metab. 1983 Jan;244(1):E93–100.
67. Robson AM, Srivastava PL, Bricker NS. The influence of saline loading on renal glucose reabsorption in the rat. J Clin Invest. 1968;47:329–35.
68. Wong J, Chase JG, Hann CE, Shaw GM, Lotz TF, Lin J, et al. A subcutaneous insulin pharmacokinetic model for computer simulation in a diabetes decision support role: Model structure and parameter identification. J Diabetes Sci Technol. 2008;2(4):658–71.
69. Wong J, Chase JG, Hann CE, Shaw GM, Lotz TF, Lin J, et al. A subcutaneous insulin pharmacokinetic model for computer simulation in a diabetes decision support role: Validation and simulation. J Diabetes Sci Technol. 2008 Jul;2(4):672–80.
70. Vogel S. Life's devices: The physical world of animals and plants. Princeton University

Press; 1988.

71. Tarín C, Teufel E, Picó J, Bondia J, Pfleiderer HJ. Comprehensive pharmacokinetic model of insulin glargine and other insulin formulations. IEEE Trans Biomed Eng. 2005;52(12):1994–2005.
72. Jay TM, Jouvet M, Des Rosiers MH. Local cerebral glucose utilization in the free moving mouse: A comparison during two stages of the activity-rest cycle. Brain Res. 1985;342(2):297–306.
73. Windmueller HG, Spaeth AE. Respiratory fuels and nitrogen metabolism in vivo in small intestine of fed rats: Quantitative importance of glutamine, glutamate, and aspartate. J Biol Chem. 1980 Jan 10;255(1):107–12.
74. Özcan U, Yilmaz E, Özcan L, Furuhashi M, Vaillancourt E, Smith RO, et al. Chemical chaperones reduce ER stress and restore glucose homeostasis in a mouse model of type 2 diabetes. Science (80-). 2006;
75. Könner AC, Janoschek R, Plum L, Jordan SD, Rother E, Ma X, et al. Insulin action in AgRP-expressing neurons is required for suppression of hepatic glucose production. Cell Metab. 2007 Jun;5(6):438–49.

CHAPTER 5

In silico investigation of the clinical translatability of competitive clearance glucose-responsive insulins

This chapter has been adapted from:

Jing Fan Yang, Sungyun Yang, Xun Gong, Naveed A. Bakh, Ge Zhang*, Allison B. Wang, and Michael S. Strano. 2022.* "In silico investigation of the clinical translatability of competitive clearance glucose-responsive insulins." *In preparation*.

5.1. Abstract

A milestone in the history of glucose-responsive insulins (GRI), Merck's MK-2640 was the first to enter the clinical stage, having demonstrated promising responsiveness in *in vitro* and preclinical studies via a novel Competitive Clearance Mechanism (CCM). Regretfully, its pharmacokinetics exhibited merely a negligible response in humans, causing the development of all candidates in this GRI family to cease. It remains uncertain what aspect of the interspecies differences caused the preclinical models to have predicted the clinical performance poorly. We investigated the clinical translatability of CCM GRIs via translational *in silico* modeling based on existing preclinical and clinical data of MK-2640 and regular human insulin (RHI). Our simulation platform, IM^{3}PACT, adds minipigs' glucoregulatory system and a mechanistic model of CCM to an earlier iteration already demonstrated to aid early-stage GRI design and development. Simulated multi-glycemic clamps (i) validated the earlier hypothesis of insufficient glucose-responsive clearance capacity in humans, but also (ii) uncovered an equally important mismatch between the *in vivo* competitiveness profile and the physiological glycemic range, which was not observed in animals. When we removed the interspecies gap in either of these two factors *in silico*, the glucose-dependent modulation of GRI clearance increased from 13.0% to beyond 20% for humans, and to a more-than-satisfactory 33.3% when both factors were corrected. Meanwhile, the GRI's intrinsic clearance rate, potency, and distribution volume were determined to not have compromised the translation. Furthermore, despite the systemic lack of glucose responsiveness in humans, we confirmed the suspicion of a responsive pharmacokinetics local to the liver. By scanning a large design space for CCM GRIs, we found that the mannose receptor physiology in humans remains limiting even for the most optimally designed candidate, which means the remainder of Merck's CCM portfolio is unlikely to translate successfully as well. We use this *in silico* study on CCM as a demonstration of a powerful computational tool which, alongside its utility in GRI design and optimization, extracts quantitative and mechanistic learnings from *a posteriori* analyses of preclinical and clinical data to benefit future therapeutic discovery and development.

5.2. Introduction

Glucose-responsive insulin analogues (GRIs) are a class of intelligent insulin delivery technology, which supplies a hormonal activity commensurate with local blood glucose concentrations in a closed-loop, autonomous fashion (1,2), referred to as "a new horizon in therapeutic technology" by some (3). In contrast to traditional, open-loop methods for glycemic control, GRIs promise added insurance against hypoglycemia, improved patient compliance, reduced side effects, and optimized, reliable dosing (4). While a closed-loop, pancreas-like regulation may also be achieved with therapies integrating continuous glucose monitoring and insulin administration (5), these sophisticated external devices remain expensive, bulky (1), and potentially associated with risks of infection, inflammation, and scarring (6). The diabetes community's persistent interest in GRIs has catalyzed a multitude of concepts for glucose responsiveness, which can be roughly classified into insulin-encapsulating polymer carriers with glucose-mediated triggers (7–9) and modified unimolecular insulin with glucose-recognizing motifs (10–12). Out of the many GRI constructs showing potential in animal studies (1,2,13–15), it was Merck's MK-2640 that marked the milestone as the first GRI to enter clinical trials (16). The phase I outcome, nevertheless, "revealed insurmountable challenges" for MK-2640's further development.

MK-2640 represents a family of GRIs whose availability *in vivo* is modulated by a Competitive Clearance Mechanism (CCM) between glucose and the therapeutic (17–20). As illustrated in Figure 5-1A, these insulin-based constructs contain added carbohydrate moieties, allowing them to be recognized and cleared away by lectins via, in the case of MK-2640, mannose receptors (MR). The envisioned responsiveness to the glycemic level is a result of the, albeit weak, affinity of glucose to MR. The competition therefore creates a difference in MK-2640 availability between eu- and hyperglycemia: Only in the latter case is the MR-mediated clearance shut off by glucose competition and the GRI made available. CCM is among many mechanisms that rely on the competition between insulin and glucose, which date back to the very first GRI system pioneered by Brownlee and Cerami four decades ago (21). That said, GRIs of the MK-2640 family uniquely modulate insulin availability by enhanced removal at euglycemia, rather than activation at hyperglycemia like their counterparts (15).

Merck's development of the competitive clearance GRIs was terminated (15) as the clinical trials reported far less responsiveness in MK-2640 clearance than that promised by the canine and porcine evaluations (16,19). This fatal limitation in pharmacokinetics was attributed to saturation of the MR-mediated clearance capacity in humans (16,22). It was, however, never proven nor quantified. Additionally, it remains to be answered whether any other distinctions between humans and preclinical animals could have played a role, or whether the rest of the portfolio, reportedly with enhanced potency and undiminished MR affinity (17,18), could have fared better in a clinical trial. On the modeling front, the Merck team performed thorough model-based meta-analysis (23), interspecies scaling studies (24), and systems pharmacology simulations with the UVa/Padova simulator (25). They established that, while the *in-silico* tools were predictive of the clinical pharmacokinetics (PK) and pharmacodynamics (PD) of regular human insulin (RHI), translational modeling based on preclinical data ended up missing the observed PK of MK-2640 (24,26). This contrast has prompted Kandala *et al*. to ascribe MK-2640's underperformance to interspecies differences in MR-specific attributes (24), yet it remains not fully understood nor further pursued whether the critical gap lies with MR distribution, competitive binding, GRI potency, or something else – a question we seek to answer in this work.

Although many have characterized the clinical trials as having failed (16,27), the MK-2640 and RHI data in humans are far from a failure in providing valuable insights into the mechanistic and translational aspects of CCM GRIs. In this paper, we compare and contrast these GRIs' PK and PD in humans and minipigs by means of an integrated translational modeling platform, with a particular focus on the decisive metric of the change in GRI clearance. We name our platform "GRI Mathematical Model Mapping Performances in Animal and Clinical Trials", or "IM^{3}PACT" for short. An expansion of our previous PAMERAH model mapping rodents and humans (28), IM^{3}PACT couples together a mechanistic model of the CCM principle and physiological models of humans' and minipigs' glucoregulatory systems, with the minipig being a new addition to the list of species accounted for. As the physiology is modelled as an interconnected network of well-mixed compartments (or mathematically, a system of differential equations), we are able to track the action of MK-2640 specific to each organ, which concurs with recommendations from Merck's modeling team. They found their modified UVa/Padova model not designed for capturing the GRI's hepatic site of action (26), and hence unable to have pictured the dilution of a locally significant PK responsiveness in the systemic pool in humans (16) – a speculation only confirmed

and quantified in this study with IM^{3}PACT. By transposing minipigs' key MK-2640 properties onto the human model one at a time, we concluded the unsuccessful clinical translation was not a result of the differences in the GRI's potency, volume of distribution, or intrinsic clearance rate. Rather, the key contributing factors were (i) insufficient clearance capacity via the MR route in humans, as already suspected following Krug *et al.*'s analyses; and (ii) incomplete switching off of MR-mediated elimination under hyperglycemia, meaning only a fraction of the already constrained capacity was utilized. Our study establishes *in silico* diabetes modeling as not just a tool for GRI design and early-stage screening (28,29), but also an investigative lens through which hypotheses are falsified/validated, unmeasurable properties are quantified, and new insights are learned for future GRIs of the CCM family and beyond.

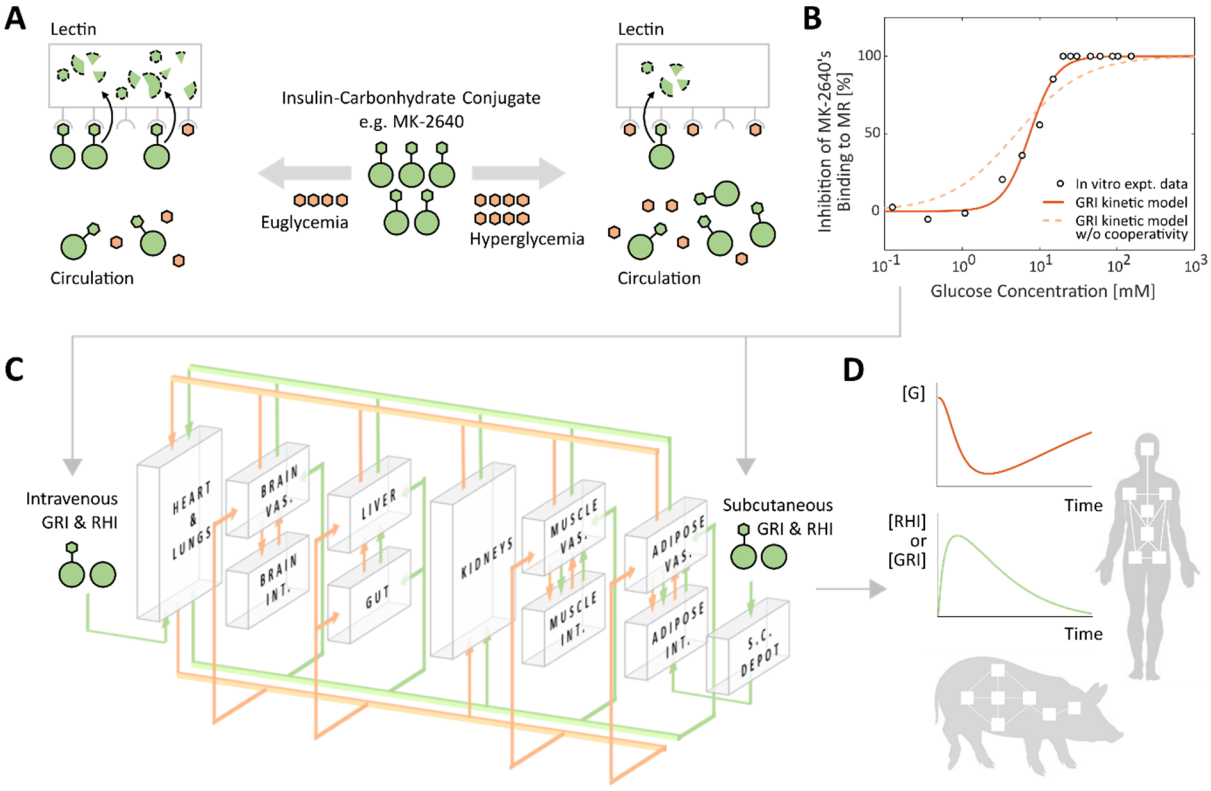

Figure 5-1. Overview of the *in silico* investigation of the competitive clearance GRIs with the IM^{3}PACT modeling platform. *A*: Illustration of the glucose-responsive mechanism of MK-2640 and its variants. The carbohydrate-conjugated insulin analogs exemplified by MK-2640 (green) undergo clearance via both the intrinsic insulin receptor (IR) route as well as the additional lectin/mannose receptor (MR) route, with the latter being responsive via the competitive binding of glucose (orange). Consequently, under euglycemia (hyperglycemia), the weak (strong) competition from glucose is designed to allow a high (low) rate of MR-mediated GRI clearance, thus lowering (enhancing) its availability in circulation. Pivotal to the design concept, therefore, is a significant difference

in clearance between eu- and hyperglycemia, which was not observed in the clinical clamp studies of MK-2640 (16). The reversible binding processes of the GRI and glucose to MR depicted in the illustration are respectively represented by rate constants $k_{\pm 1}$ and $k_{\pm 3}$, which play important roles in the mechanistic model (Equations 5-1 and 5-2). *B*: The mechanistic model almost perfectly describes the *in vitro* assay data of glucose-inhibited MK-2640 binding to MR (19) but only if the Hill coefficient h_G is incorporated which represents cooperativity. *C* and *D*: IM^{3}PACT couples the mechanistic model of MK-2640 with a physiological model symbolizing the full-body glucoregulation as a network of well-mixed compartments (*C*). By solving the equivalent system of differential equations (Equations 5-7-5-9), we are able to trace the concentrations of GRI and regular human insulin (RHI) over time, in addition to the blood glucose [G], as they are circulated and metabolized in the body of either humans or minipigs following intravenous or subcutaneous administration (*D*). Expt., experimental; vas., vascular; int., interstitial; s.c., subcutaneous.

5.3. Research Design and Methods

5.3.1. Mechanistic Model of Competitive Clearance GRIs

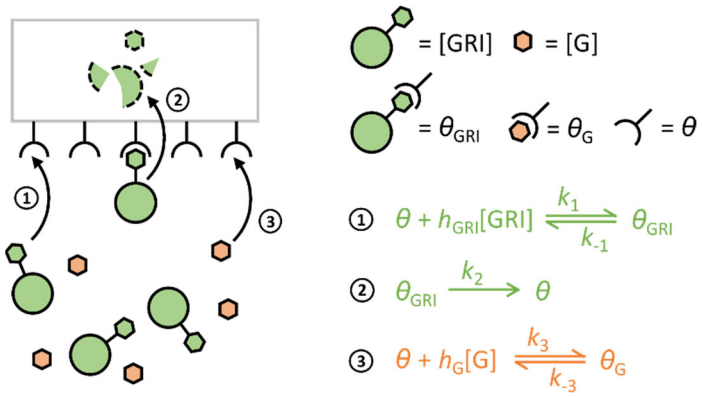

Figure 5-2. Schematic of the proposed mechanistic model for CCM. Kinetics 1, 2, and 3 respectively represent the binding of a free GRI to MR, the internalization and elimination of a bound GRI-MR complex, and the competitive binding of glucose to MR.

As with our earlier efforts (28–30), the IM^{3}PACT model comprises of two modular components: (i) a mechanistic model describing the glucose responsiveness of the GRI of choice, which is plugged into (ii) a physiological model simulating the circulation and metabolism of glucose, insulin, glucagon, and GRI over time, of humans, rodents, and, as part of the contribution from this research, minipigs. As illustrated in Figure 5-2, we model the CCM mechanism with the following kinetics analogous to that of competitive enzyme inhibition (31):

$$\theta + h_{GRI}[GRI] \underset{k_{-1}}{\overset{k_1}{\rightleftharpoons}} \theta_{GRI} \xrightarrow{k_2} \theta \tag{5-1}$$

$$\theta + h_{\mathrm{G}}[\mathrm{G}] \underset{k_{-3}}{\overset{k_3}{\rightleftharpoons}} \theta_{\mathrm{G}} \tag{5-2}$$

Equations 5-5-1 and 5-5-2 respectively describe the binding of the GRI molecule and glucose to the receptor in charge of competitive GRI clearance, as a function of their concentrations [GRI] and [G]. In the case of MK-2640, θ, θ_{G}, and θ_{GRI} denote concentrations of unbound MR sites, those bound to glucose, and those to MK-2640. Their interconversions are dictated by the corresponding rate constants k, of which k_2 in particular captures the irreversible internalization and clearance of the bound GRI, followed by the recycling of the receptor θ to the protein surface. The Hill coefficients h_{GRI} and h_{G} respectively indicate the degree of cooperativity (32) in the binding of GRI and glucose, the use of both we justify further below with published experimental data.

Figure 5-1B shows how a parameterized mechanistic model quantitatively captures the competitive inhibition of MK-2640's binding to MR with escalating concentrations of glucose, experimentally measured *in vitro* previously (19). Assuming quasi-steady-state and that the internalization and receptor recycling step is rate-limiting, we obtain the following expression for θ (and hence θ_{G} and θ_{GRI}) as a function of θ_{tot}, the time-invariant total number density of MR binding sites:

$$\left.\begin{aligned} \theta_{\mathrm{GRI}} &= [\mathrm{GRI}]^{h_{\mathrm{GRI}}}\,\theta / K_{\mathrm{M}} \\ \theta_{\mathrm{G}} &= K_{\mathrm{G}}[\mathrm{G}]^{h_{\mathrm{G}}}\,\theta \\ \theta + \theta_{\mathrm{GRI}} + \theta_{\mathrm{G}} &= \theta_{\mathrm{tot}} \end{aligned}\right\} \Rightarrow \theta = \frac{\theta_{\mathrm{tot}}}{1 + K_{\mathrm{G}}[\mathrm{G}]^{h_{\mathrm{G}}} + [\mathrm{GRI}]^{h_{\mathrm{GRI}}} / K_{\mathrm{M}}} \tag{5-3}$$

where $K_{\mathrm{G}} = k_3 / k_{-3}$ is the glucose binding equilibrium constant and $K_{\mathrm{M}} = (k_2 + k_{-1}) / k_1$ is the Michaelis constant (33). The rate of the GRI's MR-mediated clearance is thus:

$$\begin{aligned} d[\mathrm{GRI}] / dt &= k_2 \theta_{\mathrm{GRI}} \\ &= \frac{k_2 \theta_{\mathrm{tot}} [\mathrm{GRI}]^{h_{\mathrm{GRI}}}}{K_{\mathrm{M}}(1 + K_{\mathrm{G}}[\mathrm{G}]^{h_{\mathrm{G}}}) + [\mathrm{GRI}]^{h_{\mathrm{GRI}}}} \\ &= \frac{k_{\mathrm{MR}} [\mathrm{GRI}]^{h_{\mathrm{GRI}}}}{K_{\mathrm{M}}(1 + K_{\mathrm{G}}[\mathrm{G}]^{h_{\mathrm{G}}}) + [\mathrm{GRI}]^{h_{\mathrm{GRI}}}} \end{aligned} \tag{5-4}$$

where $k_{\mathrm{MR}} = k_2 \theta_{\mathrm{tot}}$ lumps together the specific rate of MR-mediated clearance and the local abundance of participating receptors. Normalizing Equation 5-4 with the uninhibited rate of

$k_{MR}[GRI]^{h_{GRI}} / (K_M + [GRI]^{h_{GRI}})$, we arrive at the glucose-dependent degree of inhibition previously probed with *in vitro* binding assay:

$$\%\text{Inhibition} = 1 - \frac{K_M + [GRI]^{h_{GRI}}}{K_M(1 + K_G[G]^{h_G}) + [GRI]^{h_{GRI}}} \quad (5\text{-}5)$$

With a given MK-2640 concentration of 4 nM, K_M of 3 nM, and h_{GRI} of 1.5, the experimental data in Figure 5-1B were fitted almost perfectly to the mechanistic model, yielding a K_G of 0.022 mM^{-h} and a h_G of 2.537. The latter falls within the typical range of 1 to 4 for Hill coefficients (34). On the other hand, removal of the glucose Hill coefficient from the mechanistic model results in a far inferior prediction of the inhibitory response (Figure 5-1B, dashed) regardless of h_{GRI} and K_G values. Given the lack of binding assay data with varying concentrations of MK-2640 at a fixed [G], h_{GRI} of 1.5 was instead inferred from the clinical clamp studies of escalating MK-2640 infusion rates (16). The need for a cooperative h_{GRI} larger than unity is clear, however, even before we attempted to quantitatively fit the model, being (i) evident from the significant initial rise in MK-2640 clearance with increasing concentrations (Figure 5-6), and (ii) consistent with literature on insulin-receptor binding (35). Lastly, the mechanistic model outputs a half maximal inhibitory concentration (IC_{50}) of 7.5 mM for glucose, which is in good agreement with the 8 mM reported in experiments.

5.3.2. Full-Body Physiological Model of the Glucoregulatory System

The physiological model component of IM^{3}PACT was constructed on the basis of Sorensen-like models (36–39) with a number of added modules and modifications, for instance accounting for subcutaneous injection kinetics (29,40,41), intraperitoneal injection kinetics (42), and oral glucose absorption following meals (30,43). Compared to semi-mechanistic parsimonious models of the glucoregulatory system (44,45), such physiology-based models enable tracking of hormone and metabolite concentrations within each organ and allow therapeutics to take effect locally in their intended compartments (30). Figure 5-1C illustrates the architecture of IM^{3}PACT's physiological model, which represents the body as an interconnected network of well-mixed compartments, mathematically equivalent to a system of ordinary differential equations (ODEs) which we solve using well-established numerical methods (ode15s, MATLAB R2020a, the MathWorks, Inc.).

Within an arbitrary compartment, the concentrations of a solute [s] in the vascular (subscript "v") and interstitial spaces (subscript "i") are respectively dictated by:

$$\underbrace{V_{\mathrm{v}}\, d[s]_{\mathrm{v}}/dt}_{\text{rate of change}} = \underbrace{Q\left([s]_{\text{heart}} - [s]_{\mathrm{v}}\right)}_{\text{in/outflow}} - \underbrace{V_{\mathrm{i}}\left([s]_{\mathrm{v}} - [s]_{\mathrm{i}}\right)/T}_{\text{transcapillary exchange}} + R_{\mathrm{v}} \tag{5-7}$$

$$V_{\mathrm{i}}\, d[s]_{\mathrm{i}}/dt = V_{\mathrm{i}}([s]_{\mathrm{v}} - [s]_{\mathrm{i}})/T + R_{\mathrm{i}} \tag{5-8}$$

where V denotes the compartmental volume and Q the arterial blood flowrate through the organ. The characteristic time of transcapillary transport, T, together with the concentration gradient, determines the mass exchange between the vascular and interstitial sub-compartments. For organs with rapid transcapillary equilibrium, only Equation 5-7 remains relevant and is simplified to:

$$V d[s]/dt = Q([s]_{\text{heart}} - [s]) + R \tag{5-9}$$

The local rate of metabolism in the compartment, R, sums up the production and uptake rates as a function of the local concentrations of glucose, insulin, glucagon, and GRI through transfer functions documented in Table 5-3. Of note, in the liver and when the solute s denotes a CCM GRI, a key component of the R term is naturally its receptor-mediated competitive clearance seen in Figures 1A and 2, the rate of which is denoted as R_{MRCL}:

$$R_{\mathrm{MRCL}} = \frac{k_{\mathrm{MR}} V [\mathrm{GRI}]^{h_{\mathrm{GRI}}}}{K_{\mathrm{M}}(1 + K_{\mathrm{G}}[\mathrm{G}]^{h_{\mathrm{G}}}) + [\mathrm{GRI}]^{h_{\mathrm{GRI}}}} \tag{5-10}$$

per Equation 5-4 of the GRI mechanistic model above, where V, k_{MR}, [GRI], and [G] are local to the liver compartment. Intravenous (i.v.) boli are initialized by distributing the dosage to all vascular compartments. The treatment of the hexamer-dimer-monomer equilibrium in the subcutaneous depot is discussed in Table 5-3.

5.3.3. Model Extension for Minipig Simulation

In contrast to the scarcity of GRI clinical data and the abundance of those in preclinical animals, the vast majority of both the parsimonious and physiology-based simulation platforms to date only model glucoregulation in humans. To facilitate the preclinical-to-clinical translation of GRI therapeutics, our recent publication extended the full-body physiological model to rats and mice with data collected experimentally and extracted from published literature (28). In the present work, using the same workflow, we adapted our model to Yucatan minipigs on which the Merck team

performed preclinical MK-2640 studies. Note that while a couple of Merck publications reported murine and canine data of similar CCM analogs, they are derivatives of MK-2640 with modified characteristics (17,18). A direct cross-comparison between clinical and animal results is therefore only possible with the model extended to minipigs.

The process of cross-species model adaption has been documented in detail in our past report (28) and is briefly described here. Instead of numerically scaling down the human parameters by bodyweight with empirical allometric exponents, systematic measurements of Yucatan minipigs were used for the anatomical parameters (Table 5-2), such as the compartment volumes (V) and hemodynamic flowrates (Q). These experimental measurements were sourced from vendor-provided datasets (46) as well as research articles (47–50). Particularly of note was a simplified physiology-based model for diabetic Göttingen minipigs by Lunze *et al.*, who determined the parameters for the liver, periphery, and plasma compartments (38). The transfer functions, which describe the glucose and insulin modulation of each compartment's metabolic rates, were not readily available from literature. With sensitivity analyses (51,52), we identified the most influential of these parameters and subsequently fitted them with regular human insulin (RHI) data of diabetic and healthy minipigs (16), further discussed in the Results section. As with our previous model adaptation to rodents (28) and consistent with other published models (45,53,54), we performed differentiating parameterization of 3 parameters for diabetic and healthy minipigs. Following the iterative parameterization process, we arrived at a final set of model parameters, including those specific to the MK-2640 characteristics (see below), that is self-consistent across RHI and MK-2640 data in minipigs and humans (summarized in Table 5-3). All parameter estimations were performed with the standard interior-point optimization algorithm in MATLAB R2020a.

5.3.4. Addressing Key Distinctions between MK-2640 and RHI

Despite that the parameterized physiological model is able to simulate the time evolution of glucose, insulin, and glucagon concentrations, and that MK-2640 as an insulin-carbohydrate conjugate functions via insulin receptors like RHI does, it is inaccurate to simulate each MK-2640 molecule merely as an insulin with added MR-mediated clearance. In addition to the MR-mediated clearance already captured as a part of the mechanistic model above, a number of key

characteristics causes the GRI behavior to depart from that of endogenous insulin, which we take into consideration with corresponding model modifications specific to the CCM GRI:

A signature of MK-2640, and in fact of the other promising CCM GRI candidates investigated preclinically by Merck, is the significantly reduced potency in terms of IR affinity (16–19). With an IR-binding IC_{50} in minipigs 19.0-fold larger than RHI (14.6-fold in humans), each MK-2640 molecule is equivalent to just a fraction of RHI regarding glucoregulation. This effective concentration used in the model's transfer functions is exactly the GRI level scaled by the IR IC_{50} ratio, which is a rigorous result derived from a kinetic model of the IR binding assay (§5.7).

In spite of the lowered affinity to IR, it is not necessary for a 19-fold increase in dose to achieve a commensurate efficacy as a unit of RHI. In the subcutaneous minipig experiments, for instance, only a 4-to-7-fold increase in dose was used. This is primarily due to a reduction of IR-mediated intrinsic clearance of MK-2640 which is "in inverse proportion to [its] *in vitro* potency"(16), a phenomenon commonly observed with chemically modified insulin analogs (55). We acknowledge this observation in IM^{3}PACT by introducing a scaling factor Λ_{IRC} to the liver, kidney, and periphery compartments, which represents the ratio between intrinsic GRI clearance and the default RHI rate. The quotient of the observed *in vivo* equivalent dose divided by the IR IC_{50} ratio (the so-called "*in vitro* potency") was used as an initial guess for Λ_{IRC} in the parameterization process.

Lastly, it was observed among the minipig i.v. bolus data that both RHI and MK-2640 exhibited a biexponentially declining plasma concentration profile with time (19), consistent with a classic two-phase model of i.v. pharmacokinetics which distributes the drug between the fast vascular compartments and the slowly equilibrating interstitial compartments (56,57). Nevertheless, the experimentally measured central volumes V_c, defined as the ratio between the i.v. dose and the onset drug concentration, differs by nearly twofold between RHI and MK-2640 (57 *vs.* 24 mL/kg). Indeed, Kaarsholm and co-workers note a low steady state volume of distribution in minipigs and dogs (19). Mathematically to account for the observed reduction in V_c, we scaled down all the vascular compartments by a factor of Λ_V when a CCM GRI is dosed instead of RHI. In the case of minipigs, Λ_V was computed directly from experimental observations, instead of being fitted, as $24/57 = 0.42$.

5.4. Results

For minipigs, predictions by the parameterized IM^{3}PACT model agree with the experimental blood glucose and insulin trajectories over time following intravenous (Figure 5-3A, B) and subcutaneous doses (Figure 5-3C) of RHI and MK-2640 (19). We particularly appreciate the *in vivo* measurements of the RHI and MK-2640 concentrations in circulation post i.v. injections (Figure 5-3A, B, right panels) which helped (i) validate the vendor-provided and literature values of the compartmental volumes and flowrates, and (ii) anchor the MK-2640 pharmacokinetic parameters directly. Of note, we mimicked the experimental administration of α-methylmannose (α-MM, a strong MR-binding antagonist) by blocking off the MR-mediated competitive clearance pathway completely (*i.e.*, enforcing an R_{MRCL} of 0 regardless of [GRI] and [G] in Equation 10). In Figure 5-3B, the corresponding hypoglycemic episode and sluggish clearance of MK-2640 clearly demonstrate the PK and PD change brought about by the competitive clearance mechanism in minipigs. As expected, the addition of α-MM is close to irrelevant to RHI's PK and PD (Figure 5-3A), as suggested by both experiments and simulations.

Unlike the ongoing clinical trials of Novo Nordisk's investigational glucose-sensitive insulin which opted for subcutaneous administration (NCT numbers: NCT04569994 and NCT05134987), MK-2640 was clinically studied with clamps (16). As illustrated in Figure 5-3D, in a clamp study (58,59), one varies the real-time intravenous glucose infusion rate (GIR) to counter a predefined insulin/GRI infusion rate (IIR) so as to maintain the plasma glucose concentration at a setpoint, shown in Figure 5-3E for the healthy individuals under a series of euglycemic clamps ("Trial 1"). The steady-state concentrations of RHI or GRI (C_{SS}) as a function of IIR serves as an indicator of the pharmacokinetics (Figure 5-3F), from which the amount of clearance can be computed as IIR/C_{SS} (Figure 5-3G). As mentioned earlier in §5.3, the marked increase in MK-2640 at low IIRs serves as a justification for the cooperative Hill coefficient h_{GRI} (see also Figure 5-6). The decline in clearance for IIRs larger than 54 pmol/kg/min, or equivalently for C_{SS} over 5 nM, is a signature of saturating elimination (16). On the other hand, the steady-state GIR is an indicator of the therapeutic's pharmacodynamics (Figure 5-3H). It is apparent in all of Figure 5-3E-H that the IM^{3}PACT-simulated PK and PD of MK-2640 in healthy humans match with those manifested through the euglycemic clamp experiments (16).

MK-2640's PD comparative to that of RHI is better visualized in Figure 5-3I where GIR is plotted as a function of C_{SS}. The simulated relations match with the clinical MK-2640 data as well as the RHI correlation summarized from a previous literature meta-analysis (16,60,61). Krug and colleagues concluded that to arrive at a GIR of 5 mg/kg/min (half of the saturation GIR), the required RHI concentration is approximately 4% that of MK-2640 due to the latter's significantly lowered potency. Indeed, IM^{3}PACT outputs a value of 4.2%. These results are not far off from the aforementioned IR IC_{50} ratio which signifies MK-2640's weak IR binding affinity (see §5.3.4).

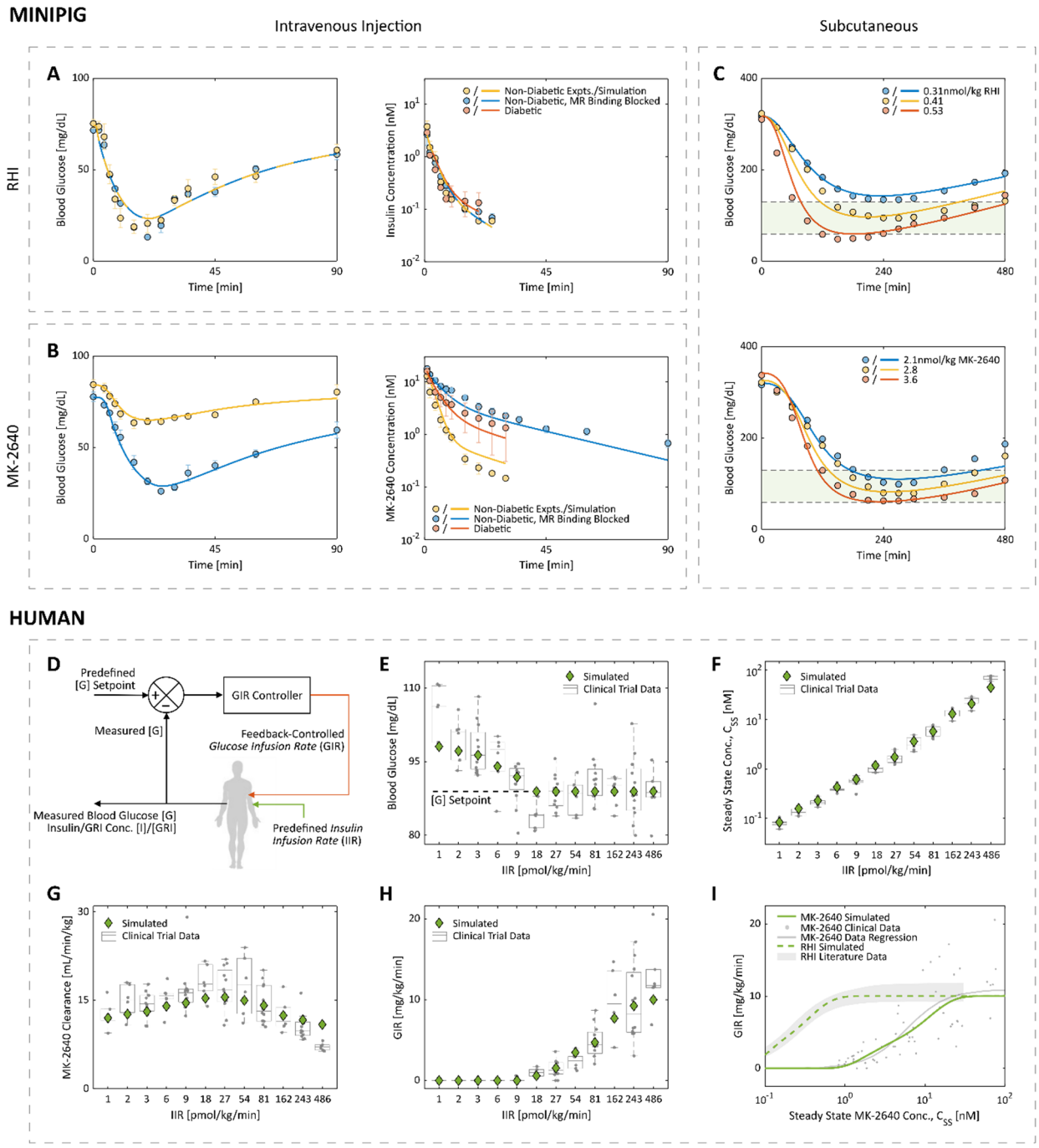

Figure 5-3. IM^{3}PACT is able to quantitatively describe RHI and MK-2640 behaviors in minipigs and humans. *A* and *B*: Experimentally measured concentrations (circles) of blood glucose, RHI, and MK-2640 in minipigs agree with IM^{3}PACT outputs (curves) following an intravenous bolus of 0.17 nmol/kg RHI (*A*) or 0.35 nmol/kg GRI (*B*). The experimental MR blockage by α-methylmannose was simulated by shutting off the MR-mediated clearance pathway completely. *C*: Similarly, the parameterized mathematical model captures the dose-dependent lowering of blood glucose levels by both RHI (top) and MK-2640 (bottom) post subcutaneous administration. Circles, minipig *in vivo* data; Curves, simulation. *D*: Schematic explaining the principles of glycemic clamps, where the intravenous

glucose infusion rate (GIR) is feedback controlled to offset a predefined insulin/GRI infusion rate (IIR), such that the blood glucose level is kept at a constant setpoint. *E*-*I*: Simulated results match with clinical results from Merck's euglycemic (80 mg/dL) Trial 1 in terms of measured blood glucose (*E*), steady-state GRI concentrations (*F*), clearance rates (*G*), and GIR (*H*), thus capturing both MK-2640's PK and PD in healthy individuals. The agreement between simulated and experimental/literature C_{SS}-GIR relations for both MK-2640 and RHI means their potency difference is quantitatively represented in IM^{3}PACT. Each of the grey circles in *E*-*H* represents a single clinical measurement. Experimental results plotted were digitized from literature reports: Ref. (19) for panels *A*-*C*; Ref. (16) for panels *E*-*I*. We refrained from reproducing certain error bars in panels *A*-*C* and all datapoints below 0.8 nM in panel *I* as their original presentation overlapped significantly with other data or figure elements and could not be faithfully digitized.

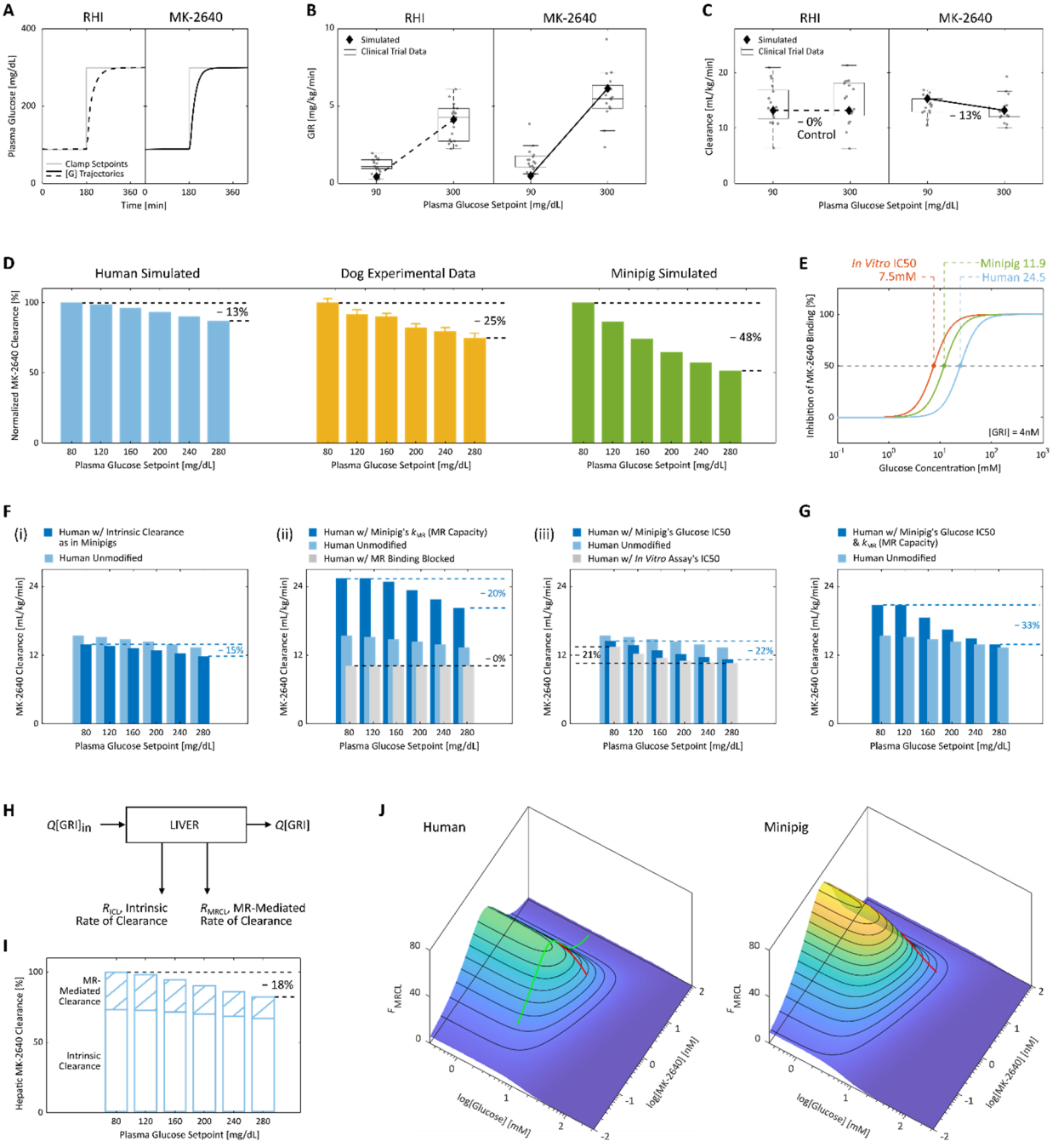

Figure 5-4. Subpar glucose responsiveness of MK-2640 clearance in humans and investigation into the hypothesized causes of the unsuccessful clinical translation. *A-C*: In Merck's clinical Trial 2 (16), type 1 diabetic patients were clamped first at 90 mg/dL for 3 hours and subsequently at 300 mg/dL for 4 hours, with continuous intravenous infusion of either 1.4 pmol/kg/min of RHI (*A*, left) or 40 pmol/kg/min of MK-2640 (*A*, right). A glucose-dependent PD response was observed (*B*), as the GIR increased by 4.1 mg/kg/min for MK-2640 (5.6 in simulation) and only 3.2 mg/kg/min for RHI (3.7 in simulation) between the two setpoints. Despite moderate PD responsiveness, the PK of MK-2640 barely changed (*C*) with a mere 6% difference in clearance (13% in simulation), which directly contradicted the essence of the design concept. Each grey circle in *B* and *C* represents a single measurement. *D*: We

performed a straightforward comparison across species by subjecting our human (blue) and minipig (green) models to the same multi-glycemic clamp protocol previously applied to dogs (yellow). The modulation in clearance was predicted to be 13% in humans between 80 and 280 mg/dL, expectedly close to the clinical Trial 2 outcome. In comparison, a 25% change was observed in canine experiments ("~30%" claimed by Kaarsholm *et al*. (19)) and 48% in simulated minipigs. Error bars: digitized standard error. *E*: Both the parameterized minipig and human models exhibited inhibition curves shifted away from that predicted by the *in vitro* MR binding assay (also see Figure 5-1B). This drift caused a 50% increase in MR IC_{50} for MK-2640 in minipigs and a 2.3-fold increase in humans, meaning reduced competition from glucose. *F*: We sought to validate or falsify a number of hypotheses regarding MK-2640 properties that hindered the clinical translation. (i) If humans hypothetically assumes the same extent of MK-2640 elimination as minipigs via the intrinsic IR-mediated route, the clearance change across the glycemic region was predicted to be 15%, not far from the original 13% in panel *D*. On the other hand, we found the interspecies differences in MR-mediated clearance capacity (ii) and MR IC_{50} (iii, representative of the glucose competitiveness) to be strongly correlated with differences in MK-2640 PK. *G*: Only the transposition of both factors in panel *F*(ii) and (iii) from minipigs to humans resulted in a modulation beyond 30%, a threshold critical to MK-2640's entry into the clinical stage. *H*: Schematic of the local mass balance of MK-2640 in the liver. *Q*, blood flowrate; $[GRI]_{in}$ and [GRI], local MK-2640 concentrations into and out of the liver compartment. *I*: IM^3PACT simulations confirmed the Merck team's hypothesis that the local hepatic MK-2640 PK demonstrates a more salient glucose responsiveness (a change of 18%) than that of the whole body. This improved result, however, still does not compare with the preclinical performances (panel *D*). *J*: A simple proxy metric for the extent of MR-mediated MK-2640 clearance, F_{MRCL}, can be derived from the liver mass balance in *H*. F_{MRCL} allows direct visualization of the dependence of competitive clearance on local glucose and GRI concentrations, based solely on MK-2640 parameters and the liver physiology without requiring simulation. Green curve, Merck's clinical Trial 1 on non-diabetic individuals (*cf*. Figure 5-G); Red curves, Trial 2 protocol applied to diabetic humans and minipigs.

While Trial 1 clamps performed on healthy individuals did show saturation of clearance at 5 nM of MK-2640 and higher, it was primarily the two-stage Trial 2 on diabetic patients that concluded the GRI's unsuccessful clinical translation (16). As shown in Figure 5-4A's simulation results, Trial 2 contrasted a therapeutic's PK and PD under euglycemic and hyperglycemic conditions by clamping the patients first at a plasma glucose setpoint of 90 mg/dL for 3 hours, followed by at 300 mg/dL for 4 hours. While the clinical GIR data (Figure 5-4B) suggested a comparatively more significant rise with MK-2640, which is also captured by the simulations, the reduction in clearance rates (Figure 5-4C) between the clamp levels was underwhelming: Krug *et al.* reported a 6% difference between the geometric means and IM^{3}PACT simulations predict a reduction of 13.0%, both far lower than the 25.1% promised by a different, but similar set of glycemic clamps on dogs reproduced in Figure 5-4D (16,19). With IM^{3}PACT, we predicted the outcomes should a diabetic human or minipig undergo the same 6-level clamp protocol as the dogs under a single fixed IIR. With the clearance rates normalized to the 80 mg/dL euglycemic rate for each corresponding species, it is apparent in Figure 5-4D that while MK-2640's clearance always drops with higher clamp setpoints, the GRI is significantly less responsive in humans than in dogs or minipigs. We note that the ability to computationally apply an experimental protocol performed on one species to another could prove powerful in reconciling otherwise incomparable literature results and aiding clinical translation.

We investigated this disparity in responsiveness by looking for key differences between humans and minipigs, particularly those pertaining to MK-2640's PK and PD as recommended by Cho and colleagues (26). Table 5-1 provides a side-by-side comparison of the relevant parameters in IM^{3}PACT's human and minipig models. The numerically largest distinction was identified between the k_{MR} values of MK-2640. The significantly lower k_{MR} value revealed by the clinical trials represents a smaller MR-mediated clearance capacity in humans than in minipigs, caused by a lower availability of participating mannose receptors in the compartment (θ_{tot}, Equation 5-1), a slower elimination of each bound MK-2640 (k_2), or a combination of both in the human body.

Apart from the total MR-mediated clearance capacity, the maximal degree of modulation in MK-2640 clearance is naturally also dependent on the capacity of IR-mediated intrinsic elimination. The latter is characterized in IM^{3}PACT by Λ_{IRC}, which expresses IR-mediated capacity of MK-2640 clearance as a fraction of its RHI counterpart (see Research Design and Methods). As seen

in Table 5-1, the reduction in IR-mediated clearance is less pronounced in humans (10% *vs.* 26% in minipigs), potentially correlated with the relatively higher affinity to IR. In humans, this larger retention of the intrinsic clearance capacity could have masked a non-negligible modulation in MR-mediated clearance when one examines the total clearance change of Trial 2. We verify the validity of this hypothesis below in Discussion.

Orthogonal to k_{MR} which determines the MR-mediated clearance capacity affordable, the glucose IC_{50} for MR binding characterizes the actual fraction of that capacity utilized as a function of [G] and [GRI] (see Equation 5-5). In agreement with a prior hypothesis that the *in vivo* relative binding strengths to MR could have shifted from the *in vitro* assay (28), we did find the MR IC_{50} in minipigs and humans to both drift upwards from the 7.5 mM predicted *in vitro*, particularly so in humans with a 2.3-fold departure (Table 5-1, Figure 5-4E). Lastly, the central compartment volume V_c of MK-2640 in humans turned out to be close to that of RHI, in contrast to a ratio of $\Lambda_V = 42\%$ observed in minipig i.v. bolus data (discussed earlier in §5.3.4).

Table 5-1. Interspecies differences in MK-2640 properties hypothesized to have contributed to the unsuccessful clinical translation. See §5.3.4 for a detailed explanation.

MK-2640 Property	Indication	Model Parameter	Human	Minipig	Dimension
Volumetric rate constant of MR-mediated elimination from the liver[a]	Clearance capacity via MR	$k_{MR} = k_2\theta_{tot}$	160.2	606.2	mU/L-min
IR-mediated clearance, as a fraction of RHI	Clearance capacity via IR	Λ_{IRC}	90%	60%	[-]
Relative affinity to IR, as a fraction of RHI	Molecular potency	$\frac{\text{IR IC}_{50}\text{ (GRI)}}{\text{IR IC}_{50}\text{ (RHI)}}$	4.5%[b]	5.5%[b]	[-]
Ratio of *in vivo* MR IC_{50} to the *in vitro* assay (7.5 mM)	Drift in the most responsive blood glucose range	$\frac{\text{MR IC}_{50}\ (\textit{in vivo})}{\text{MR IC}_{50}\ (\textit{in vitro})}$	3.3[c]	1.5[c]	[-]
Central compartment volume V_c, as a fraction of RHI	Deviation of peak post i.v. concentration from RHI	Λ_V	85%	42%[d]	[-]

[a] See Equations 5-5-4 and 5-5-10.

[b] Based on the *in vitro* IR binding assay results reported in Kaarsholm *et al*. (19).

[c] Also see Figure 5-4E.

[d] Calculated from the reported i.v. bolus data (19) as analyzed in Research Design and Methods.

5.5. Discussion

5.5.1. Analyzing Root Cause(s) of the Poor Translatability

Interspecies distinction in each of the five MK-2640's properties can be hypothesized to have contributed to the unsuccessful replication of the promising preclinical results in the clinical trials. We verified the validity of these postulated failure modes *in silico* by examining simulated clamp outcomes under hypothetical scenarios where a certain MK-2640 characteristic in minipigs is transposed to humans. For example, Figure 5-4F(i) showcases a 15.0% reduction in total clearance between euglycemic and hyperglycemic clamp simulations should the human IR-mediated clearance of MK-2640 be 60% that of RHI, instead of 90%. While this reduced intrinsic clearance did accentuate the glucose-responsive MR contribution, a mere 2.0% improvement on top of the original 13.0% modulation does not qualify the Λ_{IRC} difference as a major contributor to MK-2640's lack of clinical glucose responsiveness. Along the same lines, we demonstrate in Figure 5-7 that the GIR's glucose responsiveness does not meaningfully improve if the human MK-2640 model adopts the same IR affinity or central compartmental volume of minipigs. Interestingly, in spite of the large disparity in Λ_V across species, an MK-2640 central volume similar to RHI's actually enhances the GRI's response in humans, as the transposition of the porcine Λ_V of 42% further truncated the 13.0% clearance reduction to 8.2% (Figure 5-7).

Figure 4F(ii) suggests that the variation of clearance is boosted to 20.4% if the human model assumes the MR clearance capacity (k_{MR}) of minipigs (see Table 5-1). As expected, a nearly quadrupled k_{MR} raises the total clearance rates at all clamp setpoints, which in turn shifts the partition between glucose-responsive (MR-mediated) and intrinsic (IR-mediated) elimination pathways (Figure 5-4F(ii)). If we block off the MR binding completely by enforcing a k_{MR} of 0, the clearance rate of 10.2 mL/kg/min is made up solely of IR-mediated MK-2640 removal in the liver, kidney, and periphery. This means that with the k_{MR} of minipigs transposed to the human model, 60.2% of the total clearance at 80 mg/dL is accounted for by MR. This percentage is much closer to Merck's canine experiments which estimated an MR contribution of 80% at euglycemia (19), as the unmodified clamp simulations attributed only 33.9% of the total clearance to MR in humans. The significant change in glucose responsiveness brought about by the cross-species capacity difference, manifested in the k_{MR} values, confirms the suspicion of Krug and colleagues

who postulated that the "incomplete understanding of quantitative differences across species in [MK-2640's] clearance capacity complicate predictions of clinical GRI PK and clearance" despite the well-preserved homology of the MR protein (16).

The simulations in Figure 3F(iii) investigate the impact of the MR IC_{50} of MK-2640, which characterizes the range of blood glucose levels most sensitive to CCM (Table 5-1). We predicted a modulation beyond 20% if, hypothetically, the MR IC50 in humans is either the same as in minipigs (22.0%) or as that predicted by the *in vivo* binding assay (21.3%, see Figure 5-4E). It is not uncommon for these *in vitro* assays to deviate from the actual *in vivo* behavior (62), sometimes with binding constants differing by orders of magnitude due to changes in receptor presentation, accessibility, and microenvironment (63). While the fractional inhibition curve shifted rightwards from the *in vitro* measurements in both minipigs and humans (Figure 5-4E), only for the latter did the shift prove detrimental to the glucose responsiveness, as the clinical MR IC_{50} of 24.5 mM fell out of the 80 to 300 mg/dL (4.4 to 16.7 mM) range where clearance modulation is desired. That is, the MR-mediated clearance was far from completely switched off at hyperglycemia, and the total MR capacity was not fully utilized for glucose responsiveness. Indeed, as shown in the clinical Trial 1 data (Figure 5-3G), the total clearance at high IIRs drops to approximately 10 mL/min/kg after the mannose receptors are saturated. MK-2640 elimination mediated by IR, by deduction, cannot exceed 10 mL/min/kg. In Trial 2 (Figure 5-4C), therefore, the gentle drop in total clearance from 14.0 to 12.8 mL/min/kg has ample room for further reduction at hyperglycemia (> 2.8 mL/min/kg), which, if fully utilized, would translate to a satisfactory 28.6% of change. Figure 5-8 provides additional evidence confirming this conclusion, as an i.v. bolus simulation run on non-diabetic humans still showed a marked change when α-MM was added, suggesting an active CCM at low blood glucose (*cf*. Figure 5-3B). This result points the lack of PK modulation in humans to MR-mediated clearance remaining significant under hyperglycemic conditions, rather than a lack of which at euglycemia.

MK-2640 advanced to the clinical stage because of "30% decrease in clearance observed" in preclinical clamp studies (16,19). While the mediocre glucose-responsive behavior is predicted to be significantly enhanced when the human IM^{3}PACT model adopts the MR clearance capacity (k_{MR}) or the MR IC_{50} as in minipigs, both factors have to be combined to surpass the bar as seen in Figure 5-4G (33.3%). In other words, we conclude the underlying reasons for the failed PK

translation to be twofold: (i) the mannose receptors in humans were simply not sufficiently available or rapid for the MR-mediated portion to dominate total clearance, as Krug *et al.* suggested (16); and (ii) the concentrations able to switch on and off the competitive clearance mechanism fell out of the clinically relevant glycemic range.

5.5.2. Validating the Hypothesis of a Responsive Local PK

Upon observing the lack of a systemic modulation in MK-2640's clearance, Krug *et al.* posited a glucose- responsive PK change confined locally to the hepatic bed and splanchnic tissues (16). We hereby investigate this hypothesis by focusing on the mass balance of MK-2640 within the liver compartment (Figure 5-4H):

$$Q\left([\mathrm{GRI}]_{\mathrm{in}} - [\mathrm{GRI}]\right) = R_{\mathrm{ICL}}([\mathrm{GRI}]) + R_{\mathrm{MRCL}}([\mathrm{GRI}],\,[\mathrm{G}]) \tag{5-11}$$

where Q denotes the blood flowrate, $[\mathrm{GRI}]_{\mathrm{in}}$ and [GRI] the MK-2640 concentration entering and exiting the liver, and R_{ICL} the rate of intrinsic clearance mediated by IR. The dependence of R_{MRCL} on [GRI] and [G] is dictated by Equation 5-10 derived from MK-2640's mechanistic model. Naturally, the hepatic clearance (HCL), the volume of plasma cleared of MK-2640 per unit time in the pharmacological sense, can be extracted from the IM^{3}PACT simulations as:

$$\mathrm{HCL} = {R_{\mathrm{ICL}}}/{[\mathrm{GRI}]} + {R_{\mathrm{MRCL}}}/{[\mathrm{GRI}]} \tag{5-12}$$

which is presented in Figure 5-4I. Indeed as Krug and colleagues hypothesized, the hepatic clearance change between eu- and hyperglycemia is noticeably higher (18%) than that manifested in the systemic pool (13%). Almost the entirety of the responsiveness, as expected, is contributed by MR-mediated clearance, or the $R_{\mathrm{MRCL}}/[\mathrm{GRI}]$ term, which is 43% lower under hyperglycemic conditions compared to euglycemia. The large discrepancy between 43% and 18% is caused by the dominant contribution from intrinsic IR-mediated clearance, concurring the discussion of Figure 5-4F(ii) earlier. The sidelined role of MRCL in humans means that even the improved PK modulation within the liver is only modest in contrast to that previously observed in dogs and minipigs.

5.5.3. Visualizing the Glucose-GRI Landscape for Competitive Clearance

Besides confirming the hypothesis of a hepatic glucose-responsive PK, the local MK-2640 balance within the liver compartment additionally provides a dimensionless proxy, F_{MRCL}, for the extent of MR-mediated MK-2640 clearance, the landscape of which over [G] and [GRI] can be analytically mapped out without performing any numerical simulation. To start with, Equation 5-11 can be rearranged as:

$$\frac{\Delta[\mathrm{GRI}]}{[\mathrm{GRI}]} = \frac{R_{\mathrm{ICL}}}{Q[\mathrm{GRI}]} + \frac{R_{\mathrm{MRCL}}}{Q[\mathrm{GRI}]} = F_{\mathrm{ICL}} + F_{\mathrm{MRCL}} \tag{5-13}$$

where $\Delta[\mathrm{GRI}]$ is defined as $[\mathrm{GRI}]_{\mathrm{in}} - [\mathrm{GRI}]$. F_{MRCL} is defined as the MR-mediated contribution to $\Delta[\mathrm{GRI}]/[\mathrm{GRI}]$, which in turn represents the overall extent of MK-2640 elimination in the liver. Via the mechanistic model of MK-2640 in Equation 5-10, F_{MRCL} can be expressed as:

$$\begin{aligned} F_{\mathrm{MRCL}} &= \left\{ \frac{\Delta[\mathrm{GRI}]}{[\mathrm{GRI}]} \right\}_{\mathrm{MR}} = \frac{R_{\mathrm{GRI}}}{Q[\mathrm{GRI}]} \\ &= \frac{[\mathrm{GRI}]^{h_{\mathrm{GRI}}-1}}{K_{\mathrm{M}}(1 + K_{\mathrm{G}}[\mathrm{G}]^{h_{\mathrm{G}}}) + [\mathrm{GRI}]^{h_{\mathrm{GRI}}}} \cdot \frac{k_{\mathrm{MR}} V}{Q} \end{aligned} \tag{5-14}$$

As shown in Figure 5-4J, this analytical expression allows the F_{MRCL} landscape in minipigs and humans to be directly constructed as a function of the local glucose and MK-2640 concentrations. In contrast to the full-body IM^{3}PACT simulations performed in Figure 5-4F, G, and I, the F_{MRCL} landscapes are independent of specific clamp protocols and offers a straightforward visualization of the interplay between various levels of glucose and GRI. For example, the green curve traversing the human F_{MRCL} landscape in Figure 5-4J represents the escalating-dose clamp study in healthy human volunteers: the glucose concentration was kept constant at 80 mg/dL (4.4 mM), while the MK-2640 concentration varied from 0.08 to 68.62 nM. F_{MRCL} rises initially at lower GRI levels due to the cooperativity in binding, even more saliently so than in Figure 5-3G, before reaching a maximum and declining as the mannose receptors are saturated at high GRI concentrations.

The red curves along the F_{MRCL} surfaces in Figure 5-4J illustrate the proxy's utility by proving – in a qualitative but simulation-free manner – the previously identified root causes of the unsuccessful translation. They respectively represent the two-stage clamp protocol carried out in

diabetic humans and minipigs, which revealed PK changes between [G] = 90 and 300 mg/dL (5.0 and 16.7 mM). The interspecies disparity in the extent of PK modulation is evident, as F_{MRCL} shifts by more than 60 in minipigs and only approximately 30 in humans, hinting that the competitive clearance mechanism is significantly less responsive clinically. The first contributing factor is the generally depressed F_{MRCL} landscape in humans. For instance, the F_{MRCL} maxima over the selected [G] and [GRI] ranges are 47.2 for humans and 71.0 for minipigs. This is attributed to the lack of clearance capacity by MR in humans relative to preclinical animals, signified by a small k_{MR} in Equation 5-14 (see also Table 5-1). Second, while the F_{MRCL} progression in minipigs appears mostly linear, the noticeable curvature of tshat in humans marks a gradual descent instead. That is, the most glucose-sensitive linear section of the "S"-shaped response curve (see Figure 5-4E) is not fully utilized in humans. Both of these factors, directly visualized in the F_{MRCL} landscapes, agree with conclusions from our earlier quantitative full-body analyses (Figure 5-4F and G). Although the F_{MRCL} proxy does not take into consideration the intrinsic clearance rate (i.e., F_{ICL} in Equation 5-13), it already warns us of the GRI's diminished responsiveness in humans based on MK-2640 parameters and liver physiology alone, even before running comprehensive IM^{3}PACT simulations.

5.5.4. Exploring the GRI Design Space for Better-Performing Candidates

As the pattern of glucose binding to MRs as well as the MR distribution is intrinsic to the physiology, K_G, h_G, and k_{MR} are not considered design parameters of MK-2640 with room for adjustment. On the other hand, h_{GRI}, K_M, and the relative IR affinity of a competitive clearance GRI can be customized by, for instance, designing the linker and number of sugar molecules conjugated to the mannosylation site (17). Following the protocol previous reported (28), we scanned the GRI Design Space, or GRIDS, of MK-2640 in both humans and minipigs to identify the optimal combination of design parameters as well as the performance cap in each species. The objective function plotted in Figure 5-5A and B is the change in MK-2640's clearance between 90 and 300 mg/dL, exactly replicating the clinical trial design in diabetic individuals. For each combination of h_{GRI}, K_M, and IR affinity, we determined the ratio of MK-2640 and RHI doses corresponding to the half-maximum GIR. Identical to the clinical trial protocol, this "potency ratio" was used as a scaling factor to decide the IIR of the two-stage clamp. Since both the glucose-lowering effect and the intrinsic clearance are mediated by IR-binding, we assumed Λ_{IRC} scales with the IR affinity accordingly.

The simulation results in Figure 5-5A and B show a stark contrast: Over the selected parameter ranges, the best performing competitive clearance GRI records a mere 24% of PK change in humans, while the optimal GRI candidate in minipigs offers 73%. As shown in Figure 5-9, even over a set of expanded parameter ranges, the permitted space corresponding to a responsive clearance modulation of 30% and above is far larger in minipigs than in humans. This means that before we even consider whether the optimal parameter values identified are experimentally practical, the prospect of clinical translation is poor for MR-based competitive clearance GRIs. In other words, we predict that the variants of MK-2640 developed by the Merck team are unlikely to perform well in humans as well, in spite of their enhanced potency (17,18).

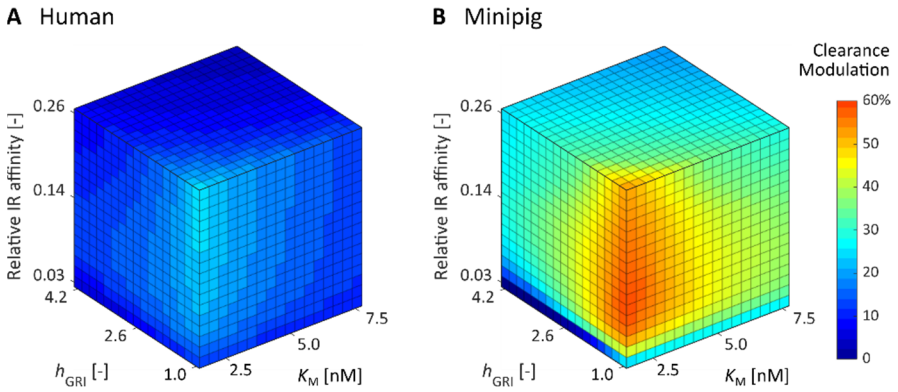

Figure 5-5. Simulated changes in clearance between eu- and hyperglycemic clamps at 90 and 300 mg/dL for competitive clearance GRI candidates spanning the entire design space. These MK-2640 derivatives are unlikely to be sufficiently responsive in humans (*A*) even with enhanced potency and optimized MR binding kinetics. In contrast, a much wider range of h_{GRI}, K_M, and relative IR affinity combinations is predicted to yield glucose-responsive PK in minipigs (*B*).

5.6. Outlook and Summary

The lack of glucose responsiveness revealed in clinical trials put a stop to MK-2640's development and destabilized the confidence in the rest of the CCM GRIs. Despite so, many have acknowledged the tremendous value of the clinical data as well as the overall workflow established by the Merck team. The use of mannoside antagonist as a mimic for hyperglycemic conditions was recognized by Hoeg-Jensen as an innovative development for *in vitro* investigations (22). The synergy between the iterative experimentation and modeling efforts throughout MK-2640's development resulted in streamlined preclinical and clinical studies as well as improved simulation tools (60). Now, via mechanistic modeling of MK-2640's glucose responsiveness and translational modeling

of the full-body physiology, we used the animal and clinical data to pinpoint the factors that challenged the translation, meanwhile obtaining critical and quantitative knowledge on the capacity and action of mannose receptors across species.

Availability of additional experimental data could address the limitations of this study. First, as already discussed, the attribute representative of the overall MR-mediated clearance capacity, k_{MR}, encompasses both the MR availability (θ_{tot}) as well as its specific rate of MK-2640 internalization (k_2). Decoupling of these two degrees-of-freedom would require *in vivo* or *in vitro* measurements additional to existing MR-mediated clearance rates, preferably isolating either the effect of k_2 or θ_{tot}. MRC1 gene expression data serve as one potential source of information on MR abundance and distribution. While the expression levels in humans and pigs have been reported, the inconsistent sequencing protocols render the cross-species comparability questionable (64–66). Furthermore, RNA and protein expression levels are only qualitative indicators of MRC1's activity and are therefore not the best sources for quantitative information we seek. Second, as Taylor and DiMarchi pointed out, it is of practical value to understand the impacts of interindividual variability given MK-2640's reliance on endogenous biological processes (27). While our investigations into population-averaged data and simulations are sufficient in identifying interspecies distinctions central to the GRI's clinical translation, future iterations of IM^{3}PACT could benefit from population statistics founded on systemically measured, individualized RHI and MK-2640 data in both animals and humans (67), ideally with a quality that parallels the clinical RHI dataset (68) upon which the acclaimed UVa/Padova model was established (69,70). An obvious starting point would be the MK-2640 clinical trial data from 36 healthy and 16 diabetic adults, although only a small subset of experimental results were made accessible and individualized in the publications (16). The glycemic clamp results were also subject to interferences from external conditions such as algorithms of the GIR feedback controller (71), and the steady-state readings may not be as informative to the mathematical model as a time-index concentration portrait.

In summary, we investigated the clinical translatability of competitive clearance GRIs via translational *in silico* modeling based on preclinical and clinical data of MK-2640 and RHI. We upgraded upon our previous platform with capabilities of simulating minipigs' glucoregulatory system as well as mechanistically describing the CCM scheme. The simulation results of our

parameterized model quantitatively match data from *in vitro* binding assays, intravenous boli, subcutaneous injections, and glycemic clamps. Expanding upon theories posited by the experimentalists, we identified and examined potential inter-species distinctions in GRI and mannose receptor properties that could have compromised the clinical translation of MK-2640. By running hypothetical clinical clamps with these MR properties varied one at a time, we concluded that the poor translatability was the consequence of a combination of insufficient clearance capacity in humans and also an *in vivo* competitiveness profile mismatched with the physiologically relevant glycemic range. Meanwhile, altered IR-mediated clearance, potency, and distribution volume of MK-2640 were found to be minimally relevant to the lack of a responsive PK in the clinic, despite them being key parameters to the design of CCM GRIs in general. We hope this study establishes the utility of *in silico* platforms like IM^{3}PACT in not just design optimization and translatability prediction (3,28,60), but also *a posteriori* analyses of preclinical and clinical data, from which quantitative, mechanistic inferences can be extracted beyond the explicit metrics. Such investigations should be an integral part of the drug development workflow, regardless of the trial outcome, as they channel the maximal value of an experimental study towards future therapeutics meaningful for patients. On a grander scale, IM^{3}PACT builds towards the new paradigm where computational tools take on a critical role in all stages of pharmaceutical research and development: from drug design, candidate screening, preclinical testing, to clinical development (3,28,60). Progressing hand-in-hand with experimentation, *in silico* tools accelerate, derisk, and optimize the experimental workflow, while at the same time improving iteratively via the additional data generated.

5.7. Appendix A: Mathematical Treatment of MK-2640's Reduced IR Affinity

The physiological model component of IM^{3}PACT was established for describing the interplay among glucose, glucagon, and regular human insulin (RHI). For the two-state GRI design studied in our previous work (28), the dormant form was assumed to be triggered by the presence of glucose to become the activated form indistinguishable from an endogenous RHI molecule. MK-2640, however, is known to be significantly less potent on the molecular scale relative to RHI due to its weak binding to insulin receptors. As briefly mentioned in Research Design and Methods,

we addressed this discrepancy by using an equivalent RHI concentration, $[\mathrm{RHI}]_{eq}$, in IM^{3}PACT simulation, scaled from the local MK-2640 concentration, [GRI]. Through the rigorous derivation below, we found the scaling factor to be exactly the ratio of RHI and GRI IC_{50} extracted from their respective IR-binding assays. These IC_{50} values should be distinguished from those obtained from the MR-binding assays where MK-2640 and glucose compete for mannose receptors. In an IR-binding assay, a generalized antagonist ("A") competes with radio-labelled RHI molecules ("I") for insulin receptors:

$$\theta + \mathrm{I} \underset{k_{-3}}{\overset{k_3}{\rightleftharpoons}} \theta_\mathrm{I} \xrightarrow{k_4} \theta + \mathrm{P} \tag{5-15}$$

$$\theta + \mathrm{A} \underset{k_{-5}}{\overset{k_5}{\rightleftharpoons}} \theta_\mathrm{A} \xrightarrow{k_4} \theta \tag{5-16}$$

The extent of competitive binding can be quantified by measuring the signal of P, the product derived from bound radio-labelled RHI. With the same quasi-steady-state assumption as in Equation 5-3, we derive:

$$\frac{d\theta_\mathrm{I}}{dt} = k_3\theta[\mathrm{I}] - \left(k_{-3} + k_4\right)\theta_\mathrm{I} = 0 \tag{5-17}$$

The same can be carried out for $d\theta_\mathrm{A}/dt$ based on Equation 5-16. We therefore relate the concentrations of free (θ), RHI-bound (θ_I), and antagonist-bound IR sites (θ_A) by:

$$\begin{cases} \theta_\mathrm{I} = \dfrac{k_3\theta[\mathrm{I}]}{k_{-3} + k_4} = \dfrac{\theta[\mathrm{I}]}{K_\mathrm{I}} \\ \theta_\mathrm{A} = \dfrac{k_5\theta[\mathrm{A}]}{k_{-5} + k_4} = \dfrac{\theta[\mathrm{A}]}{K_\mathrm{A}} \end{cases} \tag{5-18}$$

where $K_\mathrm{I} = (k_{-3} + k_4) / k_3$ and $K_\mathrm{A} = (k_{-5} + k_4) / k_5$. Given $\theta_\mathrm{I} + \theta_\mathrm{A} + \theta = \theta_{tot}$, we are able to obtain an expression for θ_I dependent only on known variables:

$$\theta_\mathrm{I} = \frac{\theta_{tot}[\mathrm{I}]}{[\mathrm{I}] + K_\mathrm{I}[\mathrm{A}]/K_\mathrm{A} + K_\mathrm{I}} \tag{5-19}$$

In a control experiment where the antagonist is absent, θ_I is obviously:

$$\theta_{\mathrm{I,\,max}} = \frac{\theta_{tot}[\mathrm{I}]}{[\mathrm{I}] + K_\mathrm{I}} \tag{5-20}$$

When $[\mathrm{A}] = [\mathrm{A}]_{IC50}$, therefore, θ_I is by definition half of $\theta_{\mathrm{I,\,max}}$:

$$\theta_{\mathrm{I,\,IC50}} = \frac{1}{2}\frac{\theta_{\mathrm{tot}}[\mathrm{I}]}{[\mathrm{I}]+K_{\mathrm{I}}} = \frac{\theta_{\mathrm{tot}}[\mathrm{I}]}{[\mathrm{I}]+K_{\mathrm{I}}[\mathrm{A}]_{\mathrm{IC50}}/K_{\mathrm{A}}+K_{\mathrm{I}}} \tag{5-21}$$

In other words,

$$[\mathrm{A}]_{\mathrm{IC50}} = \frac{K_{\mathrm{A}}}{K_{\mathrm{I}}}[\mathrm{I}]+K_{\mathrm{A}} \tag{5-22}$$

Since the derivation does not depend on specific antagonist used in the assay, the species A may represent either MK-2640 (the "GRI"), or simply RHI molecules which compete with their labelled counterparts. We derive the corresponding IC_{50} expressions from Equation 5-21:

$$[\mathrm{RHI}]_{\mathrm{IC50}} = [\mathrm{I}]+K_{\mathrm{I}} \tag{5-23}$$

$$[\mathrm{GRI}]_{\mathrm{IC50}} = \frac{K_{\mathrm{A}}}{K_{\mathrm{I}}}[\mathrm{I}]+K_{\mathrm{GRI}} \tag{5-24}$$

where K_{GRI} is the K_{A} for MK-2640. Incidentally, we notice the ratio of the IC_{50} values is exactly:

$$\frac{[\mathrm{RHI}]_{\mathrm{IC50}}}{[\mathrm{GRI}]_{\mathrm{IC50}}} = \frac{K_{\mathrm{I}}}{K_{\mathrm{GRI}}} \tag{5-25}$$

Since the glucose-lowering effect of insulin and MK-2640 takes place with bound IRs as an intermediary, we can define $[\mathrm{RHI}]_{\mathrm{eq}}$ as the concentration of RHI that yields the same θ_{I} as the θ_{GRI} resultant from a certain local MK-2640 level.

$$\theta_{\mathrm{GRI}} = \frac{[\mathrm{GRI}]}{K_{\mathrm{GRI}}}\theta = \frac{[\mathrm{RHI}]_{\mathrm{eq}}}{K_{\mathrm{I}}}\theta = \theta_{\mathrm{I}} \tag{5-26}$$

Therefore,

$$\begin{aligned}[\mathrm{RHI}]_{\mathrm{eq}} &= [\mathrm{GRI}]\frac{K_{\mathrm{I}}}{K_{\mathrm{GRI}}} \\ &= [\mathrm{GRI}]\frac{[\mathrm{RHI}]_{\mathrm{IC50}}}{[\mathrm{GRI}]_{\mathrm{IC50}}}\end{aligned} \tag{5-27}$$

given Equation 5-24. The simple yet exact relation in Equation 5-26 allows us to use the physiological model developed for RHI for MK-2640 simulation. The IR IC_{50} values for both RHI and MK-2640 have been experimentally determined *in vitro* for humans, minipigs, and dogs (19). When we used these respective *in vitro* IC_{50} as initial guesses for MK-2640's *in vivo* relative IR affinities (see Table 5-1), the parameterized values deviated very little from the *in vitro* ratios.

5.8. Appendix B: Supplementary Tables and Figures

Table 5-2. Physiological parameters for minipigs and humans based on *a priori* experimental measurements published in the literature or by the vendor.

	Physiological Parameter	Minipig	Human	Unit	Physiological Parameter	Rats	Mice	Unit
	Bodyweight	36	70	[kg]				
Volumes of Compartments[a]	$V^{G}_{brain,v}$	5.25E-1	1.69E-04	[dL]	V^{I}_{brain}	3.55E-2	1.21E-05	[L]
	$V^{G}_{brain,i}$	1.31E-1	1.07E-03					
	V^{G}_{heart}	5.83	5.79E-03		V^{I}_{heart}	2.95E-1	4.14E-04	
	V^{G}_{lungs}	8.62	1.78E-02		V^{I}_{lungs}	3.16E-1	6.86E-04	
	V^{G}_{gut}	6.13	8.26E-03		V^{I}_{gut}	5.31E-1	7.43E-04	
	$V^{G}_{kidneys}$	2.00	2.93E-03		$V^{I}_{kidneys}$	1.44E-1	2.43E-04	
	$V^{G}_{periphery,v}$	5.95	5.20E-03		$V^{I}_{periphery,v}$	4.03E-2	3.72E-04	
	$V^{G}_{periphery,i}$	2.69E1	1.62E-02		$V^{I}_{periphery,i}$	2.69	1.62E-03	
Blood Flow Rates[a]	Q^{G}_{brain}	1.97	8.88E-04	[dL/min]	Q^{I}_{brain}	1.33E-1	6.35E-05	[L/min]
	Q^{G}_{heart}	3.68E1	5.12E-02		Q^{I}_{heart}	2.49	3.66E-03	
	Q^{G}_{lungs}	1.01E1	1.73E-02		Q^{I}_{lungs}	6.85E-1	1.24E-03	
	Q^{G}_{gut}	8.85	1.47E-02		Q^{I}_{gut}	5.99E-1	1.05E-03	
	Q^{G}_{kidney}	6.56	9.21E-03		Q^{I}_{kidney}	4.44E-1	6.59E-04	
	$Q^{G}_{periphery}$	1.81E1	2.38E-02		$Q^{I}_{periphery}$	1.23	1.70E-03	
	$Q^{G}_{hepatic\ artery}$	1.27	2.66E-03		$Q^{I}_{hepatic\ artery}$	8.01E-2	1.91E-04	
	$Q_{muscle} / Q_{adipose}$	1.22[b]	2.74	[-]				
TDT[c]	$T^{G}_{periphery}$	4.0	5.0	[min]	$T^{I}_{periphery}$	1.6E1	2.0E1	[min]
	T^{G}_{brain}	1.7	2.1					

[a] Compartmental volumes used in the minipig model are based on systematic measurements done by Sinclair Bio Resources, LLC (46). Blood flow rates are based on haemodynamics measurements in Wyler *et al*. (47). Values

used in the human model are scaled 1.35-fold from those in Sorensen's original publication to match with the intrinsic RHI clearance rate observed in clinical trials (16,36).

[b] Based on the work of Suenderhauf and Parrott (72).

c TDT, the transcapillary diffusion time between the vascular and interstitial volumes, were scaled by body mass from the human models.

Table 5-3. Pharmacokinetic parameters for minipigs and humans. Estimated (*Est.*) and distinguishingly parameterized (*Dis.*; *i.e.* separately estimated for the healthy and diabetic populations) variables are marked by circles.

MINIPIGS							
			Diabetic	Healthy	Unit	Est.	Dis.
	R_{HGU}	=	$R_{HGU}^{basal} M_{HGU}^{G} M_{HGU}^{I}$		[mg/min]		
	R_{HGU}^{basal}	=	8.01		[mg/min]	○[a]	
Hepatic	M_{HGU}^{G}	=	$2.83 + 2.83\tanh\{1.60([G]_{L,n} - 1.48)\}$		[-]	○[b]	
Glucose	$\frac{dM_{HGU}^{I}}{dt}$	=	$(M_{HGU}^{I\infty} - M_{HGU}^{I}) / \tau_1$		[min^{-1}]		
Uptake	$M_{HGU}^{I\infty}$	=	$2.00\tanh(0.55[I]_{L,n})$		[-]		
	τ_1	=	25		[min]		
	R_{HGP}	=	$R_{HGP}^{basal} M_{HGP}^{G} M_{HGP}^{I} M_{HGP}^{\Gamma}$		[mg/min]		
	R_{HGP}^{basal}	=	$\sum_{k=H, P, B, RBC, G} R_{kGU}^{basal}$		[mg/min]		
	M_{HGP}^{G}	=	$1.02 - 0.02\tanh\{6.47([G]_{L,n} - 0.43)\}$	$1.19 - 1.27\tanh\{1.26([G]_{L,n} - 0.33)\}$	[-]	○[b]	○
Hepatic	$\frac{dM_{HGP}^{I}}{dt}$	=	$(M_{HGP}^{I\infty} - M_{HGP}^{I}) / \tau_1$		[min^{-1}]		
Glucose	$M_{HGP}^{I\infty}$	=	$1.01 - 0.16\tanh\{0.60([I]_{L,n} - 0.89)\}$		[-]	○	
Production	M_{HGP}^{Γ}	=	$M_{HGP}^{\Gamma 0} - f_2$		[-]		
	$M_{HGP}^{\Gamma 0}$	=	$\tanh\{19.12[\Gamma]_n\}$		[-]	○	
	df_2 / dt	=	$\{(M_{HGP}^{\Gamma 0} - 1) / 2 - f_2\} / \tau_2$		[min^{-1}]		
	τ_2	=	65		[min]		
	R_{PGU}	=	$R_{PGU}^{basal} M_{PGU}^{G} M_{PGU}^{I}$		[mg/min]		
Periphery	R_{PGU}^{basal}	=	42.88		[mg/min]	○[a]	
Glucose	M_{PGU}^{G}	=	$[G]_{P,i,n}$		[-]		
Uptake	M_{PGU}^{I}	=	$8.37 + 9.00\tanh\{0.29([I]_{P,i,n} - 4.99)\}$	$18.98 + 18.00\tanh\{0.80([I]_{P,i,n} - 5.66)\}$	[-]	○	○

Kidney Glucose Excretion[c]	R_{KGE}	=	$\begin{cases} 71+71\tanh[0.11([G]_{kidney}-460)] \\ \quad \text{if } 0 \le [G]_{kidney} < 460 \text{ mg dL}^{-1} \\ -330+0.872[G]_{kidney} \\ \quad \text{if } [G]_{kidney} > 460 \text{ mg dL}^{-1} \end{cases}$	[mg/min]		
Kidney Insulin Clearance	R_{KIC}	=	$F_{KIC} Q_K^I I_K$	[mU/min]		
	F_{KIC}	=	3.00E-1	[-]		
Liver Insulin Clearance	R_{LIC}	=	$F_{LIC}(Q^I_{adipose}[I]_{heart} + Q^I_{gut}[I]_{gut})$	[mU/min]		
	F_{LIC}	=	4.00E-1	[-]		
Muscle Insulin Clearance	R_{MIC}	=	$\frac{[I]_{muscle,i}}{\frac{1-F_{PIC}}{F_{PIC}}\frac{1}{Q^I_{muscle}} - \frac{T^I_{muscle}}{V^I_{muscle,i}}}$	[mU/min]		
	F_{PIC}	=	2.23E-2 4.21E-2	[-]	○	○
Adipose Insulin Clearance	R_{AIC}	=	$\frac{[I]_{adipose,i}}{\frac{1-F_{PIC}}{F_{PIC}}\frac{1}{Q^I_{adipose}} - \frac{T^I_{adipose}}{V^I_{adipose,i}}}$	[mU/min]		
Brain Glucose Uptake	R_{BGU}	=	2.94[c]	[mg/min]		
Red Blood Cell Glucose Uptake	R_{RBCU}	=	4.91[c]	[mg/min]		
Gut Glucose Uptake	R_{GGU}	=	27.08	[mg/min]	○[a]	
Subcutaneous Insulin Absorption[d]	$R_{SIA,adipose,i}$	=	$k_{abs}[I_{dm}]_{depot}$	[mU/L/min]		
	$\frac{d[I_{dm}]}{dt}$	=	$k_{h/dm}[I_{hex}] - (k_{abs}+k_{loss})[I_{dm}]$	[mU/L/min]		
	$\frac{d[I_{hex}]}{dt}$	=	$-(k_{h/dm}+k_{loss})[I_{hex}]$	[mU/L/min]		
	RHI k_{abs}	=	4.90E-3	[min^{-1}]	○	
	RHI $k_{h/dm}$	=	1.40E-2	[min^{-1}]	○	
	k_{loss}	=	$3D_{inj}(3V_{inj}/4\pi)^{-2/3}$	[min^{-1}]		
	D_{inj}	=	9.00E-5	[cm^2/min]		
Parameters Specific to MK-2640[e]	K_G	=	6.8E-3	[mM$^{-h_G}$]	○[f]	
	h_G	=	2.5	[-]	○[f]	
	K_M	=	3.0[g]	[nM]		
	h_{GRI}	=	1.5	[-]	○[f]	
	GRI k_{abs}	=	4.40E-3	[min^{-1}]	○[h]	
	GRI $k_{h/dm}$	=	1.40E-2	[min^{-1}]	○[h]	

HUMAN						
			Diabetic	Healthy	Unit	
Hepatic Glucose Uptake	R_{HGU}	=	$R_{HGU}^{basal} M_{HGU}^{G} M_{HGU}^{I}$		[mg/min]	
	R_{HGU}^{basal}	=	20		[mg/min]	
	M_{HGU}^{G}	=	$-1.02 + 2.26\tanh\{4.80([G]_{L,n} - 0.70)\}$	$5.66 + 5.66\tanh\{2.44([G]_{L,n} - 1.48)\}$	[-]	○[i]
	$\frac{dM_{HGU}^{I}}{dt}$	=	$(M_{HGU}^{I\infty} - M_{HGU}^{I}) / \tau_1$		[min^{-1}]	
	$M_{HGU}^{I\infty}$	=	$2\tanh(0.55[I]_{L,n})$		[-]	
	τ_1	=	25		[min]	
Hepatic Glucose Production	R_{HGP}	=	$R_{HGP}^{basal} M_{HGP}^{G} M_{HGP}^{I} M_{HGP}^{\Gamma}$		[mg/min]	
	R_{HGP}^{basal}	=	$\sum_{k=H,\,P,\,B,\,RBC,\,G} R_{kGU}^{basal}$		[mg/min]	
	M_{HGP}^{G}	=	$1.42 - 1.41\tanh\{0.62([G]_{L,n} - 0.50)\}$		[-]	
	$\frac{dM_{HGP}^{I}}{dt}$	=	$R_{HGP}^{basal} M_{HGP}^{G} M_{HGP}^{I} M_{HGP}^{\Gamma}$		[min^{-1}]	
	$M_{HGP}^{I\infty}$	=	$1.21 - 1.14\tanh\{1.66([I]_{L,n} - 0.89)\}$		[-]	
	M_{HGP}^{Γ}	=	$M_{HGP}^{\Gamma 0} - f_2$		[-]	
	$M_{HGP}^{\Gamma 0}$	=	$2.7\tanh\{0.39[\Gamma]_n\}$		[-]	
	df_2 / dt	=	$\{(M_{HGP}^{\Gamma 0} - 1) / 2 - f_2\} / \tau_2$		[min^{-1}]	
	τ_2	=	65		[min]	
Periphery Glucose Uptake	R_{PGU}	=	$R_{PGU}^{basal} M_{PGU}^{G} M_{PGU}^{I}$		[mg/min]	
	R_{PGU}^{basal}	=	40		[mg/min]	
	M_{PGU}^{G}	=	$[G]_{P,i,n}$		[-]	
	M_{PGU}^{I}	=	$7.03 + 6.52\tanh\{0.34([I]_{P,i,n} - 5.82)\}$	$11.00 + 16.96\tanh\{0.07([I]_{P,i,n} - 10.84)\}$	[-]	○[i]
Kidney Glucose Excretion	R_{KGE}	=	$\begin{cases} 71 + 71\tanh[0.11([G]_{kidney} - 460)] & \text{if } 0 \le [G]_{kidney} < 460\ \text{mg dL}^{-1} \\ -330 + 0.872[G]_{kidney} & \text{if } [G]_{kidney} > 460\ \text{mg dL}^{-1} \end{cases}$		[mg/min]	
Kidney Insulin Clearance	R_{KIC}	=	$F_{KIC} Q_K^I I_K$		[mU/min]	
	F_{KIC}	=	3.00E-1		[-]	
Liver Insulin Clearance	R_{LIC}	=	$F_{LIC}(Q_{adipose}^{I}[I]_{heart} + Q_{gut}^{I}[I]_{gut})$		[mU/min]	
	F_{LIC}	=	4.00E-1		[-]	

Muscle Insulin Clearance	R_{MIC}	=	$\frac{[\mathrm{I}]_{\mathrm{muscle,i}}}{\frac{1-F_{PIC}}{F_{PIC}}\frac{1}{Q^{\mathrm{I}}_{\mathrm{muscle}}}-\frac{T^{\mathrm{I}}_{\mathrm{muscle}}}{V^{\mathrm{I}}_{\mathrm{muscle,i}}}}$	[mU/min]	
	F_{PIC}	=	1.50E-1	[-]	
Adipose Insulin Clearance	R_{AIC}	=	$\frac{[\mathrm{I}]_{\mathrm{adipose,i}}}{\frac{1-F_{PIC}}{F_{PIC}}\frac{1}{Q^{\mathrm{I}}_{\mathrm{adipose}}}-\frac{T^{\mathrm{I}}_{\mathrm{adipose}}}{V^{\mathrm{I}}_{\mathrm{adipose,i}}}}$	[mU/min]	
Brain Glucose Uptake	R_{BGU}	=	70	[mg/min]	
Red Blood Cell Glucose Uptake	R_{RBCU}	=	10	[mg/min]	
Gut Glucose Uptake	R_{GGU}	=	20	[mg/min]	
Subcutaneous Insulin Absorption[d]	$R_{\mathrm{SIA,adipose,i}}$	=	$k_{\mathrm{abs}}[\mathrm{I}_{\mathrm{dm}}]_{\mathrm{depot}}$	[mU/L/min]	
	$\frac{d[\mathrm{I}_{\mathrm{dm}}]}{dt}$	=	$k_{\mathrm{h/dm}}[\mathrm{I}_{\mathrm{hex}}]-(k_{\mathrm{abs}}+k_{\mathrm{loss}})[\mathrm{I}_{\mathrm{dm}}]$	[mU/L/min]	
	$\frac{d[\mathrm{I}_{\mathrm{hex}}]}{dt}$	=	$-(k_{\mathrm{h/dm}}+k_{\mathrm{loss}})[\mathrm{I}_{\mathrm{hex}}]$	[mU/L/min]	
	RHI k_{abs}	=	8.90E-03	[min^{-1}]	
	$k_{\mathrm{h/dm}}$	=	5.65E-02	[min^{-1}]	
	k_{loss}	=	$3D_{\mathrm{inj}}(3V_{\mathrm{inj}}/4\pi)^{-2/3}$	[min^{-1}]	
	D_{inj}	=	9.00E-5	[cm^2/min]	
Parameters Specific to MK-2640[e, j]	K_{G}	=	1.1E-3	[$\mathrm{mM}^{-h_{\mathrm{G}}}$]	○[f]
	h_{G}	=	2.5	[-]	○[f]
	K_{M}	=	3.4[g]	[nM]	
	h_{GRI}	=	1.5	[-]	○[f]

[a] Estimated from literature-based initial guesses (38,48,50).

[b] $[\mathrm{G}]_{k,\mathrm{n}}$,$[\mathrm{I}]_{k,\mathrm{n}}$, and $[\Gamma]_{\mathrm{n}}$ denote glucose, insulin, and glucagon concentrations normalized by the steady state levels, where k denotes the corresponding compartment. Naturally, all multipliers (M) should assume a value of 1 for a normalized concentration of 1.

[c] Based on measurements previously reported in the literature (49,73).

[d] Simulation of the subcutaneous injection depot follows the work by Bakh *et al.* (29), which in turn was based on Wong *et al.* (40,41). This model assumes an equilibrium between hexameric insulin and dimeric/monomeric insulins. The latter are absorbed from the injection depot into circulation at a rate dictated by k_{abs}.

[e] Excluding the parameter values already shown in Table 5-1 of the Main Text.

[f] See Research Design and Methods.

[g] Directly measured experimentally by Kaarsholm *et al*. (19).

[h] MK-2640's subcutaneous injection rate constants in minipigs were estimated from the diabetic subcutaneous injection data reported in Kaarsholm *et al*. (19).

[i] Expressions of M^{G}_{HGU} in diabetic humans and M^{I}_{PGU} in non-diabetic humans were adjusted to match the clinical results. Previously in the original Sorensen report (36), M^{G}_{HGU} was only parameterized with measurements on healthy individuals and M^{I}_{PGU}, diabetic patients. Their respective application to diabetic and healthy humans, therefore, called for refinement with the most recent data with matching health conditions.

[j] MK-2640's k_{abs} and $k_{h/dm}$ in humans are unavailable since no subcutaneous clinical data were published.

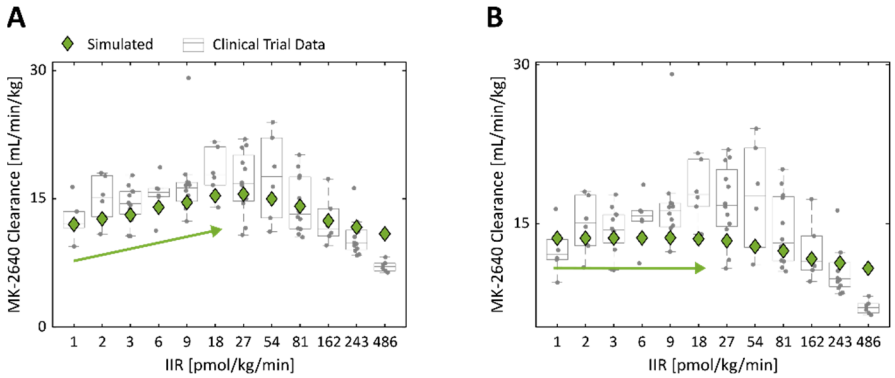

Figure 5-6. A cooperative Hill coefficient hGRI is necessary to capture the initial rise in MK-2640 clearance at lower IIRs as reported in Trial 1 clamp study of MK-2640 (16). This is evident by contrasting the simulated clearances with $h_{GRI} = 1.5$ (*A*) and $h_{GRI} = 1$ (*B*). In both panels, $h = 2.537$ and $K_M = 3.4$. K_G was adjusted to 1.41E-2 in panel *B* to match the *in vitro* inhibition curve. The arrows serve as guides for the eye.

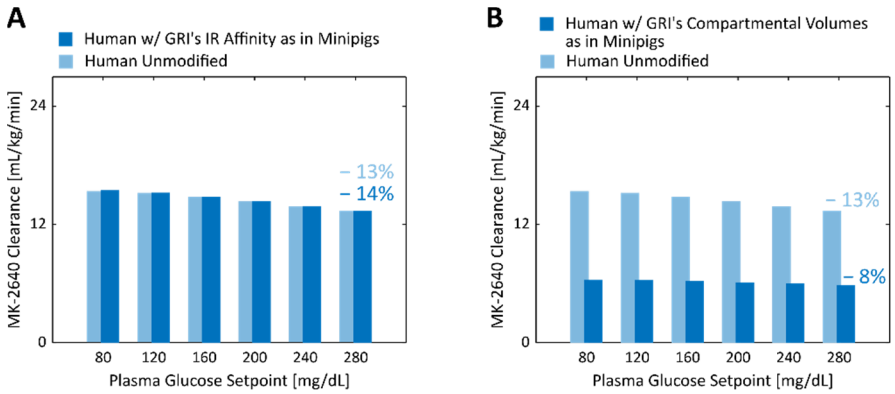

Figure 5-7. MK-2640 parameters found to not have contributed to the clinical underperformance despite their significant interspecies differences in minipigs and humans (*cf*. Figure 5-4F, G, also see Table 5-1). *A*: A modulation of 14% was observed if the same MK-2640 IR affinity was simulated in humans as in minipigs, which was a minimal

improvement from the base case (13%). *B*: If MK-2640's compartmental volumes in minipigs were used for the human physiological model, the change in GRI clearance would be even worse (8%) than the base case scenario.

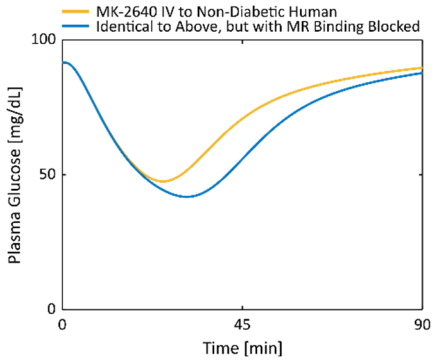

Figure 5-8. Simulated plasma glucose response to an intravenous dose of MK-2640 in a non-diabetic human, with (yellow) and without (blue) competitive clearance by MR. While the difference between the two scenarios is smaller than in a non-diabetic minipig (see Figure 5-3B), it was evident that MR-mediated clearance was not completely shut off under eu- and hypoglycemic conditions in humans. The MK-2640 dose was selected to be 4.85nmol/kg, scaled from the RHI dose of 0.17nmol/kg (19) by the same factor used in the clinical trial (16).

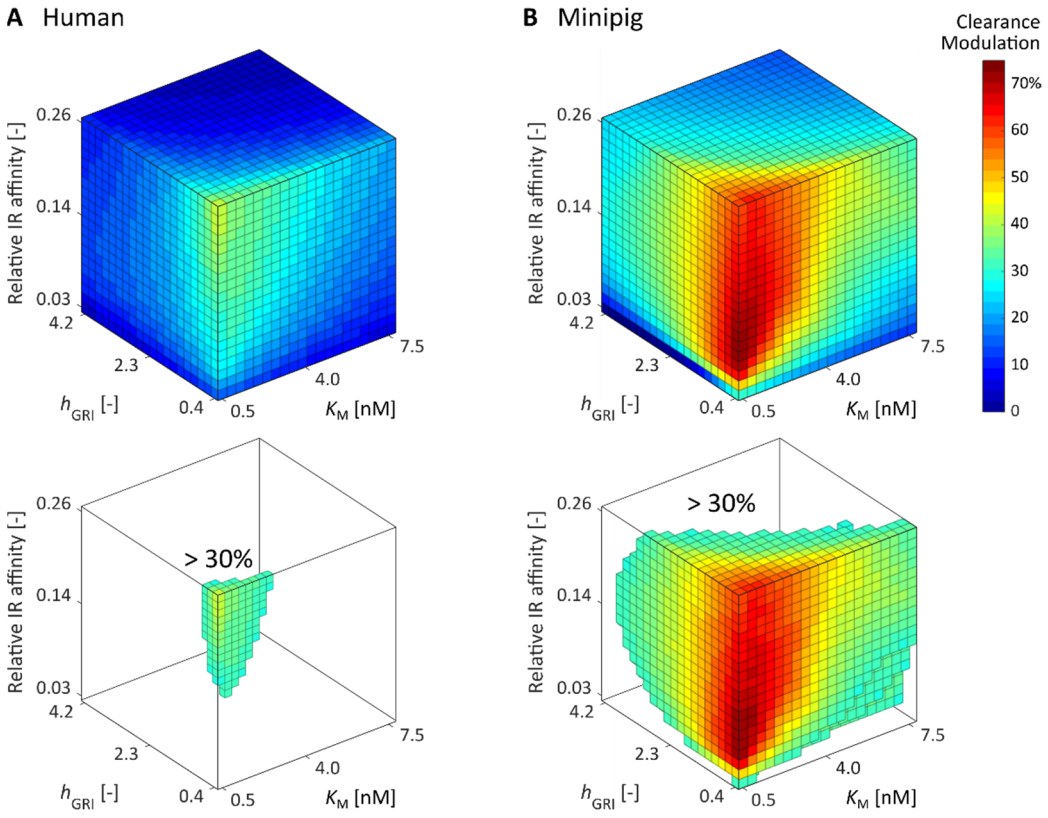

Figure 5-9. Simulated changes in clearance between eu- and hyperglycemic clamps at 90 and 300 mg/dL for competitive clearance GRI candidates spanning a design space expanded from that in Figure 5-5. Even with wider

parameter ranges, only a minimal set of parameter combinations translates to a clearance modulation above 30% in humans (*A*), in stark contrast to the minipig simulations (*B*).

5.9. References

1. Webber MJ, Anderson DG. Smart approaches to glucose-responsive drug delivery. J Drug Target. 2015;23(7–8):651–5.

2. VandenBerg MA, Webber MJ. Biologically inspired and chemically derived methods for glucose-responsive insulin therapy. Adv Healthc Mater. 2019 Jan 3;1801466:1801466.

3. Bakh NA, Cortinas AB, Weiss MA, Langer RS, Anderson DG, Gu Z, et al. Glucose-responsive insulin by molecular and physical design. Nat Chem. 2017;9(10):937–43.

4. Satin LS, Soleimanpour SA, Walker EM. New aspects of diabetes research and therapeutic development. Pharmacol Rev. 2021;73(3):1001–15.

5. Vettoretti M, Facchinetti A. Combining continuous glucose monitoring and insulin pumps to automatically tune the basal insulin infusion in diabetes therapy: A review. Biomed Eng Online [Internet]. 2019;18(1):1–17. Available from: https://doi.org/10.1186/s12938-019-0658-x

6. Pickup JC. Management of diabetes mellitus: Is the pump mightier than the pen? Nat Rev Endocrinol. 2012;8(7):425–33.

7. Chen Z, Wang J, Sun W, Archibong E, Kahkoska AR, Zhang X, et al. Synthetic beta cells for fusion-mediated dynamic insulin secretion. Nat Chem Biol. 2018;14(1):86–93.

8. Matsumoto A, Tanaka M, Matsumoto H, Ochi K, Moro-Oka Y, Kuwata H, et al. Synthetic “smart gel” provides glucose-responsive insulin delivery in diabetic mice. Sci Adv. 2017;3(11):1–13.

9. Yu J, Wang J, Zhang Y, Chen G, Mao W, Ye Y, et al. Glucose-responsive insulin patch for the regulation of blood glucose in mice and minipigs. Nat Biomed Eng [Internet]. 2020;1–8. Available from: http://www.nature.com/articles/s41551-019-0508-y

10. Chou DHC, Webber MJ, Tang BC, Lin AB, Thapa LS, Deng D, et al. Glucose-responsive insulin activity by covalent modification with aliphatic phenylboronic acid conjugates. Proceedings of the National Academy of Sciences. 2015;112(8):2401–6.

11. Chen YS, Gleaton J, Yang Y, Dhayalan B, Phillips NB, Liu Y, et al. Insertion of a synthetic switch into insulin provides metabolite-dependent regulation of hormone–receptor activation. Proc Natl Acad Sci U S A. 2021;118(30):1–12.

12. Wang J, Yu J, Zhang Y, Kahkoska AR, Wang Z, Fang J, et al. Glucose transporter inhibitor-conjugated insulin mitigates hypoglycemia. Proc Natl Acad Sci U S A. 2019;166(22):10744–8.

13. Zaykov AN, Mayer JP, DiMarchi RD. Pursuit of a perfect insulin. Nat Rev Drug Discov. 2016 Jun 18;15(6):425–39.

14. Wang J, Wang Z, Yu J, Kahkoska AR, Buse JB, Gu Z. Glucose-responsive insulin and delivery systems: Innovation and translation. Advanced Materials [Internet]. 2019 Aug 18;1902004:1902004. Available from: https://onlinelibrary.wiley.com/doi/abs/10.1002/adma.201902004

15. Jarosinski MA, Dhayalan B, Rege N, Chatterjee D, Weiss MA. 'Smart' insulin-delivery technologies and intrinsic glucose-responsive insulin analogues. Diabetologia. 2021 May 12;64(5):1016–29.

16. Krug AW, Visser SAG, Tsai K, Kandala B, Fancourt C, Thornton B, et al. Clinical evaluation of MK-2640: An insulin analog with glucose-responsive properties. Clin Pharmacol Ther. 2019 Feb 30;105(2):417–25.

17. Yang R, Wu M, Lin S, Nargund RP, Li X, Kelly T, et al. A glucose-responsive insulin therapy protects animals against hypoglycemia. JCI Insight. 2018;3(1).

18. Moore MC, Kelley DE, Camacho RC, Zafian P, Ye T, Lin S, et al. Superior glycemic control with a glucose-responsive insulin analog: Hepatic and nonhepatic impacts. Diabetes. 2018;67(6):1173–81.

19. Kaarsholm NC, Lin S, Yan L, Kelly T, van Heek M, Mu J, et al. Engineering glucose responsiveness into insulin. Diabetes. 2018;67(2):299–308.

20. Zion TC, Lancaster TC. Conjugate based systems for controlled drug delivery. WO2010088294, 2010.

21. Brownlee M, Cerami A. A glucose-controlled insulin-delivery system: Semisynthetic insulin bound to lectin. Science (1979). 1979 Dec 7;206(4423):1190–1.

22. Hoeg-Jensen T. Review: Glucose-sensitive insulin. Mol Metab [Internet]. 2021;46(October 2020):101107. Available from: https://doi.org/10.1016/j.molmet.2020.101107

23. Burroughs E, Fancort C, Dykstra K, Visser SAG. A model-based meta-analysis of insulin PK-PD in glucose clamp studies of diabetes mellitus type 1 and non-diabetic human subjects. J Pharmacokinet Pharmacodyn. 2015;(42).

24. Kandala B, Fancourt C, Cho C, Carballo-Jane E, Zafian P, Bergstrand M, et al. Translational modeling of minipig and dog glucose and insulin data accurately predicts human insulin action for MK2640 but not its glucose-responsive pharmacokinetics. Clin Pharmacol Ther. 2018;103:S71.

25. Fancourt C, Campos-Nanez E, Breton M, Riddle S, Kongable G, Crutchlow M, et al. Using T1DMS simulation for the conceptualization and design of clinical clamp studies in the development of modified insulin therapeutic agents. Part 1 – Regular Human Insulin (RHI). In: 17th Annual Diabetes Technology Meeting. Rockville, MD; 207AD.

26. Cho C, Campos-Nanez E, Breton M, Riddle S, Kongable G, Fancourt C, et al. Using T1DMS simulation for the conceptualization and design of clinical clamp studies in the development of modified insulin therapeutic agents: Part II – MK-2640. 2019.

27. Taylor SI, DiMarchi RD. Smarter modeling to enable a smarter insulin. Diabetes. 2020;69(August):1608–10.

28. Yang JF, Gong X, Bakh NA, Carr K, Phillips NFB, Ismail-Beigi F, et al. Connecting rodent and human pharmacokinetic models for the design and translation of glucose-responsive insulin. Diabetes [Internet]. 2020 Aug 9;69(8):1815–26. Available from: http://diabetes.diabetesjournals.org/lookup/doi/10.2337/db19-0879

29. Bakh NA, Bisker G, Lee MA, Gong X, Strano MS. Rational design of glucose-responsive insulin using pharmacokinetic modeling. Adv Healthc Mater. 2017;6(22):1–10.

30. Bisker G, Iverson NM, Ahn J, Strano MS. A pharmacokinetic model of a tissue implantable insulin sensor. Adv Healthc Mater. 2015;4(1):87–97.

31. Berg JM, Tymoczko JT, Stryer L. Biochemistry. 5th ed. Biochemistry. New York, NY; 2002.

32. Stefan MI, Le Novère N. Cooperative binding. Wodak S, editor. PLoS Comput Biol. 2013 Jun 27;9(6):e1003106.

33. Michaelis L, Menten ML. Die Kinetik der Invertinwirkung. Biochem Z. 1913;49:333–69.

34. Cortés A, Cascante M, Cárdenas ML, Cornish-Bowden A. Relationships between inhibition constants, inhibitor concentrations for 50% inhibition and types of inhibition: New ways of analysing data. Biochemical Journal. 2001 Jul 1;357(1):263.

35. Distefano A, Antonio Zingale G, Grasso G. An SPR-based method for Hill coefficient measurements: The case of insulin-degrading enzyme. Anal Bioanal Chem [Internet]. 2022;4793–802. Available from: https://doi.org/10.1007/s00216-022-04122-3

36. Sorensen JT. A physiologic model of glucose metabolism in man and its use to design and assess improved insulin therapies for diabetes. Massachusetts Institute of Technology; 1985.

37. Panunzi S, Pompa M, Borri A, Piemonte V, de Gaetano A. A revised Sorensen model: Simulating glycemic and insulinemic response to oral and intra-venous glucose load. PLoS One [Internet]. 2020;15(8):1–30. Available from: http://dx.doi.org/10.1371/journal.pone.0237215

38. Lunze K, Woitok A, Walter M, Brendel MD, Afify M, Tolba R, et al. Analysis and modelling of glucose metabolism in diabetic Göttingen minipigs. Biomed Signal Process Control [Internet]. 2014;13(1):132–41. Available from: http://dx.doi.org/10.1016/j.bspc.2014.04.003

39. Vahidi O, Kwok KE, Gopaluni RB, Knop FK. A comprehensive compartmental model of blood glucose regulation for healthy and type 2 diabetic subjects. Med Biol Eng Comput. 2016;54(9):1383–98.

40. Wong J, Chase JG, Hann CE, Shaw GM, Lotz TF, Lin J, et al. A subcutaneous insulin pharmacokinetic model for computer simulation in a diabetes decision support role: Model structure and parameter identification. J Diabetes Sci Technol. 2008;2(4):658–71.

41. Wong J, Chase JG, Hann CE, Shaw GM, Lotz TF, Lin J, et al. A subcutaneous insulin pharmacokinetic model for computer simulation in a diabetes decision support role: Validation and simulation. J Diabetes Sci Technol. 2008 Jul;2(4):672–80.

42. Flessner MF. The transport barrier in intraperitoneal therapy. American Journal of Physiology-Renal Physiology. 2005;288(3):F433–42.

43. Lehmann ED, Deutsch T. A physiological model of glucose-insulin interaction in type 1 diabetes mellitus. J Biomed Eng. 1992;14(3):235–42.

44. Hovorka R, Chassin LJ, Ellmerer M, Plank J, Wilinska ME. A simulation model of glucose regulation in the critically ill. Physiol Meas. 2008;29(8):959–78.

45. Silber HE, Jauslin PM, Frey N, Gieschke R, Simonsson USH, Karlsson MO. An integrated model for glucose and insulin regulation in healthy volunteers and type 2 diabetic patients following intravenous glucose provocations. J Clin Pharmacol. 2007;47(9):1159–71.

46. Brown LD, Liu J, Shoemake C, Brocksmith D, Trickey J, Teel A. Miniature Swine Book of Normal Data. 2019.

47. Wyler F, Käslin M, Hof R, Beglinger R, Becker M, Stadler G, et al. Das Göttinger Miniaturschwein als Versuchstier - 5. Mitteilung: Das Herzminutenvolumen, seine prozentuale Verteilung auf den Organismus und die effektive Organdurchblutung. Research in Experimental Medicine [Internet]. 1979 Feb;175(3):31–6. Available from: http://link.springer.com/10.1007/BF01851231

48. Chandrasena LG, Fettman MJ, Hand MS. Endotoxin dose. II. Effects on glucose biokinetics in Yucatan minipigs. Am J Physiol Endocrinol Metab. 1983;7(4).

49. Sanguinetti E, Liistro T, Mainardi M, Pardini S, Salvadori PA, Vannucci A, et al. Maternal high-fat feeding leads to alterations of brain glucose metabolism in the offspring:

positron emission tomography study in a porcine model. Diabetologia. 2016;59(4):813–21.

50. Muller MJ, Paschen U, Seitz HJ. Glucose production measured by tracer and balance data in conscious miniature pig. American Journal of Physiology-Endocrinology and Metabolism [Internet]. 1983 Mar 1;244(3):E236–44. Available from: https://www.physiology.org/doi/10.1152/ajpendo.1983.244.3.E236

51. Zhu JY, Dittmeyer R, Hofmann H. Application of sensitivity analysis to the reduction of a complex kinetic model for the homogeneous oxidative coupling of methane. Chemical Engineering and Processing. 1993;32(3):167–76.

52. Dickinson RP, Gelinas RJ. Sensitivity analysis of ordinary differential equation systems-A direct method. J Comput Phys. 1976;21(2):123–43.

53. Schaller S, Willmann S, Lippert J, Schaupp L, Pieber TR, Schuppert A, et al. A generic integrated physiologically based whole-body model of the glucose insulin-glucagon regulatory system. CPT Pharmacometrics Syst Pharmacol. 2013;2(8).

54. Schaller S, Lippert J, Schaupp L, Pieber TR, Schuppert A, Eissing T. Robust PBPK/PD-based model predictive control of blood glucose. IEEE Trans Biomed Eng. 2016 Jul;63(7):1492–504.

55. Ribel U, Hougaard P, Drejer K, Sorensen AR. Equivalent in vivo biological activity of insulin analogues and human insulin despite different in vitro potencies. Diabetes. 1990;39(9):1033–9.

56. Greenblatt DJ, Abernethy DR, Divoll M. Is volume of distribution at steady state a meaningful kinetic variable? The Journal of Clinical Pharmacology. 1983 Aug 9;23(8–9):391–400.

57. Ahmed TA. Pharmacokinetics of drugs following IV bolus, IV infusion, and oral administration. In: Ahmed TA, editor. Basic Pharmacokinetic Concepts and Some Clinical Applications. InTech; 2015.

58. DeFronzo RA, Tobin JD, Andres R. Glucose clamp technique: A method for quantifying insulin secretion and resistance. American Journal of Physiology-Endocrinology and Metabolism. 1979 Sep 1;237(3):E214.

59. DeFronzo RA, Ferrannini E. Regulation of intermediary metabolism during fasting and feeding. In: Jameson JL, de Groot LJ, editors. Endocrinology: Adult and Pediatric [Internet]. Seventh Ed. Elsevier; 2016. Available from: http://dx.doi.org/10.1016/B978-0-323-18907-1.00035-4

60. Visser SAG, Kandala B, Fancourt C, Krug AW, Cho CR. A model-informed drug discovery and development (MID3) strategy for the novel glucose-responsive insulin MK-2640 enabled rapid decision making. Clin Pharmacol Ther. 2019;0(0).

61. Yki-Jarvinen H, Young AA, Lamkin C, Foley JE. Kinetics of glucose disposal in whole body and across the forearm in man. Journal of Clinical Investigation. 1987;79(6):1713–9.

62. McCready DR, Balch CM, Fidler IJ, Murray JL. Lack of comparability between binding of monoclonal antibodies to melanoma cells in vitro and localization in vivo. J Natl Cancer Inst. 1989;81(9):682–7.

63. Berk DA, Yuan F, Leunig M, Jain RK. Direct in vivo measurement of targeted binding in a human tumor xenograft. Proc Natl Acad Sci U S A. 1997;94(5):1785–90.

64. Fagerberg L, Hallström BM, Oksvold P, Kampf C, Djureinovic D, Odeberg J, et al. Analysis of the human tissue-specific expression by genome-wide integration of transcriptomics and antibody-based proteomics. Molecular and Cellular Proteomics [Internet]. 2014 Feb;13(2):397–406. Available from: https://linkinghub.elsevier.com/retrieve/pii/S1535947620346338

65. Duff MO, Olson S, Wei X, Garrett SC, Osman A, Bolisetty M, et al. Genome-wide identification of zero nucleotide recursive splicing in Drosophila. Nature [Internet]. 2015 May 13;521(7552):376–9. Available from: http://www.nature.com/articles/nature14475

66. Li M, Chen L, Tian S, Lin Y, Tang Q, Zhou X, et al. Comprehensive variation discovery and recovery of missing sequence in the pig genome using multiple de novo assemblies.

Genome Res [Internet]. 2017 May;27(5):865–74. Available from: http://genome.cshlp.org/lookup/doi/10.1101/gr.207456.116

67. Cobelli C, Dalla Man C. Minimal and maximal models to quantitate glucose metabolism: Tools to measure, to simulate and to run in silico clinical trials. J Diabetes Sci Technol [Internet]. 2021 May 25;7:193229682110152. Available from: http://journals.sagepub.com/doi/10.1177/19322968211015268

68. Basu R, Man CD, Campioni M, Basu A, Klee G, Toffolo G, et al. Effects of age and sex on postprandial glucose metabolism differences in glucose turnover, insulin secretion, insulin action, and hepatic insulin extraction. Diabetes. 2006;55(7):2001–14.

69. Dalla Man C, Rizza RA, Cobelli C. Meal simulation model of the glucose-insulin system. IEEE Trans Biomed Eng. 2007 Oct;54(10):1740–9.

70. Dalla Man C, Micheletto F, Lv D, Breton M, Kovatchev B, Cobelli C. The UVA/PADOVA type 1 diabetes simulator: New features. J Diabetes Sci Technol. 2014;8(1):26–34.

71. Benesch C, Kuhlenkötter M, Nosek L, Heise T. New clamp-PID algorithm for automated glucose clamps improves clamp quality. J Diabetes Sci Technol. 2022;16(2):408–14.

72. Suenderhauf C, Parrott N. A physiologically based pharmacokinetic model of the minipig: Data compilation and model implementation. Pharm Res. 2013;30(1):1–15.

73. Murphy JR. Erythrocyte metabolism. II. Glucose metabolism and pathways. J Lab Clin Med. 1960 Feb;55:286–302.

CHAPTER 6

Emergent low-frequency self-oscillation in the microscale and its application as an autonomous oscillatory microgenerator

This chapter has been adapted from:

Jing Fan Yang, Thomas A. Berrueta*, Allan M. Brooks, Albert Tianxiang Liu, Ge Zhang, David Gonzalez-Medrano, Sungyun Yang, Volodymyr B. Koman, Pavel Chvykov, Lexy N. LeMar, Marc Z. Miskin, Todd D. Murphey, and Michael S. Strano. 2022. "Emergent Microrobotic Oscillators via Asymmetry-Induced Order." arXiv: 2205.09814. Nature Communications.*

(Equal contribution)*

6.1. Abstract

Spontaneous low-frequency oscillations on the order of several hertz are the drivers of many crucial processes in nature. From bacterial swimming to mammal gaits, the conversion of static energy inputs into slowly oscillating electrical and mechanical power is key to the autonomy of organisms across scales. However, the fabrication of slow artificial oscillators at micrometre scales remains a major roadblock towards the development of fully-autonomous microrobot. Here, we study a low-frequency relaxation oscillator that emerges from the interactions of a simple collective of active microparticles at the air-liquid interface of a hydrogen peroxide drop. Their collective oscillations form chemomechanical and electrochemical limit cycles that enable the transduction of ambient chemical energy into periodic mechanical motion and on-board electrical currents. Surprisingly, the collective can oscillate robustly even as more particles are introduced, but only when we add a single particle with modified reactivity to intentionally break the system's permutation symmetry. We explain such emergent order through the discovery of a thermodynamic mechanism for asymmetry-induced order. The energy harvested from the stabilized oscillations enables the use of on-board electronic components, which we demonstrate by cyclically and synchronously driving a microrobotic arm. This work highlights a new strategy for achieving low-frequency oscillations at the microscale that are otherwise difficult to observe outside of natural systems, paving the way for future microrobotic autonomy.

6.2. Introduction

The ability to produce low-frequency oscillations is central to the autonomy of living beings, and is essential to key biological processes such as heartbeats, neuron firings, breathing, and locomotion (1–3). While complex electronics operate at ever-increasing clock rates of many gigahertz, the frequency of many important biological oscillations seldom exceeds 100Hz. The slow rate of these oscillations stems from a need to be commensurate with both the energy budget and the natural timescales of underlying biological processes, as in the transport of CO2 in plants (4) and in the galloping of horses (5). Unlike oscillations arising from external periodic forcing (6–9), these self-oscillations emerge spontaneously from the balancing of competing dynamical processes driving systems away from equilibrium (10–12) – a signature of living systems (13). In artificial microsystems, however, the production of slow self-sufficient self-oscillations is counterintuitively difficult (14, 15). Generating self-sustaining mechanical scillations at the microscale typically requires the transduction of complex chemical oscillators (e.g., Belousov-Zhabotinsky reaction (16)) into periodic changes to a system's physical configuration (8, 17–21). Alternative mechanisms for producing self-sufficient mechanical oscillations based on carefully designed dynamic coupling between responsive elastic materials and thermal (12, 22), chemical (11, 12, 23), or moisture stimuli (24) have typically been demonstrated in millimetre-scale (and larger) devices. In contrast, generating slow periodic electrical signals remains prohibitively challenging aboard untethered microscale devices (§6.7), given the limited downward scalability of capacitors and inductors (25, 26), as well as the power and footprint demands of CMOS oscillators, frequency dividers, and energy modules (27–29). Despite these challenges, recent progress has shown that self-sustaining electrical oscillations can be produced by modulating electrical resistance with mechanical feedback loops in carefully designed devices, presenting a promising mechanism for sub-500μm electrical self-oscillators (14). In this work, instead of relying on complex chemistries, integrated electronics, or elaborate mechanical microstructures, we produce robust electromechanical oscillations aboard a collective of deceptively simple microparticles by exploiting the self-organized properties of their far-from-equilibrium dynamics. By breaking the permutation symmetry of a homogeneous particle collective situated at an air-liquid interface, we reliably control their dynamics to realize simultaneous chemomechanical and electrochemical periodic energy transduction. We achieve this by introducing a particle with an

enhanced reaction rate, whose stabilizing effect on the system behaviour we analyze through the lens of asymmetry-induced order. In turn, through a simple bimetallic on-board fuel cell design, we transduce the system's self-oscillations into periodic electrical work to power state-of-the-art microrobotic components, without the need for batteries or external sources of energy.

6.3. Emergent Low-Frequency Oscillation

Figure 6-1 presents a system of simple microparticles where low frequency chemomechanical self-oscillations emerge from the coupling of otherwise self-limiting catalytic reactions easily trapped at equilibrium. Figure 6-1a shows that each of these microparticles, composed of nothing more than a nanometre-thick Pt patch of radius 125μm microfabricated beneath a polymeric microdisc, generates a gas bubble when placed at the curved air-liquid interface of a H_2O_2 drop via

$$H_2O_2 \xrightarrow{Pt} H_2O + 1/2\,O_2 \uparrow \tag{6-1}$$

This well-studied catalytic reaction has been a long-time favourite in both micro- (30–33) and macroscopic robotics (12, 34), noted for the fuel's high energy density and simple chemistry (34). For a single microparticle situated at the interface, the chemical reaction in Figure 6-1a is self-limiting as the bubble grows and gradually blocks off the fuel's access to the catalyst. Consequently, the single-particle system reaches its equilibrium state promptly: The microparticle remains motionless for a prolonged time (Figure 6-1d) and the bubble asymptotically reaches a terminal radius without rupture (Figure 6-1c). However, a drastic change occurs when a second identical particle is introduced to the system. Figure 6-1b shows that as the microparticles enter each other's proximity, the separately-formed gas bubbles merge. The freed-up catalytic surface area then disrupts the self-limiting chemistry, destabilizing the original single-particle steady state. This allows the merged bubble to grow beyond its threshold, leading to its rupture (Figure 6-1e, t = 3.2s). The collapse imparts an impulse onto the microparticles and propels them in opposite directions, at which point the particles are drawn back towards one another by the restorational forces: First, the radial component of buoyancy, $\mathbf{F}_g$, globally directs the particles towards the apex of the concave air-liquid interface (9). Second, the local interfacial deformations result in a mutual attractive capillary force $\mathbf{F}_c$, affectionately known as the "Cheerios effect" (35, 36). The combination of this Cheerios effect and catalytic bubble generation has been observed to produce repetitive back-and-forth motion (37, 38) in swarms of tubular swimmers (39, 40). All of these

factors sum up to a repeatable cycle of mutual approach, contact, bubble merger, and bubble collapse that we refer to as particle beating (Figure 6-1e). The robustness of this self-sustained cycle is evidenced by the tracked coordinates of the two particles over a course of 280s (Figure 6-1f), which contrast the single particle scenario where practically no motion was observed. Notably, while the central challenge in self-oscillatory systems is to keep them away from equilibria (11, 15), such states are virtually eliminated from our system by the effectively instantaneous nature of bubble collapse.

We monitored the oscillatory behaviour of the system by tracking its breathing radius $r(t)$ over time, defined as:

$$r(t) = \frac{1}{N}\sum_{i=1}^{N}\sqrt{(x_i(t)-\bar{x})^2 + (y_i(t)-\bar{y})^2} \tag{6-2}$$

for a collection of N particles each with coordinate $(x_i(t), y_i(t))$ at time t. In other words, $r(t)$ is the Euclidean distance from the collective's centroid $(\bar{x}, \bar{y})$ to each particle, averaged over all particles (see annotations in Figure 6-1e). The system's periodic beating is evident in the time evolution of $r(t)$ (Figure 6-1g, left panel), the limit cycle of its $r(t)$ phase portrait (Figure 6-1h, Methods), as well as the narrow peak in the recurrence time histogram (Figure 6-1i, Methods). Taken together, these analyses serve as conclusive evidence of the long-term stability of system oscillations. The analysis in Figure 6-1i shows a period of 3.2s for the two-particle system in 10.7wt% H_2O_2, consistent with Figure 6-1g. The period remains constant throughout as revealed by the moving-window recurrence analyses (Methods), since a negligible 0.02% of the fuel is consumed over 280s based on stoichiometry. We developed a mechanistic model based on calculated $\mathbf{F}_g$, $\mathbf{F}_c$, and the non-Stokesian drag force $\mathbf{F}_d$ (§7), and found that it captured even the detailed dynamics of the breathing radius' time evolution (Figure 6-1g right panel, also Figure 7-2). We verified the consistency of the beating frequency across 8 sets of independent experiments with 10.7wt% H_2O_2 in Figure 6-1j. Additionally, the beating frequency's dependence on H_2O_2 concentrations points to a mechanism for exerting fine control over the beating frequency, as predicted by our mechanistic model based on a Langmuir-Hinshelwood kinetics of the catalytic surface (Figure 6-1j) (41, 42).

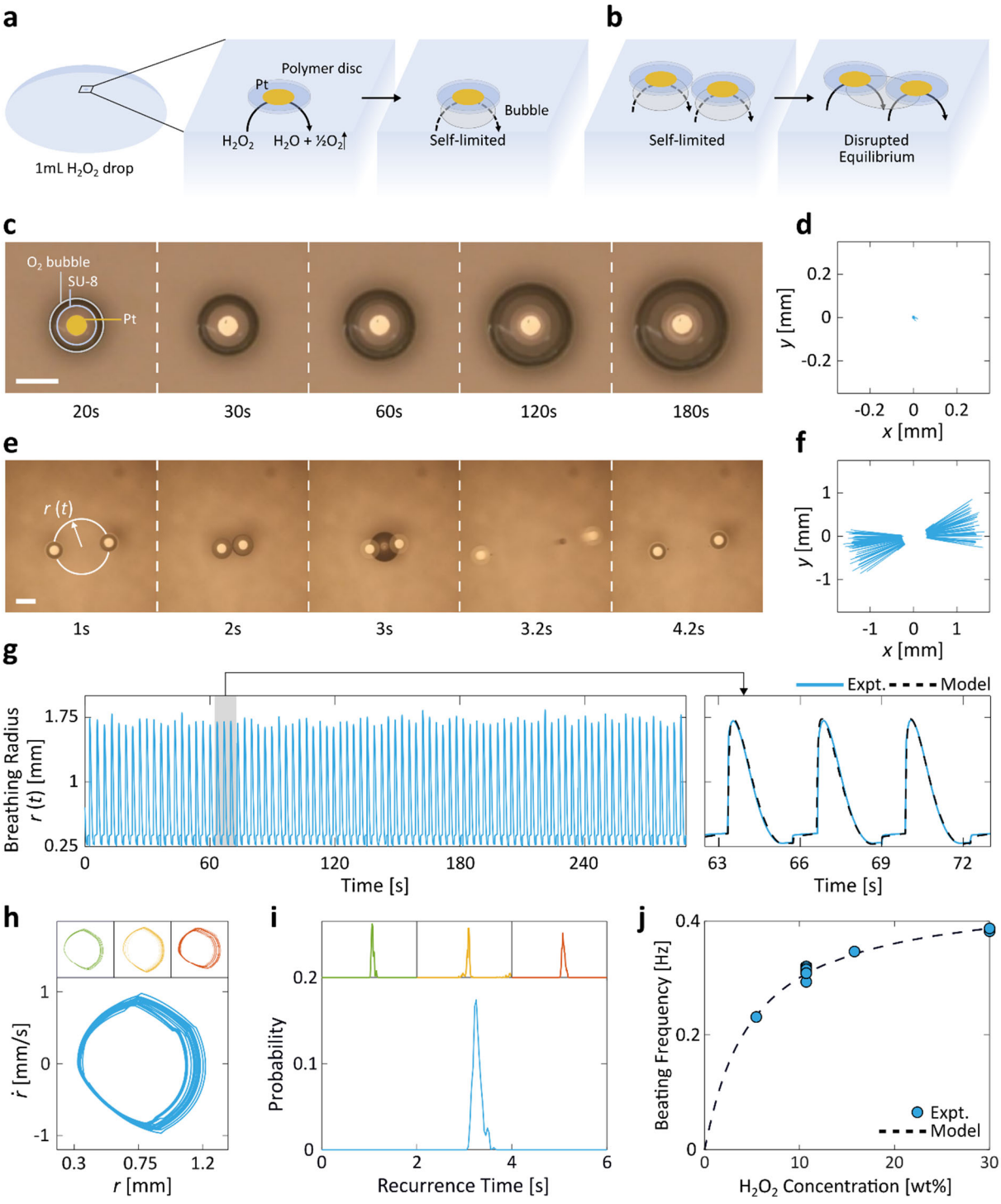

Figure 6-1. Emergence of chemomechanical microparticle self-oscillation. a, Schematic of a self-limited system of a single particle resting still at the air-liquid interface of a H2O2 drop. The particle is composed of a catalytic patch of Pt (yellow) underneath a polymeric disc (blue). The O2 formation slows down asymptotically over time as the gas bubble restricts the available catalytic surface area. b, A 2-particle system, in contrast, exhibits an emergent and self-sustained beating behaviour as the bubble merger restores the previously hindered reactivity, thus disrupting the

equilibrium state. c,d, Micrograph sequence (c) and tracked particle coordinates (d) of a 1-particle system that remains still for an extended period of time. e,f, Micrograph sequence (e) and tracked coordinates (f) of a 2-particle system with emergent beating. The breathing radius, r(t), is the distance from the collective's centroid to each particle, averaged over all particles. g, The long-term breathing radius trajectory of the same system as in (e) and (f) demonstrates the robustness of the beating behaviour. The shaded portion is magnified in the right panel, where the mechanistic model simulations (black, §7) are shown to match the experimental curve (blue). h, The phase portraits of 4 independent 2-particle experiments demonstrate reproducible limit cycles with closed-loop orbits, confirming the periodicity of collective beating. Note that to calculate the phase portraits the system's bubble-driven discontinuities were processed through a standard finite-impulse response filter (see Methods). All phase portraits share the same axes. i, The recurrence histograms of the same 4 experiments all display a narrow peak centred at a period of 3.2s, consistent with visual evidence in (e). All histograms share the same axes. j, The beating frequency can be tuned with the concentration of H2O2. The dependence predicted by the mechanistic simulations on the basis of a Langmuir-Hinshelwood kinetics (black curve) matches the experimental measurements (blue markers). Scale bars, 500μm.

6.4. Persistent Periodicity via Symmetry-Breaking

Our findings in Figures 6-2 and 6-3 show that the stable emergent self-oscillation can be extended well beyond $N = 2$, although curiously only when the system's permutation symmetry is broken and not in a homogeneous system of identical particles. We extracted the bubble burst interarrival time statistics by tracking the time that transpires between each pair of consecutive bursts in recorded experiments (Figure 6-2a). In homogeneous systems of identical particles (Figure 6-2b), we show that the likelihood of periodic beating dwindles gradually with rising particle counts N, reflected in the progressive decay in the sharpness and amplitude of the initial 3.2s peak corresponding to periodic beating. The decay of collective periodicity is accompanied by an increase in the probability mass of frequent and unpredictable bubble bursts taking place less than a second from one another—a result of bubble mergers and collapses among subsets of particles (see representative $N = 5$ and 8 micrographs in Figure 6-2b). Interestingly, we find that the interarrival time distributions of systems beyond $N = 7$ become statistically indistinguishable from those of a Poisson process (Figure 6-2b, bottom panel) (43). This shows that our system's phenomenology can remarkably vary from coordinated and reliable periodic beating to independent and effectively stochastic bubble bursts merely as a function of N. The breathing radius trajectory in Figure 6-2c confirms the loss of periodicity, as no structure can be discerned from the noisy low-amplitude fluctuations.

The gradual transition towards aperiodicity in Figures 6-2b and c points to the nominal fragility of periodic beating as the system size increases. Reasoning that the deliberate introduction of heterogeneity has been shown to produce asymmetry-induced order (44) in complex networked systems (45–47), we investigated the effect of permutation symmetry-breaking on the robustness of particle beating across system sizes. Based on the role buoyancy plays in the beating physics (§7), we hypothesized that particles could be made dynamically distinct from one another by controlling the relative size of their accompanying bubble. We tested the impact of this heterogeneity on collective order with Rattling Theory (48, 49). This thermodynamic theory explains the way in which correlations among driven degrees of freedom give rise to system-level fluctuations that govern the long-term stability of system configurations. The magnitude of these fluctuations, as quantified by Rattling $\mathscr{R}$, serves as an index describing the system's degree of

disorder. Since lowering $\mathscr{R}$ requires substantial correlations among degrees of freedom, systems in low-$\mathscr{R}$ configurations often exhibit emergent order.

We constructed a theoretical model that analytically connects a bubble's relative size with its contribution to system-level fluctuations, and in turn collective order. The model's predictions in Figure 6-2d suggest that any deviation in a single particle's bubble size relative to the rest of the ensemble (i.e., with relative burst intensity away from 1x) results in a more orderly system as quantified by lower $\mathscr{R}$. Interestingly, the reduction in $\mathscr{R}$ is found to be particularly significant when a bubble larger (and stronger) than its peers is introduced, which we confirmed with experiments. We note that this novel mechanism for asymmetry-induced order applies to a broad class of complex systems wherein parametric heterogeneities control the fluctuations of strongly interacting elements.

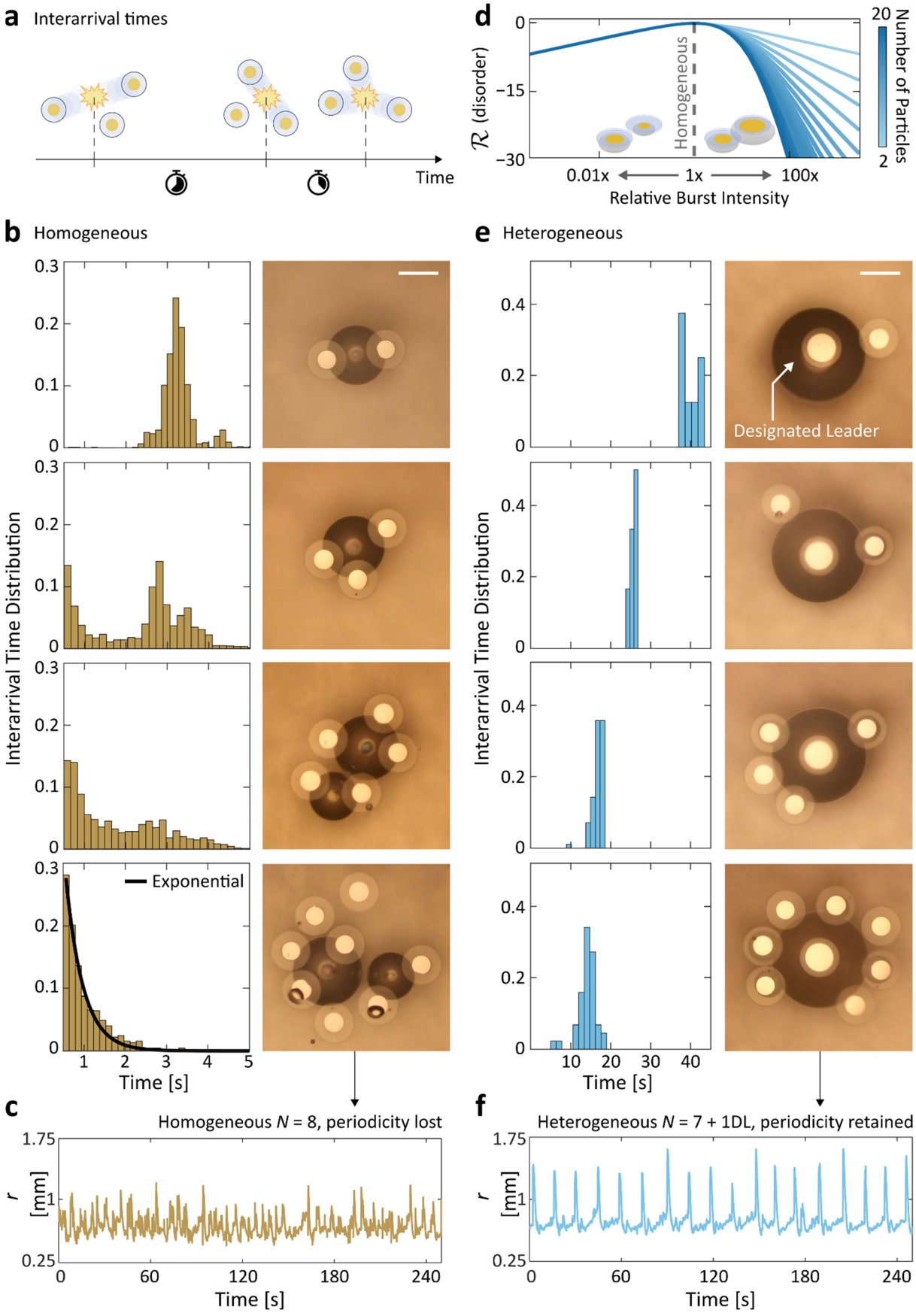
a
Interarrival times
Time
d
0
−15
−30
$\mathcal{R}$ (disorder)
Homogeneous
20
2
Number of Particles
0.01x
1x
100x
Relative Burst Intensity
b
Homogeneous
Interarrival Time Distribution
0.3
0.2
0.1
0
Exponential
1
2
3
4
5
Time [s]
e
Heterogeneous
0.4
0.2
0
Designated Leader
10
20
30
40
Time [s]
c
Homogeneous N = 8, periodicity lost
r [mm]
1.75
1
0.25
0
60
120
180
240
Time [s]
f
Heterogeneous N = 7 + 1DL, periodicity retained
r [mm]
1.75
1
0.25
0
60
120
180
240
Time [s]

Figure 6-2: Observations of emergent order via symmetry-breaking. a, Schematic of interarrival times in a system of beating microparticles, defined as the time that transpires between two consecutive bubble collapses. The interarrival time distribution should be tight (i.e., a single peak) in a perfectly periodic system, and broad in an aperiodic system. b, (top to bottom) Interarrival time distributions and optical micrographs for homogeneous systems of N = 2, 3, 5, and 8 identical particles. As N increases, the collective system periodicity gradually decays and transitions to an exponential interarrival distribution at N = 8 (bottom, black curve). Scale bar, 500μm. c, Indeed, we observe that the breathing radius of a homogeneous N = 8 system is not periodic. d, Asymmetry-induced order across N predicted by Rattling Theory. A quantification of collective disorder, the system's Rattling $\mathscr{R}$ is predicted to be lower (i.e. more orderly) if the relative burst intensity of one particle is increased beyond or decreased below 1x, which signifies homogeneity. This is experimentally realized by modulating the Pt patch size on a "designated leader" (DL) particle relative to the others. The curves are offset to make all $\mathscr{R}$ = 0 at 1x intensity to highlight the effect of system heterogeneity on Rattling. e, Same as (b), but for heterogeneous systems of equal particle numbers, where the DL broke the permutation symmetry. In contrast to the homogeneous systems (b), they remain robustly periodic across N. It is important to recognize that the polymeric disc size of a DL is unchanged. Scale bar, 500μm. f, Breathing radius for an 8-particle DL system (i.e., N = 7 + 1DL), which reliably beats periodically. The period of 14.2s extracted from r(t) coincides with the most probable interarrival time in (e, bottom).

We broke the permutation-symmetry of the original system experimentally by adding a "designated leader" (DL) particle with an enlarged Pt patch of radius 175μm (Figure 6-2e). Note that since the nanometre-scale thickness of the Pt layer is negligible compared to that of the unchanged 10μm-thick polymeric microdisc, the DL design does not alter the particle's volumetric geometry. However, the heterogeneity among the catalytic surface areas translates directly to unequal bubble growth rates between the DL and its neighbours, which in turn drastically affects their collective dynamics in accordance with our theoretical predictions in Figure 6-2d: We observe robustly periodic bubble collapses across N in the sharp peaks of the interarrival distributions in Figure 6-2e, suggesting that DLs are able to sustain the periodicity of particle beating even at high particle counts. Figure 6-2f depicts the time evolution of the breathing radius for a system of $N = 7 + 1$DL particles. In contrast to the homogeneous $N = 8$ system (Figure 6-2c), the heterogeneous DL system exhibits a stable long-term self-oscillation with a period of 14.2s, owing to the broken permutation symmetry.

Figures 6-3a(i-vii) and b(i-vii) explain the microscale physics arising from the intentionally broken symmetry. When a DL particle with an enlarged Pt patch is paired with a non-DL particle, the heterogeneity in bubble sizes leads to the subsumption of the non-DL particle bubble into the DL bubble upon contact (Figures 6-3a(ii-v) and b(ii-v)). This coalescence behaviour is distinct from that of equal-sized bubbles previously shown in Figure 6-1b, where an unstable merged bubble forms halfway between the particles. Instead, the merged bubble sticks to the former location of the large parent bubble underneath the DL particle, seen in Figures 6-3a(iii) and (v). This behaviour falls under the sticking bubble regime in the literature, a phenomenon long observed in experiments (50, 51) but only recently thoroughly studied and theorized in a catalytic H_2O_2 bubble system (52). Importantly, contrary to the more intuitive moving bubble regime where the merged bubble sits at the centre of mass of its parents (53, 54), the coalescence behaviour transitions into the sticking regime only as the parent bubbles differ sufficiently in size (52), or, in other words, with sufficient particle heterogeneity. As shown in the rest of Figures 6-3a and b, the two particles in the system undergo several rounds of small-scale bubble coalescence, eventually causing the DL bubble to collapse. We find that the bubble's rupture radius is approximately 1.7 times larger than that for a homogeneous system shown in Figure 6-1f, stabilized by the particle sitting directly on top. This contributes to an even lower-frequency chemomechanical oscillation (Figures 6-2f and 6-3f) than that previously observed in homogeneous systems (Figure 6-1i and 6-2c).

Figures 6-3c and d contrasts the breathing radius phase portraits between homogeneous and heterogeneous systems of different *N*. We observe that the homogeneous systems experience a decay of periodicity evidenced by the gradual collapse of limit cycle orbits in its phase portraits as a function of *N*, consistent with trends in Figure 6-2b. In contrast, the heterogeneous systems' limit cycles are robust to variations in *N*, retaining their closed-loop phase-space orbits. To rigorously quantify the effect that DLs have on collective periodicity, we analysed the recurrence structure of the dynamical trajectories across system sizes (see Methods) (55). As sketched in Figure 6-3e, recurrence analyses capture the dynamical properties of system behaviours by measuring the time the system takes to return to a given state's neighbourhood. The set of all such time intervals is compiled into a recurrence histogram (Figure 6-3f) whose recurrence entropy can be used to quantify the complexity of dynamical trajectories (56), with perfect periodicity corresponding to zero entropy. The linear entropy increase for homogeneous systems as a function of *N* (Figure 6-3g) corresponds to the increasing disorder in the system's recurrences that is consistent with the progressive loss of periodicity observed in Figures 6-2c and 6-3c. Also in accordance with earlier qualitative trends in Figures 6-2f and 6-3d, the recurrence entropy of the DL system is locally invariant to changes in *N*, thereby providing quantitative evidence of the robustness of the periodic beating induced via symmetry-breaking. While we find that the system's invariance to particle number holds up to $N = 11$, we leave the study of larger particle systems for future work.

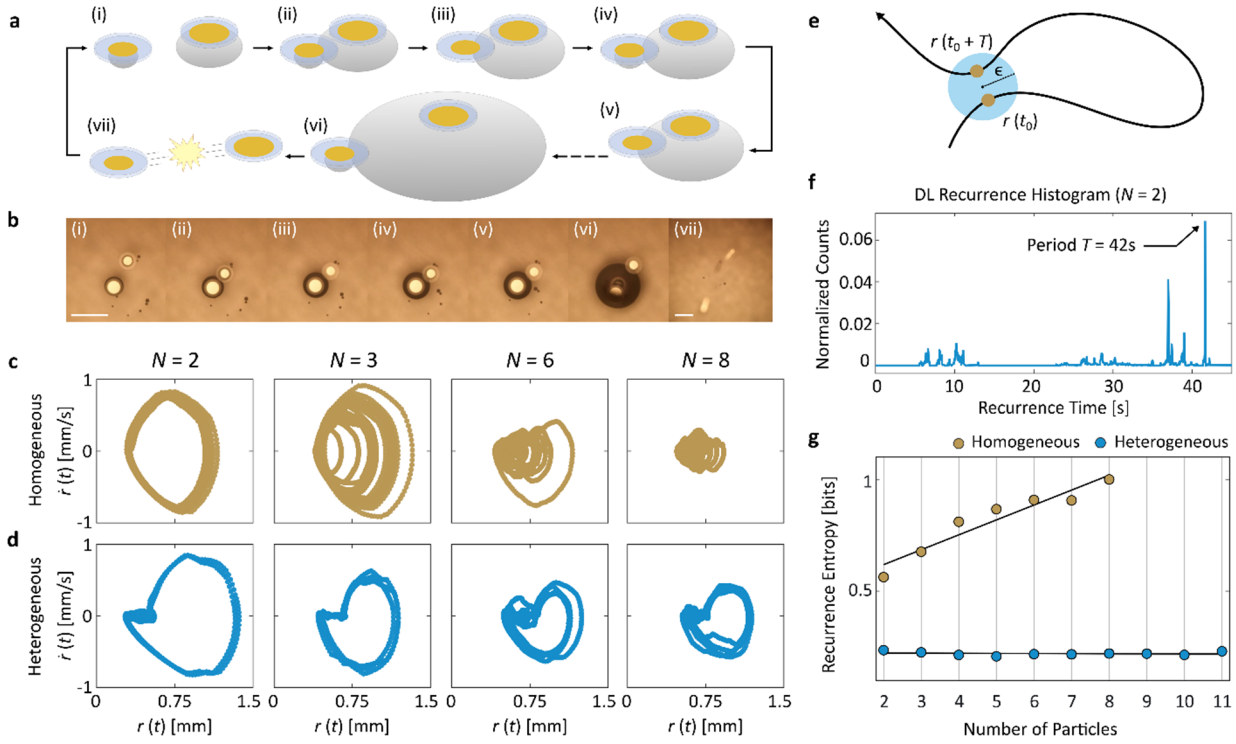

Figure 6-3: Designated leaders induce periodic limit cycles. a,b, Features of DL beating explained with schematic (a) and micrograph sequence (b) of a 2-particle heterogeneous system. The leader particle is able to grow a large bubble promptly and subsume the smaller bubbles of neighbouring particles across several rounds of bubble coalescence. Scale bars, 1mm. c,d, Phase portraits of homogeneous (c) and heterogeneous (d) systems of $N = 2$, 3, 6, and 8. Only the latter is able to maintain the closed-loop orbits at high particle counts. e, Schematic of recurrence time calculation. The recurrence time is the time it takes to return from a given system configuration to the neighborhood of said configuration (see Methods). f, Recurrence histogram compiling all of the recurrence times observed across experiments of the 2-particle heterogeneous system ($N = 1 + 1$DL). g, Recurrence entropy as a function of N for both homogeneous (yellow) and heterogeneous/DL (blue) systems. Low recurrence entropy is a quantitative indicator of periodic behaviour. The homogeneous system's recurrence entropy trends upward, suggesting a decay in periodicity, while the DL system's entropy remains low in accordance with its observed periodicity even at high N.

6.5. Self-Oscillating Microgenerators

Through a simple modification to the particle design, we are able to harness the robust chemomechanical beating to generate an oscillatory electric signal. As illustrated in Figure 6-4a and b, we fabricated particles with a Pt pattern closely lined up with (though spatially separate from) an additional metal patch of either Au or Ru (see Methods). With the bimetallic design, the previously auto-redox catalytic decomposition of H2O2 on Pt is in part separated into an oxidation half-reaction on Pt and a reduction half-reaction on Ru (Au) (30, 31, 57):

$$\text{Pt: } H_2O_2 \rightarrow O_2 + 2H^+ + 2e^- \tag{6-2}$$

$$\text{Ru (Au): } H_2O_2 + 2H^+ + 2e^- \rightarrow 2H_2O \tag{6-3}$$

$$\text{Overall: } 2H_2O_2 \rightarrow 2H_2O + O_2 \tag{6-4}$$

Consequently, a potential difference is established at the two electrodes that essentially transforms the particle into an on-board fuel cell. These same principles have been previously used to generate voltages in nanomotors, where bimetallic rods and nanoparticles are propelled electrokinetically by the accompanying electric field (58–60). A micrograph of our fabricated prototype is displayed in Figure 6-4b. Note that the metallic leads extending outwards were added to facilitate electrical characterization of the devices and are not necessary to their operation. The leads were passivated and hence do not participate in any electrochemical reactions. The Pt-Ru and Pt-Au fuel cell devices measured open-circuit voltages of 144.9mV ± 2.4 and 21.4mV ± 3.5, respectively, in a 25.8wt% H_2O_2 solution with 0.075M KNO_3 added for conductivity (see Methods). These values are in line with prior mechanistic studies (30, 31) (§6.8). Under the same conditions, the Pt-Ru fuel cell delivers a short-circuit current density of 1.71mA/cm^2 ± 0.38 and a current of 56.7nA ± 12.4. As a benchmark, a significantly larger 1.5 × 6cm thermo-mechano-electrical self-oscillator reported recently recorded a peak current of ~47nA (61). The dependence of the current density on H_2O_2 concentration is summarized in Figure 6-4c.

As before, the system's collective beating drives the synchronized formation and collapse of bubbles on each particle. However, unlike previous experiments, here the instantaneous size of the bubble also modulates the electrical conductance from one electrode to the other (Figure 6-4a, N = 2 for demonstration). This effect, in conjunction with the fuel cell's voltage, enables the onboard

generation of oscillatory currents that are in phase with the mechanical beating. In a Pt-Ru device, we observe that the ON/OFF ratio between maximal and minimal currents can exceed 106, corresponding to when the bubble is absent and at its threshold size. Importantly, the same chemical energy harnessed from the environment is used to simultaneously drive the mechanical oscillation, generate the electrical voltage, and modulate the electrical conductance. Multifunctionality of this kind is emblematic of emerging paradigms such as embodied energy (62), and is crucial to the development of efficient microsystems.

Figures 4d and e exemplify the beating system's capability to cyclically drive a microrobotic load with its self-generated oscillatory electrical current. In this proof-of-concept demonstration, we wired the Ru electrode of a fuel cell particle to a state-of-the-art Pt-Ti electrochemical microactuator (see Figure 6-4d and Methods), originally invented for a tethered sub-100μm walker (63). In our experimental configuration, charged species from the electrolyte is desorbed from the Pt surface of the bimorph microactuator as current passes through, causing it to deswell and its curvature/length to change. Evident in Figure 6-4e, the periodic actuation of the bimorph (red curve, representative snapshots in Figure 6-4d) is driven by the periodic spikes in the current signal (blue curve), which in turn is modulated by the chemomechanical beating of two particles. Because the outer radius of the Pt electrode (Figure 6-4b) exceeds the 125μm patch radius of a standard particle, the system is stabilized by the added heterogeneity, which also explains the observed sub-0.03Hz beating frequency. In contrast, the control experiments in Figure 6-4e show the actuator idling in the absence of a second particle and hence any mechanical beating. By harnessing the emergent power generation of an ensemble of microparticles, we have demonstrated the design and modular interoperability of key microrobotic components—energy sources and locomotive elements—based on the physics of self-organization.

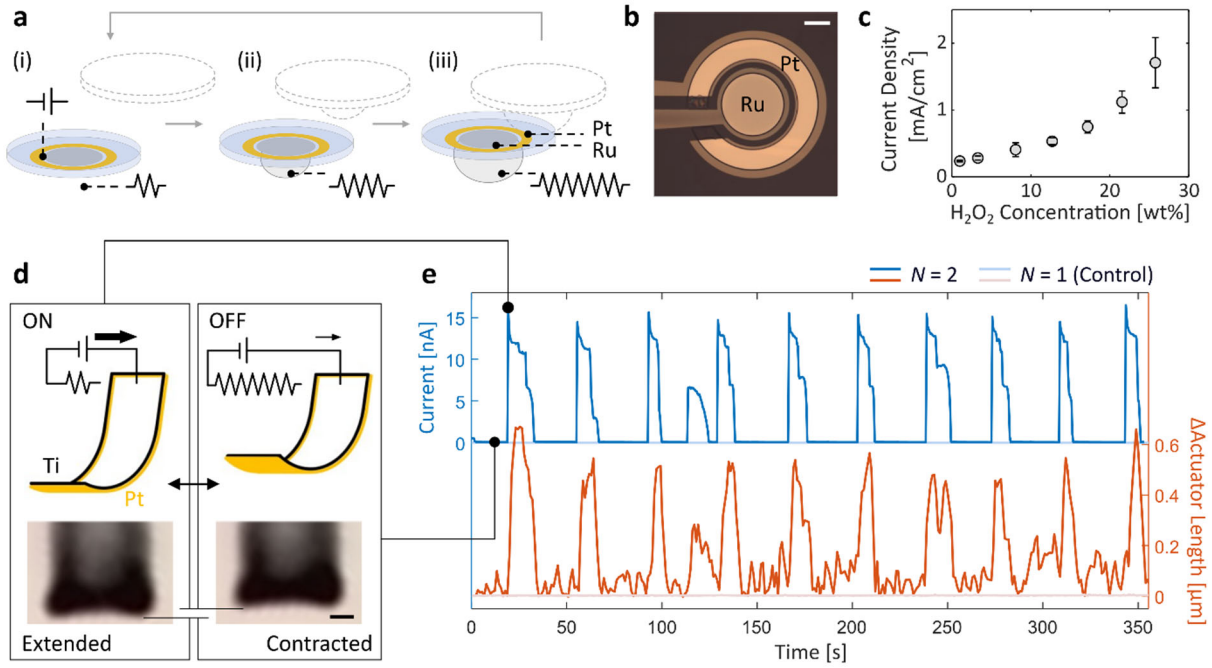

Figure 6-4: Self-organized oscillation powers a microrobotic arm. a, Schematics of the generation of an oscillatory electrical current from chemomechanical beating. The pair of metals (Pt-Ru or Pt-Au) patterned on a polymer base constitute the electrodes of a H2O2 fuel cell, which serves as an on-board voltage source. The periodic bubble growth and collapse in a beating system separately modulates the electrical resistance between the electrodes, leading to an oscillatory current. b, Optical micrograph of a typical Pt-Ru fuel cell particle. The entire surface, less the electrode area, is passivated with a thin layer of insulating SU-8 polymer (shaded). The metallic leads on the left are not necessary for device operation and are included to facilitate measurement. Scale bar, 100μm. c, Short-circuit current density as a function of H2O2 concentration for a Pt-Ru device. d,e, Cyclic motion of a microrobotic actuator driven by the oscillatory current. The schematics and micrographs in (d) show the extended and contracted states of the actuator respectively under the ON and OFF current conditions, as modulated by the bubble size. The current measurement over time and the actuator length change (e) closely match, confirming that the cyclic actuation is driven by the oscillatory current, which itself is emergent from the particle beating. Scale bar, 2μm.

6.6. Discussion

Through the discovery of physical mechanisms for asymmetry induced order, we constructed self-oscillating electrical generators capable of powering on-board microrobotic components from the interactions of simple microparticles. Our results stand in contrast to more traditional microrobotic approaches focusing on the design of intricate electromechanical assemblies to produce alternating electrical currents (14). By relying on our system's self-organized behaviours, we circumvented the design of complex contraptions to harvest and transduce chemical energy into periodic electrical and mechanical work—a crucial step towards fully-autonomous microrobots (62, 64). The use of on-board electrical currents will enable the integration of sensors and computational elements to enrich physical microparticle interactions (65), forming the basis for future collectives wherein the long-envisioned potential of complex inter-particle communications can be implemented (40). We plan on extending our approach into studying larger collections of microparticles in search of general principles for the top-down design of active matter systems, where an understanding of system symmetries and environmental forcing may enhance their task-capability. Unifying perspectives from their respective fields, our work suggests that future microrobots and active matter systems may become more robust and task-capable when we design them to exploit the physics of the environments they inhabit.

6.7. Appendix A: Methods

6.7.1. Fabrication and Liftoff of Microparticles

The fabrication process is summarized in Figure 6-5. SU-8 2010 photoresist was spun on a Si wafer at 3000rpm for 1 minute. It was baked at 65◦C for 1 minute and 95◦C for 2 minutes. The SU-8 discs were defined by exposure with a Karl Suss MA6 Mask Aligner at a dose of 140mJ (365nm). The wafer was baked post-exposure at 65˚C and 95˚C respectively for 1 and 2.5 minutes. The resist was developed in SU-8 developer for 2.5 minutes, soaked in isopropanol, and blow dried. The wafer was optionally hard baked at 115 to 180˚C for 10 minutes to 2 hours.

LOR 3A photoresist was spun onto the sample at 1000rpm for 1 minute. This was optionally followed by a second spinning step at 2000rpm for 30 seconds to ensure that the coating was uniform at the periphery. The sample was baked at 180˚C for 4 minutes. Shipley S1818 photoresist

was spun at 2000rpm for 1 minute and subsequently heated at 115°C for 1 minute. The LOR and Shipley parameters were optimized to ensure a full coverage over the 10μm-thick SU-8 discs. The sample was aligned and exposed at 140mJ (405nm). It was then developed in AZ 726 MIF for 1.5 minutes. The sample was washed with running DI water and blow dried.

The Pt metal patches were deposited with a Denton e-Beam Evaporator. A typical patch consists of 5nm of Cr or Ti adhesion layer and 50nm of Pt. The photoresists were stripped in Remover PG.

The fabricated microparticles were lifted off the wafer substrate in 45°C 1M KOH solution, which etched away Si (Figure 6-5b). The process typically took 30 to 50 minutes. The microparticles were collected by a transfer pipette and then washed repeatedly with DI water until the solution's pH was neutral. Alternatively, the microparticles were first coated with PMMA A4 (polymethyl methacrylate) before being lifted off in 90°C 1M KOH solution (Figure 6-5c). The microparticle array on the PMMA sheet was picked up by a clean piece of wafer. The PMMA was carefully dissolved away with acetone and the particles were washed by and stored in DI water.

6.7.2. Experimental Characterization of Beating Behaviour

In a typical experiment, 1mL of H_2O_2 solution (10.7% unless otherwise noted, VWR International, LLC, Radnor, PA) is dispensed gently onto a polystyrene Petri dish (VWR International, LLC, Radnor, PA). Two methods were used to transfer the micro-oscillators from their vial to the H_2O_2 droplet. In the "wet" method, they could be collected with a narrow-tipped transfer pipette along with a small amount of water, and subsequently transferred onto the droplet. The introduction of a minor amount of diluent as well as the occasional need to flip over a particle can be avoided with an alternative "dry" process. First, a particle was wet transferred onto a glass slide with a transfer pipette. Excess water was carefully wiped off while the particle was not completely dried. A drop of H_2O_2 solution was then added. This step allowed 8 the operator to check the orientation of the particle on the glass slide prior to its transfer to the droplet. A quartz NMR sample tube was used to directly pick up the particle dry, a process assisted by surface tension. Note that the other end of the tube was, of course, capped. Lastly, the dry particle with the correct orientation was gently placed atop the 1mL H_2O_2 droplet under the camera.

The beating behaviour was recorded as 30fps videos with a Canon Rebel T6i camera (Canon U.S.A., Inc., Huntington, NY). The optical system comprised a magnification lens (MVL12X20L),

a coaxially focusable zoom lens (MVL12X3Z), and an extension tube (MVL12X3Z), all purchased from Thor-labs, Inc., Newton, NJ. The setup followed that described previously in (66). The illumination source was a MI-150 Fiber Optic Illuminator from Edmund Optics Inc., Barrington, NJ.

6.7.3. Phase and recurrence analyses of particle beating

The recorded videos of the beating systems were processed with the Image Processing Toolbox of MATLAB (MathWorks, Inc., Natick, MA). The particle centres were identified from each frame of the videos with the standard imfindcircles function, a circle-finding algorithm based on circular Hough transform (67). Given a collection of particle trajectories from an experimental trial, the main observable from which to construct the phase portraits shown in Figure 6-3 was the breathing radius $r(t)$ as defined in Equation (6-2). The phase portraits were then constructed by plotting the coordinates of $v(t)=\left[\dot{r}(t), r(t)\right]$ after applying a low-pass filter, and the time-derivative of the breathing radius was estimated via finite differencing.

Equipped with the dynamical observables defined above, the recurrence properties of a system can be analysed by finding how often and how quickly the system returns to a neighborhood of $v(t)$. Hence, for a given experiment comprised of K samples we collect data at times $t_i = i\Delta t, \forall i \in \{0,\cdots,K-1\}$ with sampling rate Δt. While in principle this is all one needs in order to quantify recurrence statistics (55), an additional step must be taken in order make the calculation robust. We augmented our $v(t_i)$ vectors by "embedding" the time-series according to an integer parameter m (56). This resulted in a modified set of coordinates, $v_m(t_i)=[v(t_i),\cdots,v(t_{i+m-1})]^T$, from which to robustly calculate our recurrence statistics. Finally, to derive the recurrence properties of a system from an experimental dataset we calculated its recurrence set

$$R_s = \{|\, t_i - t_j \,| : \| v_m(t_i) - v_m(t_j) \| < \epsilon, \forall i, j\}, \tag{6-5}$$

over all valid indices. Note that m and ϵ are a fixed choice of positive non-zero embedding dimension and neighborhood size parameters, respectively. With this set now defined, we could calculate a recurrence histogram from the set R_s using any standard scientific computing package, as in Figure 6-3. Additionally, we note that the histogram can be normalized into a pseudo-probability distribution that expresses the likelihood $p(T)$ that a system exhibits a recurrence after

T seconds. The dominant frequencies plotted in Figures 6-1, 6-3, and 6-6 were computed from the *T* of maximum likelihood from the corresponding recurrence analyses.

As we are interested in characterizing the onset of periodicity across collectives of beating particles, we must construct a measure capable of differentiating the diversity of behaviours we observed. For this purpose, we made use of the entropy of the recurrence probability distributions. As an example, consider a system with a single perfectly oscillatory mode. Then, its recurrence distribution would be a delta function corresponding to its period of oscillation, and thus have zero entropy. If one were to introduce noise or uncertainty into that single oscillatory mode, then probability mass would spread around the delta peak and generate non-zero entropy. Likewise, if the system were to have multi-modal (but deterministic) oscillation, probability mass is now shared between the peaks of the distribution, leading to non-zero entropy.

As the behaviour of a system becomes increasingly complex, it has been shown that the recurrence distribution entropy is a useful metric to quantify this shift that has known connections to both Kolmogorov-Sinai and Renyi entropies (68), as well as the correlation sum in chaos theory (69). However, in order to compare the recurrence entropies of systems with different maginitude- and time-scales, we first normalized our data in two ways. First, we applied min-max normalization to the coordinates of $p(T)$, which allows one to use the same ϵ in the calculation of the recurrence set. Second, we normalized the elements of R_s according to its maximum (while keeping the number of histogram bins constant across systems) in order to study the structure of system recurrences without confounding variables. The result of this process can be seen in Figure 6-3.

Fuel cell fabrication LOR 20B photoresist was spun onto a Schott Borofloat 33 wafer (UniversityWafer, Inc., Boston, MA) at 3000rpm for 1 minute and baked at 180˚C for 4 minutes. Shipley S1805 photoresist was spun at 3000rpm for 1 minute and baked at 115˚C for 1 minute. The sample was exposed at 82.5mJ (405nm). It was then developed in Microposit MF-319 developer for 65 seconds. The sample was washed with running DI water and blow dried. A Denton e-Beam Evaporator was used to deposit 10nm of Ti and 50 to 100nm of Pt. The photoresists were stripped in Remover PG. For the deposition of a second metal, be it Au or Ru, LOR and Shipley resists were spun, baked, exposed, and developed the same as described above. 10nm of Ti and 100nm of Au was deposited with an electron beam evaporator. Alternatively, 50nm of Ru was deposited as the deposition was slow. The photoresists were stripped in Remover PG.

The SU-8, LOR, and Shipley resists were all purchased from Kayaku Advanced Materials, Inc., Westborough, MA, in addition to the SU-8 developer, MF-319 developer, Remover PG, and PMMA. The AZ 726 MIF was purchased from MicroChemicals GmbH, Ulm, Germany.

Finally, a passivation layer of SU-8 was defined on top of the metal electrodes. For the convenience of the electrical measurements that followed, the SU-8 were patterned as either 5mm-by-5mm or 11mm-by-11mm square islands with the active electrode area at the centre exposed. SU-8 2002 was used but the precise thickness was inconsequential.

6.7.4. Fabrication and Characterization of Microactuators

The Pt-Ti bimorph microactuators were fabricated on a Cu sacrificial layer at University of Pennsylvania's microfabrication facility according to the procedures previously reported (63). The actuators were lifted off overnight in a 4mg/mL ammonium sulfate solution, which etched away the Cu substrate. The actuators were subsequently transferred to a phosphate-buffered saline (PBS) solution.

In Figure 6-4, the bimorph microactuators were cyclically driven by the oscillatory electrical current signal generated by the oscillatory beating between a Pt-Ru fuel cell device and a Pt-decorated beating particle. Each microactuator was picked up by a parylene-coated Pt-Ir monopolar electrode (PI2003X.XA3, 0.1MΩ, Microprobes for Life Science, Gaithersburg, MD) in PBS. The parylene coating prevented unnecessary current leakage into the electrolyte. The Pt-Ir electrode connected to the Ru electrode of the fuel cell device via a probe station (Advanced Research Systems, Macungie, PA) and a W probe (The Micromanipulator Company, Carson City, NV). The probe station read out the real-time current with a custom MATLAB code. The Pt electrode of the fuel cell, via a W probe, was connected to a Pt wire partially immersed in the PBS solution.

A 30% H_2O_2 solution and a 0.5M KNO_3 solution were mixed at a volumetric ratio of 85:15. The salt was included to enhance the electrolyte's electrical conductivity. For the self-oscillation to take place, 8.5μL of the prepared mixture was dropped atop a fuel cell device on the wafer. A beating particle was subsequently transferred to the same solution using the transfer method described earlier. The actuation was recorded with the same optical setup described above mounted over the probe station.

6.7.5. Actuation Analysis of Microactuators

The extent of actuation as a function of time was extracted from the recorded videos described in the previous section. A standard canny edge detection algorithm with pixel magnitude thresholds was applied via OpenCV (70). A boundary representing the outline of the actuator was extracted, which could then be used to define a coordinate system aligned and centred along the long edge of the actuator over the duration of the video---a crucial step for reducing measurement drift. From this coordinate system, the length of the actuator was then simply defined according to the nearest actuator boundary pixels along the vertical axis. Finally, in order to mitigate the effect of fluctuations and mechanical vibrations, a standard low-pass finite impulse response (FIR) interpolation scheme was applied to the actuator length signal over time (71).

6.8. Appendix B: Note on Microelectronic Low-Frequency Oscillators

In this section, we elaborate on the design and fabrication challenges of microelectronic oscillators with a frequency on the order of a hertz, which we briefly alluded to earlier. Given the relatively large footprints of integrated capacitors and inductors available, RC- and LC-based oscillators are hardly compatible with the limited space on micrometre-sized machines (72). For example, the frequencies of RC oscillators, such as a bi-inverter or a Schmidt Trigger oscillator, are on the order of the reciprocal of their respective RC constants, i.e. $f_{\mathrm{RC}} \sim \mathcal{O}(1/RC)$. Taking the capacitance to be a generous 40pF for an area of 100µm×100µm (73), one would require a massive resistor of 25GΩ to achieve an RC time constant of 1s. Assuming a resistivity of 100kΩ/µm^2 of polysilicon, this resistor alone would occupy 2.5×105µm^2. Alternatively, one may opt to use a frequency divider to bring the kHz-order frequency of a typical microelectronic relaxation oscillator down to 1Hz. Suppose the starting frequency is 17kHz (74), a cascade of 15 T flip-flops is needed, each of which is constructed from at least 20 transistors (75). Should 300 transistors be fabricated onto a 100µm×100µm microchip, the appropriate transistor node would be 500nm. While well within the realm of possibility, such technology typically still requires the involvement of a commercial foundry outside of academic institutions. Similarly, thyristor-based oscillators of frequencies from 20Hz and up have been foundry-fabricated with a feature size of 180nm (72). The integrated circuit design expertise and capital investment required are the reasons for a high barrier-to-entry. Note

that the area reserved for onboard energy harvesting and storage units, as well as for miscellaneous electronics, may further constrain the real estate available to the microelectronic oscillator.

6.9. Appendix C: Note on the Fuel Cell's Open-Circuit Voltage

Figure 6-11 shows that the open-circuit voltages of the Pt-Au and Pt-Ru fuel cell devices, V_{OC}, exhibits a very weak dependence on the peroxide concentration H_2O_2, unlike the trend of the short-circuit current densities (Figure 6-4c and Figure 6-11). Here we provide a simple explanation based on electrochemical kinetics. We consider the following two pairs of forward and reverse reactions taking place on a single electrode:

$$\left.\begin{aligned} &H_2O_2 \longrightarrow O_2 + 2H^+ + 2e^- \\ &O_2 + 2H^+ + 2e^- \longrightarrow H_2O_2 \end{aligned}\right\} R_1,\ \phi^\circ_{eq,1} = +0.68\text{V} \tag{6-6}$$

$$\left.\begin{aligned} &2H_2O \longrightarrow H_2O_2 + 2H^+ + 2e^- \\ &H_2O_2 + 2H^+ + 2e^- \longrightarrow 2H_2O \end{aligned}\right\} R_2,\ \phi^\circ_{eq,2} = +1.77\text{V} \tag{6-7}$$

where ϕ°_{eq} denotes the standard equilibrium potentials. The Butler–Volmer equation suggests that only one half-reaction from R_1 and R_2 each is dominant at the mixed potential ϕ_{mix}, defined as the potential where the total current equals 0 (76). If we consider the oxidative half-reaction of R_1 and the reductive half-reaction of R_2 (choosing the other two half-reactions does not alter the conclusion), the full Butler-Volmer kinetic expression is given by Ref. (77):

$$i_1(\phi) = nFk_1[H_2O_2]^{\nu_{H_2O_2}} \exp\left[\frac{\alpha_1 F}{\bar{R}T}\phi\right] \tag{6-8}$$

$$i_2(\phi) = -nFk_2[H_2O_2]^{\nu_{H_2O_2}}[H^+]^{\nu_H} \exp\left[-\frac{(1-\alpha_2)F}{\bar{R}T}\phi\right] \tag{6-9}$$

where ϕ is the applied potential on the absolute scale, $i_1(\phi)$ and $i_2(\phi)$ the respective current densities, n the number of electrons transferred, F the Faraday constant, k the rate constants, υ the reaction orders, α the transfer coefficients, $\bar{R}$ the universal gas constant, T the absolute temperature. We can obtain the mixed potential ϕ_{mix} by solving:

$$i_1(\phi_{\text{mix}}) + i_2(\phi_{\text{mix}}) = 0 \tag{6-10}$$

which is equivalent to $-i_1(\phi_{\text{mix}}) / i_2(\phi_{\text{mix}}) = 1$. While the exact form of the solution is of little relevance to us, the division of the right-hand side of Equation 6-8 by that of Equation 6-9 reveals the cancellation of the [H_2O_2] terms under the typical assumption of equal reaction order. That is, ϕ_{mix} is independent of the peroxide concentration for a given electrode. Because the open-circuit voltage between two spatially separated electrodes (such as Pt and Ru) is essentially the difference in the respective mixed potentials ($\Delta\phi_{\text{mix}}$), V_{OC} naturally sees little dependence on [H_2O_2]. This allows us to compare our V_{OC} measurements with past mixed potential studies carried out at lower [H_2O_2]. For example, Wang and colleagues (78) measured a $\Delta\phi_{\text{mix}}$ of 30mV between Pt and Au, and 140mV between Pt and Ru, both consistent with our results.

6.10. Appendix D: Note on the Energy Expenditure

6.10.1. Energy Conversions of the Mechanical Oscillation

Within each period of the emergent mechanical oscillation, chemical energy stored in the H_2O_2 fuel is converted into the particles' kinetic energy upon the collapse of the O_2 bubble. The kinetic energy imparted to two outgoing particles simply take the form of $E_k = mv^2$, where m is the mass of each particle and v the maximal velocity right following the bubble collapse. With $m = 2.34$ μg for a 500μm-diameter particle and $v = 3.2\times10^4$ μm/s measured from experiments, E_{out} is estimated to be 2.40×10^{-12} J per cycle.

The chemical energy consumed per cycle may be computed as:

$$E_{\text{chem}} = \frac{2PV_{\text{b,th}}\Delta H}{RT} \tag{6-11}$$

where $V_{\text{b,th}}$ denotes the bubble volume at threshold, estimated to be 9.81×10^{-2} μL in a 2-particle homogeneous system in 1mL of 10% H_2O_2. We assume an ambient pressure P of 1atm and temperature T of 25°C, as the excess Laplace pressure within the bubble before collapse is a negligible 5.0×10^{-3} atm. ΔH, the enthalpy change of the decomposition reaction, is 98.24kJ/mol at given conditions, equivalent to an energy density of 2.89kJ/g H_2O_2 or 0.29kJ/g 10wt% H_2O_2

solution (79). E_{chem} per cycle is computed to be 7.88×10^{-4} J. The portion of the chemical energy converted to the work of expansion is:

$$W_{PV} = P_{\text{atm}} V_{\text{b,th}} + 4\pi\gamma R_{\text{b,th}}^2 \tag{6-12}$$

where $R_{\text{b,th}}$ is the threshold radius assuming a spherical bubble. The latter term of 7.41×10^{-8} J is the surface energy E_{surf}, i.e., the work against the Laplace pressure during bubble growth. To summarize, therefore, 1.26% of the original chemical energy contributes to a W_{PV} of 1.00×10^{-5} J. 0.74% of the work of expansion is stored as the surface energy. Finally, the kinetic energy gained by the particles account for 0.032‰ of surface energy stored in the bubble.

6.10.2. Energy Conversions of the Microgenerators

As the microgenerator converts the chemical energy from H_2O_2 decomposition to electrical work, it is of interest to calculate the proportion of total H_2O_2 molecules consumed which contributed to the electrical current (80, 81). Given that each electrochemically redoxed H_2O_2 molecule transfers an electron, ON-state currents of 180.66nA (in the absence of an electrical load) and 15.27nA (with a load, i.e. the actuator) are respectively attributed to 1.87×10^{-12} and 1.58×10^{-13} moles of H_2O_2 per second. These correspond to 0.76‰ and 0.063‰ of the total peroxide consumption rate ($2P/RT\cdot dV_{\text{b}}/dt = 2.45\times10^{-9}$ mol/s), respectively. The former is in agreement with prior literature (80), which estimated an electrochemical contribution of 0.5‰. Since more than 99.9% of the consumed H_2O_2 decompose via the same non-electrochemical pathway as in the beating particles with no fuel cells aboard, generation of the electrical current has a negligible impact on the mechanical oscillation if all other conditions are kept the same. Along the same lines, additional fuel cell particles are not expected to diminish the electrical signals observed.

6.11. Appendix E: Supplementary Figures

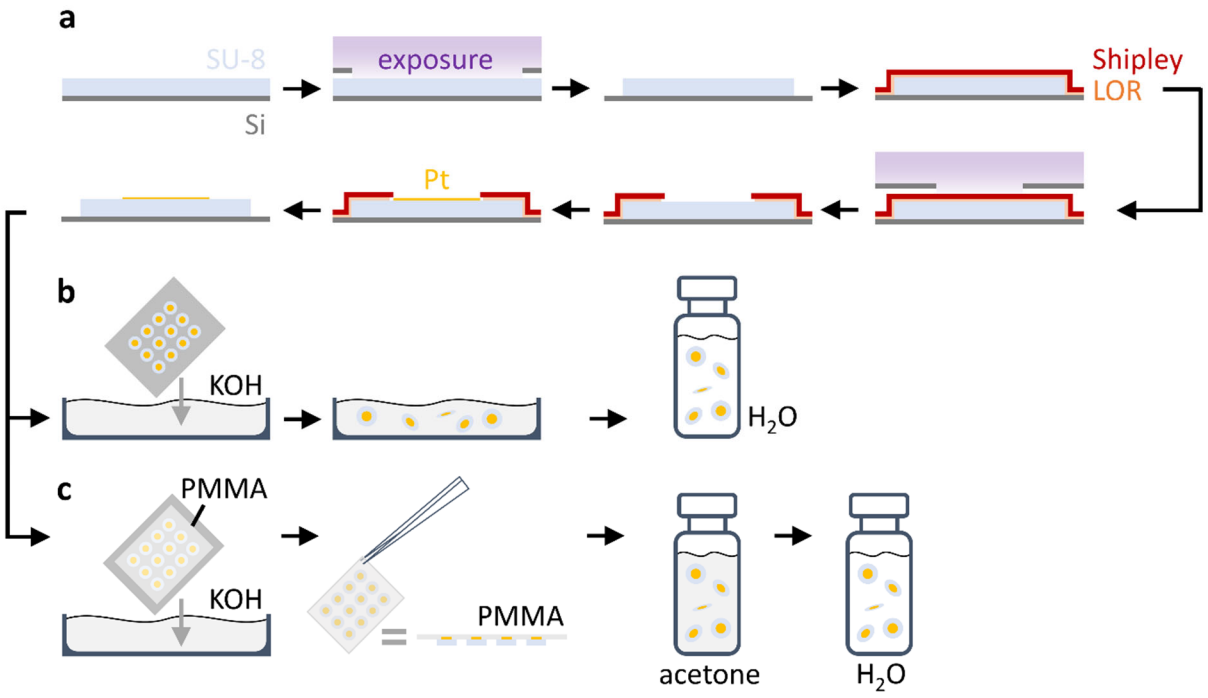

Figure 6-5. Beating particle fabrication steps. a, An array of SU-8 polymeric microdiscs were defined and patterned on a Si wafer with standard photolithography, followed by electron-beam physical vapor deposition of Pt on top. b, The particles were subsequently lifted off in heated KOH solution which etched into the Si substrate. The KOH was displaced by water in which the lifted off microparticles were stored. c, Alternatively, a film of PMMA polymer was spun over the microparticle array. Together they would delaminate from the substrate in heated KOH solution. The PMMA was then removed with an acetone rinse. The lifted off particles were transferred to water for storage.

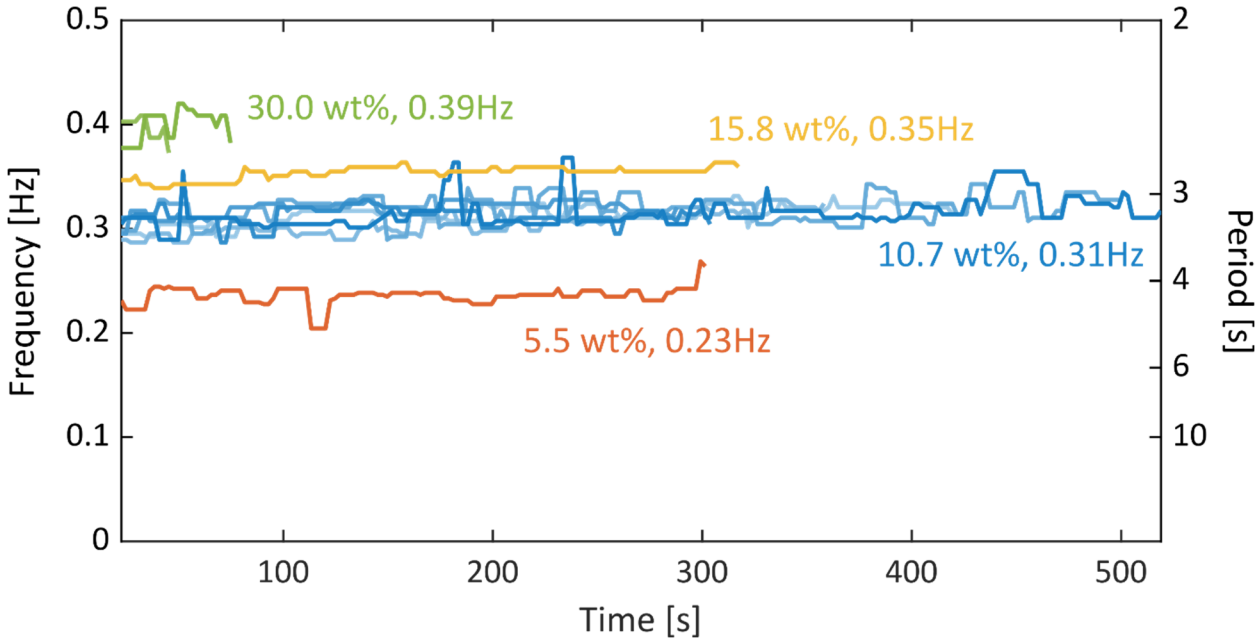

Figure 6-6. Beating frequencies over time from moving window recurrence analyses. The same histograms as in Figure 6-1i were generated, but here only for breathing radius data within a moving window of 150 frames (5s). Frequencies calculated from the most probable recurrence time of each window were plotted as a function of time. The beating frequencies in all experiments are constant throughout, demonstrating robust periodicity. Furthermore, curves from experimental replicates overlap. The frequencies from moving window analyses agree with those shown in Figure 6-1j for all the H_2O_2 concentrations. These concentrations respectively correspond to 6-, 3-, 2-, and 1-fold volumetric dilution of a 30wt% H_2O_2 solution.

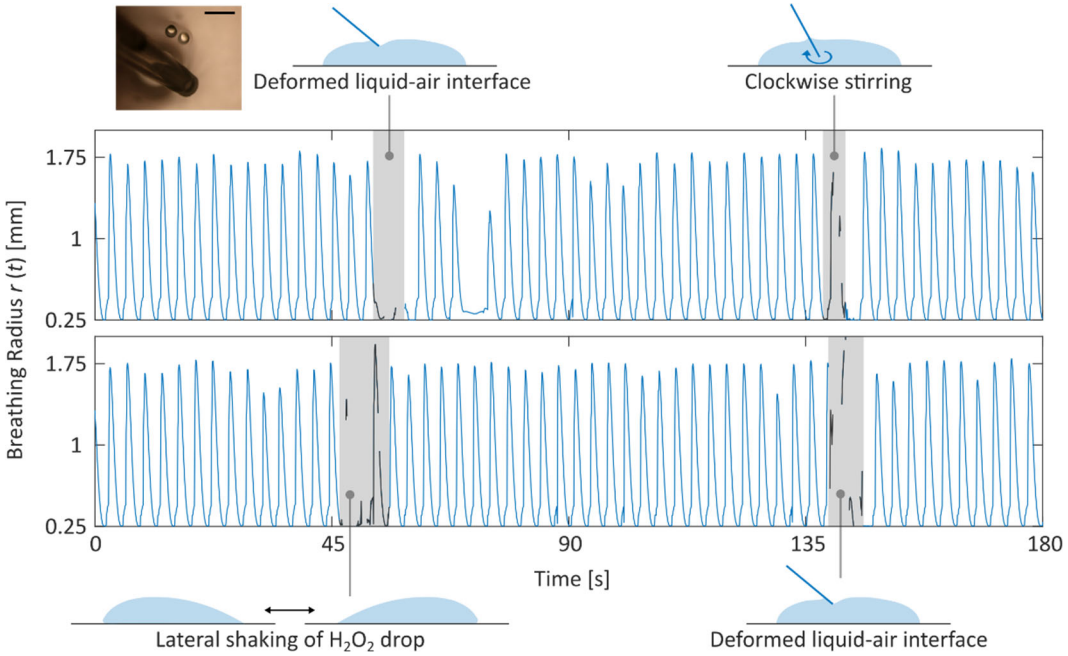

Figure 6-7. Robustness of the emergent oscillation to perturbations. In these two experiments, we intentionally disturbed a system of two identical particles by (i) deforming the liquid-air interface with a pipette (82), (ii) stirring the H_2O_2 drop, and (iii) shaking the drop back and forth. It is evident in the breathing radius trajectories that the collective oscillation resumes promptly following the perturbations (shaded region) with its amplitude and periodicity unchanged, thus demonstrating robustness. Data discontinuities during the perturbations are a result of blurry frames or particles temporarily exiting the camera field-of-view. The inset micrograph shows the particles approaching the pipette due to the deformed interface. Scale bar, 1mm.

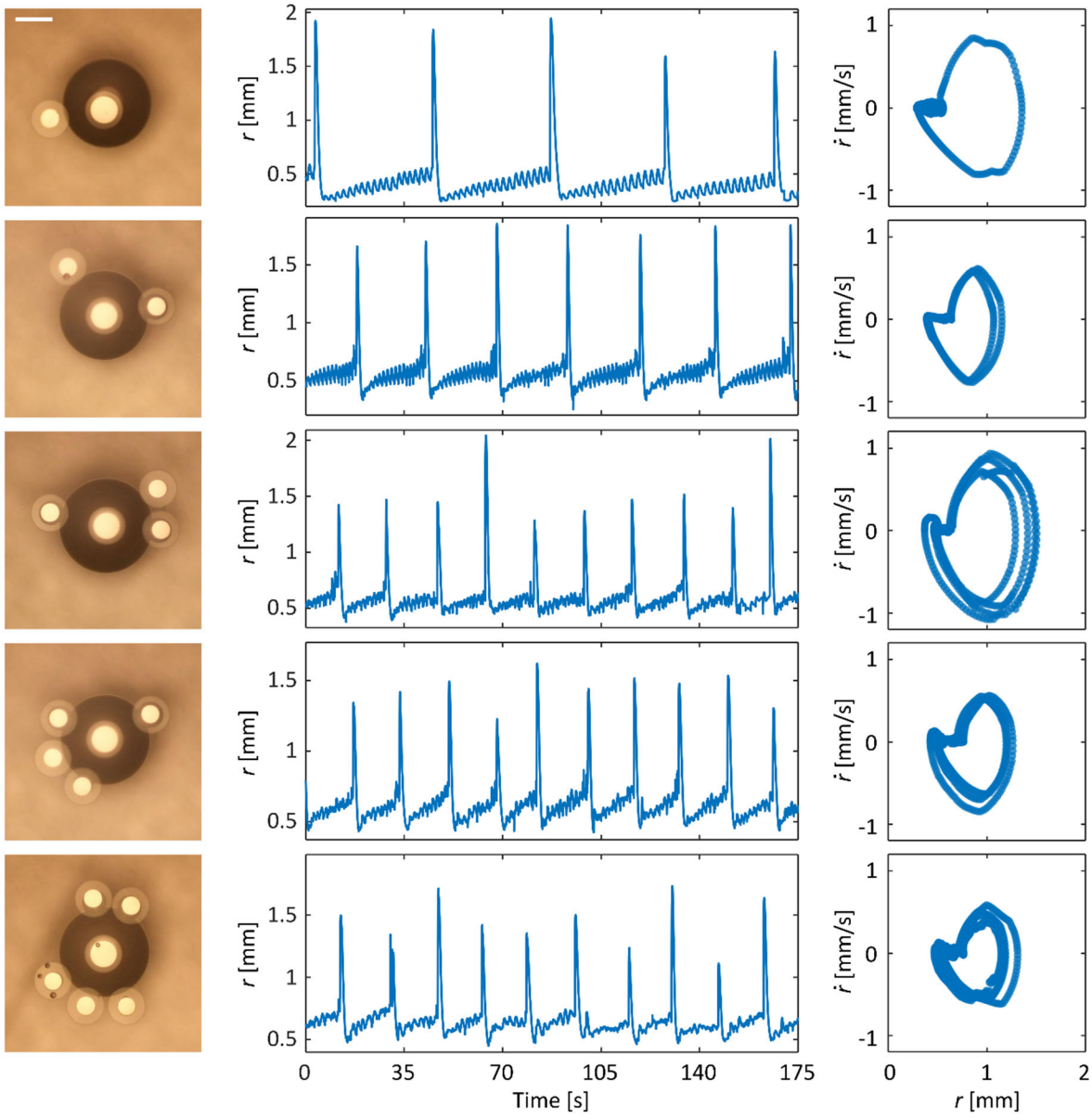

Figure 6-8. Compiled snapshots, breathing radius trajectories, and phase portraits for heterogeneous/DL systems of N = 2 to 6. Systems of all sizes exhibited clear periodicity in their beating behaviours with stable limit cycles. Scale bar, 500μm. All experiments were performed in 1mL of 10.7wt% H_2O_2.

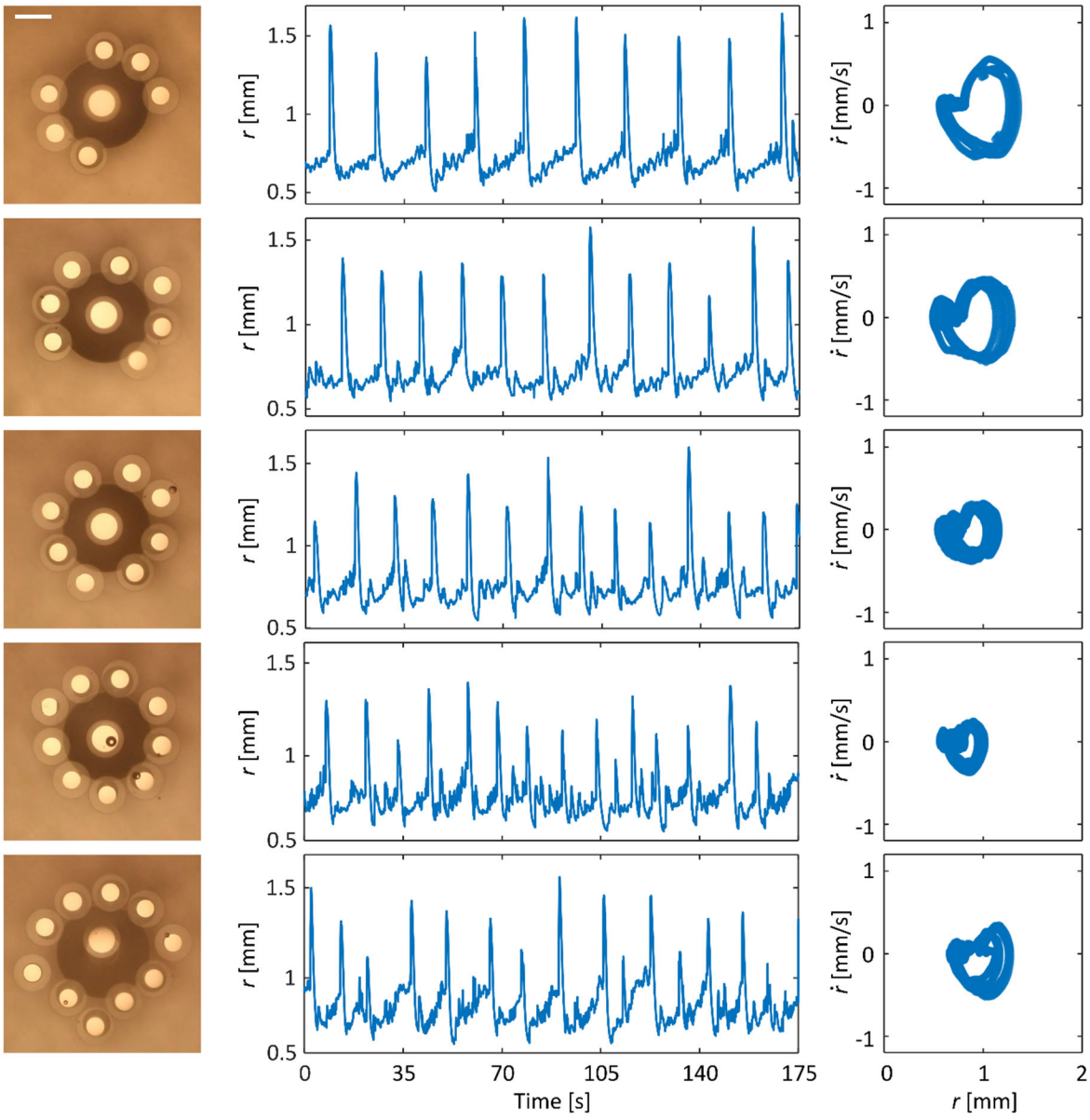

Figure 6-9. Compiled snapshots, breathing radius trajectories, and phase portraits for heterogeneous/DL systems of N = 7 to 11. Systems of all sizes exhibited clear periodicity in their beating behaviours with stable limit cycles. Scale bar, 500µm. All experiments were performed in 1mL of 10.7wt% H_2O_2.

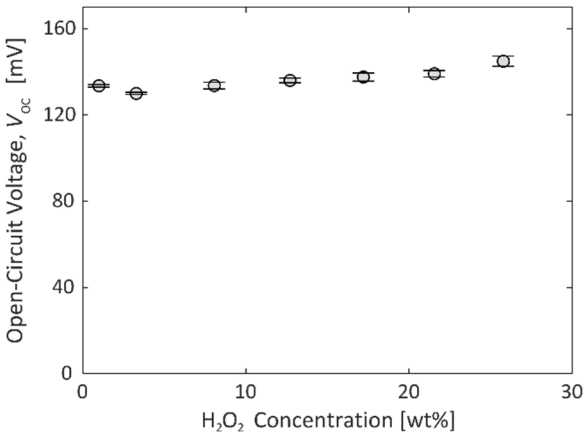

Figure 6-10. Open-circuit voltage of a Pt-Ru device as a weak function of H_2O_2 concentration. The observation is explained by the auto-redox nature of the H_2O_2 decomposition reaction (§6.8). Error bar, standard deviation.

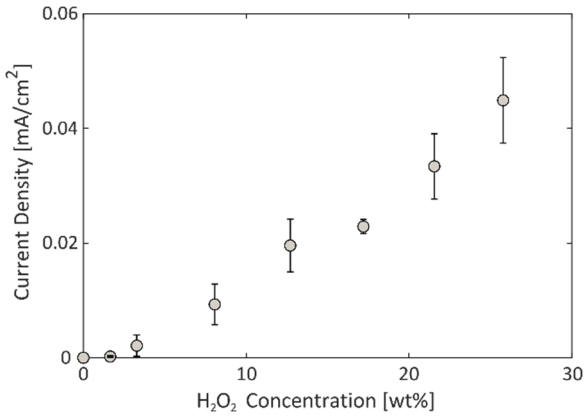

Figure 6-11. Short-circuit current density as a function of H_2O_2 concentration for a Pt-Au device. (*cf*. Figure 6-4c). Error bar, standard deviation.

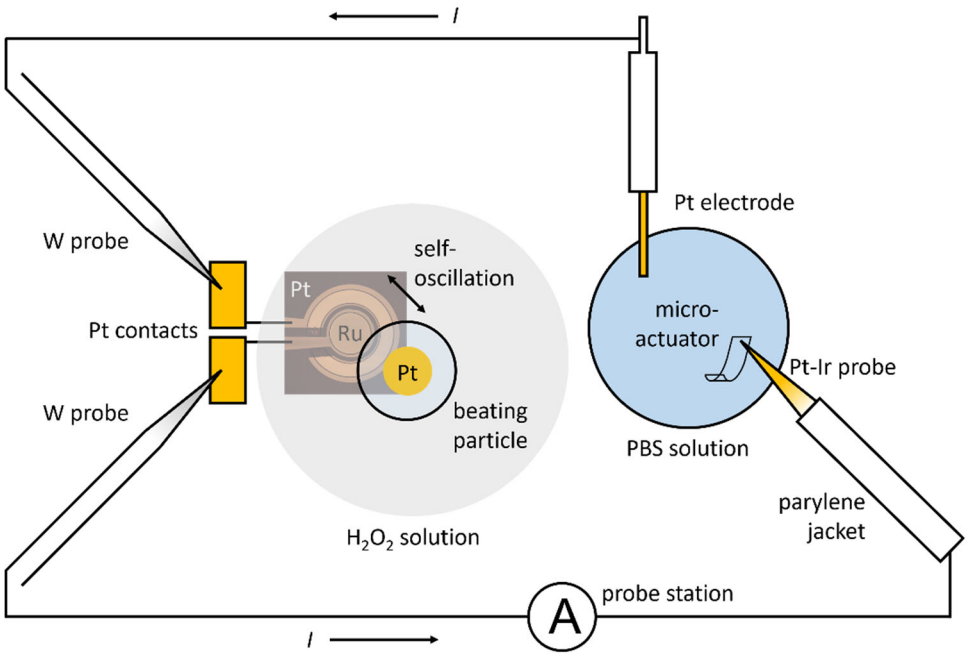

Figure 6-12. Bimorph actuator experimental setup. The microactuator in PBS solution is connected via external wiring to the beating system in an H2O2 drop. The mechanical self-oscillation is translated to an oscillatory electrical current as illustrated in Figure 6-4a, which powers cyclic motion of the actuator (Figure 6-4e).

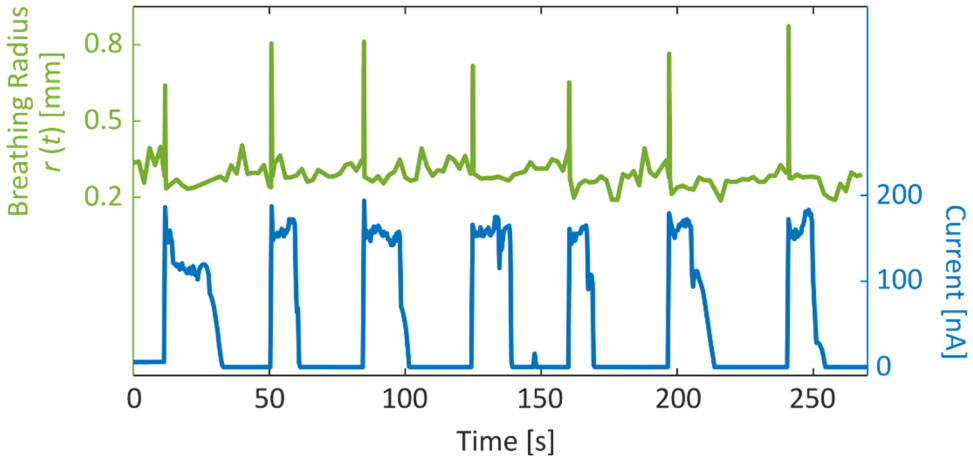

Figure 6-13. Oscillatory mechanical beating drives on-board oscillatory current. (See also Figure 6-4e). As a standard 500-µm particle beats with a Pt-Ru fuel cell device (Figure 6-4b, also Methods), the bubbles collapse at regular intervals as indicated by the spikes in the breathing radius trajectory (r(t), top). Removal of the bubbles restores the electrochemical reactivity of the fuel cell electrodes, and therefore the current (bottom) peaks precisely as r(t) does. The current measured in this experiment is an order of magnitude higher than that in Figure 6-4e since the system characterized here was not connected to an actuator.

6.12. References

1. Buzsaki, G. & Draguhn, A. Neuronal Oscillations in Cortical Networks. Science 304, 1926–1929 (2004).
2. Kruse, K. & Julicher, F. Oscillations in Cell Biology. Current Opinion in Cell Biology 17, 20–26. issn: 0955-0674 (2005).
3. Katz, P. S. Evolution of central pattern generators and rhythmic behaviours. Philosophical Transactions of the Royal Society B: Biological Sciences 371, 20150057 (2016).
4. Minguet-Parramona, C. et al. An optimal frequency in Ca2+ oscillations for stomatal closure is an emergent property of ion transport in guard cells. Plant Physiology 170, 33–42. issn: 15322548 (2016).
5. Hoyt, D. F. & Taylor, C. R. Gait and the energetics of locomotion in horses. Nature 292, 239–240. issn: 1476-4687 (July 1981).
6. Yao, X. S. & Maleki, L. Optoelectronic microwave oscillator. Journal of the Optical Society of America 13, 1725–1735 (1996).
7. White, T. J. et al. A high frequency photodriven polymer oscillator. Soft Matter 4, 1796–1798 (9 2008).
8. Lagzi, I., Kowalczyk, B., Wang, D. & Grzybowski, B. A. Nanoparticle oscillations and fronts. Angewandte Chemie 49, 8616–8619 (2010).
9. Gardi, G., Ceron, S., Wang, W., Petersen, K. & Sitti, M. Microrobot collectives with reconfigurable morphologies, behaviors, and functions. Nature Communications 13, 2239. issn: 2041-1723 (Apr. 2022).
10. Jenkins, A. Self-oscillation. Physics Reports 525, 167–222. issn: 0370-1573 (2013).
11. Hua, M. et al. Swaying gel: Chemo-mechanical self-oscillation based on dynamic buckling. Matter 4, 1029–1041. issn: 2590-2385 (2021).
12. He, X. et al. Synthetic homeostatic materials with chemo-mechano-chemical self-regulation. Nature 487, 214–218 (2012).
13. Grzybowski, B. A. & Huck, W. T. The nanotechnology of life-inspired systems. Nature Nanotechnology 11, 585–592. issn: 17483395 (2016).
14. Akbar, F. et al. Self-sufficient self-oscillating microsystem driven by low power at low Reynolds numbers. Science Advances 7, eabj0767 (2021).

15. Shen, B. & Kang, S. H. Designing self-oscillating matter. Matter 4, 766–769. issn: 2590-2385 (2021).
16. Hudson, J. & Mankin, J. Chaos in the Belousov–Zhabotinskii reaction. The Journal of Chemical Physics 74, 6171–6177 (1981).
17. Maeda, S., Hara, Y., Sakai, T., Yoshida, R. & Hashimoto, S. Self-Walking Gel. Advanced Materials 19, 3480–3484 (2007).
18. Altemose, A. et al. Chemically controlled spatiotemporal oscillations of colloidal assemblies. Angewandte Chemie International Edition 56, 7817–7821 (2017).
19. Zhou, C. et al. Coordinating an Ensemble of Chemical Micromotors via Spontaneous Synchronization. ACS Nano 14, 5360–5370. issn: 1936–0851 (2020).
20. Yoshida, R. Self-Oscillating Gels Driven by the Belousov–Zhabotinsky Reaction as Novel Smart Materials. Advanced Materials 22, 3463–3483 (2010).
21. Onoda, M., Ueki, T., Tamate, R., Shibayama, M. & Yoshida, R. Amoeba-like self-oscillating polymeric fluids with autonomous sol-gel transition. Nature Communications 8, 15862. issn: 2041-1723 (2017).
22. Zhao, Y. et al. Soft phototactic swimmer based on self-sustained hydrogel oscillator. Science Robotics 4, eafax7112 (2019).
23. Horvath, J., Szalai, I., Boissonade, J. & De Kepper, P. Oscillatory dynamics induced in a responsive gel by a non-oscillatory chemical reaction: experimental evidence. Soft Matter 7, 8462–8472 (2011).
24. Shin, B. et al. Hygrobot: A self-locomotive ratcheted actuator powered by environmental humidity. Science Robotics 3, eaar2629 (2018).
25. Funaki, T. et al. Miniaturized 3D Functional Interposer Using Bumpless Chip-on-Wafer (COW) Integration with Capacitors in 2021 IEEE 71st Electronic Components and Technology Conference (ECTC) (2021), 185–190.
26. Molnar, A. C. et al. Nanoliter-scale autonomous electronics: Advances, challenges, and opportunities in 2021 IEEE Custom Integrated Circuits Conference (CICC) (IEEE, Apr. 2021), 1–6. isbn: 978-1-7281-7581-2.
27. Funke, D. A. et al. Ultra low-power,-area and-frequency CMOS thyristor based oscillator for autonomous microsystems. Analog Integrated Circuits and Signal Processing 89, 347–356 (2016).

28. Hwang, C., Bibyk, S., Ismail, M. & Lohiser, B. A very low frequency, micropower, low voltage CMOS oscillator for noncardiac pacemakers. IEEE Transactions on Circuits and Systems I: Fundamental Theory and Applications 42, 962–966 (1995).
29. Galea, F., Casha, O., Grech, I., Gatt, E. & Micallef, J. Ultra Low Frequency Low Power CMOS Oscillators for MPPT and Switch Mode Power Supplies in IEEE Conference on Ph.D. Research in Microelectronics and Electronics (2018), 121–124.
30. Wang, Y. et al. Bipolar Electrochemical Mechanism for the Propulsion of Catalytic Nanomotors in Hydrogen Peroxide Solutions. Langmuir 22, 10451–10456 (2006).
31. Paxton, W. F. et al. Catalytically Induced Electrokinetics for Motors and Micropumps. Journal of the American Chemical Society 128, 14881–14888 (2006).
32. Brooks, A. M. et al. Shape-directed rotation of homogeneous micromotors via catalytic self-electrophoresis. Nature Communications 10, 495 (2019).
33. Bandari, V. K. et al. A flexible microsystem capable of controlled motion and actuation by wireless power transfer. Nature Electronics 3, 172–180 (2020).
34. Wehner, M. et al. An integrated design and fabrication strategy for entirely soft, autonomous robots. Nature 536, 451–455 (2016).
35. Vella, D. & Mahadevan, L. The “Cheerios effect”. American Journal of Physics 73, 817–825 (2005).
36. Xie, G. et al. Continuous, autonomous subsurface cargo shuttling by nature-inspired meniscus-climbing systems. Nature Chemistry 14, 208–215. issn: 1755-4349 (2022).
37. Mei, Y. et al. Versatile Approach for Integrative and Functionalized Tubes by Strain Engineering of Nanomembranes on Polymers. Advanced Materials 20, 4085–4090 (2008).
38. Solovev, A. A., Mei, Y., Berm´udez Ure˜na, E., Huang, G. & Schmidt, O. G. Catalytic Microtubular Jet Engines Self-Propelled by Accumulated Gas Bubbles. Small 5, 1688–1692 (2009).
39. Solovev, A. A., Mei, Y. & Schmidt, O. G. Catalytic Microstrider at the Air–Liquid Interface. Advanced Materials 22, 4340–4344 (2010).
40. Solovev, A. A., Sanchez, S. & Schmidt, O. G. Collective behaviour of self-propelled catalytic micromotors. Nanoscale 5, 1284–1293 (4 2013).

41. Lin, S.- S. & Gurol, M. D. Catalytic Decomposition of Hydrogen Peroxide on Iron Oxide: Kinetics, Mechanism, and Implications. Environmental Science & Technology 32, 1417–1423. issn: 0013-936X (1998).
42. Plauck, A., Stangland, E. E., Dumesic, J. A. & Mavrikakis, M. Active sites and mechanisms for H2O2 decomposition over Pd catalysts. Proceedings of the National Academy of Sciences 113, E1973–E1982 (2016).
43. Gallager, R. G. Stochastic Processes: Theory for Applications (Cambridge University Press, 2013).
44. Medeiros, E. S., Feudel, U. & Zakharova, A. Asymmetry-induced order in multilayer networks. Phys. Rev. E 104, 024302 (2 2021).
45. Zhang, Y., Ocampo-Espindola, J. L., Kiss, I. Z. & Motter, A. E. Random heterogeneity outperforms design in network synchronization. Proceedings of the National Academy of Sciences 118. issn: 0027-8424 (2021).
46. Zhang, Y., Nishikawa, T. & Motter, A. E. Asymmetry-induced synchronization in oscillator networks. Phys. Rev. E 95, 062215 (6 2017).
47. Nicolaou, Z. G., Case, D. J., Wee, E. B. v. d., Driscoll, M. M. & Motter, A. E. Heterogeneity-stabilized homo-geneous states in driven media. Nature Communications 12, 4486. issn: 2041-1723 (2021).
48. Chvykov, P. et al. Low rattling: A predictive principle for self-organization in active collectives. Science 371, 90–95. issn: 0036-8075 (2021).
49. Chvykov, P. & England, J. Least-rattling feedback from strong time-scale separation. Phys. Rev. E 97, 032115 (2018).
50. Chen, S.- l., Lin, C.- t., Pan, C., Chieng, C. - c. & Tseng, F.-g. Growth and detachment of chemical reaction generated micro-bubbles on micro-textured catalyst. Microfluidics and Nanofluidics 7, 807. issn: 1613-4990 (2009).
51. Moreno Soto, A., Maddalena, T., Fraters, A., van der Meer, D. & Lohse, D. Coalescence of diffusively growing gas bubbles. Journal of Fluid Mechanics 846, 143–165 (2018).
52. Lv, P. et al. Self-Propelled Detachment upon Coalescence of Surface Bubbles. Phys. Rev. Lett. 127, 235501 (2021).
53. Weon, B. M. & Je, J. H. Coalescence Preference Depends on Size Inequality. Phys. Rev. Lett. 108, 224501 (2012).

54. Chen, R., Yu, H. W., Zhu, L., Patil, R. M. & Lee, T. Spatial and temporal scaling of unequal microbubble coalescence. AIChE Journal 63, 1441–1450 (2017).
55. Eckmann, J. - P., Kamphorst, S. O. & Ruelle, D. Recurrence Plots of Dynamical Systems. Europhysics Letters 4, 973–977 (1987).
56. Marwan, N., Romano, M. C., Thiel, M. & Kurths, J. Recurrence plots for the analysis of complex systems. Physics Reports 438, 237–329 (2007).
57. Wang, W., Chiang, T.- y., Velegol, D. & Mallouk, T. E. Understanding the efficiency of autonomous nano- and microscale motors. Journal of the American Chemical Society 135, 10557–10565 (July 2013).
58. Wang, W., Duan, W., Sen, A. & Mallouk, T. E. Catalytically powered dynamic assembly of rod-shaped nanomotors and passive tracer particles. Proceedings of the National Academy of Sciences 110, 17744–17749 (2013).
59. Lee, T.- C. et al. Self-Propelling Nanomotors in the Presence of Strong Brownian Forces. Nano Letters 14, 2407–2412 (2014).
60. Zhang, Y. & Hess, H. Chemically-powered swimming and diffusion in the microscopic world. Nature Reviews Chemistry 5, 500–510 (2021).
61. Wang, X.- Q. et al. In-built thermo-mechanical cooperative feedback mechanism for self-propelled multimodal locomotion and electricity generation. Nature Communications 9, 3438. issn: 2041-1723 (2018).
62. Aubin, C. A. et al. Towards enduring autonomous robots via embodied energy. Nature 602, 393–402. issn: 1476-4687 (2022).
63. Miskin, M. Z. et al. Electronically integrated, mass-manufactured, microscopic robots. Nature 584, 557–561. issn: 1476-4687 (2020).
64. Brooks, A. M. & Strano, M. S. A conceptual advance that gives microrobots legs. Nature 584, 530–531. issn:1476-4687 (2020).
65. Yang, J. F. et al. Memristor Circuits for Colloidal Robotics: Temporal Access to Memory, Sensing, and Actuation. Advanced Intelligent Systems 4, 2100205 (2022).
66. Zhao, Q., Wang, T., Ryu, Y. K., Frisenda, R. & Castellanos-Gomez, A. An inexpensive system for the deterministic transfer of 2D materials. Journal of Physics: Materials 3, 016001 (2020).
67. The MathWorks Inc. imfindcircles: Find circles using circular Hough transform.

68. Faure, P. & Korn, H. A new method to estimate the Kolmogorov entropy from recurrence plots: its application to neuronal signals. Physica D: Nonlinear Phenomena 122, 265–279. issn: 0167-2789 (1998).
69. March, T. K., Chapman, S. C. & Dendy, R. O. Recurrence plot statistics and the effect of embedding. Physica D: Nonlinear Phenomena 200, 171–184. issn: 0167-2789 (2005).
70. Bradski, G. The OpenCV Library. Dr. Dobb's Journal of Software Tools (2000).
71. Schafer, R. W. & Rabiner, L. R. A digital signal processing approach to interpolation. Proceedings of the IEEE 61, 692–702 (1973).
72. Funke, D. A. et al. Ultra low-power,-area and-frequency CMOS thyristor based oscillator for autonomous microsystems. Analog Integrated Circuits and Signal Processing 89, 347–356 (2016).
73. Molnar, A. C. et al. Nanoliter-scale autonomous electronics: Advances, challenges, and opportunities in 2021 IEEE Custom Integrated Circuits Conference (CICC) (IEEE, Apr. 2021), 1–6. isbn: 978-1-7281-7581-2.
74. Lee, S. et al. A 250 μm × 57 μm microscale opto-electronically transduced electrodes (MOTEs) for neural recording. IEEE Transactions on Biomedical Circuits and Systems 12, 1256–1266. issn: 1932-4545. https://ieeexplore.ieee. org/document/8491379/ (Dec. 2018).
75. Harris, S. L. & Harris, D. Digital Design and Computer Architecture RISC-V. isbn: 9780128200643 (Elsevier Inc., 2021).
76. Park, J. H. et al. Open circuit (mixed) potential changes upon contact between different inert electrodes-size and kinetic effects. Analytical Chemistry 85, 964–970. issn: 00032700 (2013).
77. Corbin, N., Zeng, J., Williams, K. & Manthiram, K. Heterogeneous molecular catalysts for electrocatalytic CO2 reduction. Nano Research 12, 2093–2125. issn: 1998-0124 (Sept. 2019).
78. Wang, Y. et al. Bipolar electrochemical mechanism for the propulsion of catalytic nanomotors in hydrogen peroxide solutions. Langmuir 22, 10451–10456. issn: 07437463 (2006).
79. Wehner, M. et al. An integrated design and fabrication strategy for entirely soft, autonomous robots. Nature 536, 451–455 (2016).

80. Wang, W., Chiang, T.-y., Velegol, D. & Mallouk, T. E. Understanding the efficiency of autonomous nano- and microscale motors. Journal of the American Chemical Society 135, 10557–10565 (July 2013).
81. Paxton, W. F. et al. Catalytically Induced Electrokinetics for Motors and Micropumps. Journal of the American Chemical Society 128, 14881–14888 (2006).
82. Solovev, A. A., Mei, Y. & Schmidt, O. G. Catalytic Microstrider at the Air–Liquid Interface. Advanced Materials 22, 4340–4344 (2010).

CHAPTER 7

Mechanistic modeling of the emergent microrobotic oscillators

As was §6, this chapter has been adapted from:

Jing Fan Yang, Thomas A. Berrueta*, Allan M. Brooks, Albert Tianxiang Liu, Ge Zhang, David Gonzalez-Medrano, Sungyun Yang, Volodymyr B. Koman, Pavel Chvykov, Lexy N. LeMar, Marc Z. Miskin, Todd D. Murphey, and Michael S. Strano. 2022. "Emergent Microrobotic Oscillators via Asymmetry-Induced Order." arXiv: 2205.09814. Nature Communications.*

(Equal contribution)*

7.1. Abstract

In this chapter we describe in detail the mechanistic model of the emergent mechanical oscillation observed and discussed in §6. Situated at an air-liquid interface, each particle is subject to a global gravitational force oriented towards the H_2O_2 drop's apex, local "Cheerios effect" forces arising from interfacial distortion in each particle's immediate neighbourhood, as well as hydrodynamic interactions. Interestingly, through the attempts to fit the mechanistic model to experimental data, we identified both a global and a local aspect of the hydrodynamic drag, the latter arising when particles approach one another and causing the drag to significantly rise. We demonstrated the rate of H_2O_2 decomposition (and hence bubble generation) could be quantitatively described by a Langmuir-Hinshelwood kinetics. Combining the calculated interfacial profile, the global and local interactions of the particles, and the bubble generation dynamics, we were able to capture even the fine details of the experimental oscillation trajectories to high fidelity, beyond simply predicting the oscillation amplitude and frequency.

7.2. Calculation of the Interfacial Profile

As the microparticles beat at the curved liquid-air interface of a drop of aqueous H_2O_2 solution, we start by solving the Laplace equation of capillarity (1, 2). We solved the following system of ordinary differential equations (ODEs) with MATLAB's ode45 Runge-Kutta solver (MathWorks, Inc., Natick, MA):

$$\begin{aligned}
\frac{d\rho}{ds} &= \cos\theta \\
\frac{dz}{ds} &= \sin\theta \\
\frac{d\theta}{ds} &= \begin{cases} \beta, s = 0 \\ 2\beta + \gamma_c z - \dfrac{\sin\theta}{\rho}, s > 0 \end{cases} \\
\frac{dV}{ds} &= \pi\rho^2 \sin\theta \\
\rho(0) = z(0) &= \theta(0) = V(0) = 0
\end{aligned} \qquad \text{(7-1 to 7-5)}$$

where β is the curvature at the apex $s = 0$ and V is the volume. $\gamma_c = g(\rho_l - \rho_a)/\gamma$ denotes the capillary constant, where γ is the interfacial tension, ρ_l density of the liquid phase, and ρ_a that of air. θ, r, z, and s are defined in Figure 7-1. For each value of β, a solution to the initial value problem can be obtained which describes the profile of a Laplacian axisymmetric interface. A unique β can be identified such that $V = V_{drop}$ and $\theta = \theta_c$ at the three-phase contact line. In our experimental system, the contact angle $\theta_c = 87.4°$ for the peroxide-polystyrene interface in air. Figure 7-1below presents the interface profile for a series of V_{drop} values. β is solved to be 17.56m^{-1} for V_{drop} = 1mL.

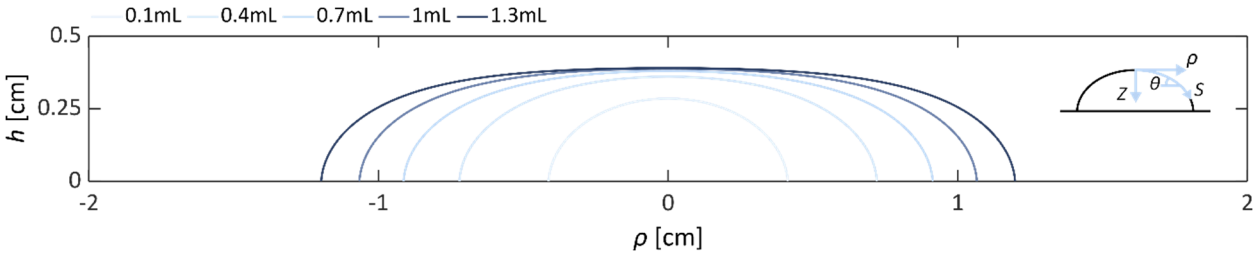

Figure 7-1. Coordinate system of the H_2O_2 drop and the solved interface profiles for a series of drop volumes V_{drop}.

7.3. Global and Local Interactions

The microparticles are driven outward by the collapse of a shared bubble and come together via a global and a local restorational force. As the SU-8 polymer is barely denser than the peroxide solution, the buoyancy from a small gas bubble underneath the disc is able to overcome the particle's weight and create a net force upward. As the microparticle is constrained to the liquid-air interface, it climbs the global drop profile defined by the above solution of the Laplace equation. One can formulate the energy as the product of the particle's vertical displacement and its weight after the subtraction of the Archimedes force. Thus, the lateral component of this global restorational force is given by:

$$F_{\mathrm{g}} = \left[m - \rho_{\mathrm{l}} \Lambda_{\mathrm{b}} V_{\mathrm{b}}(t) \right] g \frac{dz}{d\rho} \tag{7-6}$$

where $V_{\mathrm{b}}(t)$ is the instantaneous bubble volume. Only the mass of the particle, m, is considered as that of the bubble is insignificant. The dimensionless factor Λ_{b} is the volume fraction of the gas bubble lying below the undisturbed interface, as it is the displaced liquid in this region that gives rise to buoyancy. Note that we only included Λ_{b} for the generality of Equation 7-6. We use a Λ_{b} of unity in the simulations hereafter in accordance with experimental observations. Given the drop profile, the force always points towards the apex.

To quantify the "Cheerios effect", i.e. the inter-particle capillary attraction as a result of the local interfacial distortion, we adopt the Nicolson approximation (3) which assumes that (i) the horizontal force from capillary pressure is insignificant compared to that from buoyancy, and (ii) the small interfacial distortions may be superposed (4). Prior results show that the Nicolson approximation is justified for small Bond numbers $B = R^2 / L_{\mathrm{c}}^2$, or equivalently if the floating object's radius $R \ll L_{\mathrm{c}} = \sqrt{\gamma / \rho_{\mathrm{l}} g}$, the capillary length. Indeed, the L_{c} of our experimental system is approximately 2.7mm, far exceeding the spatial scale of the beating physics. The surface height in the neighbourhood of a floating bubble follows:

$$h(l) = -B\Sigma R K_0(l / L_{\mathrm{c}}) \tag{7-7}$$

where l is the lateral distance from the bubble centre, K_n the modified Bessel function of the second kind of order n, and Σ the buoyancy-corrected dimensionless weight defined by

$2\pi\gamma RB\Sigma = \left[m - \rho_l \Lambda_b V_b(t)\right] g$. Equation 7-7 is a simplified asymptotic result true for $l \ll L_c$. The lateral capillary force experienced by a bubble of volume V_b at a distance l away is therefore:

$$F_c = \left[m - \rho_l \Lambda_b V_b'\right] g B^{3/2} \Sigma K_1(l / L_c) \tag{7-8}$$

Needless to say, the capillary attraction force points towards the centre of the other particle. The $K_1(l/L_c)$ dependence is in agreement with the results derived from an energy approach (5). Readers are directed to (6) for the treatment of scenarios with more than 2 particles.

We next consider the hydrodynamic interactions. In the regime of low Reynolds number and low capillary number such as our system, the drag force for an object at the liquid-air interface is expressed as:

$$\mathbf{F}_d = -6\pi\mu\Lambda_d R_b(t)\mathbf{v}(t) \tag{7-9}$$

where μ is the liquid's dynamic viscosity, R_b the bubble radius, and $\mathbf{v}$ the instantaneous velocity. The drag coefficient Λ_d is a scaling factor depending on the object's geometry, its depth of immersion, the contact angle, surface tension, and the densities of the object and the liquid (6). As Λ_d is difficult to estimate analytically, we assume it is a constant for simplicity and leave it as one of the two free parameters we estimate from experiments, a practice consistent with published models of microparticle motion along a curved interface (2).

An important additional consideration is the significantly increased drag when multiple particles approach one another, caused by the increased resistance to removing the liquid between them (7). We note this inter-particle hydrodynamic interaction particularly because of the noticeable deceleration in our beating system when the edge-to-edge distance between particles were less than $2R_p$ (see, for example, Figure 7-1g between 68 and 69s). The approach velocity was virtually 0 right before contact, suggesting a drag significantly larger than that given by Equation 7-9. Indeed, some previous studies predicted two floating microparticles to accelerate towards each other all the way until they collide if the Stokes' drag expression was not corrected for inter-particle interactions (4).

The most numerically convenient means of accounting for said interactions is to adopt the concept of hydrodynamic mobility (8), as with a number of previous works (6, 9). This correction factor as a function of the inter-particle spacing, l, is given by:

$$G(\lambda) = 1 - \frac{1}{3}\lambda^{-1} + \lambda^{-3} - \frac{15}{4}\lambda^{-4} - \frac{4.46}{1000}(\lambda - 1.7)^{-2.867} \tag{7-10}$$

where $\lambda = l/\max(R_b(t), R_p)$. G, which is typically multiplied to the terminal velocity, approaches 1 for large separations $\lambda \to \infty$ and 0 for $\lambda = 2$ when the objects contact. Equivalently, we divided the drag expression in Equation 7-9 with G in our numerical simulations.

The force expressions in Equations 7-6, 7-8, 7-9, and 7-10 allow us to simulate the motion of each beating particle i with Newton's second law:

$$\frac{d\mathbf{v}_i}{dt} = \frac{1}{m_{\text{eff}}}(\mathbf{F}_{g,i} + \mathbf{F}_{c,i} + \mathbf{F}_{d,i}) \tag{7-11}$$

We followed Ref. (2) in introducing a scaling factor for the effective mass ($m_{\text{eff}} = \Lambda_m m$) to account for the added mass of liquid experienced during particle acceleration. The two fitted parameters of the model, Λ_m = 11.25 and Λ_d = 0.35, were kept constant across simulations of different H_2O_2 concentrations. The model outlined above was solved numerically again with MATLAB's ode45 Runge-Kutta solver. As all three forces are also dependent on the instantaneous bubble volume (equivalently, the radius), we zoom in to the catalytic surface and study the reaction kinetics as the final piece of the puzzle.

7.4. Reaction Kinetics for O_2 Generation

The volume of the O_2 bubble as a function of time, $V_b(t)$, is dictated by the rate of O_2 generation, which in turn is dependent on the free platinum patch surface area $A_{Pt,free}$, as well as the peroxide concentration $[H_2O_2]$. For a given experiment, we assume that the peroxide is in excess and $[H_2O_2]$ is a constant throughout, based on the absence of a shift in the beating frequency (Figure 6-6). A well-studied catalytic reaction, the decomposition kinetics of H_2O_2 on noble metal and oxide surfaces can be described by the classic Langmuir-Hinshelwood mechanism (10, 11):

$$\frac{dV_b}{dt} = \frac{kA_{Pt,free}(V_b)[H_2O_2]}{1 + K_H[H_2O_2]} \tag{7-12}$$

where k is a constant encompassing the reaction rate constant, the specific volume of O_2, and the areal density of the surface sites. The kinetic equation represents that the rate is first order with respect to the concentration of bound surface sites, which are saturated at increasing peroxide

concentration modulated by the binding constant K_H. In the single particle scenario, $A_{Pt,free}$ decreases over time as the bubble underneath the particle starts to limit the accessible catalytic surface area. This leads to a reduced dV_b/dt and therefore a self-limiting reaction. Inspection of the 2-particle beating videos, on the other hand, shows a near-linear increase of the bubble volume up until the moment of merger (Figure 7-2). This observation suggests that the bubbles in the beating system do not grow beyond the critical V_b which marks the onset of catalytic surface blockage, and that $A_{Pt,free} \approx A_{Pt}$. The resultant time-independent reaction rates at different H_2O_2 molarities were fitted to the Langmuir-Hinshelwood kinetics, outputting $k = 3.025 \times 10^{-10} m^4 s^{-1} mol^{-1}$ and K_H = 0.677L/mol (Figure 7-3). This parameterized kinetics was used in our quantitative model to account for the effects of H_2O_2 concentration and Pt surface area, described earlier in Figure 6-1j. All parameters used in the mechanistic model are listed in Table 7-1.

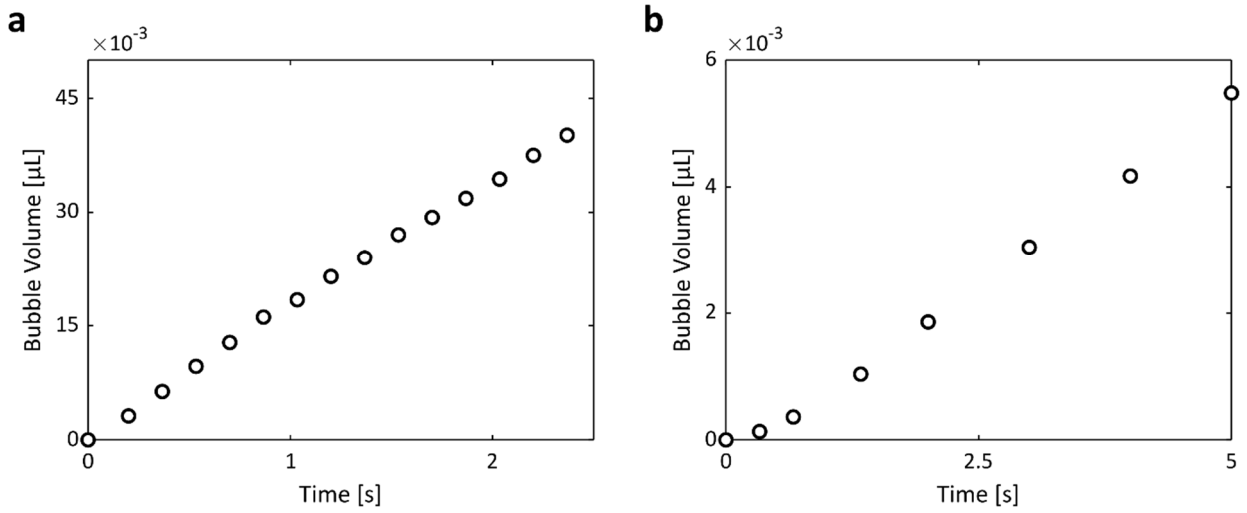

Figure 7-2. While the bubble growth in a single-particle system eventually saturates due to catalytic surface blockage, the bubble volumes in 2-particle systems remain linear with time until their collapse. Thus a constant *k* may be used in 2-particle emergent oscillations. a, two identical 500µm-diameter particles with 250µm-diameter Pt patches. b, two identical 100µm-diameter particles with 100µm-diameter Pt patches.

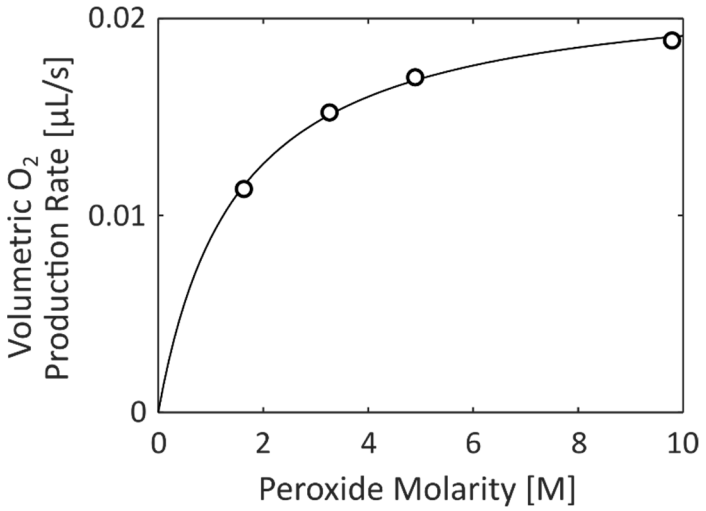

Figure 7-3. The time-independent volumetric bubble production rates as a function of the H_2O_2 concentration is fitted to a Langmuir-Hinshelwood reaction mechanism. The experimental data were collected from a system of two identical 500µm-diameter particles.

Table 7-1. Parameters used in the mechanistic model.

Symbol	Parameter	Conventional Unit
β	Curvature at the apex of the drop	[m^{-1}]
γ	Interfacial tension of the liquid-air interface	[N/m]
γ_c	Capillary constant of the liquid drop	[m^{-2}]
θ	Angle of the liquid-air interface relative to the lateral dimension	[rad]
θ_c	Three phase contact angle	[rad]
λ	Dimensionless distance between two floating objects used in hydrodynamic mobility	[-]
Λ_b	Volume fraction of gas bubble lying below the undisturbed interface	[-]
Λ_d	Effective drag scaling factor	[-]
Λ_m	Effective mass scaling factor	[-]
μ	Dynamic viscosity of the liquid	[$N \cdot s \cdot m^{-2}$]
ρ	Lateral coordinate relative to the drop's apex	[m]
ρ_a	Density of air	[kg/m^3]
ρ_l	Density of liquid	[kg/m^3]
Σ	Buoyancy-corrected dimensionless weight	[-]
A_{Pt}	Surface area of the Pt patch	[m^2]
$A_{Pt,free}$	Accessible area of the Pt patch	[m^2]
B	Bond number	[-]
F_c	Lateral component of the local capillary force between floating objects	[N]
F_d	Lateral component of the drag force	[N]
F_g	Lateral component of the global buoyancy-corrected gravitational force towards the apex	[N]
g	Gravitational acceleration	[m/s^2]
G	Hydrodynamic mobility	[-]
$[H_2O_2]$	Concentration of hydrogen peroxide	[mol/L]
k	Rate constant of peroxide decomposition per unit area	[$m^4 \cdot s^{-1} \cdot mol^{-1}$]
K_H	Surface binding constant of peroxide decomposition	[L/mol]
K_n	Modified Bessel function of the second kind of order n	[-]
l	Lateral coordinate from the centre of a floating object	[m]
L_c	Capillary length	[m]
m	Mass of a microparticle	[kg]
m_{eff}	Effective mass of a microparticle	[kg]
R	Radius of a floating object	[m]
R_b	Instantaneous radius of a bubble	[m]
s	Coordinate along the liquid-air interface relative to the drop's apex	[m]
t	Time	[s]
v	Lateral component of a microparticle's velocity	[m/s]
V	Integral volume used in calculating the drop profile	[m^3]
V_b, V_b'	Volume of a bubble	[m^3]
V_{drop}	Volume of the drop	[m^3]
z	Vertical coordinate relative to the drop's apex	[m]

7.5. Comparison between Mechanistic Model Simulations and Experiments

We have previously demonstrated the agreement between experimental and simulated frequency-concentration curves in Figure 6-1j. In addition, the mechanistic simulation captured even the detailed dynamics of the breathing radius' time evolution (Figure 7-4b), in addition to the oscillation's amplitude and frequency. That is, each phase within the cycle of mutual approach, contact, bubble merger, and bubble collapse is accounted for (Figure 7-4a), furthermore with the simulated bubble radius over time matching very well with that extracted from the 2-particle oscillation video (Figure 7-4c).

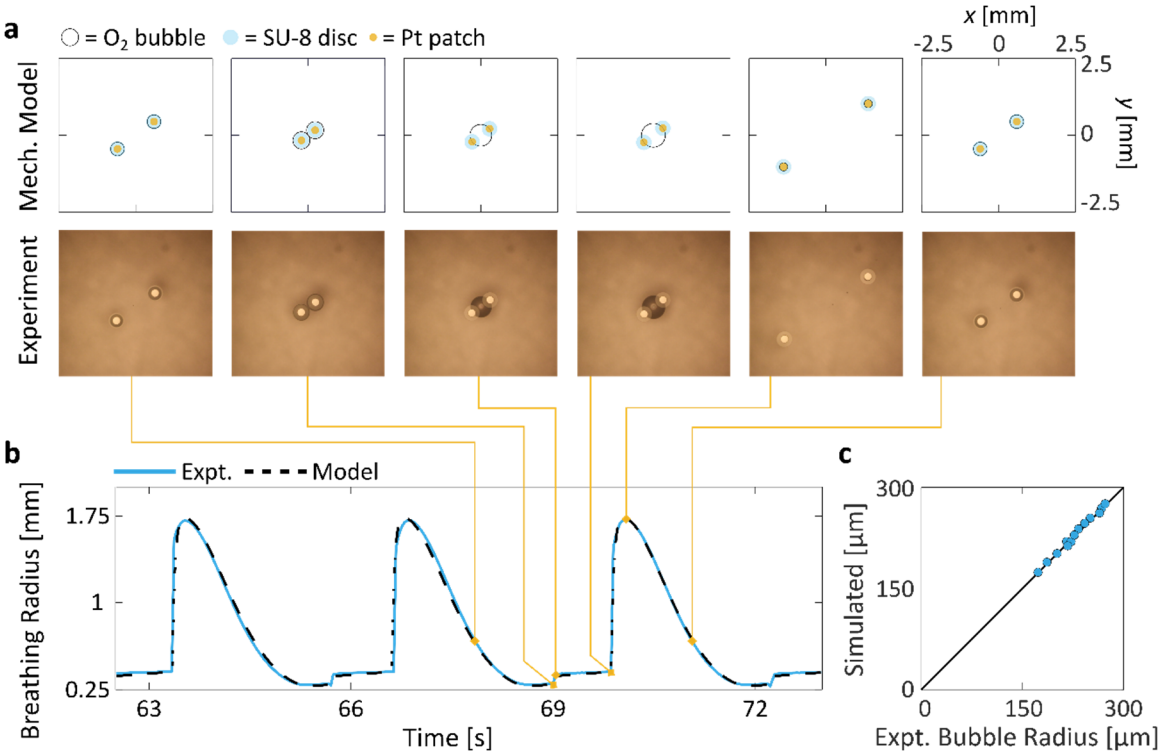

Figure 7-4. Detailed comparison between experimental and simulated beating behaviours of two particles. a, Mechanistic model simulations and experimental snapshots taken at representative stages of a beating cycle. b, The simulation and experiments are in excellent agreement, evident from the matching curves of the breathing radius, previously also shown in Figure 6-1g. We note that the mechanistic model captures fine details of the self-oscillation, such as the subtle step change in (b) at approximately 69s. The step increase was a result of the merged bubble pushing the particles outwards slightly, reflected by both the experiment and simulation in (a). c, This panel shows the excellent agreement between the experimental bubble radii and those predicted by the mechanistic model. The former were measured manually from the raw video data.

The mechanistic model furthermore was able to capture the dependence of the oscillation amplitude and frequency on the H_2O_2 drop volume (Figure 7-5) as well as the particle size (Figure 7-6). A larger drop of H_2O_2 solution corresponds to a reduced curvature of the liquid-air interface the particles reside in, which in turn weakens the global restorational force that resists parting of the particles. The breathing radius (Figure 7-5a) therefore increases with the H_2O_2 volume, which consequently lengthens the intervals between consecutive bubble collapses (Figure 7-5a). Due to the periodicity of all these 2-particle systems, the respective interarrival times are equivalent to the periods of oscillation, or the reciprocal of the oscillation frequencies. The scaling factors Λ_d and Λ_m were assumed to be unchanged from the 1mL base case, but the threshold bubble diameter increases with increasing drop size, as expected. We modeled the threshold diameter with a simple linear relation of $(143.7V_{drop} + 652.8)\mu m$, where V_{drop} is in mL. Naturally, a larger threshold bubble diameter corresponds to a larger amount of surface energy stored, which scales with R_b squared (§6.10.1). Given that the particle properties remain the same, the impulse resulting from the bubble collapse was proportionally scaled with the threshold R_b from the 1mL base case. The mechanistic model (solid blue curves) captures both the maximum breathing radius (i.e., the oscillation amplitude) as well as the interarrival times satisfactorily as a function of the drop volume.

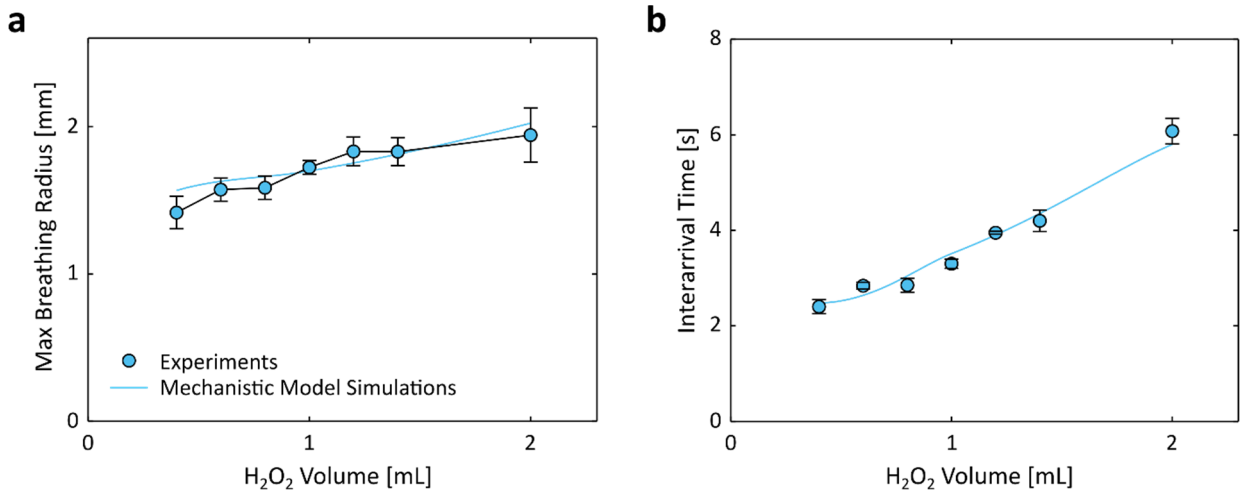

Figure 7-5. Maximum breathing radius and interarrival time of two identical particles as a function of the H_2O_2 volume. Each error bar denotes a standard deviation among the oscillation cycles within an experiment.

The robust 2-particle emergent oscillation among 500µm-diameter particles was observed to scale downwards to at least 100µm-diameter particles as well. As expected, smaller particles do not travel as far when they mechanically beat (Figure 7-6a), as the threshold bubble size is significantly

reduced which translates to a reduced impulse imparted onto the outgoing particles upon collapse. Contrary to the trend seen above in Figure 7-5, however, the lower oscillation amplitude is accompanied by a longer, rather than shorter, period (Figure 7-6b). This is attributed to the downsized catalytic patch, which causes the O_2 generation rate to be scaled down: the Pt patch size on 100µm particles is 16% that on 500µm particles. Of note, the effect is partially offset by the reduced threshold R_b for smaller particles, which was determined to be 250, 265, and 388µm respectively for 100, 250, and 500µm particles. As with the simulations in Figure 7-5, the impulse upon bubble collapse was scaled proportionally by the threshold radius. Additionally, however, the impulse was also scaled with the particle mass, m, to a half order. Equivalently, it scales proportionally with the particle diameter. Without any additional adjustment or data fitting, the mechanistic model captures the impact of particle diameters rather well on the oscillation amplitude and frequency, evident from the agreement show in Figure 7-6.

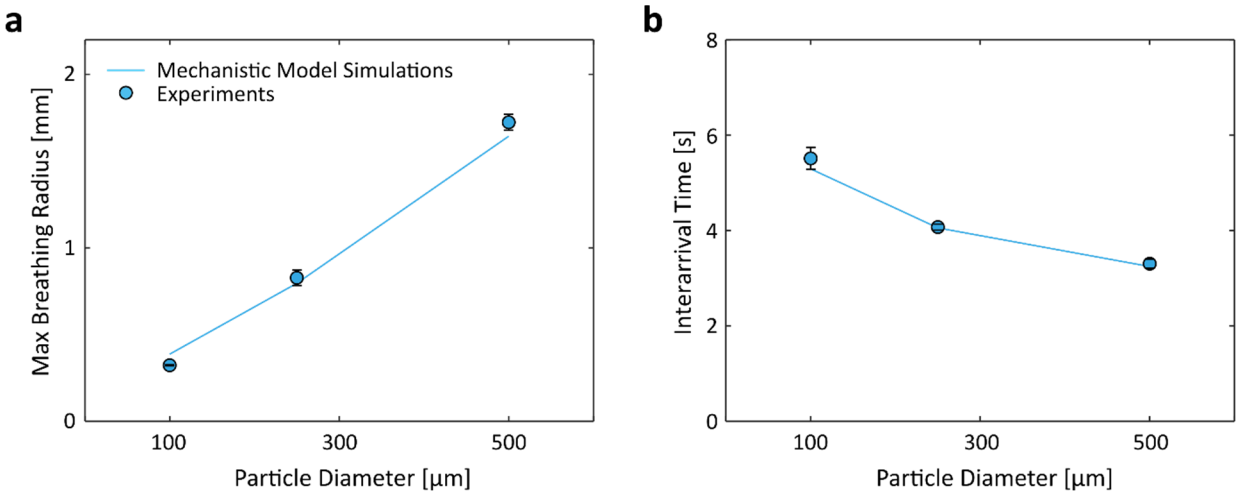

Figure 7-6. Maximum breathing radius and interarrival time of two identical particles as a function of the particle size. All particles were fabricated by depositing 5nm Cr and 50nm Pt onto 10µm-thick SU-8 polymer. The 500µm, 250µm, and 100µm-diameter particles were designed to have Pt patches 250µm, 125µm, and 100µm in diameter, respectively. Each error bar denotes a standard deviation among the oscillation cycles within an experiment.

7.6. References

1. Del Rio, O. I. & Neumann, A. W. Axisymmetric drop shape analysis: Computational methods for the measurement of interfacial properties from the shape and dimensions of pendant and sessile drops. Journal of Colloid and Interface Science 196, 136–147. issn: 00219797 (1997).
2. Hauser, A. W., Sundaram, S. & Hayward, R. C. Photothermocapillary oscillators. Physical Review Letters 121, 158001. issn: 0031-9007 (Oct. 2018).
3. Nicolson, M. M. The interaction between floating particles. Mathematical Proceedings of the Cambridge Philosophical Society 45, 288–295. issn: 14698064 (1949).
4. Vella, D. & Mahadevan, L. The "Cheerios effect". American Journal of Physics 73, 817–825 (2005).
5. Kralchevsky, P. A. & Nagayama, K. Capillary interactions between particles bound to interfaces, liquid films and biomembranes. Advances in Colloid and Interface Science 85, 145–192. issn: 00018686 (2000).
6. Dalbe, M.-J., Cosic, D., Berhanu, M. & Kudrolli, A. Aggregation of frictional particles due to capillary attraction. Physical Review E 83, 051403. issn: 1539-3755. arXiv: 1104.3820 (May 2011).
7. Das, S., Koplik, J., Somasundaran, P. & Maldarelli, C. Pairwise hydrodynamic interactions of spherical colloids at a gas-liquid interface. Journal of Fluid Mechanics 915, A99. issn: 0022-1120 (May 2021).
8. Batchelor, G. K. Brownian diffusion of particles with hydrodynamic interaction. Journal of Fluid Mechanics 74, 1–29. issn: 14697645 (1976).
9. Vassileva, N. D., Van Den Ende, D., Mugele, F. & Mellema, J. Capillary forces between spherical particles floating at a liquid-liquid interface. Langmuir 21, 11190–11200. issn: 07437463 (2005).
10. Plauck, A., Stangland, E. E., Dumesic, J. A. & Mavrikakis, M. Active sites and mechanisms for H2O2 decomposition over Pd catalysts. Proceedings of the National Academy of Sciences 113, E1973–E1982 (2016).

11. Lin, S.-S. & Gurol, M. D. Catalytic Decomposition of Hydrogen Peroxide on Iron Oxide: Kinetics, Mechanism, and Implications. Environmental Science & Technology 32, 1417–1423. issn: 0013-936X (1998).